

Univerzita Karlova v Praze  
Matematicko-fyzikální fakulta  
a  
L'Université Paris-Sud XI

# DISERTAČNÍ PRÁCE



David Šálek

## Měření longitudinální strukturní funkce protonu v difrakci na experimentu H1

Ústav částicové a jaderné fyziky

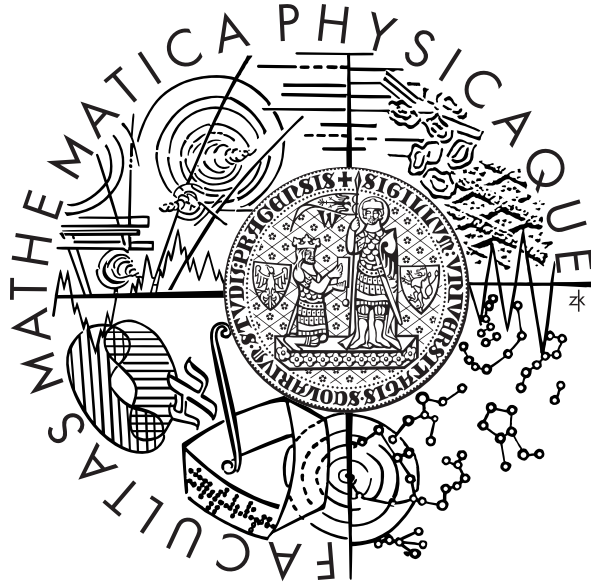
Vedoucí práce: RNDr. Alice Valkárová, DrSc.  
Dr. Christophe Royon

Studijní program: Subjaderná fyzika (F9)



Charles University in Prague  
Faculty of Mathematics and Physics  
and  
Univeristy Paris XI in Orsay

# DOCTORAL THESIS



David Šálek

**Measurement of the Longitudinal Proton  
Structure Function in Diffraction  
at the H1 Experiment  
and  
Prospects for Diffraction at LHC**

Institute of Particle and Nuclear Physics

Supervisors: RNDr. Alice Valkárová, DrSc.  
Dr. Christophe Royon

Field of Study: Particle Physics

Prohlašuji, že jsem svou disertační práci napsal samostatně a výhradně s použitím citovaných pramenů. Souhlasím se zapůjčováním práce.

V Praze dne

# Abstract

A measurement of the longitudinal diffractive structure function  $F_L^D$  using the H1 detector at HERA is presented. The structure function is extracted from first measurements of the diffractive cross section  $ep \rightarrow eXY$  at centre of mass energies  $\sqrt{s}$  of 225 and 252 GeV at high values of inelasticity  $y$ , together with a new measurement at  $\sqrt{s}$  of 319 GeV, using data taken in 2006 and 2007. Previous H1 data at  $\sqrt{s}$  of 301 GeV complete the kinematic coverage needed to extract  $F_L^D$  in the range of photon virtualities  $2.5 < Q^2 < 100 \text{ GeV}^2$  and fractional proton longitudinal momentum loss  $10^{-4} < x_{\mathbb{P}} < 10^{-2}$ . The measured  $F_L^D$  is compared with leading twist predictions based on diffractive parton densities extracted in NLO QCD fits to previous diffractive DIS data and to a model which additionally includes a higher twist contribution derived from a colour dipole approach. The photoabsorption ratio for diffraction  $R^D$  is extracted for  $Q^2 > 7 \text{ GeV}^2$  and compared to the analogous quantity for inclusive DIS.



# Acknowledgements

In the first place, I would like to express my gratitude towards Alice Valkárová as she has been my supervisor since the beginning of my Master studies, and opened my way to become a member of the H1 Collaboration. She has always been there to help me in all the difficult decisions I had to take, and supported me in all the activities I took part in, being both critical and encouraging.

I am also grateful I had a chance to work on the analysis presented here. It brought me together with Paul Laycock and Paul Newman, who I enjoyed working with a lot. It was a challenging and rewarding work (sometimes hard, mostly enjoyable). Especially with Paul Laycock, we had almost day-to-day fruitful discussions over e-mail or skype (or over a pint of beer when we met). At this point, I would also like to thank to Sasha Glazov and Alexey Petrukhin for their expertise.

Let me also thank to Christophe Royon who kindly offered me cooperation on various projects across the field of particle physics, and thus enabled me to gain work experience beyond H1, which I value very much. He also acquainted me with Jean-François Genat to whom I owe sincere apologies for not being able to finish what we agreed on.

Thanks to my colleagues from Prague Richard Polifka and Karel Černý as it was always nice to take a break and chat.

And finally, a special thanks to my parents, grandparents, my brother and especially to my beloved wife Jiřina for giving me all the support as well as for their patience. I dedicate this work to my family since it would not have happened without them being around.

The work was supported by the R&D project LA09042 provided by the Ministry of Education, Youth and Sports (MŠMT) and the grant SVV-2010-261 309.



# Contents

<b>1</b>	<b>Introduction</b>	<b>1</b>
<b>2</b>	<b>DIS at HERA</b>	<b>3</b>
2.1	Deep Inelastic Scattering . . . . .	3
2.1.1	Kinematics . . . . .	3
2.1.2	Elastic Scattering . . . . .	4
2.1.3	Deep Inelastic Scattering of Electronson Protons . . . . .	4
2.1.4	Quark Parton Model . . . . .	5
2.1.5	Quantum Chromodynamics . . . . .	6
2.1.6	Cross Sections . . . . .	8
2.1.7	Longitudinal Proton Structure Function . . . . .	9
2.2	Diffraction . . . . .	9
2.2.1	Regge Theory . . . . .	9
2.2.2	The Pomeron . . . . .	10
2.3	Diffraction DIS at HERA . . . . .	11
2.3.1	Diffraction Kinematics . . . . .	11
2.3.2	Diffraction Cross-Sections . . . . .	14
2.3.3	QCD Hard Scattering Factorisation . . . . .	15
2.3.4	Regge Factorisation and the Resolved Pomeron Model . . . . .	15
2.3.5	Dipole and Saturation Models . . . . .	15
<b>3</b>	<b>Motivation and Recent Results</b>	<b>19</b>
3.1	QCD Fits . . . . .	19
3.1.1	QCD Fit to the Inclusive DIS Data . . . . .	19
3.1.2	The $\lambda$ Fit . . . . .	20
3.1.3	QCD Fit to the Diffraction Data . . . . .	24
3.1.4	Analysis with Higher Twist . . . . .	25
3.2	Testing the Diffraction Gluon Densities . . . . .	25
3.2.1	Diffraction Open Charm Production in DIS . . . . .	25
3.2.2	Diffraction Dijets in DIS . . . . .	30
3.2.3	Diffraction Longitudinal Proton StructureFunction . . . . .	33
3.3	Geometric Scaling . . . . .	33
3.3.1	First Observation . . . . .	33
3.3.2	Scaling Properties in DIS . . . . .	35
3.4	From HERA to Tevatron . . . . .	35
3.4.1	Selection of Diffraction Events . . . . .	35
3.4.2	Testing QCD Factorisation at Tevatron . . . . .	36

3.4.3	Diffractive Exclusive Event Production . . . . .	38
3.4.4	Exclusive Dijet Production . . . . .	40
3.5	Prospects for Diffraction at LHC . . . . .	40
3.5.1	Physics Motivation . . . . .	42
3.5.2	Forward Detectors . . . . .	42
<b>4</b>	<b>HERA and the H1 Detector</b>	<b>45</b>
4.1	HERA Accelerator . . . . .	45
4.2	Overview of the H1 Detector . . . . .	45
4.3	Tracking . . . . .	46
4.3.1	The Central Track Detectors . . . . .	46
4.3.2	The Backward Silicon Tracker . . . . .	49
4.4	Calorimetry . . . . .	49
4.4.1	The Liquid Argon Calorimeter . . . . .	49
4.4.2	The Plug Calorimeter . . . . .	51
4.4.3	The SPACAL Calorimeter . . . . .	51
4.5	The Forward Detectors . . . . .	51
4.5.1	The Forward Muon Detector . . . . .	51
4.5.2	The Forward Tagger System . . . . .	53
4.6	The Time of Flight System . . . . .	53
4.7	The Luminosity System . . . . .	53
4.8	Data Acquisition and Triggering . . . . .	53
<b>5</b>	<b>Measurement Strategy</b>	<b>57</b>
5.1	Extraction of the Longitudinal Proton Structure Functions . . . . .	57
5.1.1	Extraction of $F_L$ . . . . .	57
5.1.2	Extraction of $F_L^D$ . . . . .	58
5.2	Running at Low Proton Beam Energies . . . . .	59
5.3	Overview of the $F_L^D$ Analysis . . . . .	60
<b>6</b>	<b><math>F_L</math></b>	<b>63</b>
6.1	Data . . . . .	63
6.2	Monte Carlo . . . . .	63
6.3	Selection of NC DIS Events . . . . .	64
6.3.1	Run Selection . . . . .	64
6.3.2	The Trigger Selection . . . . .	65
6.3.3	Vertex Requirement . . . . .	66
6.3.4	The Scattered Positron Finder . . . . .	67
6.3.5	Reconstruction of the Inclusive Final State . . . . .	74
6.3.6	Background Rejection . . . . .	77
6.3.7	The Final Inclusive NC DIS Selection . . . . .	78
6.3.8	Photoproduction Background Subtraction . . . . .	78
6.4	Accuracy of the Simulation . . . . .	83
6.4.1	Trigger Efficiency . . . . .	85
6.4.2	Vertex Reconstruction Efficiency . . . . .	90
6.4.3	Track–Cluster Link Efficiency . . . . .	93
6.4.4	Charge Reconstruction Efficiency . . . . .	98
6.4.5	Efficiency of the $r_{log}$ Cut . . . . .	100

	6.4.6 Hadronic Final State Calibration . . . . .	100
6.5	Description of Data . . . . .	106
6.6	Cross Section . . . . .	108
	6.6.1 Cross-Section Definition . . . . .	113
	6.6.2 Cross Section . . . . .	114
6.7	Summary of the $F_L$ Analysis . . . . .	114
<b>7</b>	<b><math>F_L^D</math></b>	<b>117</b>
7.1	Data . . . . .	117
7.2	Monte Carlo . . . . .	117
	7.2.1 Simulation of Signal Processes . . . . .	117
	7.2.2 Simulation of Background Processes . . . . .	118
	7.2.3 Simulation of Proton Dissociation . . . . .	120
7.3	Selection of Diffractive DIS Events . . . . .	120
	7.3.1 $\eta_{max}$ Selection . . . . .	121
	7.3.2 Forward Detector Selection . . . . .	122
	7.3.3 Reconstruction of Diffractive Kinematics . . . . .	127
	7.3.4 Vertex Requirement . . . . .	128
	7.3.5 The Final Diffractive Selection . . . . .	128
	7.3.6 Photoproduction Background Subtraction . . . . .	129
7.4	Accuracy of the Simulation . . . . .	131
	7.4.1 Efficiency of the Forward Detector Selection . . . . .	131
	7.4.2 Vertex Reconstruction Efficiency . . . . .	134
	7.4.3 Track–Cluster Link Efficiency . . . . .	138
	7.4.4 Hadronic Final State Calibration . . . . .	138
7.5	Description of Data . . . . .	142
	7.5.1 RAPGAP components . . . . .	142
	7.5.2 Normalization of the DIFFVM Simulation . . . . .	142
	7.5.3 Normalisation of the COMPTON Simulation . . . . .	146
	7.5.4 Control Plots . . . . .	146
7.6	Cross Section . . . . .	148
	7.6.1 Cross Section Definition . . . . .	148
	7.6.2 Bin Selection . . . . .	148
	7.6.3 Acceptance, Purity, Stability . . . . .	153
	7.6.4 Correcting Data using Simulations . . . . .	154
	7.6.5 Correlated Systematics . . . . .	156
	7.6.6 Uncorrelated Systematics . . . . .	160
	7.6.7 Cross Section . . . . .	162
7.7	Longitudinal Structure Function . . . . .	164
	7.7.1 Sensitivity to $F_L^D$ and Relative Normalisation . . . . .	164
	7.7.2 Extraction of the Structure Functions from the Fits . . . . .	164
	7.7.3 Ratio $R^D$ . . . . .	172
	7.7.4 Ratio $R^D/R$ . . . . .	174

<b>8</b>	<b>Results and Interpretation</b>	<b>177</b>
8.1	Summary of the Results . . . . .	177
8.1.1	$F_L^D$ . . . . .	177
8.1.2	$R^D$ . . . . .	177
8.1.3	$R^D/R$ . . . . .	180
8.2	Conclusions . . . . .	180
<b>A</b>	<b>Hadronic Final State Calibration</b>	<b>189</b>
A.1	Introduction . . . . .	189
A.2	Reference for the Hadronic Calibrations . . . . .	190
A.3	Iterative Calibration Method . . . . .	192
A.4	Calibration Procedure . . . . .	193
A.4.1	Calibration Constants . . . . .	193
A.4.2	Data Selection . . . . .	194
A.4.3	Iterative Method . . . . .	196
A.4.4	Weighting Schemes . . . . .	196
A.4.5	Extraction of the Calibration Constants . . . . .	198
A.4.6	Convergence . . . . .	201
A.5	Results . . . . .	202
A.5.1	HERA-I Data . . . . .	202
A.5.2	HERA-II Data . . . . .	202
A.5.3	Model Dependence . . . . .	205
A.6	Summary . . . . .	205
<b>B</b>	<b>Simulation of Fast Timing Electronics</b>	<b>213</b>
<b>C</b>	<b>Geometric Scaling</b>	<b>215</b>
<b>D</b>	<b>Cross Section Tables</b>	<b>217</b>
<b>E</b>	<b>H1 Preliminary <math>F_L^D</math> Results</b>	<b>223</b>

# Chapter 1

## Introduction

The observation that a significant subset of Deep-Inelastic Scattering (DIS) events at HERA contains a large gap in activity in the forward region [9], signifying a colour singlet exchange, prompted much theoretical and experimental activity. Since then, HERA has proved to be a rich playground for the study of diffraction. In particular, the study of inclusive and exclusive diffractive DIS (DDIS) events has provided a wealth of experimental data with a hard scale provided by the virtual photon, stimulating theoretical hopes of understanding diffraction in terms of perturbative quantum chromodynamics (QCD). Descriptions of DDIS where the photon fluctuates into a colour dipole which subsequently scatters elastically from the proton have also been shown to be successful [10].

It has been shown by Collins [11] that, among other processes, the NC DDIS process  $ep \rightarrow eXp$  at HERA obeys the QCD factorisation theorem. While such a proof allows for a description of DDIS in terms of parton densities convoluted with hard scattering matrix elements, these diffractive parton density functions (DPDFs) depend on four kinematic variables. In order to proceed in this picture, an additional approximation is often made whereby the proton vertex dynamics factorise from the hard scattering - proton vertex factorisation. While this factorisation has no sound basis in theory, measurements of the diffractive cross section from both H1 and ZEUS [12, 13, 14] show that it holds well enough such that meaningful next-to-leading order (NLO) QCD fits can be made to the data [12, 15, 16].

Measurements of the dijet cross section in DDIS allow tests of the DPDFs extracted in fits to inclusive DDIS data. This process, which is known to be dominated by boson-gluon fusion, is particularly sensitive to the gluon DPDF at large fractional momenta  $z_P$ , and has been successfully used to distinguish between different gluon DPDFs [17]. DDIS events containing charm particles in the final state have similarly been used to test the gluon DPDF [18], although these data have less sensitivity to large fractional momenta.

By analogy with the inclusive DIS case, the cross section for DDIS can be expressed in terms of a linear combination of structure functions,  $F_2^D$  and  $F_L^D$ . While  $F_2^D$  describes the total photon-proton cross section,  $F_L^D$  is only sensitive to the longitudinally polarised photon contribution. As for its inclusive counterpart,  $F_L^D$  is thus zero in the quark-parton model, but may acquire a non-zero value,  $0 < F_L^D < F_2^D$  in QCD, with leading twist contributions dependent on both the diffractive quark and gluon densities at leading twist [19]. The dominant role played by gluons in the diffractive parton den-

sities [12, 15] implies that the leading twist  $F_L^D$  should be approximately proportional to the diffractive gluon density and should be correspondingly large. A measurement of  $F_L^D$  to even modest precision would provide a powerful independent tool to verify our understanding of the underlying dynamics and to test the gluon DPDF. In particular, the jet and  $D^*$  data are not able to determine the gluon density at lowest  $x$  values where novel effects such as parton saturation [20] or non-DGLAP dynamics [21, 22] could be important.

In this analysis, positron-proton collision data taken with the H1 detector at HERA in 2006 and 2007 are used to measure the reduced cross-section at large inelasticity,  $y$ , using datasets with different proton beam energies, leading to an extraction of  $F_L^D$ . Dedicated low and medium energy data with proton beam energies of  $E_p = 460$  and  $575$  GeV, together with data at the nominal beam energy of  $920$  GeV are analysed. The  $920$  GeV data are limited to  $Q^2 > 7$  GeV<sup>2</sup>, while the  $460$  and  $575$  data extend down to  $Q^2 = 2.5$  GeV<sup>2</sup>. Previously published data at  $820$  GeV [12] are therefore used in addition.  $F_L^D$  is extracted using data in the ranges  $2.5 < Q^2 < 100$  GeV<sup>2</sup> and  $10^{-4} < x_P < 10^{-2}$ . The ratio of  $F_L^D$  to the inclusive longitudinal structure function  $F_L$  is measured for  $Q^2 > 7$  GeV<sup>2</sup> and  $10^{-3} < x_P < 10^{-2}$ .

# Chapter 2

## DIS at HERA

### 2.1 Deep Inelastic Scattering

#### 2.1.1 Kinematics

This section introduces kinematical quantities for any process, elastic as well as inelastic, where a lepton of any kind scatters on a proton

$$l(k) + p(p) \rightarrow l(k') + X. \quad (2.1)$$

Here,  $X$  denotes any final state allowed by conservation laws and  $k$ ,  $p$ ,  $k'$  denote the four-momenta of the corresponding particles. Depending on the charge of the lepton, the processes are referred to as either **neutral current** or **charged current** processes. Diagrams of these processes are shown in Fig. 2.1.

The following set of Lorentz invariant variables is introduced to describe the kinematics of a process:

$$s = (k + p)^2, \quad (2.2)$$

$$Q^2 = -q^2 = -(k - k')^2, \quad (2.3)$$

$$y = \frac{qp}{kp} = \frac{E_{lab} - E'_{lab}}{E_{lab}}, \quad (2.4)$$

$$x = \frac{Q^2}{2pq}, \quad (2.5)$$

$$W^2 = (q + p)^2, \quad (2.6)$$

where  $E_{lab}$  and  $E'_{lab}$  are the energies of the initial and the scattered lepton in the laboratory frame. The interpretation of  $s$  as the squared energy in the central mass system, and  $Q^2$  as the squared momentum transfer is straightforward. The variable  $y$ , expressed in the laboratory frame, describes the relative loss of energy of the scattered lepton and is interpreted as a measure of inelasticity of the process. The interpretation of  $x$  as a fraction of the proton momentum carried by a struck parton is explained in Section 2.1.4. The variable  $W$  is the invariant mass of the hadronic system  $X$ .

An inelastic scattering process is fully described by any two kinematic variables from  $Q^2$ ,  $x$ ,  $y$ . In other words, only two of the kinematic variables from the list are independent. In case of an elastic process, the full kinematics is described by a single kinematic variable.

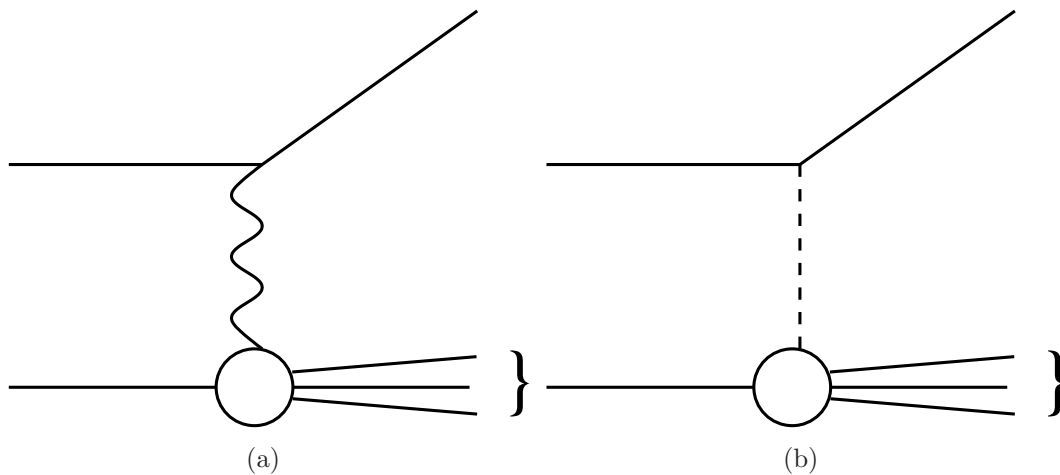


Figure 2.1: Standard Model diagrams for a neutral current (a) and charged current (b) deep-inelastic scattering processes.

### 2.1.2 Elastic Scattering of an Electron on a Pointlike Fermion or Boson

In the lowest order quantum electrodynamics, the process of scattering an electron on another fermion or boson particle is described by one photon exchange diagram. [23] In case of a spin  $\frac{1}{2}$  fermion, the cross section of such process reads

$$\frac{d\sigma}{dQ^2} = \frac{2\pi\alpha^2}{Q^4} \left[ 1 + (1-y)^2 - \frac{M^2 y}{kp} \right], \quad (2.7)$$

where the electron mass is neglected and  $M$  is the mass of the other fermion. The elastic scattering of an electron and a spin 0 boson of mass  $M$  is described by the cross section

$$\frac{d\sigma}{dQ^2} = \frac{2\pi\alpha^2}{Q^4} \left[ (1-y) - \frac{M^2 y}{kp} \right]. \quad (2.8)$$

The two equations above lead to the following observation. To see a difference between the scattering on fermions and bosons requires large inelasticity  $y$ .

### 2.1.3 Deep Inelastic Scattering of Electrons on Protons

The inelastic scattering of unpolarised electrons on unpolarised protons is uniquely specified by two independent kinematical variables. In terms of  $Q^2$  and  $x$ , the deep inelastic cross section in its general form reads

$$\frac{d^2\sigma}{dx dQ^2} = \frac{4\pi\alpha^2}{xQ^4} \left[ \left( 1 - y - \frac{M_p^2 xy}{s} \right) F_2(x, Q^2) + y^2 2xF_1(x, Q^2) \right], \quad (2.9)$$

where  $F_1(x, Q^2)$  and  $F_2(x, Q^2)$  are the structure functions of the proton. The form of Eq. 2.9 follows from the fundamental properties of electromagnetic interactions: Lorentz invariance, unitarity, gauge invariance and parity conservation. [23]

### 2.1.4 Quark Parton Model

The concept of partons as constituents of the proton emerged from Feynman's idea that the deep inelastic scattering cross section can be expressed as a sum of elastic cross sections of the electron on partons. In deep inelastic scattering, which is characterised by  $Q^2 \gg M_p^2$ , the proton can be viewed in the infinite momentum frame where the transverse momenta of constituent partons can be safely neglected with respect to the longitudinal momentum of the proton. The parton four-momentum can be expressed as  $p = \xi P$ , where  $0 < \xi < 1$ . The momentum conservation in the elastic scattering of the parton and the exchanged photon gives

$$(p')^2 = (p + q)^2 = p^2 - Q^2 + 2pq. \quad (2.10)$$

Neglecting the parton mass in this equation leads to the following prescription

$$\xi = \frac{Q^2}{2pq}. \quad (2.11)$$

Therefore, the variable  $\xi$  can be identified with  $x$  which can be interpreted as a proton momentum fraction carried by the interacting parton.

The deep inelastic cross section given in Eq. 2.9 in a limit  $s \rightarrow \infty$  reduces to

$$\frac{d^2\sigma}{dx dQ^2} = \frac{4\pi\alpha^2}{xQ^4} \frac{F_2(x, Q^2)}{x} \quad (2.12)$$

where only one structure function is involved. In the same limit, both elastic cross sections given in Eq. 2.7 and 2.8 transform into

$$\frac{d\sigma}{dQ^2} = \frac{4\pi\alpha^2 e_p^2}{Q^4}. \quad (2.13)$$

The similarity of these two equations together with the concept of partons lead to the following definition of the structure function

$$F_2(x) = x \sum_i e_i^2 d_i(x) \quad (2.14)$$

where  $d_i(x)$  describes the probability of finding a parton with fraction  $x$  of the proton momentum and electric charge  $e_i$ .

Choosing the structure function  $F_1$  so that

$$F_2(x) = 2xF_1(x) \quad (2.15)$$

directly transforms the deep inelastic scattering cross section in Eq. 2.9 into

$$\frac{d^2\sigma}{dx dQ^2} = \frac{2\pi\alpha^2}{xQ^4} [1 + (1 - y)^2] \cdot F_2(x). \quad (2.16)$$

The form of the structure function  $F_2$  in Eq. 2.14 and the cross section for the elastic scattering of electrons and fermions in Eq. 2.7 lead to the following conclusion. If the so-called **Callan–Gross relation** [24] in Eq. 2.15 holds then the constituent partons are spin  $\frac{1}{2}$  particles. The SLAC experiment proved that the **Callan–Gross relation**

is correct [23]. Partons were identified with quarks, and the **quark parton model** was born. However, it is important to stress that originally, the concepts of quarks and partons are not identical.

The structure function  $F_2$  in the **quark parton model** can be written in terms of quark and anti-quark distribution functions,  $q(x)$  and  $\bar{q}(x)$ , as

$$F_2(x, Q^2) = x \sum_i e_i^2 [q_i(x) + \bar{q}_i(x)]. \quad (2.17)$$

Both quark and anti-quark distribution functions behave roughly as  $1/x$  for  $x \rightarrow \infty$  causing the integrals  $\int_0^1 q(x)dx$  to diverge. This implies that the number of partons in the proton is finite. However, there is a class of distribution functions, called **valence**, that lead to finite integrals that are consistent with the prediction of the additive quark model. They are defined as

$$q_{valence}(x) = q(x) - \bar{q}(x). \quad (2.18)$$

All the remaining quarks emerge from a gluon radiation and production of virtual quark anti-quark pairs. These are described by the **sea** distributions

$$q_{sea}(x) = \bar{q}_{sea}(x). \quad (2.19)$$

### 2.1.5 Quantum Chromodynamics

Interactions of quarks are described by a field theory of strong interactions, Quantum Chromodynamics (QCD) [25]. It is a non-Abelian gauge theory based on the SU(3) gauge group, and has the following characteristics

- Each quark is ascribed a new quantum number called colour. There are three colours, R, G, B, and corresponding anti-colours.
- The gauge bosons of the strong interactions are eight massless gluons with no electric charge. As a consequence of the non-Abelian nature of QCD, gluons carry colour charges and are therefore able to self-interact, producing three-gluon as well as four-gluon vertices.
- The strong interaction is characterised by a strong coupling constant  $\alpha_s$ .
- All physically observable objects are colour singlets. They are either the  $q\bar{q}$  states called mesons, or  $qqq$  states called baryons. Quarks and gluons carry colour charge and therefore do not appear as free particles. This behaviour is known as **colour confinement**.

#### Running Coupling Constant and Asymptotic Freedom

The colour confinement together with the QPM assumption of quasi-free partons is reflected in the form of the strong potential. The coupling strength of the interaction is small at short distances (high momentum transfer regime) and large at long distances. This leads to the confinement of quarks in hadrons. To account for these changes, the coupling strength should vary with the momentum transfer (running coupling constant).

Due to the gluon self-interactions the higher order contributions to the gluon propagator lead to infinities. These infinities are removed by a renormalisation procedure which introduces a renormalisation scale  $\mu^2$  at which the ultraviolet loop divergences are subtracted. This leads to a dependence of the renormalised coupling constant  $\alpha_s$  on the renormalisation scale  $\mu^2$ . However, physical observables  $R(Q^2/\mu^2, \alpha_s)$  when computed up to all orders of perturbation theory should not depend on an arbitrary renormalisation scale. Any explicit dependence of  $R$  on  $\mu^2$  should therefore be cancelled by the dependence of  $\alpha_s$  on  $\mu^2$ . This is mathematically expressed in the so-called renormalisation group equation

$$\mu^2 \frac{\partial R}{\partial \mu^2} + \mu^2 \frac{\partial \alpha_s}{\partial \mu^2} \frac{\partial R}{\partial \alpha_s} = 0. \quad (2.20)$$

In a one-loop approximation, the solution for the dependence of the strong coupling constant  $\alpha_s$  on the renormalisation scale  $\mu^2$  can be written as

$$\alpha_s(\mu^2 = Q^2) = \frac{\alpha_s(\mu_0^2)}{1 + \alpha_s(\mu_0^2)\beta_0 \ln(\frac{Q^2}{\mu_0^2})} \quad (2.21)$$

where  $\mu_0^2$  is a chosen reference scale and  $\beta_0 = 33 - 2n_f$ . At small distances, large energy scale  $\mu^2 \rightarrow \infty$ , the coupling between quarks and gluons becomes small,  $\alpha_s \rightarrow 0$ , and the quarks inside a proton can be treated as quasi-free particles. This behaviour is called **asymptotic freedom**. This property is unique to non-Abelian gauge theories. For  $\mu^2 \rightarrow 0$ , the coupling is seen to diverge. This can be viewed as a reason for the confinement of quarks and gluons inside hadrons. [23]

### DGLAP Evolution Equations

The parton distribution functions (PDF) cannot be calculated from first principles. However, the  $Q^2$  dependence of PDF's can be calculated within perturbative QCD using the DGLAP (Dokshitzer-Gribov-Lipatov-Altarelli-Parisi) evolution equations [26, 27, 28, 29]:

$$\frac{dq_i(x, M)}{d \ln M} = \frac{\alpha_s(M)}{\pi} \left[ \int_x^1 \frac{dy}{y} P_{qq}\left(\frac{x}{y}\right) q_i(y, M) + \int_x^1 \frac{dy}{y} P_{qg}\left(\frac{x}{y}\right) g(y, M) \right] \quad (2.22)$$

$$\frac{dg_i(x, M)}{d \ln M} = \frac{\alpha_s(M)}{\pi} \left[ \int_x^1 \frac{dy}{y} P_{gq}\left(\frac{x}{y}\right) q_i(y, M) + \int_x^1 \frac{dy}{y} P_{gg}\left(\frac{x}{y}\right) g(y, M) \right] \quad (2.23)$$

where  $M = \ln(Q^2/\mu_0^2)$  and  $P_{ij}(\frac{x}{y})$  are the splitting functions which represent the probability of finding a parton  $i$  with momentum  $x$  originating from a parton  $j$  with momentum  $y$ . The splitting functions are schematically shown in Fig. 2.2.

### QCD Hard Scattering Factorisation

The concept of QCD hard scattering factorisation [30] introduces a factorisation scale  $\mu_f^2$  that separates soft and hard processes. For momentum transfers  $Q^2 > \mu_f^2$ ,  $\alpha_s$  is taken to be small and perturbation theory is applicable. This is the 'hard' regime of short range, high momentum transfer interactions. Processes belonging to the 'soft' regime,  $Q^2 < \mu_f^2$ , lead to the so-called infrared divergences. They are absorbed in the

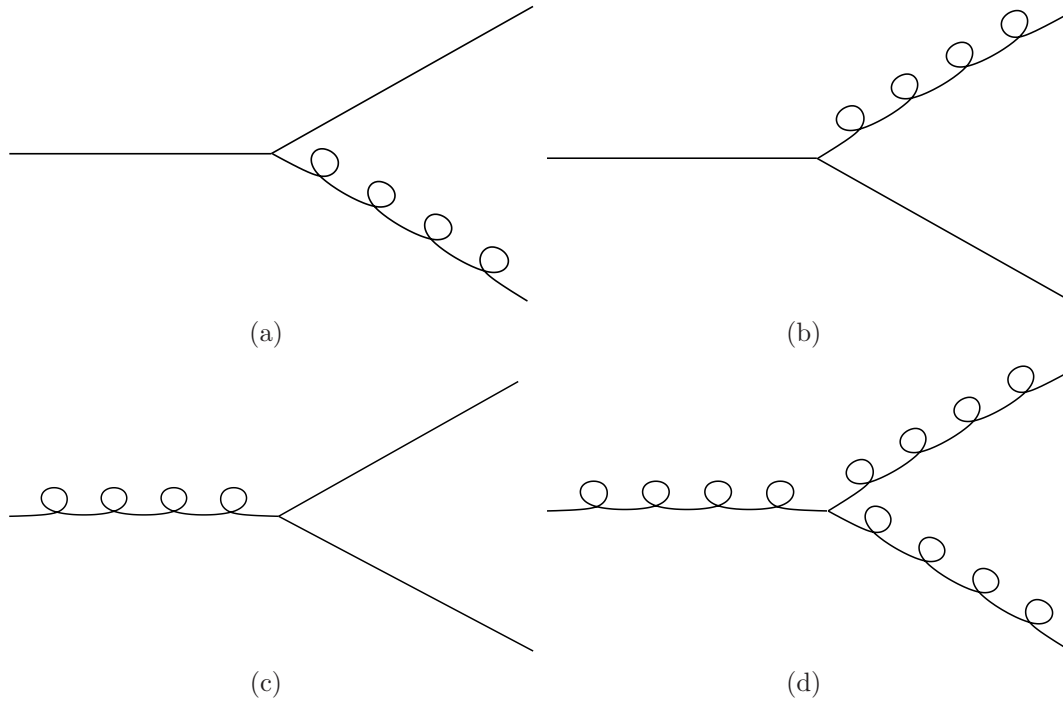


Figure 2.2: Diagrams showing the quark (a), (b) and gluon (c), (d) splitting functions.

renormalised parton distribution functions which depend on the factorisation scale  $\mu_f^2$ . The proton structure function  $F_2$  is given by

$$F_2(x, Q^2) = \sum_i \int_x^1 \sigma\left(\frac{x}{x'}, Q^2, \mu_F^2\right) [q_i(x', \mu_F^2) + \bar{q}_i(x', \mu_F^2)]. \quad (2.24)$$

### 2.1.6 Cross Sections

The inclusive deep inelastic electron-proton scattering cross section at low  $Q^2$  is given by

$$\frac{d^2\sigma}{dx dQ^2} = \frac{2\pi\alpha^2 Y^+}{Q^4 x} \left[ F_2(x, Q^2) - \frac{y^2}{Y^+} F_L(x, Q^2) \right] \quad (2.25)$$

where

$$Y^+ = 1 + (1 - y)^2. \quad (2.26)$$

Eq. 2.9 uses the structure functions  $F_1$  and  $F_2$  instead. Considering the polarization of the virtual photon exchanged in deep inelastic scattering, the cross section can be written as a sum of transversal and longitudinal component

$$\sigma^{\gamma^*p} = \sigma_T + \sigma_L \quad (2.27)$$

where each component involves its own proton structure function  $F_T$  and  $F_L$ . These are related to the structure functions  $F_1$  and  $F_2$  in the following way

$$2xF_1 = F_T, \quad (2.28)$$

$$F_2 = F_T + F_L. \quad (2.29)$$

It is also useful to define a ratio of the longitudinal and transverse structure functions

$$R = \frac{F_L}{F_T} = \frac{F_L}{F_2 - F_L}. \quad (2.30)$$

### 2.1.7 Longitudinal Proton Structure Function

In the **quark parton model**, the longitudinal proton structure function  $F_L$  is zero since longitudinally photons do not couple to spin  $\frac{1}{2}$  quarks. In the lowest order of the DGLAP approximation of perturbative QCD, the longitudinal structure function is given by [24]

$$F_L(x) = \frac{\alpha_s}{4\pi} x^2 \int_x^1 \frac{dz}{z^3} \left[ \frac{16}{3} F_2(z) + 8 \sum e_q^2 \left(1 - \frac{x}{z}\right) z g(z) \right] \quad (2.31)$$

where both quarks and gluon contribute. At low  $x$ ,  $F_L$  thus essentially determines the gluon distribution  $xg(x, Q^2)$  as can be illustrated by solving this equation approximately [31]

$$xg(x) = 1.8 \left[ \frac{3\pi}{2\alpha_s} F_L(0.4x) - F_2(0.8x) \right] \simeq \frac{8.3}{\alpha_s} F_L(0.4x). \quad (2.32)$$

The gluon distribution at low  $x$  can be constrained indirectly by the  $Q^2$  evolution of  $F_2$ . However, this relies on the DGLAP theory assumption which becomes questionable at low  $x$  [32]. The  $F_L$  measurement described in the following chapters represents a direct measure of the gluon density and thus provides an important cross check of the whole understanding of low  $x$  physics.

## 2.2 Diffraction

### 2.2.1 Regge Theory

The Regge theory [33, 34] investigates the dynamics of hadrons by studying the two particle scattering  $A + B \rightarrow C + D$ . It relates the spin  $J$  and the mass  $M$  of particles with the same quantum numbers. When such particles are plotted in the so-called Chew-Frautschi plane ( $J$  vs.  $M^2$ ) [35, 36] they all seem to lie on the same line called the **Regge trajectory**. Figure 2.3 shows such plot for low mass mesons.

The Regge theory predicts that the high energy behaviour of all processes, where the same quantum numbers are exchanged, should be similar. The early description of two body interactions was based on the picture of one pion exchange. However, there is a serious shortcoming of this model since some processes cannot be described by the exchange of a single pion due to quantum number conservation laws. The Regge theory solves such problems by introducing an exchange of whole Regge trajectories instead of just one particle. One talks about a Reggeon exchange which is equivalent to the exchange of many particles with different spins.

In the so-called Regge limit, where  $s \gg |t|$ , the scattering amplitude of the two body interaction can be written as

$$A(s, t) \sim s^{\alpha(t)}, \quad (2.33)$$

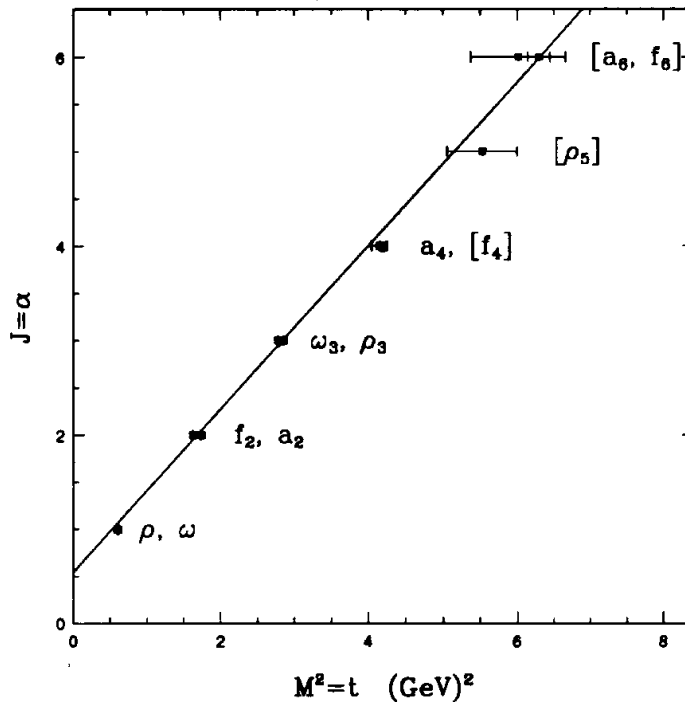


Figure 2.3: The Chew-Frautschi plot for low mass mesons. [37]

where

$$\alpha(t) = \alpha(0) + \alpha't. \quad (2.34)$$

It can be shown that in the Regge limit the total cross section can be related to  $s$  via

$$\sigma_{tot} \sim s^{(\alpha(0)-1)}. \quad (2.35)$$

$s$  and  $t$  are the standard Mandelstam variables<sup>1</sup>.

## 2.2.2 The Pomeron

Since all known trajectories of existing particles have  $\alpha(0) < 1$ , the Eq. 2.35 predicts that  $\sigma_{tot}$  should decrease with rising  $s$ . However, the experimental data did not support this conclusion. In order to keep the Regge picture consistent with the experimental data a trajectory with an intercept of  $\alpha(0) \simeq 1$  has to be introduced. It is called the **Pomeron trajectory** and it is referred to as a diffractive exchange that is characterised by the exchange of vacuum quantum numbers.

The  $pp$  and  $p\bar{p}$  cross sections were seen experimentally to rise at large  $s$  as  $s$  increases, as shown in Fig. 2.4. Donnachie and Landshoff [38] successfully attempted a global fit to all existing  $\sigma_{tot}$  data where they took the total cross section as a sum of two terms

$$\sigma_{tot} = As^{\alpha_P(0)-1} + Bs^{\alpha_R(0)-1} \quad (2.36)$$

representing the Pomeron and Reggeon trajectories.

<sup>1</sup> Mandelstam variables describe two-body to two-body processes  $A + B \rightarrow C + D$ . They are  $s = (p_a + p_b)^2$ ,  $t = (p_a - p_c)^2$  and  $u = (p_a - p_d)^2$ , where  $p_a, p_b, p_c, p_d$  are the corresponding four-momenta of the particles.

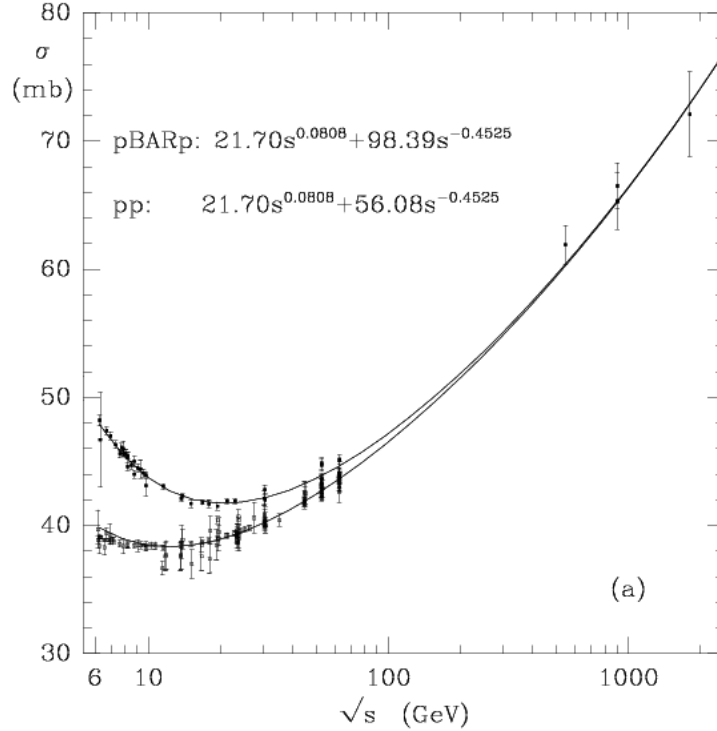


Figure 2.4: The total cross sections of  $pp$  and  $p\bar{p}$  interactions as a function of  $\sqrt{s}$  compared with the parametrisation of Donnachie and Landshoff. [37]

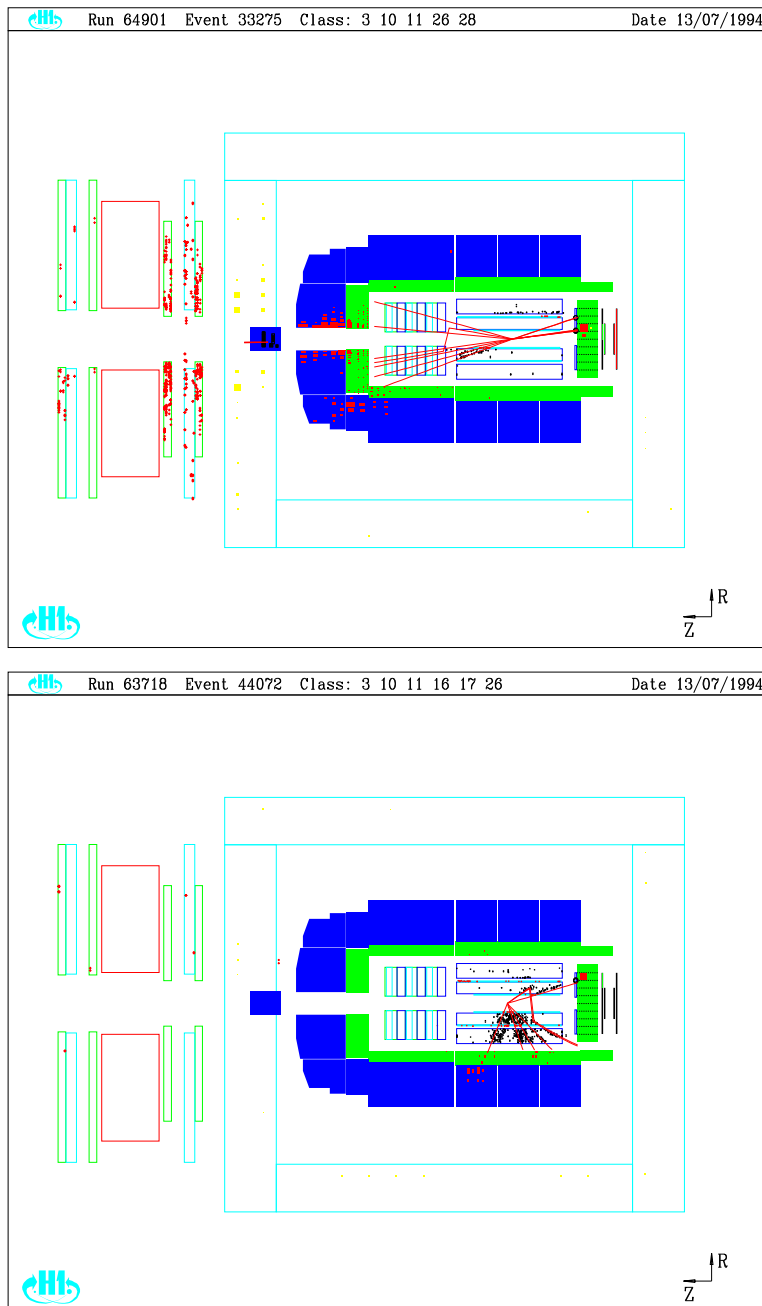
## 2.3 Diffractive DIS at HERA

The early studies of the DIS processes at H1 revealed that a substantial portion, roughly 10%, of them do not show any forward activity (in the direction of the proton beam). These are called the diffractive processes. Standard DIS and diffractive processes are compared in Fig 2.5. The lack of activity in the forward region is phenomenologically explained by the exchange of a colourless object emerging directly from the proton which remains intact. Due to the vacuum quantum numbers of the exchanged object, there is no colour string between the final state proton and the remaining hadronic final state that could hadronize. The exchanged object was successfully identified with the Pomeron and the Regge picture plays an important role in description of the diffractive DIS processes.

Fig. 2.6 shows a distribution of the polar position of the most forward cluster in the DIS processes as seen in the H1 detector. The difference between diffractive and standard DIS processes is clearly visible in the simulation.

### 2.3.1 Diffractive Kinematics

Fig. 2.7 shows the diagram for the generic diffractive DIS process at HERA. In addition to the kinematic variables defined in Section 2.1.1 there are two more variables,  $\beta$  and  $x_P$ , introduced to describe a diffractive interaction. These reflect the slightly more complicated structure of diffractive processes, compared to the standard DIS processes, due to the assumed presence of a colourless object. The variable  $x_P$  describes the



1

Figure 2.5: Comparison of the standard DIS process (top) and the diffractive DIS process (bottom) which is characterised by the lack of activity in the forward region.

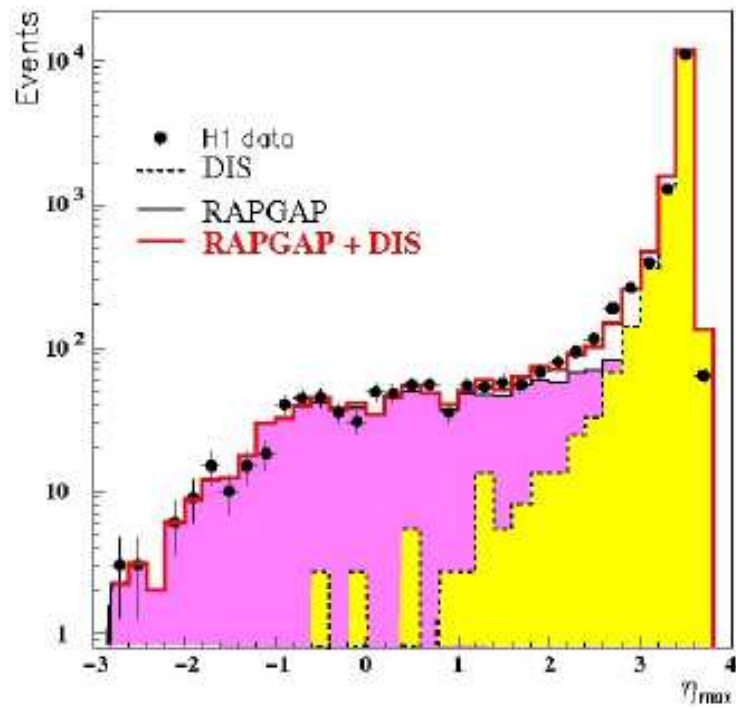


Figure 2.6: The variable  $\eta_{max}$  describes the polar position of the most forward cluster. Pseudorapidity  $\eta$  is defined as  $\eta = -\ln \tan(\theta/2)$ . The full DIS data (points) is well described by the sum of simulations of the standard DIS processes (yellow) and the diffractive processes (magenta). The diffractive processes do not show any activity in the forward region (high  $\eta$ ).

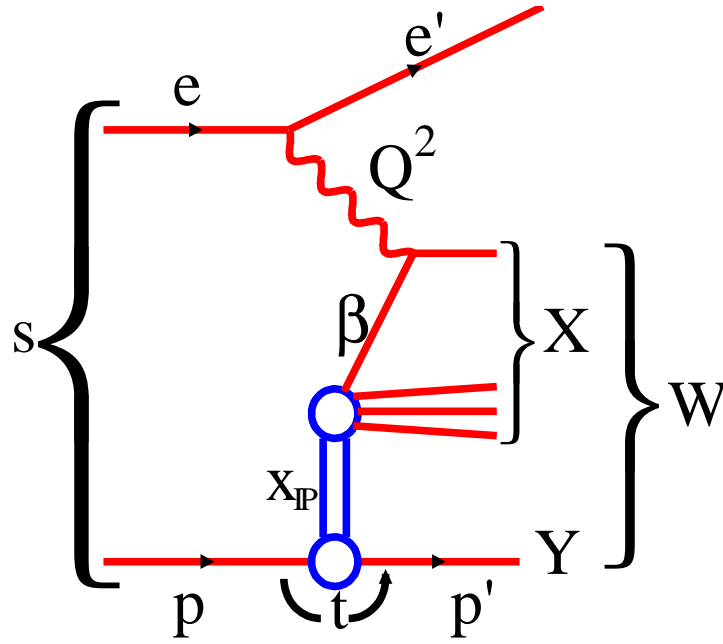


Figure 2.7: A schematic diagram of the diffractive DIS process at HERA.

fractional momentum of the Pomeron with respect to the proton, and  $\beta$  is the fractional momentum of the struck parton with respect to the Pomeron. They are defined as

$$\beta = \frac{Q^2}{Q^2 + M_X^2 - t}, \quad (2.37)$$

$$x_{\mathcal{P}} = \frac{Q^2 + M_X^2 - t}{Q^2 + W^2 - M_p^2} = \frac{x}{\beta} \quad (2.38)$$

where  $M_X$  is the mass of the hadronic final system  $X$  and  $M_p$  is the mass of the proton.

### 2.3.2 Diffractive Cross-Sections

Following the same formalism as described in Section 2.1.6 for the DIS processes, the differential cross section for diffractive DIS as a function of three measured kinematic variables can be written as

$$\frac{d^3\sigma_{ep \rightarrow eXp}}{d\beta dQ^2 dx_{\mathcal{P}}} = \frac{2\pi\alpha^2 Y^+}{\beta Q^4} \sigma_r^{D(3)}(\beta, Q^2, x_{\mathcal{P}}) \quad (2.39)$$

where  $\sigma_r^{D(3)}(\beta, Q^2, x_{\mathcal{P}})$  is the diffractive reduced cross section. The number in brackets denotes the number of variables that are used to define the reduced cross section. The reduced cross section can be related to the structure functions by

$$\sigma_r^{D(3)} = F_2^{D(3)}(\beta, Q^2, x_{\mathcal{P}}) - \frac{y^2}{Y^+} F_L^{D(3)}(\beta, Q^2, x_{\mathcal{P}}). \quad (2.40)$$

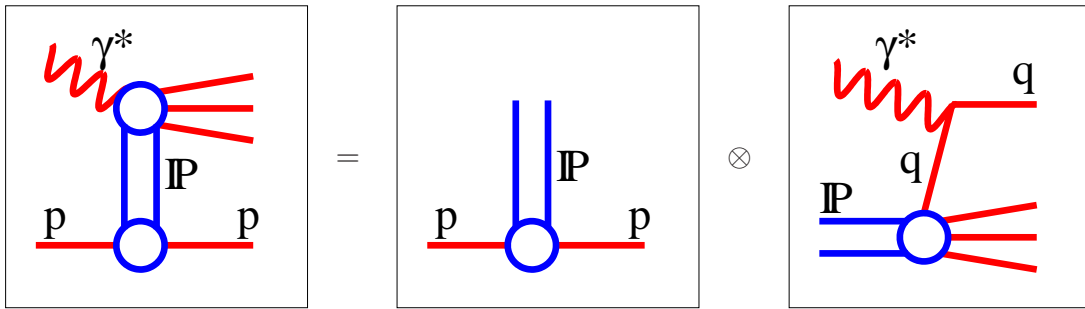


Figure 2.8: Sketch of Regge factorisation. The diffractive exchange is viewed in two parts: a long time scale flux component, and a short time scale hard scattering process.

### 2.3.3 QCD Hard Scattering Factorisation

It has been proven by Collins [11] that the diffractive  $\gamma^*p$  cross section can be written in terms of diffractive parton distribution functions (DPDF's)  $f_i^D(x, Q^2, x_{\mathbb{P}}, t)$  convoluted with the hard-scattering cross section  $\hat{\sigma}_{\gamma^*i}$

$$\sigma^{\gamma^*p \rightarrow Xp}(x, Q^2, x_{\mathbb{P}}, t) = \sum_i f_i^D(x, Q^2, x_{\mathbb{P}}, t) \otimes \hat{\sigma}_{\gamma^*i}(x, Q^2) \quad (2.41)$$

The DPDF's here depend on four kinematic variables. At fixed  $x_{\mathbb{P}}$  and  $t$ , they evolve in exactly the same way as the proton PDF's in Eq 2.22. This makes it possible to perform a full QCD fit to the diffractive data without any additional assumptions. The partonic cross sections are the same as for inclusive DIS.

### 2.3.4 Regge Factorisation and the Resolved Pomeron Model

The Regge factorisation makes the extra assumption that the diffractive PDF's do not depend (other than in normalisation) on  $x_{\mathbb{P}}$  and  $t$ . This leads to a formalism where the Pomeron flux and the hard scatter of the photon with the Pomeron are described separately. The first one involves the  $x_{\mathbb{P}}$  and  $t$  variables, the latter one is described by  $\beta$  and  $Q^2$  only. The Regge factorisation scheme is illustrated in Fig. 2.8 and can be written as

$$f_i^D(x, Q^2, x_{\mathbb{P}}, t) = f_{\mathbb{P}/p}(x_{\mathbb{P}}, t) \cdot f_{i/\mathbb{P}}(\beta = x/x_{\mathbb{P}}, Q^2), \quad (2.42)$$

where  $f_{\mathbb{P}/p}$  is the Pomeron flux and  $f_{i/\mathbb{P}}$  represents the Pomeron PDF's, i.e. the probability of finding a parton  $i$  with a momentum fraction  $\beta$  at a given  $Q^2$  in the Pomeron. The Pomeron flux gives the probability that a Pomeron with particular values  $x_{\mathbb{P}}$  and  $t$  couples to the proton.

The time scales for the two processes described by the two terms are different. At the proton vertex, the relevant scale is  $t$  which is small in the diffractive limit. Any dynamics occurring here will appear frozen when viewed from the hard scatter vertex where the relevant scale is  $Q^2$ .

### 2.3.5 Dipole and Saturation Models

The basic concept of saturation [20] in Deep Inelastic Scattering (DIS) is related to the transition from high to low  $Q^2$  which can be observed in the total  $\gamma^*p$  cross section. This type of saturation occurs when the photon wavelength  $1/Q$  becomes comparable

to the size of the proton. Another form of saturation is related to DIS at small  $x$ . In this regime, the partons in the proton form a dense system with mutual interaction and recombination which also leads to the saturation of the total cross section [20]. Both aspects of saturation are closely linked to confinement and unitarity. The first one is genuinely nonperturbative, while the latter one can be approached perturbatively [39].

The basic concept of the dipole picture [10] is the photon that splits into a quark-antiquark pair (dipole) which then scatters on the proton. The mechanism leading to the dissociation of the photon and the subsequent scattering can be factorized and written in terms of a **photon wave function** convoluted with a quark-antiquark cross section  $\hat{\sigma}$ , so called **dipole cross section**.

The total  $\gamma^*p$  cross section for transversely (T) or longitudinally (L) polarized virtual photon (emitted by the incident electron) can be written as

$$\sigma_{L,T}(x, Q^2) = \int d^2\mathbf{r} \int_0^1 dz |\Psi_{L,T}(r, z, Q^2)|^2 \hat{\sigma}(r, x) \quad (2.43)$$

where  $\Psi_{L,T}$  is the wave function for the splitting of the virtual photon into a  $q\bar{q}$  pair (dipole), and  $\hat{\sigma}$  is the imaginary part of the forward scattering amplitude of the  $q\bar{q}$  dipole on the proton, the dipole cross section, that describes the interaction of the dipole with the proton. The variable  $\mathbf{r}$  defines the transverse separation of the quarks in the  $q\bar{q}$  pair, and  $z$  is the light-cone momentum fraction of the photon carried by the quark (or antiquark) [40]. The standard DIS proton structure functions are related to  $\sigma_{L,T}$  by

$$F_{T,L}(x, Q^2) = \frac{Q^2}{4\pi^2\alpha_{em}} \sigma_{L,T}(x, Q^2). \quad (2.44)$$

The main assumption of the saturation model is the saturation property of the dipole cross section which can be incorporated as

$$\hat{\sigma}(r, x) = \sigma_0 g\left(\frac{r}{R_0(x)}\right). \quad (2.45)$$

The function  $R_0(x)$  is called **saturation radius** and decreases with decreasing  $x$ . When  $\hat{r} \equiv r/R_0(x) \rightarrow \infty$  the function  $g(\hat{r})$  saturates to 1. The parameter  $\sigma_0$  is a normalisation constant. The realisation [10] of the saturation uses the following definitions

$$g(\hat{r}) = 1 - \exp(-\hat{r}^2/4) \quad (2.46)$$

$$R_0(x) = \frac{1}{Q_0} \left(\frac{x}{x_0}\right)^{\lambda/2} \quad (2.47)$$

where the parameters  $Q_0$ ,  $x_0$  and  $\lambda > 0$  have to be obtained from the fits to inclusive data.

The diffractive data are successfully described by a picture where the diffractive system is formed by the quark-antiquark ( $q\bar{q}$ ) and quark-antiquark-gluon ( $q\bar{q}g$ ) systems (see Fig. 2.9 and 2.10) [10], as the smallest color singlet that can be exchanged consists of two gluons.

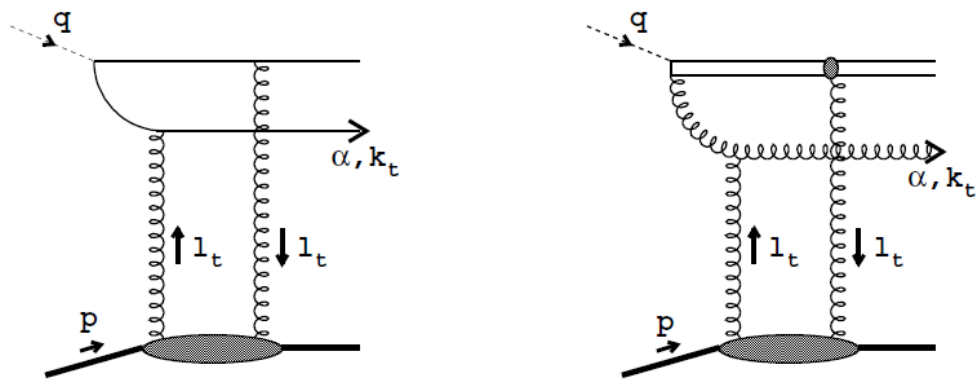


Figure 2.9: Diffractive production of a  $q\bar{q}$ -pair (left) and the emission of an additional gluon (right).

## ZEUS 1994

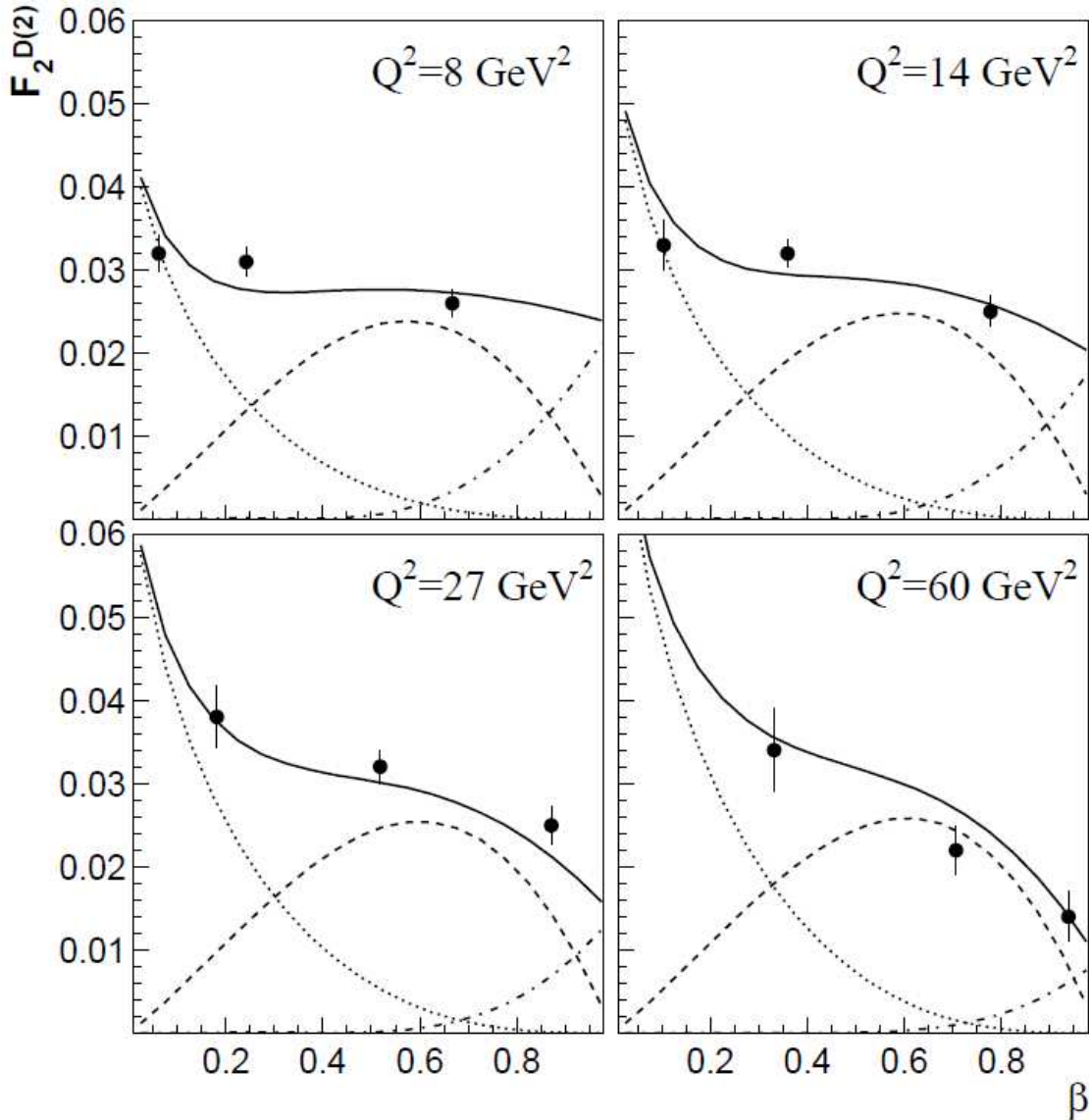


Figure 2.10: The diffractive structure function  $x_{\mathbb{P}}F_2^D(x_{\mathbb{P}}, \beta, Q^2)$  for  $x_{\mathbb{P}} = 0.0042$  as a function of  $\beta$ . The dashed lines show the  $q\bar{q}$  contribution for transverse photons, the dot-dashed lines correspond to the contribution from longitudinal photons and the dotted lines illustrate the  $g\bar{q}q$  component. The solid line is the total contribution and the data are from ZEUS. [10]

# Chapter 3

## Motivation and Recent Results

### 3.1 QCD Fits

#### 3.1.1 QCD Fit to the Inclusive DIS Data

In [41], a measurement of the inclusive deep inelastic neutral current  $ep$  scattering cross section is presented in the region of four-momentum transfer squared,  $12 \text{ GeV}^2 < Q^2 < 150 \text{ GeV}^2$ , and Bjorken  $x$ ,  $2 \cdot 10^{-4} < x < 0.1$ . The results are based on the analysis of data collected by the H1 Collaboration at positron energy  $E_e = 27.6 \text{ GeV}$  and proton energy  $E_p = 920 \text{ GeV}$ . In order to ensure high accuracy of the measurement, the data are also combined with previously published data taken at  $E_p = 820 \text{ GeV}$  [42]. The combined measurement leads to an accuracy typically in the range  $1.3 - 2\%$ . A QCD analysis at next-to-leading order is performed in order to determine the parton distributions in the proton (see Fig. 3.1) from the data in the  $Q^2$  region starting at a few  $\text{GeV}^2$  up to about  $150 \text{ GeV}^2$ .

The DGLAP evolution equations determine the derivative  $(\partial F_2 / \partial \ln Q^2)_x$  taken at fixed  $x$ , and show a dominant contribution at low  $x$  coming from gluon splitting into a quark-antiquark pair. The measurement of this derivative gives a powerful constraint on the gluon distribution  $xg(x)$  as well as on the strong coupling constant  $\alpha_s$  [43]. The results are shown in Fig. 3.2 for different  $x$  values as a function of  $Q^2$ . The dependence of the derivative on  $Q^2$  is well reproduced by the QCD fit. Measuring the gluon density in this way, from the so-called scaling violations, is indirect as it is determined from the structure function  $F_2$ , which is directly sensitive only to quarks. Therefore, a direct measurement of the structure function  $F_L$  that probes gluons is welcome, and would give an important cross check of our understanding of the proton structure.

The observed rise of the structure function  $F_2(x, Q^2)$  towards low  $x$  can be quantified by the derivative

$$\lambda = -(\partial \ln F_2 / \partial \ln x)_{Q^2}. \quad (3.1)$$

H1 shows that within the uncertainty of the data, the derivative is constant at small  $x < 0.01$ , i.e.  $F_2$  for fixed  $Q^2$  is consistent with power law  $F_2 \propto x^{-\lambda}$ . The value of  $\lambda$  increases from about 0.1 to 0.3 in the  $Q^2$  region from about 1 to  $100 \text{ GeV}^2$  [41].

A new QCD analysis, referred to as H1 PDF 2009, is performed, which supersedes the previous H1 PDF 2000 fit [44], as it relies on the more accurate new data. The QCD fit is performed with the evolution starting at  $Q_0^2 = 1.9 \text{ GeV}^2$ , and a parametrisation

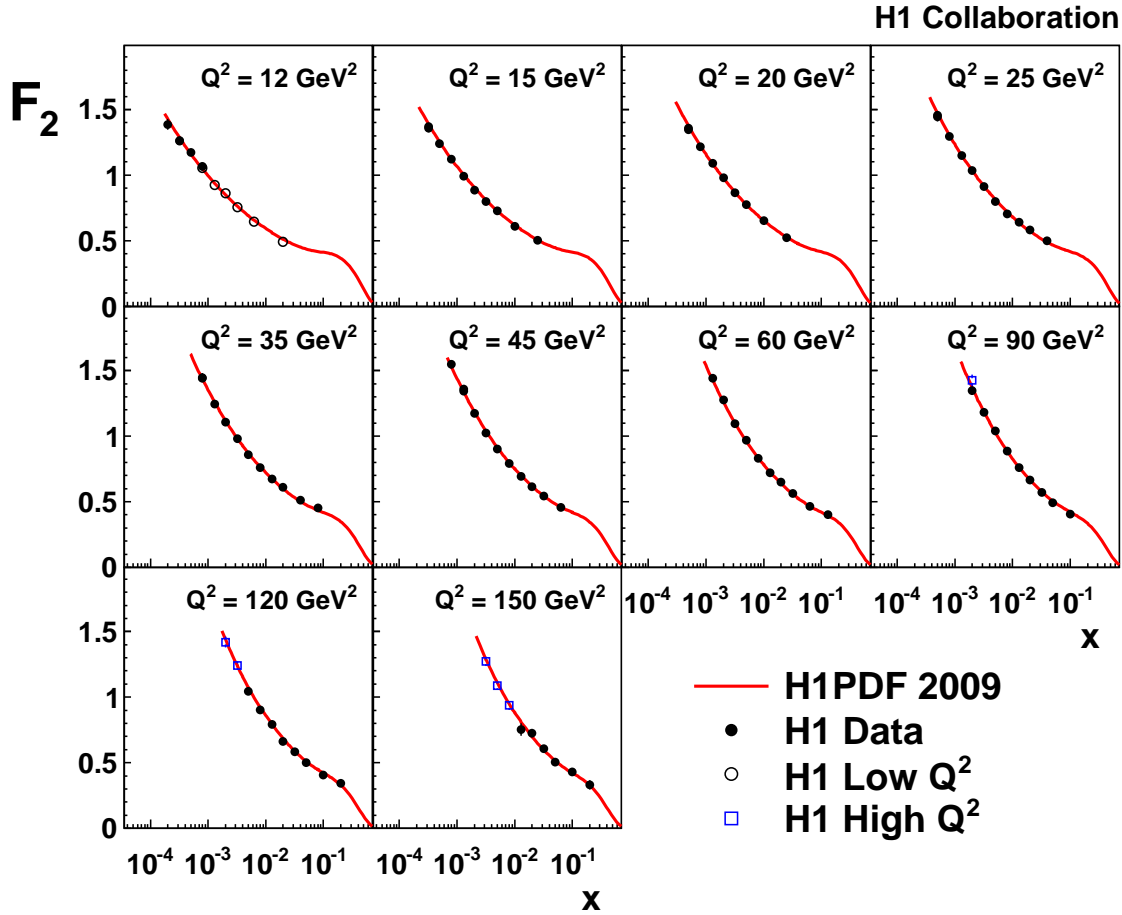


Figure 3.1: Measurement of the structure function  $F_2$  at fixed  $Q^2$  as a function of  $x$ . The data of this measurement (closed circles) are complemented by the previously published data at low  $Q^2$  (open circles) [42] and high  $Q^2$  (open boxes) [45]. The error bars represent the total measurement uncertainties. The curve represents the H1 PDF 2009 fit. [41]

of  $xq(x) = Ax^B(1-x)^C$  and  $xg(x) = Ax^B(1-x)^C[1+Dx]$  for the quark and the gluon densities, respectively (see Fig. 3.3).

### 3.1.2 The $\lambda$ Fit

In a separate analysis [46], the H1 data from 1995-1997 at  $E_p = 820$  GeV and the data taken in 1999-2000 at  $E_p = 920$  GeV are studied in order to test the following assumption. Assuming a power law in  $x$  of the proton structure function  $F_2$ , and constant  $R = \frac{F_L}{F_T}$  the reduced cross section can be fitted in the following way

$$\sigma_r = cx^{-\lambda} \left[ 1 - \frac{y^2}{1 + (1-y)^2} \cdot \frac{R}{1+R} \right]. \quad (3.2)$$

The fit is referred to as the  $\lambda$  fit and involves three parameters: normalisation factor  $c$ , power  $\lambda$  and the ratio  $R$ . The reduced cross sections are fitted in separate  $Q^2$  bins and the assumption of constant  $R$  is made only within a particular bin. Fig. 3.4 shows the fitted data. The turnover in  $\sigma_r$  at low  $x$  is due to  $R > 0$  in this model.

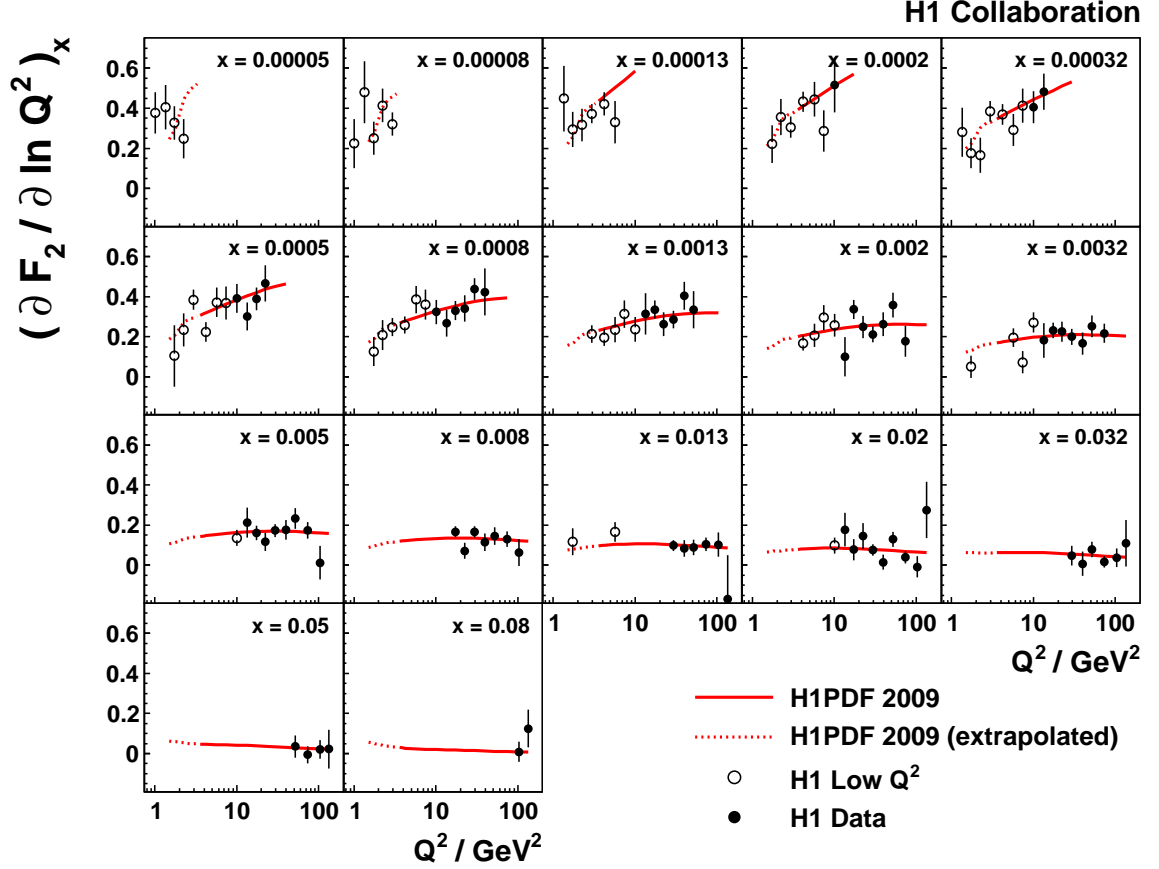


Figure 3.2: Logarithmic  $Q^2$  derivative of the structure function  $F_2$  as a function of  $Q^2$  at various values of  $x$ . The data of this measurement (closed circles) are complemented with the published data at lower  $Q^2$  (open circles) [42]. The error bars represent the total measurement uncertainties. The solid curve represents the prediction of the QCD fit for  $Q^2 \geq 3.5 \text{ GeV}^2$ , which is also shown extrapolated down to  $Q^2 = 1.5 \text{ GeV}^2$  (dashed). [41]

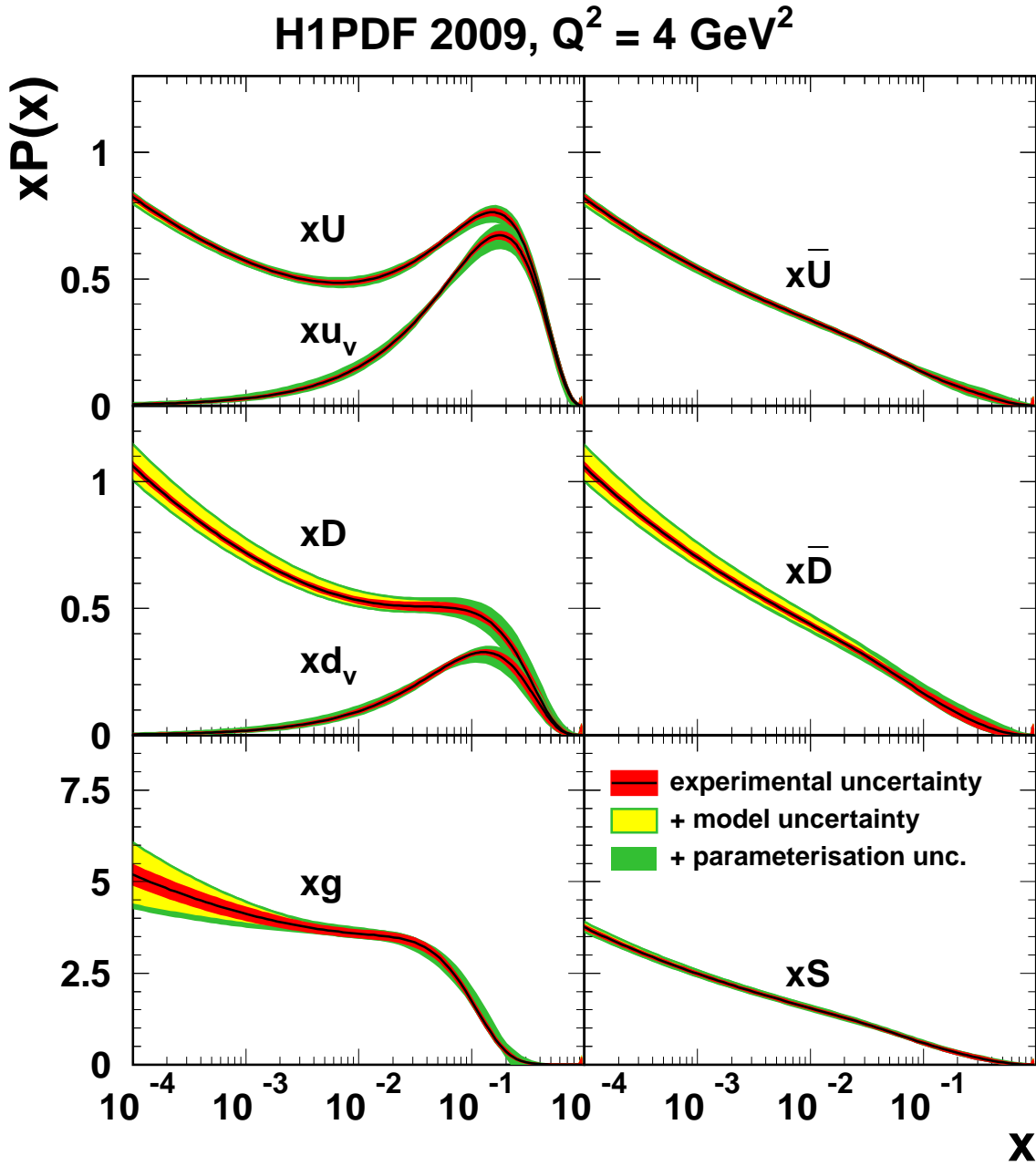


Figure 3.3: Parton distributions as determined by the H1PDF 2009 QCD fit at  $Q^2 = 4 \text{ GeV}^2$ . Shown are the combined up and down quark distributions,  $xU = x(u + c)$  and  $xD = x(d + s)$ , their anti-quark counter parts,  $x\bar{U}$  and  $x\bar{D}$ , the valence quark distributions,  $xu_v$  and  $xd_v$ , the total total sea distribution  $xS = 2x(\bar{U} + \bar{D})$ , and the gluon distribution,  $xg$ . The inner error bands show the experimental uncertainty, the middle error bands include the theoretical model uncertainties of the fit assumptions, and the outer error band represents the total uncertainty including the parameterisation uncertainty. [41]

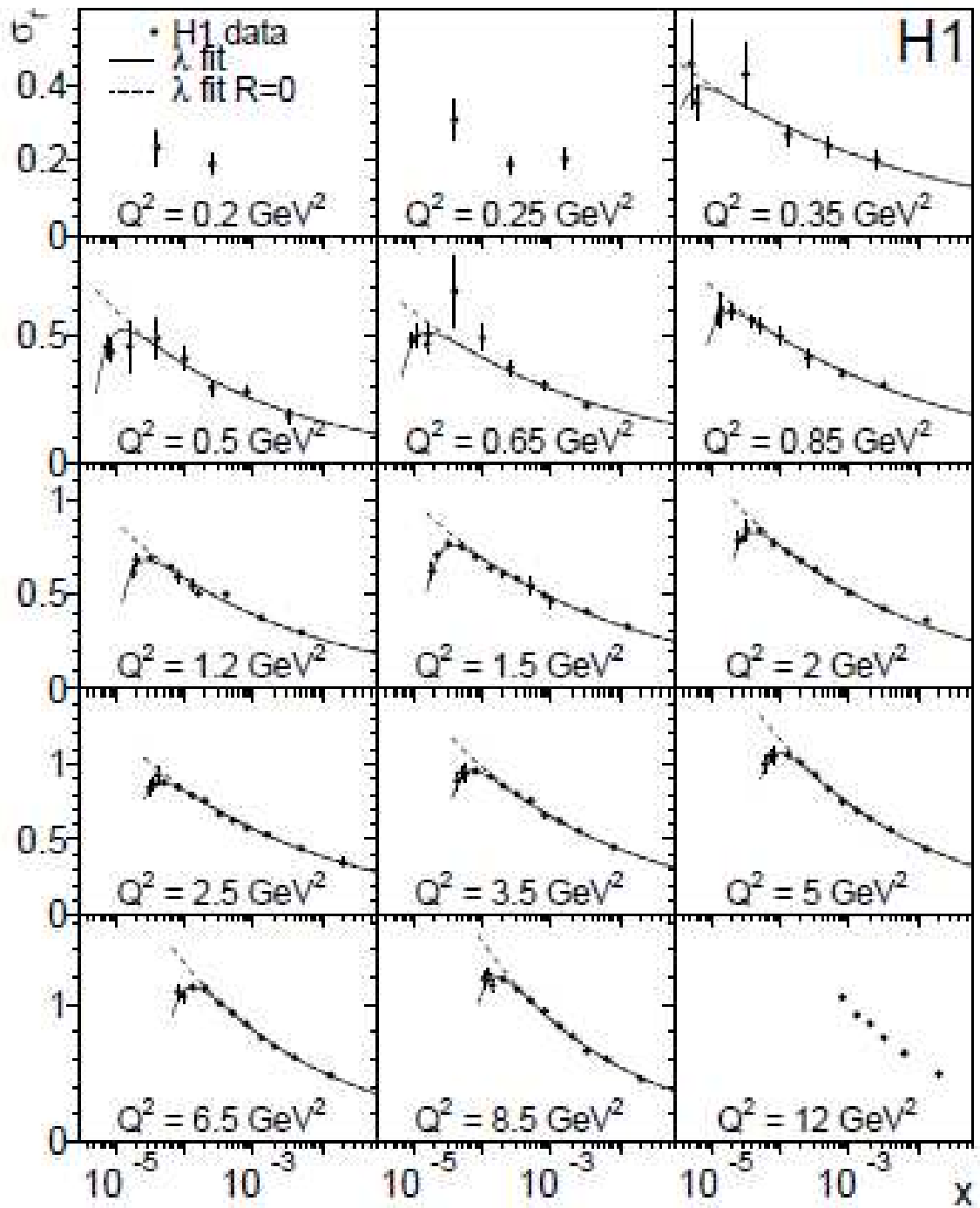


Figure 3.4: The  $\lambda$  fit to the H1 data. Reduced cross sections from data (points) are fitted with the  $\lambda$  fit prescription (solid line) in bins of  $Q^2$ . A fit holding the parameter  $R = 0$  fixed is also shown (dashed line). The turn-over at low  $x$  in the reduced cross section comes from the contribution of the longitudinal structure function ( $R > 0$ ). [46]

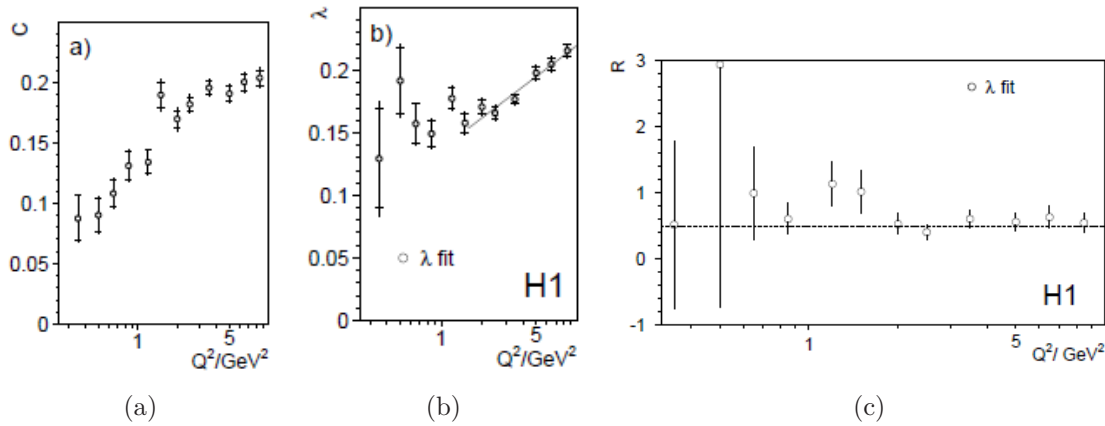


Figure 3.5: Results of the  $\lambda$  fit in separate  $Q^2$  bins. The coefficient  $c$  (a) is approximately constant, while the coefficient  $\lambda$  (b) shows a linear rise for  $Q^2 > 2 \text{ GeV}^2$ , as expected from perturbative QCD. The parameter  $R$  (c) is constant and consistent with  $R = 0.5$ . [46]

Fig. 3.5 shows the results of the fit. The coefficient  $\lambda(Q^2)$  shows a linear rise, as expected from perturbative QCD. The coefficient  $R$  is constant and consistent with  $R = 0.5$ .

### 3.1.3 QCD Fit to the Diffractive Data

The DPDF's are not known from first principles, but can be determined from fits to the data using the DGLAP evolution equations. The framework of the QCD hard factorisation and the Regge factorisation is applied when the full QCD fit to the diffractive data in H1 is performed. The H1 data at wide  $Q^2$  range starting at  $Q^2 = 3.5 \text{ GeV}^2$  are analysed in [12].

The DPDF's are parametrised in terms of a light flavour singlet distributions  $\Sigma(z)$ , consisting of  $u$ ,  $d$  and  $s$  quarks and anti-quarks with  $u = d = s = \bar{u} = \bar{d} = \bar{s}$ , and a gluon distribution  $g(z)$ . Here,  $z$  is the longitudinal momentum fraction of the parton entering the hard sub-process with respect to the diffractive exchange. For the lowest order quark-parton model process  $z = \beta$ , whereas it is found in the range  $0 < z < \beta$  for higher order processes. The quark singlet and gluon distributions are parametrised at  $Q_0^2$  such that the most general form is

$$z f_{i/P}(y, Q_0^2) = A_i z^{B_i} (1-z)^{C_i}. \quad (3.3)$$

The  $x_P$  dependence is parametrised using a flux factor based on Regge theory

$$f_{P/p}(x_P, t) = \frac{e^{B_P t}}{x_P^{2\alpha_P(t)-1}} \quad (3.4)$$

where the Pomeron trajectory is assumed to be linear,  $\alpha_P(t) = \alpha_P(0) + \alpha'_P t$ , and the parameters  $B_P$  and  $\alpha'_P$  are obtained experimentally, from fits to H1 FPS data. Analogously, a Reggeon exchange is considered as well in the fit.

The input parameters describing the DPDF's at a starting scale  $Q_0^2$  are adjusted to obtain the best description of the data using the NLO DGLAP evolution at  $Q^2 > Q_0^2$ .

Two results are obtained using different  $Q_0^2$  for the DGLAP evolution. The fit referred to as 'H1 2006 DPDF Fit A' uses  $Q_0^2 = 1.75 \text{ GeV}^2$ , and the fit called 'H1 2006 DPDF Fit B' uses  $Q_0^2 = 2.5 \text{ GeV}^2$ . Fit B also uses simpler parametrisation for the gluon density than Fit A.

A significant sensitivity of the fit result to the choice of the minimum  $Q^2$  value of the data included in the fit is observed. Whereas the quark distributions remain stable, the gluon distribution changes by  $\sim 40\%$  as the minimum  $Q^2$  varies between  $3.5 \text{ GeV}^2$  and  $8.5 \text{ GeV}^2$ . Therefore, only data at  $Q^2 > 8.5 \text{ GeV}^2$  are included in the fit. Data at  $M_X < 2 \text{ GeV}$  or  $\beta > 0.8$  are also excluded because of the low mass resonances.

### 3.1.4 Diffractive Parton Distributions from the Analysis with Higher Twist

In this section, a fit of the diffractive parton distributions to diffractive data from the H1 and ZEUS collaborations at HERA is described. K. Golec-Biernat and A. Łuszczak also consider the twist-4 contribution in addition to the standard twist-2 formulae [51]. The higher twist dominates in the region of large  $\beta$ . This contribution comes from the diffractive production of the  $q\bar{q}$  pair by the longitudinally polarised virtual photons. The effect of the twist-4 contribution on the diffractive structure functions is shown in Fig. 3.8 and 3.9. The twist-4 contribution leads to the gluon distribution which is peaked stronger at  $\beta \approx 1$  than in the case without twist-4. The main result of the analysis is a prediction for the longitudinal diffractive structure function  $F_L^D$ . The twist-4 term significantly enhances  $F_L^D$  in the region of large  $\beta$ .

## 3.2 Testing the Diffractive Gluon Densities

If QCD factorization is fulfilled, NLO QCD calculations based on the diffractive parton density functions should be able to predict the production rates of more exclusive diffractive processes like dijet and open charm production in shape and normalization. Fig. 3.10 shows the leading order diagrams for both processes and indicate their sensitivity to gluon densities. The diagrams also introduce a variable  $z_P$  which has a similar meaning as  $\beta$  in the inclusive processes and describes the fractional momentum of the parton entering the hard process with respect to the diffractive exchange.

### 3.2.1 Diffractive Open Charm Production in DIS

In the collinear factorization approach, diffractive open charm production at HERA is expected to occur mainly via boson gluon fusion (BGF), as illustrated in Fig 3.10(a). In the BGF process a charm quark anti-quark pair  $c\bar{c}$  is produced. One of them couples to the photon with virtuality  $Q^2$  and the other to a gluon that is emitted by the pomeron. Therefore, it is directly sensitive to the gluon content of the diffractive exchange, which can be only determined indirectly from the scaling violations in inclusive diffractive scattering for low momentum fractions  $z_P$ .

Fig. 3.11 displays the  $x_P \tilde{\sigma}_D^{c\bar{c}}$  cross section measurement by H1 and ZEUS collaborations [18]. H1 probes the kinematic range of  $2 < Q^2 < 100 \text{ GeV}^2$ ,  $0.05 < y < 0.7$ ,  $x_P < 0.04$ , ZEUS measurements are interpolated to the same kinematic domain. Both

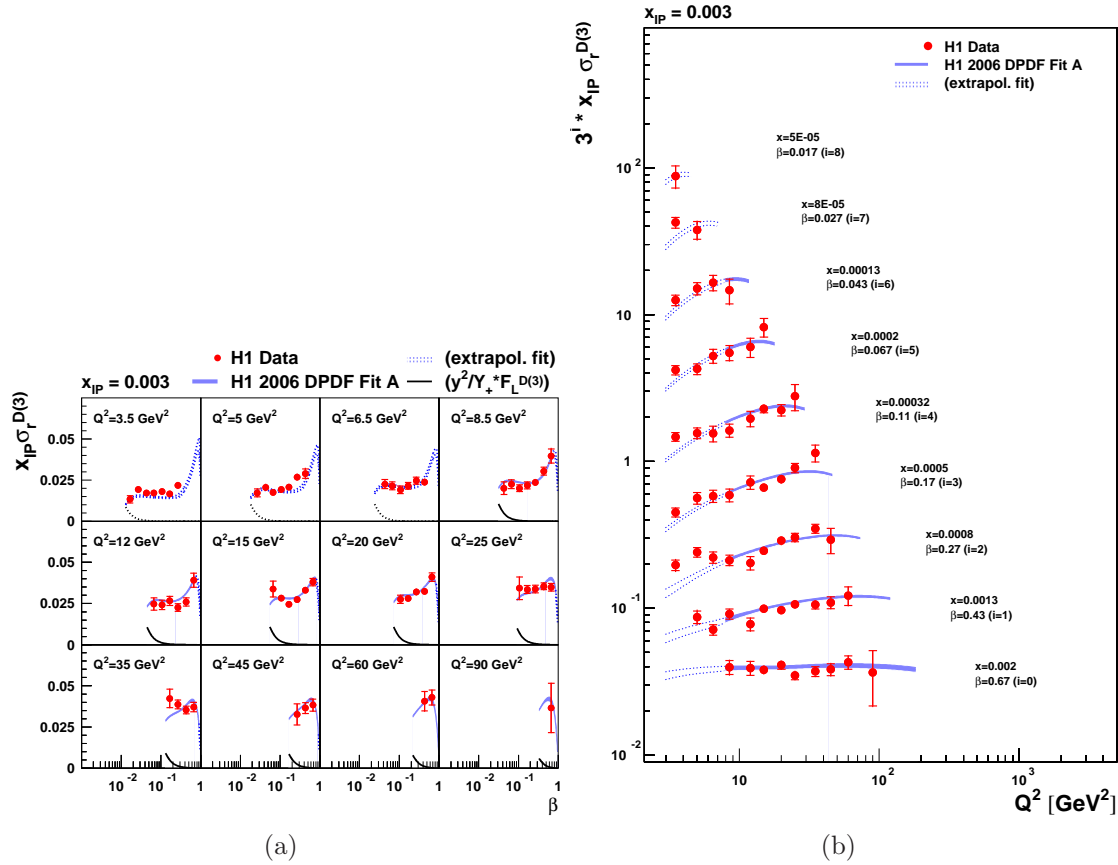


Figure 3.6: The  $\beta$  and  $Q^2$  dependences of the diffractive reduced cross section, multiplied by  $x_P$ , at  $x_P = 0.003$ . In (a), the quantity  $y^2/Y_+ \cdot F_L$  is also shown, as extracted from the ‘H1 2006 DPDF Fit A’. Adding this quantity to the reduced cross section yields  $F_2$ . In (b) the data are multiplied by a further factor of  $3^i$  for visibility, with  $i$  as indicated. The inner and outer error bars on the data points represent the statistical and total uncertainties, respectively. Normalisation uncertainties are not shown. The data are compared with the reduced cross section at  $E_p = 820$  GeV derived from the results of ‘H1 2006 DPDF Fit A’, which is shown as a shaded error band (experimental uncertainties only) in kinematic regions which are included in the fit and as a pair of dashed lines in regions which are excluded from the fit. [12]

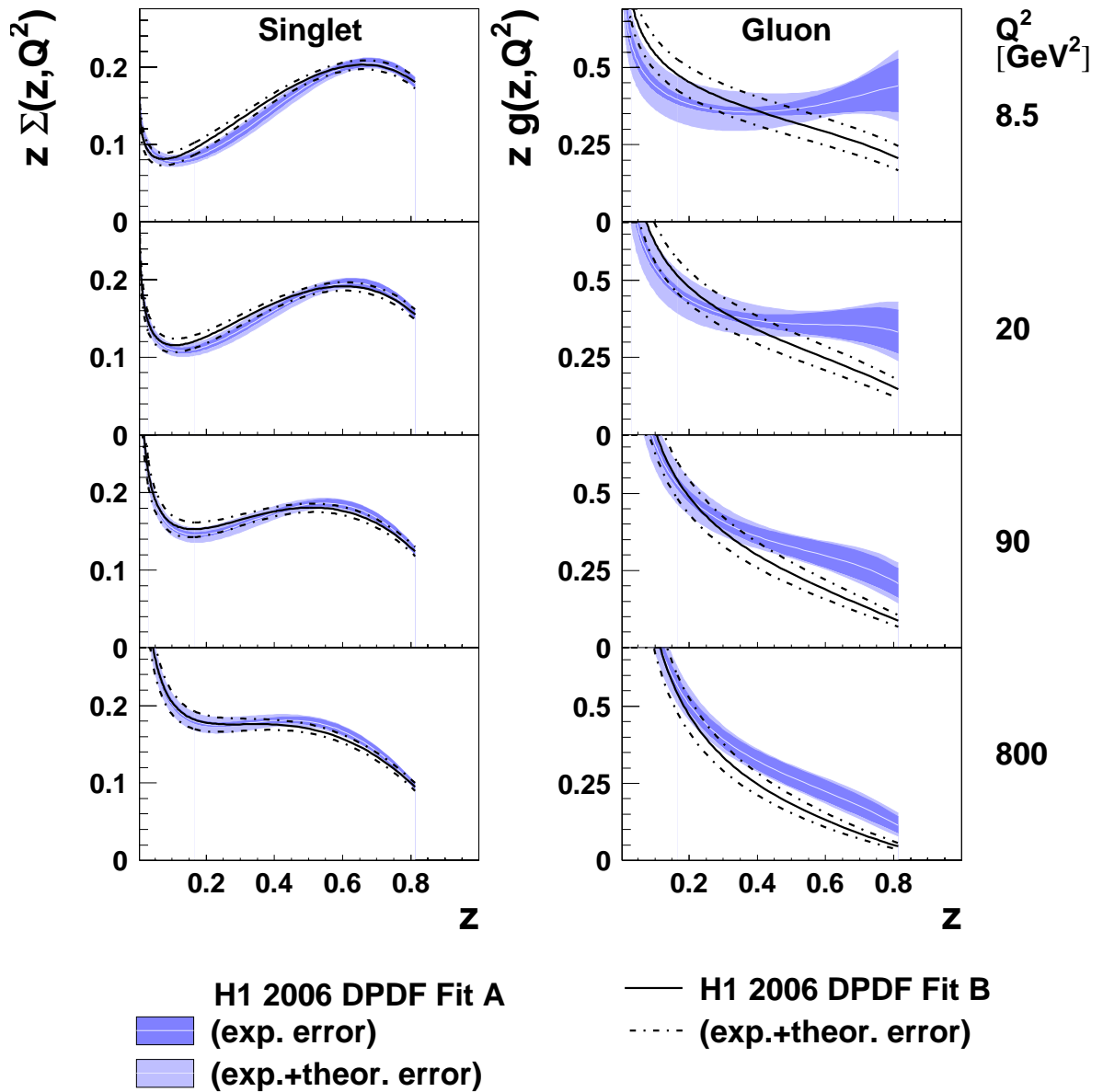


Figure 3.7: Comparison on a linear  $z$  scale between the total quark singlet and gluon distributions obtained from the ‘H1 2006 DPDF Fit A’ and the ‘H1 2006 DPDF Fit B’. These two fits differ in the parameterisation chosen for the gluon density at the starting scale for QCD evolution. The DPDFs are shown at four different values of  $Q^2$  for the range  $0.0043 < z < 0.8$ , corresponding approximately to that of the measurement. For ‘Fit A’, the central result is shown as a light coloured central line, which is surrounded by inner error bands corresponding to the experimental uncertainties and outer error bands corresponding to the experimental and theoretical uncertainties added in quadrature. For ‘Fit B’, only the total uncertainty is shown. [12]

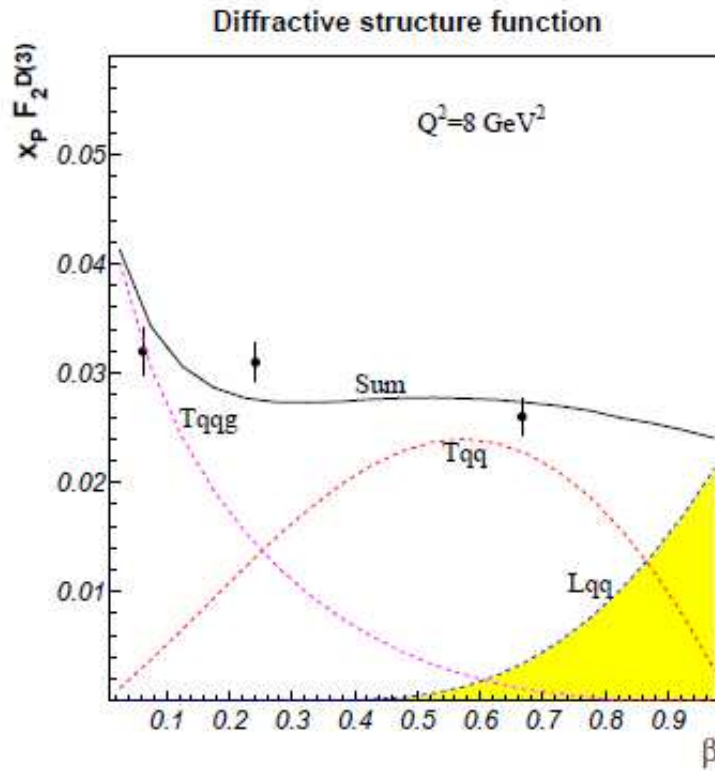


Figure 3.8: Three contributions to  $F_2^D$  from:  $q\bar{q}$  and  $q\bar{q}g$  from transverse (T) and longitudinal (L) photons for  $x_P = 0.003$ . The twist-4 contribution  $Lq\bar{q}$  is indicated by the yellow band. Old ZEUS data points are shown. [51]

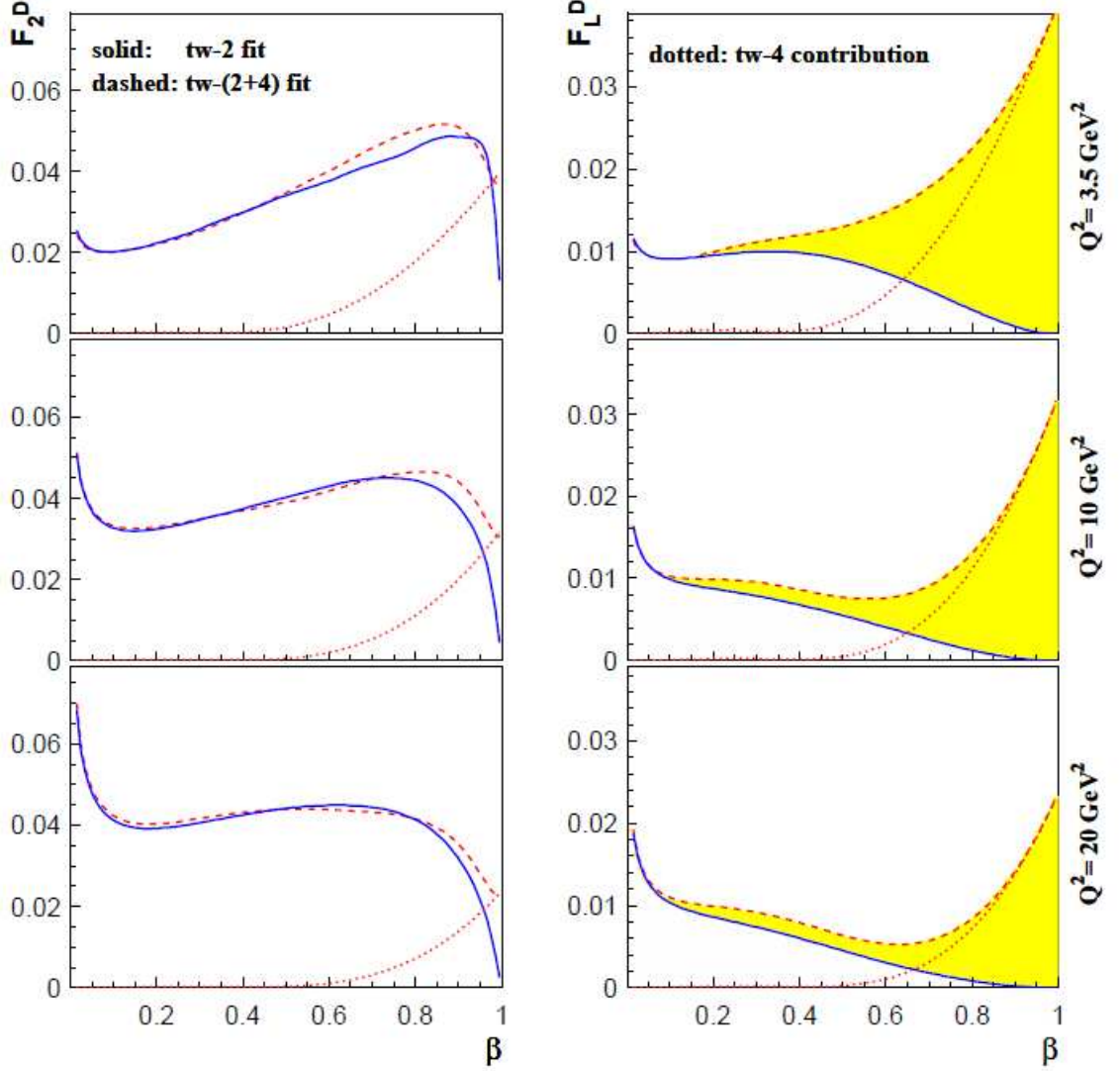


Figure 3.9: Diffractive structure functions  $F_2^{D(3)}$  (left) and  $F_L^{D(3)}$  (right) from the fits to H1 data for  $x_P = 0.001$ . The yellow band shows the effect of the twist-4 contribution on the prediction for  $F_L^{D(3)}$ . [51]

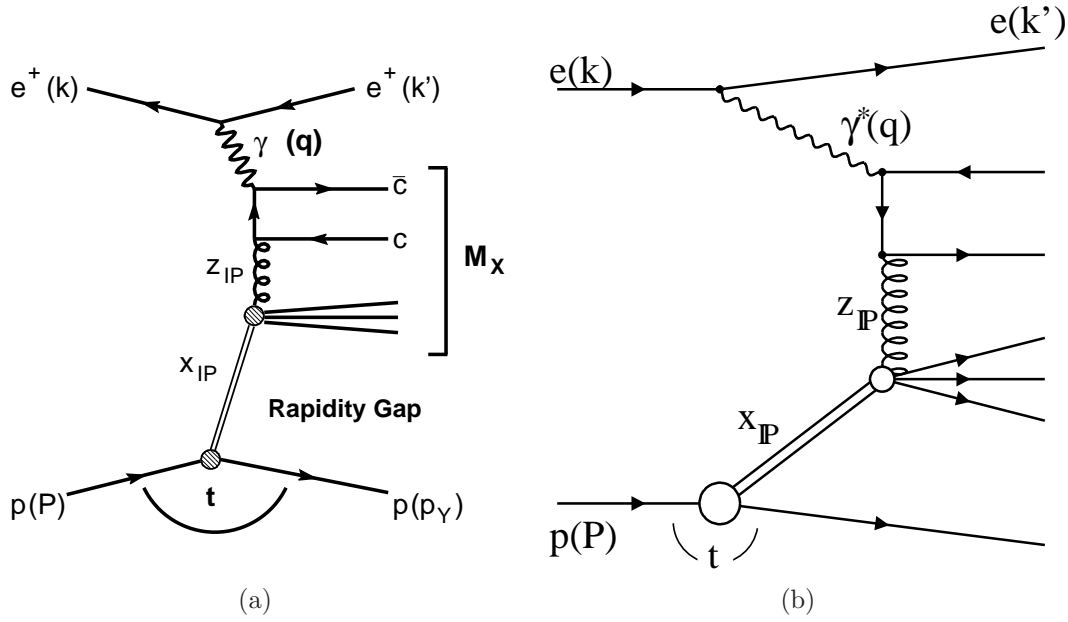


Figure 3.10: Leading order diagram for diffractive open charm production (a) and diffractive dijet production in DIS (b).

experiments give consistent results that are in agreement with the NLO DPDF predictions.

### 3.2.2 Diffractive Dijets in DIS

Measurements of diffractive dijet production can directly constrain the diffractive gluon density at high momentum fractions, extending the kinematic range of reliably determined diffractive parton densities.

H1 measures dijets in the kinematic range of  $4 < Q^2 < 80 \text{ GeV}^2$ ,  $0.1 < y < 0.7$  and  $x_P < 0.03$  [17], and compares the cross section with the predictions from two sets of parton densities, H1 2006 DPDF Fit A and Fit B, which differ in the parametrisation of the gluon density. Both DPDF sets provide a good description of the inclusive data. However, as displayed in Fig. 3.12, H1 2006 DPDF Fit A does not succeed to describe the dijet data. The large difference between the two predictions at high  $z_P$  reflects the large uncertainty on the gluon density in this range as determined from inclusive data alone.

In order to improve the gluon density parametrisation, a combined fit to diffractive inclusive and dijet data is performed, 'H1 2007 Jets DPDF Fit', using NLO QCD calculations based on QCD factorisation and DGLAP evolution. Both data sets are described well by the fit. Including the dijet data in the fit allows to simultaneously determine both the diffractive gluon and the singlet quark distribution with good and comparable accuracy in the range  $0.05 < z_P < 0.9$ . It is the first reliable determination of the diffractive gluon density up to large momentum fractions.

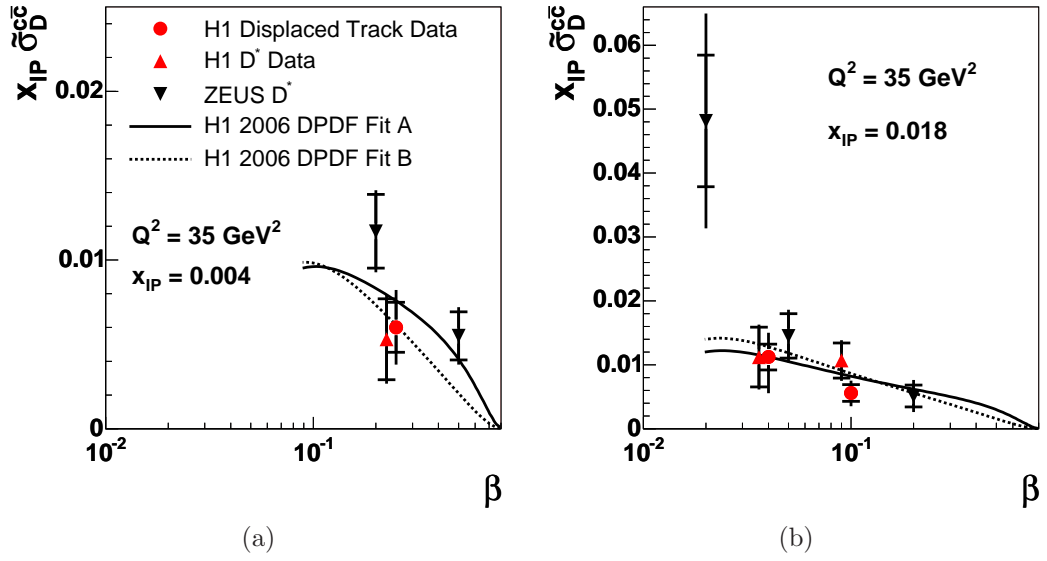


Figure 3.11: The measured reduced cross section  $x_{IP} \tilde{\sigma}_D^{c\bar{c}}$  shown as a function of  $\beta$  for two different values of  $x_{IP}$ . The inner error bars of the data points represent the statistical error, while the outer error bars represent the statistical and systematic uncertainties added in quadrature. The measurements obtained from  $D^*$  mesons from H1 and ZEUS are also shown. Measurements at the same values of  $\beta$  are displaced for visibility. The measurements are compared with NLO predictions based on two alternative sets of diffractive parton density functions (Fit A and Fit B) extracted by H1. [18]

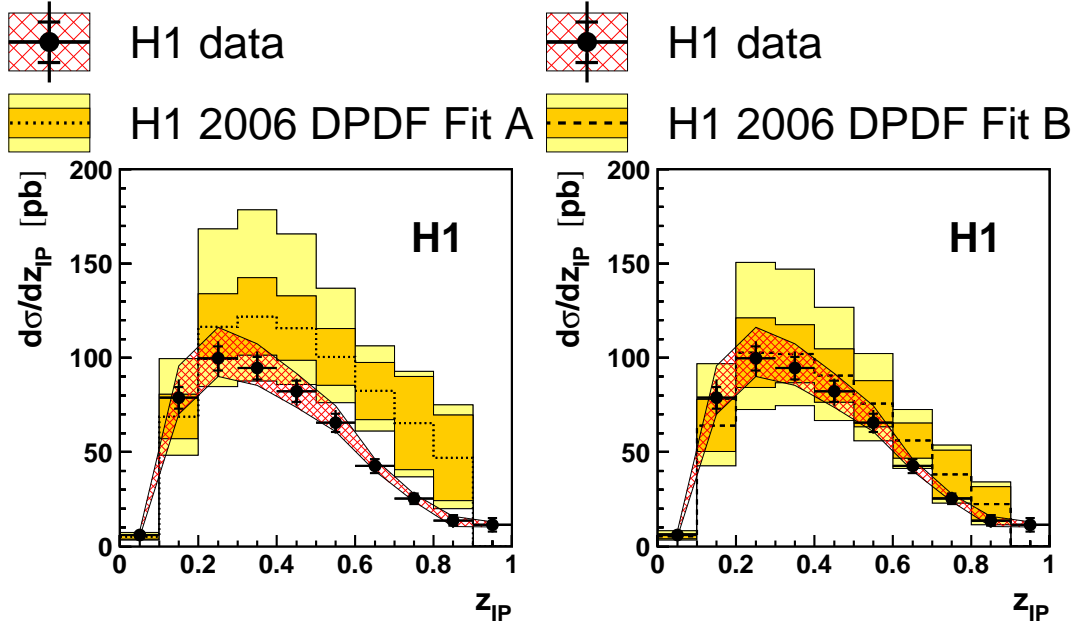


Figure 3.12: Cross section for diffractive dijets, differential in  $z_{IP}$  compared to NLO predictions based on the parton densities from the H1 2006 DPDF fits. The data are shown as black points with the inner and outer error bars denoting the statistical and quadratically added uncorrelated systematic uncertainties, respectively. The hatched band indicates the correlated systematic uncertainty. In the left panel the data are compared to the NLO QCD prediction based on the H1 2006 DPDF fit A (dotted line) and in the right panel to the prediction based on the H1 2006 DPDF fit B (dashed line). The lines are surrounded by a dark shaded band indicating the parton density and hadronisation uncertainties. In the light shaded band the scale uncertainty is added quadratically to the parton density and hadronisation uncertainties. The prediction for  $z_{IP} > 0.9$  is not shown since the hadronisation corrections for this bin cannot be determined reliably. [17]

### 3.2.3 Diffractive Longitudinal Proton Structure Function

The diffractive DIS cross section can be expressed in terms of linear combination of structure functions  $F_2^D$  and  $F_L^D$ . While  $F_2^D$  is sensitive to the total photon-proton cross section,  $F_L^D$  is only sensitive to the longitudinally polarised photon contribution. Similarly as for its inclusive counterpart, the diffractive longitudinal structure function is thus zero in the quark-parton model, but may acquire a non-zero value in QCD, with contributions dependent on both the diffractive quark and gluon densities at leading twist [19]. The dominant role played by gluons in the diffractive parton densities [12, 15] implies that the leading twist  $F_L^D$  should be approximately proportional to the diffractive gluon density and should be correspondingly large. A measurement of  $F_L^D$  would provide a powerful independent tool to verify our understanding of the underlying dynamics and to test the gluon density extracted indirectly in QCD fits from the scaling violations of  $F_2^D$ . This is particularly important at the lowest  $x$  values, where direct information on the gluon density cannot be obtained from jet or  $D^*$  data due to kinematic limitations and where novel effects such as parton saturation or non-DGLAP dynamics are most likely to become important.

A previous attempt to measure  $F_L^D$  [47] exploited the azimuthal decorrelation between the proton and electron scattering planes caused by interference between the transverse and longitudinal photon contributions [48]. However, due to the relatively poor statistical precision available with proton-tagged data, the results were consistent with zero. The H1 collaboration has recently published measurements of the inclusive longitudinal structure function,  $F_L(x, Q^2)$  [49], separated from  $F_2(x, Q^2)$  on the basis of the centre of mass energy dependence of the DIS cross section at fixed  $x$  and  $Q^2$ . A similar approach can be taken to extract  $F_L^D$  [50].

## 3.3 Geometric Scaling

### 3.3.1 First Observation

The geometric scaling follows from the concept of dipole picture of the DIS  $ep$  scattering. The prescription for the dipole cross section  $\hat{\sigma}(x, r)$  in Eq. 2.45) only depends on the dimensionless ratio  $r/R_0(x)$  and its energy dependence is entirely driven by the saturation radius  $R_0(x)$  [40]. This property of  $\hat{\sigma}(x, r)$  is referred to as **geometric scaling**. It has a consequence on the prescription for the total  $\gamma^*p$  cross section given by the dipole model in Eq. 2.43. After the integration, the total cross section  $\sigma_{\gamma^*p}$  becomes a function of only one dimensionless variable

$$\tau = Q^2 R_0^2(x) \quad (3.5)$$

instead of  $x$  and  $Q^2$  separately

$$\sigma_{\gamma^*p}(x, Q^2) = \sigma_{\gamma^*p}(\tau). \quad (3.6)$$

The first observation of the geometric scaling, by A. Stasto *et al.* [40], in data at  $0.045 < Q^2 < 450 \text{ GeV}^2$  and  $x < 0.01$  is shown in Fig. 3.13.

Such scaling was initially attributed to the saturation of the parton density. In the small  $x$  regime the standard perturbation theory is not well justified due to the strong

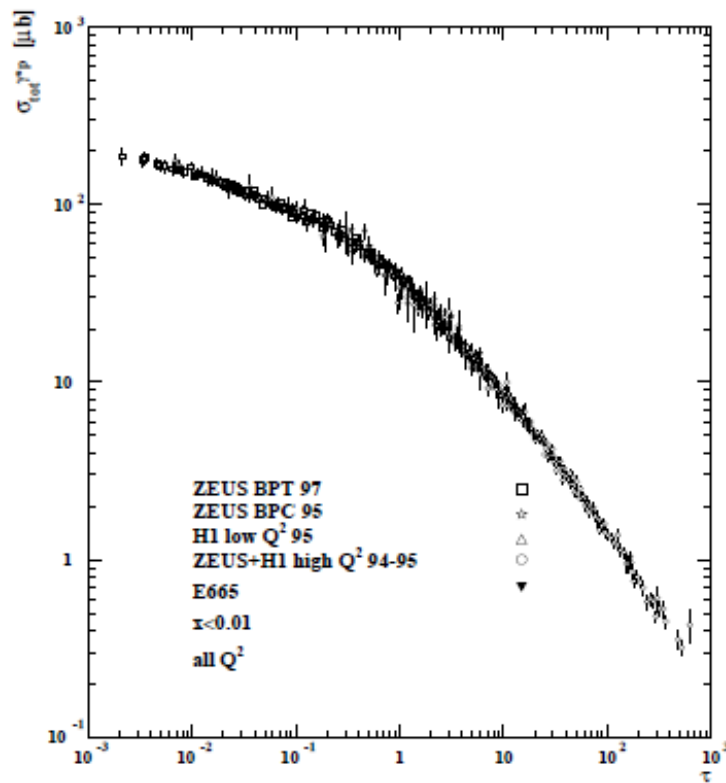


Figure 3.13: Experimental data on  $\sigma_{\gamma^*p}$  from the region  $x < 0.01$  plotted versus the scaling variable  $\tau = Q^2 R_0^2(x)$ . [40]

growth of the gluon density with decreasing  $x$ . As a consequence, the saturation models also predict the very high parton densities to saturate [52]. The validity of the applicability of the linear evolution equations for the parton densities is therefore limited. However, they can be modified to include the nonlinear terms in the parton density responsible for the gluon recombination. It turns out that, the solutions to the nonlinear equations for the gluon density at small  $x$  do indeed lead to the geometric scaling property. [5]

### 3.3.2 Scaling Properties in DIS

Geometric scaling directly follows from the solutions to the nonlinear equations in the saturated regime. However, the DGLAP evolution is also compatible with geometric scaling. It is known that the DGLAP evolution describes the deep inelastic data even at very low  $x$  and  $Q^2$ . This raises questions whether geometric scaling can be attributed directly to saturation or not. [5]

In Appendix C, a thorough analysis of the scaling properties in DIS data can be found. The analysis tests the predictions for the geometric scaling following from the non-linear Balitsky-Kovchegov equation [53]. The predictions are fitted to data from HERA and fixed-target experiments. Standard DIS and DVCS data samples are considered for the studies. The scaling properties are also tested on the elastic vector meson and diffractive data.

## 3.4 From HERA to Tevatron

### 3.4.1 Selection of Diffractive Events

Similarly as at HERA, the diffractive events in the hadron-hadron collisions at Tevatron are characterised by the exchange of colourless object, pomeron, that leads to a gap in rapidity. Since there are two hadrons involved in the interaction, the classification of events is the following:

- **non-diffractive events (ND):** The hadrons are directly involved in the interaction. No pomerons are exchanged and consequently no rapidity gap is observed.
- **single diffractive events (SD):** Only one hadron exchanges a pomeron and stays intact, leading to a rapidity gap on one side of the rapidity spectrum.
- **double pomeron exchange (DPE):** Both hadrons exchange a pomeron and stay intact. Therefore, the produced final state is separated from the scattered protons by a rapidity gap on both sides.

The diffractive events at HERA and Tevatron are selected in a similar way.

- **Large Rapidity Gap Method (LRG)** A simple selection demanding no signal (above certain noise level) close to the direction of the proton beam, and thus ensuring the presence of a rapidity gap in an event. In case of  $\bar{p}p$  collisions at Tevatron, a gap can be required only on one side of the rapidity spectrum for SD events, or on both sides for DPE events.

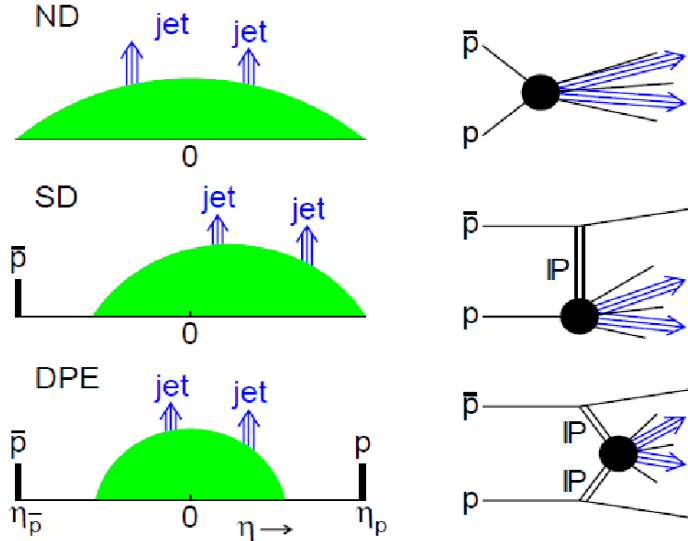


Figure 3.14: Non-diffractive (top), single diffractive (middle) and double pomeron exchange (bottom) event.

- Proton Tagging** Diffractive events can also be recognized by detecting the scattered proton which stays intact in the diffractive interactions. Special detectors, called Roman pots, can be installed close to the beam pipe in the direction of the proton beam far from the central detector, in order to detect the protons scattered under small angles. The Roman pot detectors have high requirement of radiation hardness as the active part of the detector is positioned very close to the beam. The detectors are usually designed so that they can move away from the beam in case of high radiation. As an illustration of such detector, the Forward Proton Spectrometer (FPS) at H1 is shown in Fig. 3.15.

The proton tagging has a disadvantage of low acceptance. On the other hand, it can reconstruct the momentum of the scattered proton and thus provide more constraints on kinematics of the process.

### 3.4.2 Testing QCD Factorisation at Tevatron

H1 provided two sets of diffractive parton densities based on the inclusive measurements of the diffractive DIS NC processes: H1 2006 DPDF Fit A and Fit B. The inclusive measurements are able to well constraint the quark densities. However, the gluon densities are determined only weakly from the scaling violations. The concept of QCD hard factorisation was tested on exclusive measurements that are more sensitive to gluons. These are the studies of open charm production in diffraction and diffractive dijets. Both measurements are successfully described by the structure functions from the fits to the inclusive data. The dijet data are even able to further constrain the gluon density and give a preference to H1 2006 DPDF Fit B (over the Fit A), as illustrated in Fig. 3.12.

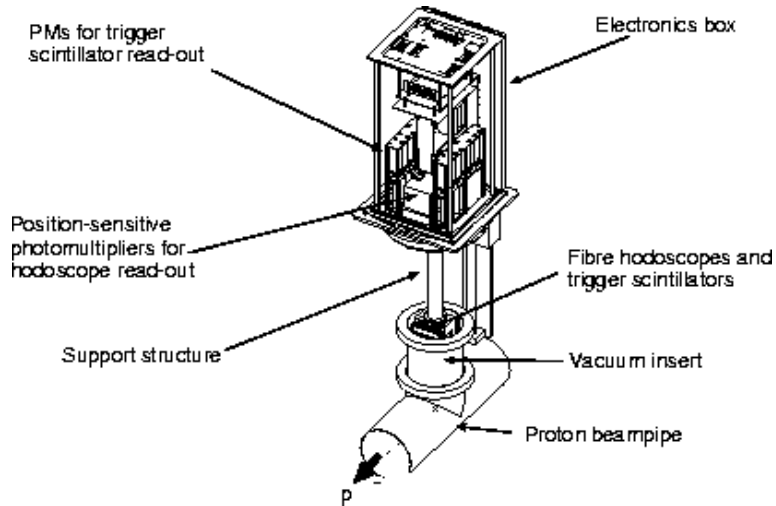


Figure 3.15: Forward Proton Spectrometer (H1).

The analysis of diffractive longitudinal proton structure function, the main topic of this work, also gives an important cross check of the validity of the description of diffractive processes based on QCD.

The concept of QCD factorisation was tested in many ways at HERA, and it is successful in describing all kinds of diffractive processes in terms of diffractive parton densities. Therefore, it is natural to assume that the diffractive parton densities derived at HERA are universal and applicable also at other colliders. The measurement of the diffractive proton structure function is also possible at Tevatron. The CDF collaboration measured the ratio of dijet events in single diffractive and non-diffractive events, which is directly proportional to the ratio of the diffractive to the inclusive proton structure functions:

$$R(x) = \frac{N_{jj}^{SD}(x)}{N_{jj}^{ND}(x)} \sim \frac{(F)_{jj}^{SD}(x)}{F_{jj}^{ND}(x)} \quad (3.7)$$

The comparison between the CDF measurement (black points, with systematic errors as shaded area) and the expectation from the H1 QCD fits in full line is shown in Fig. 3.16 shows the well known comparison of the diffractive structure function, plotted as a function of the fractional parton momentum with respect to the diffractive exchange  $\beta$ , as measured by the CDF collaboration with the expectations from the QCD fits to the H1 data. The predictions overestimate the CDF data by a factor of  $\sim 10$ .

The observation stimulated theoretical work in this field. It was shown that the QCD factorisation is not expected to hold in hadron-hadron collisions [54]. Additional soft exchanges with respect to the hard interaction are expected to fill in the rapidity gap, and thus spoil the experimental signature of the diffractive event. The probability that the large rapidity gap is not destroyed by the additional interactions is quantified by the variable  $S^2$  called **survival probability** [55]. It is defined in such a way that  $S^2 = 1$  for processes where no gap destruction occurs.

The other interesting measurement carried out at Tevatron is the test of factorisation between single diffraction and double pomeron exchange. The results from the CDF Collaboration are shown in Fig. 3.17 [56]. Whereas the factorisation does not

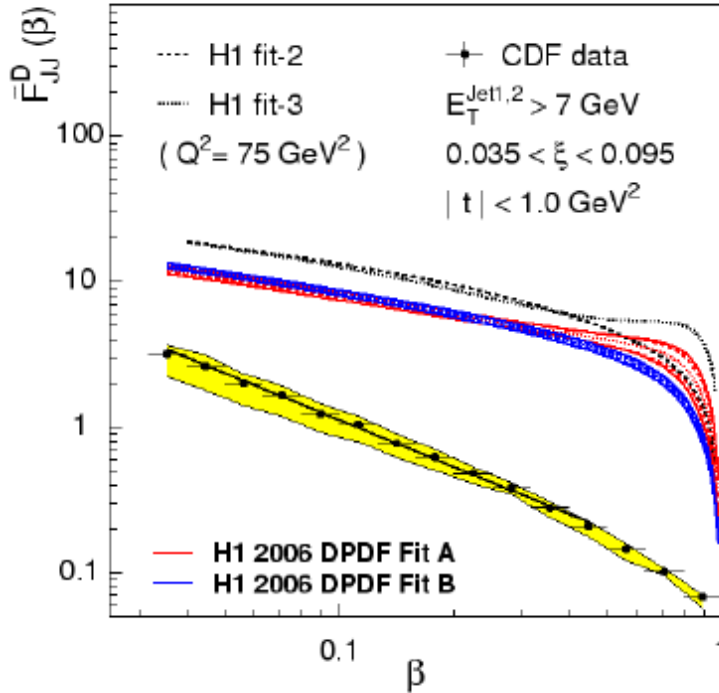


Figure 3.16: Comparison of the CDF measurement of diffractive structure function (black points) with the expectations of the H1 QCD fits (red full line).

hold for the ratio of single diffraction to non-diffractive events, the factorisation works for the ratio of double pomeron exchange to single diffraction. In other words, the gap survival probability is not sensitive to whether there is only one or two rapidity gaps.

To summarize, the QCD factorisation is not observed to hold between HERA and Tevatron. However, it holds between the single diffraction and double pomeron exchange which means that the soft exchanges do not depend on the hard scattering. The concept of gap survival probability was studied also at HERA. [57, 15] The diffractive dijet photoproduction has, in LO QCD, so called resolved contribution which is a process with similar topology to the diffractive interactions at Tevatron (see Fig. 3.18). The H1 experiment observed factorisation breaking pointing to an additional soft exchange between the proton and the photon remnant [57]. However, the results from ZEUS [15] are compatible with a gap survival probability close to 1. The results from H1 and ZEUS are not in contradiction since both measurements were carried out in different kinematical domain, and hint a possible  $E_T$  dependence of the gap survival probability. It has to be admitted that the mechanism is not fully understood and further studies are welcome. Of special interest will be the diffractive processes at LHC that will allow to test the concept of QCD factorisation even at higher energies.

### 3.4.3 Diffractive Exclusive Event Production

Fig. 3.19 gives a schematic view of non-diffractive, inclusive double pomeron exchange and exclusive diffractive processes at Tevatron. All three types of processes can contain the same specific final states such as Higgs boson, dijets or diphotons. In the standard

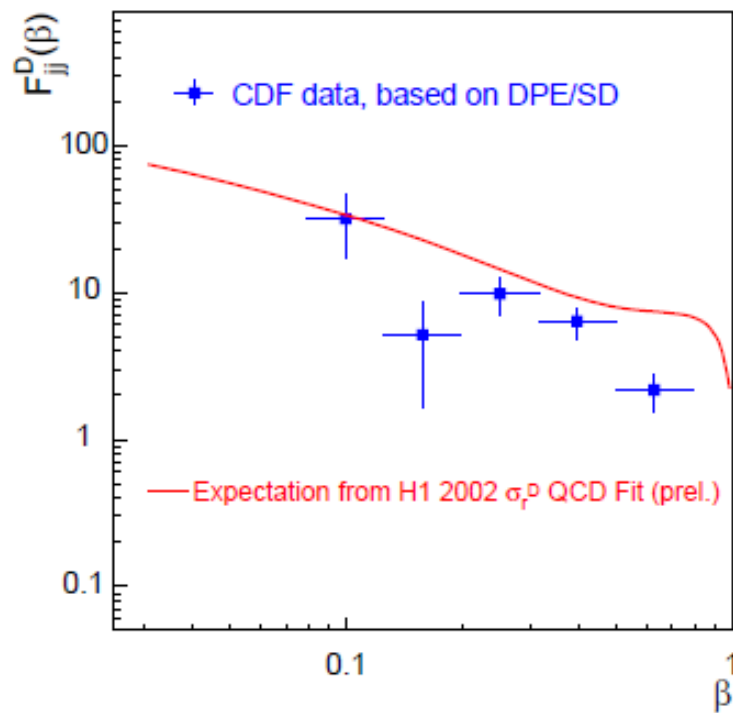


Figure 3.17: Restoration of factorisation for the ratio of double pomeron exchange to single diffractive events (CDF Collaboration).

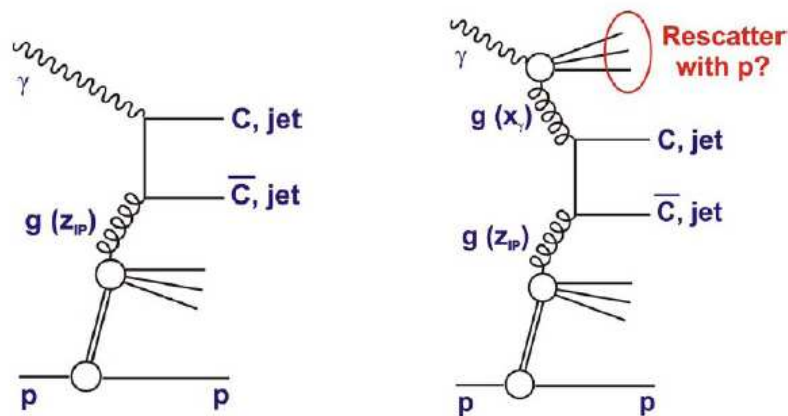


Figure 3.18: Diagram of the direct (left) and resolved (right) diffractive photoproduction process at HERA. The resolved processes are similar to the diffractive hadron-hadron interactions at Tevatron, as an additional soft interactions can occur between the photon remnant and the proton.

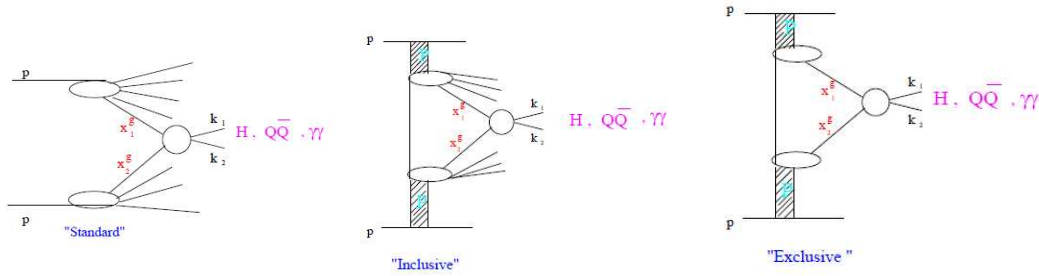


Figure 3.19: Diagrams of non-diffractive, inclusive double pomeron exchange and exclusive diffractive events at Tevatron.

non-diffractive process, these final states are produced directly by a coupling to the proton, and proton remnants occur in the final state too. In the double pomeron exchange processes, both protons remain intact and the total available energy is used to produce the heavy object and the pomeron remnants. A special class of the diffractive exchange processes exists such that no energy is lost in the pomeron remnants. This has an important kinematical consequence: the mass of the produced object can be directly computed from the momenta of the scattered protons  $\xi_1$  and  $\xi_2$  that can be measured in the Roman pot detectors

$$M^2 = \xi_1 \xi_2 s. \quad (3.8)$$

Therefore, one can benefit from the good resolution of the Roman pots and accurately reconstruct the mass in the central detector. The information on kinematics can also be used to increase the signal over background ratio.

### 3.4.4 Exclusive Dijet Production

The first results on the exclusive dijet production in high energy  $\bar{p}p$  collisions at CDF are presented in [58]. The analysed data sample of integrated luminosity  $310 \text{ pb}^{-1}$  demonstrates the presence of exclusively produced dijets  $\bar{p}p \rightarrow \bar{p} + \text{dijet} + p$ , by means of detailed studies of distributions of the **dijet mass fraction**  $R_{jj}$ , defined as the dijet mass divided by the mass of the system produced by the double pomeron exchange.

Fig. 3.20 compares data  $R_{jj}$  distributions with inclusive POMWIG Monte Carlo simulations [59]. An excess of events in the data over the Monte Carlo predictions at high  $R_{jj}$  is observed, which is consistent in terms of kinematic distribution shapes with the presence of an exclusive dijet signal as modeled by the ExHuME [60] and exclusive DPE in DPEMC [61] Monte Carlo simulations.

## 3.5 Prospects for Diffraction at LHC

The large rapidity gap method is widely used at HERA and Tevatron. However, it may be problematic at LHC as there is huge pile-up expected of up to 35 interactions per bunch crossing. There is also the fact that the ATLAS detector does not have a full coverage in rapidities. Searching for smaller gaps in rapidities may therefore be difficult due to the contamination from the other interactions in the bunch crossing. And the

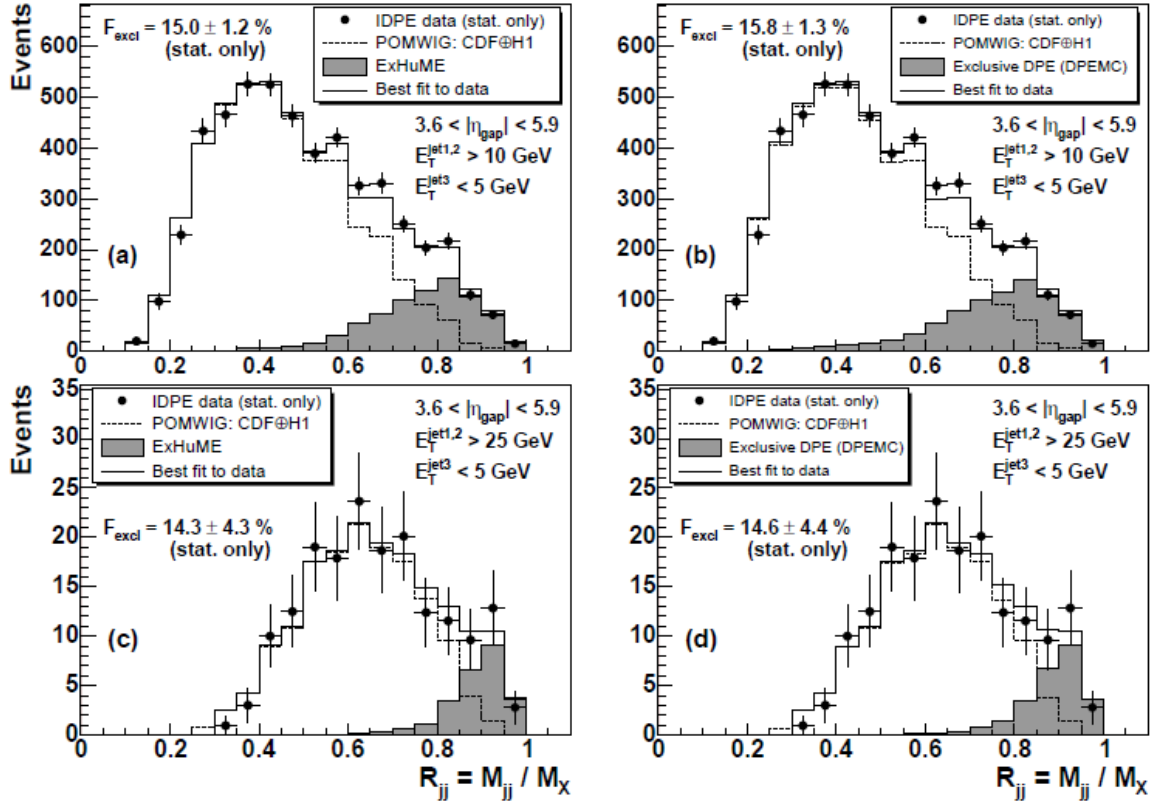


Figure 3.20: Dijet mass fraction in inclusive DPE data (points) and best fit (solid histograms) with a mixture of (i) POMWIG generated events composed of pomwig DPE signal and SD plus ND background events (dashed histogram), and (ii) exclusive dijet Monte Carlo events (shaded histogram). [58]

larger gaps cannot be fully seen because of the limited rapidity coverage that decreases the efficiency of the LRG selection.

The proton tagging technique detects directly the scattered proton from the diffractive process and also allows to reconstruct its momentum. However, the pile-up puts high demands on the detectors used since there is a precise timing information needed in order to assign the tagged proton to the correct interaction vertex in the central detector.

The idea to install the forward detectors at ATLAS is motivated by the possibility to search for novel physics in the diffractive channels [62]. Two locations for the forward detectors are considered at 220 and 420 m to ensure a good coverage in  $\xi$  or in mass of the diffractively produced object. Installing forward detectors at 420 m is a challenging task since the detectors should be located in the cold region of LHC, where the available place is limited because of the cryostat. The **ATLAS Forward Physics (AFP)** [62] project is under discussion in the ATLAS collaboration and includes both 220 and 420 m detectors on both sides of the main ATLAS detector.

### 3.5.1 Physics Motivation

The physics motivation of the project corresponds to different domains of diffraction that were described in the previous sections. The following text lists the main topics.

- Search for the diffractive Higgs boson production via double pomeron exchange. This is especially challenging in case of low Higgs boson masses, where the Higgs boson decays into  $b\bar{b}$  and the standard non-diffractive search is difficult [63].
- Measurement of the exclusive production of diffractive events and its cross section in the jet channel as a function of jet transverse momentum. Its understanding is necessary to control the background to Higgs signal [64].
- Testing the QCD picture of the proton structure functions determined at HERA. Because of the different kinematical coverage (see 3.21) the evolution dynamics can be probed as the obtained structure functions have to be evolved to as yet experimentally unknown domain. Here, the concept of the gap survival probability will be important.
- Sensitivity to other topics such as the anomalous coupling of the photon to  $W$  or  $Z$  bosons. It can be measured in the QED production of  $W$  or  $Z$  boson pairs [65], and it provides the cleanest way to detect Higgsless or extra dimensions models at LHC [66].

### 3.5.2 Forward Detectors

Two kinds of detectors are proposed to be put into the forward detectors: 3D Silicon detectors to precisely measure the position of the scattered protons, and precise timing detectors with a pico-second resolution.

The 3D Silicon detectors allow to measure a position with better than  $10\ \mu\text{m}$  resolution. The detectors consist of many layers of 3D silicon pixels, and will be read out by the FEI4 chip. The chip is fast enough to send back the local L1 trigger decision

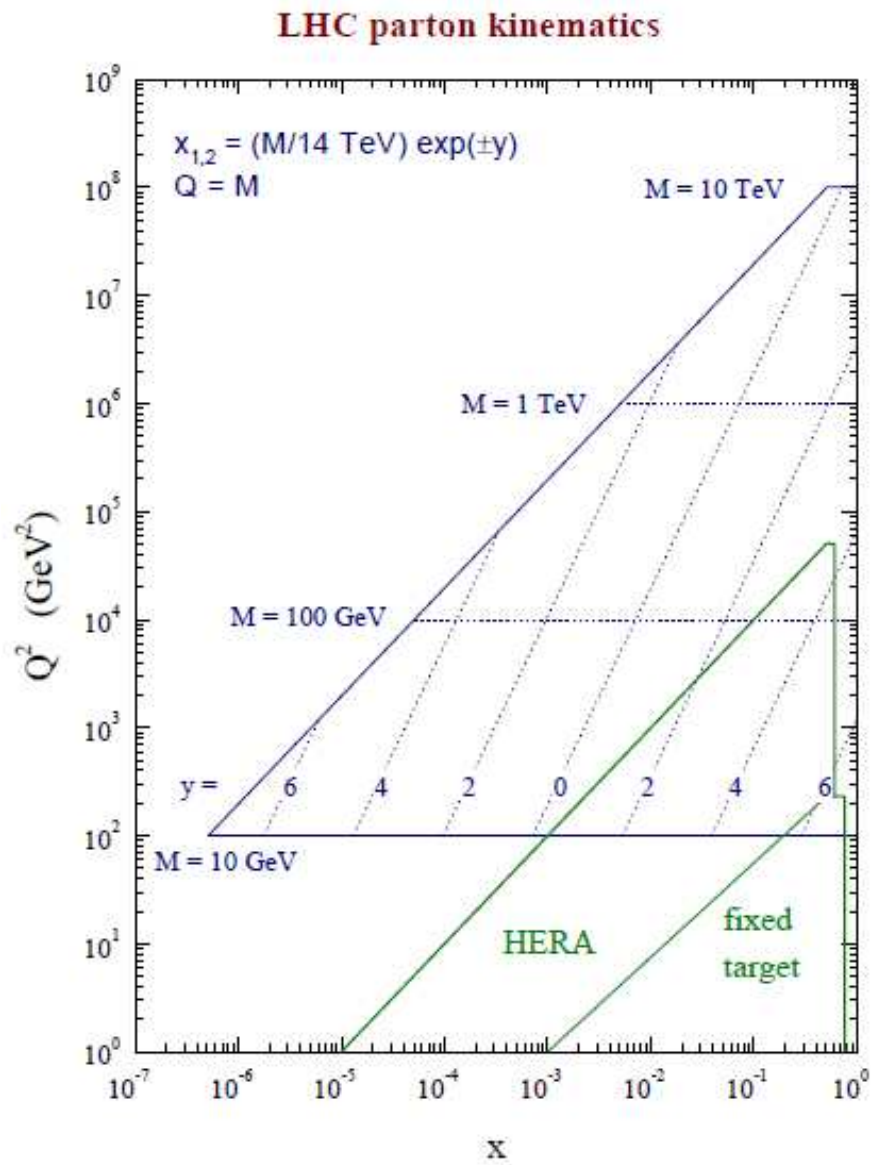


Figure 3.21: Kinematical coverage. [5]

from the forward detectors to ATLAS, and take it into account in the full L1 decision. [62]

Up to 35 interactions per bunch crossing are expected during the highest luminosity of LHC. The timing detectors are necessary in order to identify the interaction vertex of the detected scattered proton. Therefore, a precision of  $\sim 1$  mm is required, which corresponds to 2 – 5 ps resolution in time.

Pico-second timing resolution is very challenging and there is an independent R&D project [67], that will find applications in medicine, security as well as particle physics. The diffractive protons emit photons in a gas medium or in a crystal, which are then read by the Micro-Channel Plate (MCP) photomultipliers [62]. Appendix B includes a publication of a study where the simulations predict measuring both space with millimeter precision and fast timing at a few pico-seconds resolution.

# Chapter 4

## HERA and the H1 Detector

### 4.1 HERA Accelerator

The HERA accelerator ring is located at DESY laboratory in Hamburg, Germany. It has a circumference of approximately 6.3 km and consists of four 360 m long straight sections connected by four circular segments with a radius of 797 m. An overview of the accelerator can be found in Fig. 4.1. The tunnel contains a beam-pipe with normal conducting magnets for the electron beam, and a superconducting proton ring. The electrons and protons circulate in bunches, containing roughly  $10^{11}$  particles with a Gaussian density distribution of  $\sigma \approx 11$  cm each. Both rings can store up to 220 bunches and the time between two consecutive bunches is 96 ns.

There are two general purpose experiments that study the  $ep$  collisions at HERA. The H1 detector was built around the north interaction point. The ZEUS detector is located in the south.

During the HERA-I running period (1992-2000) the electrons at the energy of  $E_e = 27.6$  GeV collided with the protons at the energy of  $E_p = 820$  GeV. The total integrated luminosity of  $L \approx 140 \text{ pb}^{-1}$  was collected during this period. In the years 2000-2003, new focusing magnets were installed close to the interaction regions in order to increase the luminosity. After the upgrade, the HERA-II running period started, and the nominal proton beam energy was increased to  $E_p = 920$  GeV. Almost  $L \approx 400 \text{ pb}^{-1}$  of data had been collected by the end of the HERA data taking in June 2007.

### 4.2 Overview of the H1 Detector

The H1 detector is a multipurpose detector consisting of a set of subdetectors designed for a full reconstruction of  $ep$  interactions. Due to the different energies of the colliding beams, the H1 detector has an asymmetric design with the forward region highly segmented to reconstruct hadronic final states of high multiplicities. The backward region is optimised for detection of the scattered electron. The H1 detector is embedded in the right-handed Cartesian coordinate system such that the  $z$ -axis follows the direction of the proton beam, the  $y$ -axis points vertically upwards and the  $x$ -axis points to the centre of the HERA machine. The origin of the H1 coordinate system is defined at the nominal interaction point. As indicated in Fig. 4.2, the electrons go in the  $-z$  direction

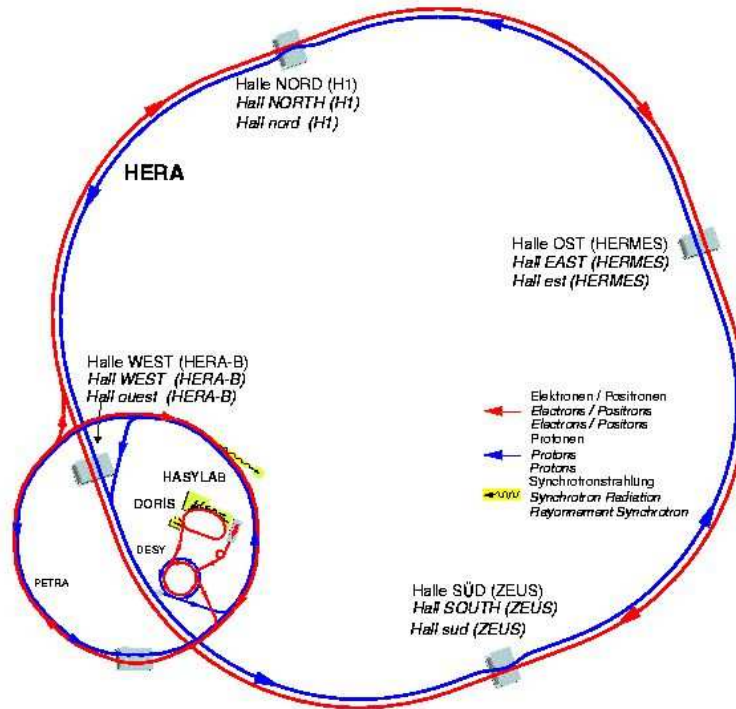


Figure 4.1: The HERA accelerator.

and enter the detector through the beam pipe [1] on the left side in the picture. The protons go in the opposite direction. The interaction point is surrounded by silicon detectors that are followed by the central [2] and forward [3] tracking detectors. These are surrounded by a large calorimeter system consisting of the Liquid Argon (LAr) calorimeter [4] and [5] in the central and forward region, and the SPACAL calorimeter [12] in the backward region. Both calorimeters are divided into an electromagnetic and hadronic parts. An additional plug calorimeter [13] is installed in the forward direction close to the beam pipe. The LAr calorimeter is surrounded by a superconducting coil [6] which provides a homogeneous magnetic field of 1.15 T and helps to reconstruct the charge of the detected particles. The iron return yoke [10] is used to detect muons and to measure the energy leakage from hadrons that are not fully contained within the LAr calorimeter. The forward muon detector [11] is designed to identify and measure the momentum of muons penetrating in the forward direction. Away from the central detector in the  $-z$  direction, a set of electromagnetic calorimeters is situated to measure the final state particles from Bethe-Heitler processes that are used to determine the luminosity. A more detailed description of the H1 detector can be found in [68].

## 4.3 Tracking

### 4.3.1 The Central Track Detectors

Silicon strip detectors are placed close to the beam pipe in order to provide a precise vertex information. The Central Silicon Tracker (CST) is located around the nominal

### The H1 Detector at HERA

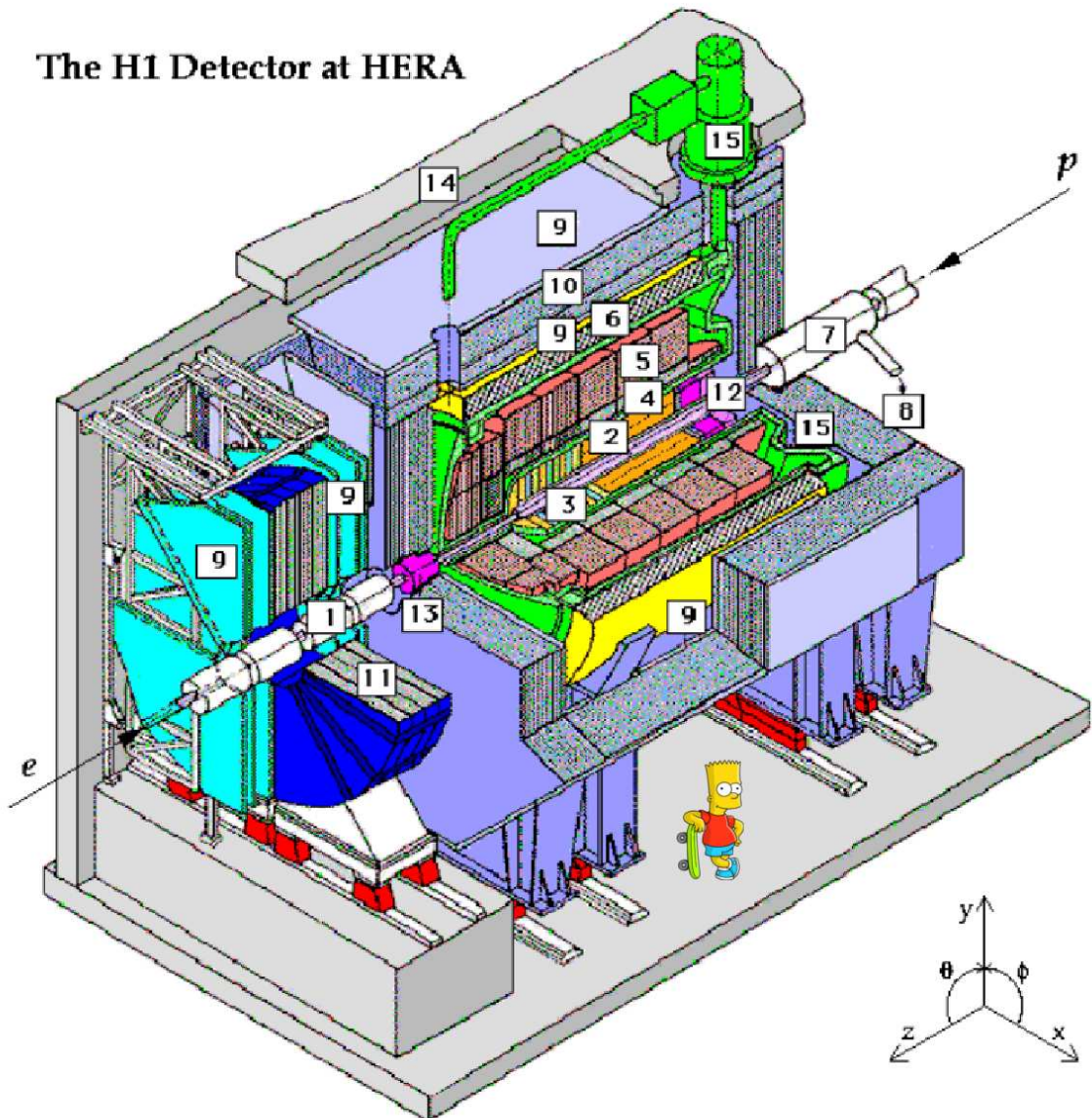


Figure 2.2: 3D view of the H1 Detector. The numbers denote:

1	Beam pipe and beam magnets	9	Muon chambers
2	Central tracking chambers	10	Instrumented iron yoke
3	Forward tracking chambers	11	Forward muon toroid
4	Electromagnetic LAr calorimeter	12	Backward calorimeter SpaCal and backward drift chamber
5	Hadronic LAr calorimeter	13	Forward plug calorimeter
6	Superconducting coil (1.16 T)	14	Concrete shielding
7	Compensating magnet	15	Liquid argon cryostat
8	Helium supply for 7		

Figure 4.2: The H1 detector.

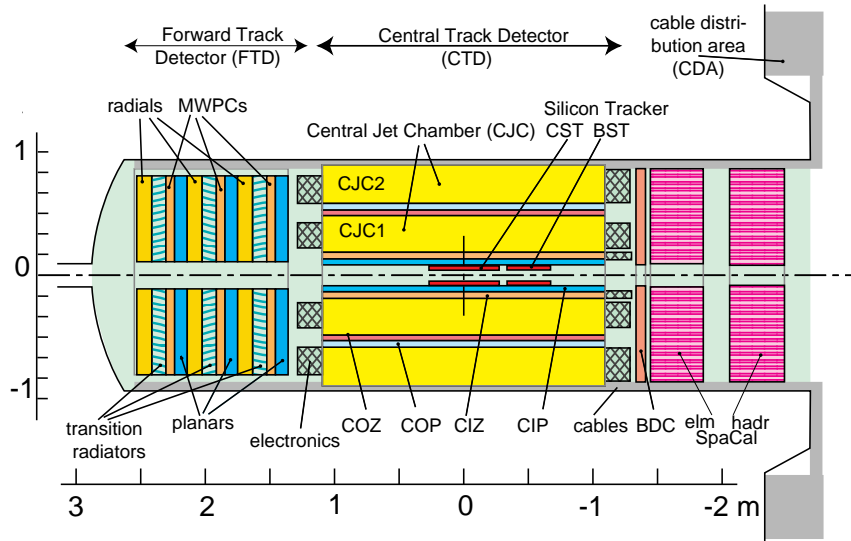


Figure 4.3: Longitudinal view of the H1 tracking system.

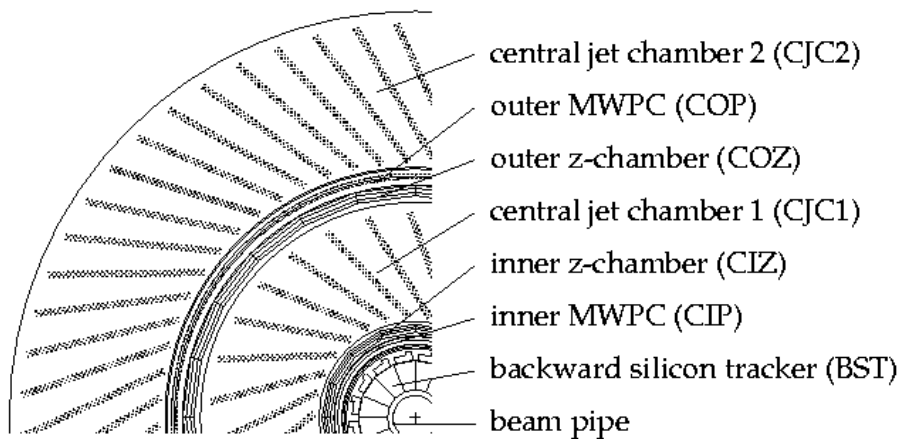


Figure 4.4: Radial view of the H1 tracking system.

interaction point in the region that corresponds to the polar angles between  $29^\circ$  and  $151^\circ$ . It comprises 32 ladders in two layers at the radius of 6 cm and 10 cm, and allows to measure the  $r$  and  $\varphi$  coordinates of a track with an impact parameter resolution of  $57\ \mu\text{m}$ . It also provides a measurement of secondary vertices.

The track reconstruction in the central region is based on two concentric drift chambers, the central jet chamber 1 (CJC1) and the central jet chamber 2 (CJC2), and the central inner (CIZ) and central outer (COZ) drift chambers. The central tracking system has a full azimuthal acceptance, and covers the  $\theta$  range between  $15^\circ$  and  $165^\circ$ . The Central Jet Chambers CJC1 and CJC2 are 2.2 m long and consist of wires parallel to the beam pipe. Jet cells are tilted by  $30^\circ$  in the transverse plane. The space point resolution is  $170\ \mu\text{m}$  in the  $r$ - $\varphi$  plane, whereas the  $z$  coordinate of a hit is measured with an uncertainty of 2.2 cm. The specific energy loss  $dE/dx$  is measured to improve the particle identification. The  $x$  and  $y$  positions of the interaction vertex are determined using high momentum tracks and the  $z$  coordinate is reconstructed from all tracks fitting the vertex. The resolution in  $z$  is improved by involving the CIZ and COZ chambers. They are located inside and outside of CJC1 at a radius of 18 m and 24 m, respectively. The resolution in  $z$  is  $260\ \mu\text{m}$ .

The combination of CJC1 and CJC2 with the CIZ and COZ chambers leads to a momentum resolution of  $\sigma(p)/p^2 < 0.01\ \text{GeV}^{-1}$ . Two central multiwire proportional chambers CIP and COP have a response time faster than the beam crossing rate and provide level 1 trigger information (see Section 4.8).

### 4.3.2 The Backward Silicon Tracker

The Backward Silicon Tracker (BST) is located close to the beam pipe between the CST and the SPACAL calorimeter and covers the range of polar angles between  $165^\circ < \theta < 175^\circ$ . The BST consists of 8 planes of silicon detectors arranged perpendicular to the  $z$  axis. Each plane is divided into 16 segments in azimuthal angle. Every segment consists of two silicon strip detectors which are oriented both in perpendicular and radial direction. The tracks in the backward region are reconstructed from the hits with a polar angle resolution of  $0.03^\circ$ . The BST allows a charge reconstruction of the scattered electron at smaller scattering angles with respect to the CJC.

## 4.4 Calorimetry

### 4.4.1 The Liquid Argon Calorimeter

The LAr calorimeter is a non-compensating calorimeter designed to detect electrons, muons and neutral particles, as well as high energy jets. It has a high granularity and contains 44000 cells, each cell containing plates of absorber and active medium.

The liquid argon calorimeter (LAr) is a sandwich type calorimeter with the coverage of  $3.8^\circ < \theta < 155^\circ$ . The LAr calorimeter consists of eight wheels, each segmented in  $\varphi$  into eight identical octants (see Fig. 4.5). The wheels are divided into the inner electromagnetic region containing absorbers made of 2.3 mm thick lead plates, and the outer hadronic region with absorber plates 16 mm thick. The plates are supplemented with a high voltage and are surrounded by liquid argon that serves as the active detection material. The size of the electromagnetic part corresponds to  $20 - 30$

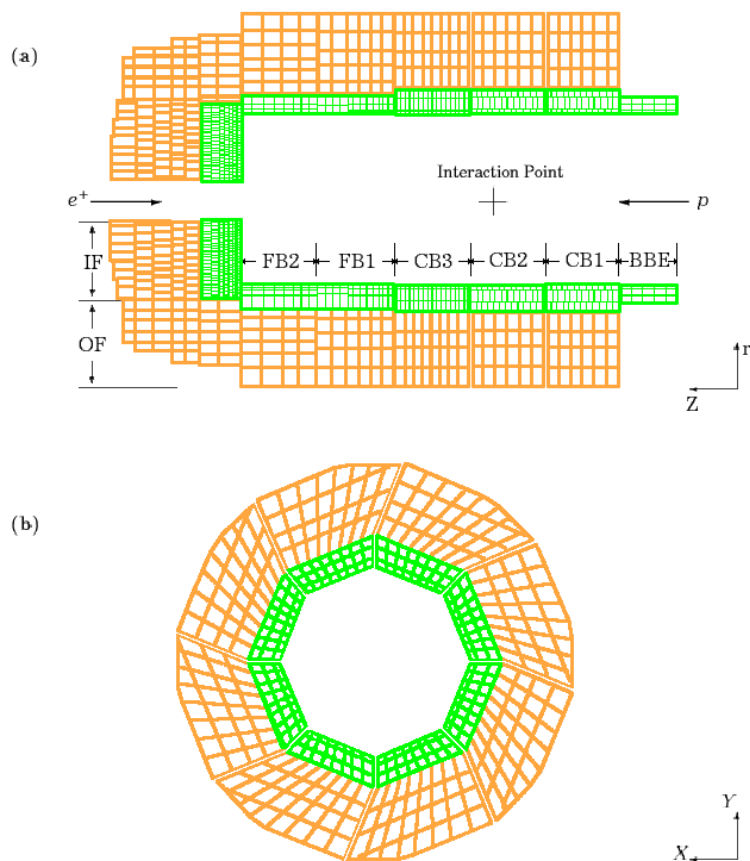


Figure 4.5: The Liquid Argon Calorimeter. Longitudinal view (a) shows the wheel structure, radial view (b) shows the octant structure of wheels.

radiation lengths, and the hadronic part corresponds to 5 – 8 interaction lengths, depending on the polar angle. The LAr is non-compensating, therefore the calorimeter response to hadrons of the same energy as leptons is reduced, typically by 30%. This difference is adjusted by adjusting the hadronic energy in the offline reconstruction software. The energy resolutions for the electromagnetic and hadronic showers are  $\sigma_{em}(E)/E = 0.12/\sqrt{E[\text{GeV}]} \oplus 0.01$  and  $\sigma_{had}(E)/E = 0.50/\sqrt{E[\text{GeV}]} \oplus 0.02$ , respectively.

#### 4.4.2 The Plug Calorimeter

The Plug calorimeter was specially designed to fill the gap in acceptance between the LAr calorimeter and the beampipe in order to minimize the energy losses in the forward region. Its coverage is  $0.6^\circ < \theta < 3.5^\circ$ . Given the geometrical constraints the Plug calorimeter is very compact in design. It is a sampling calorimeter consisting of 9 sheets of copper as the absorber medium. It has a rather poor resolution of  $\sigma_{had}(E)/E = 1.5/\sqrt{E[\text{GeV}]}$ .

#### 4.4.3 The SPACAL Calorimeter

The SPACAL calorimeter covers the backward scattering region between  $153^\circ < \theta < 173^\circ$ . It is a non-compensating sampling calorimeter, and it is divided into inner electromagnetic and outer calorimetric sections. Contrary to the LAr calorimeter, the absorber material in both sections is lead with embedded scintillating fibres as the active material. Due to the limited space available for the calorimeter, both sections are 25 cm thick and correspond to 28 radiation lengths in the electromagnetic part, and only 1 interaction length in the hadronic part. The number of combined interaction lengths for both sections is 2.2. Therefore, the SPACAL calorimeter is not suitable to detect jets. On the other hand, it is an excellent tool to measure the scattered electron in the DIS processes with virtualities roughly in the region of  $4 \text{ GeV}^2 < Q^2 < 100 \text{ GeV}^2$ . The energy resolutions of the electromagnetic and hadronic parts are  $\sigma_{em}(E)/E = 0.07/\sqrt{E[\text{GeV}]} \oplus 0.01$  and  $\sigma_{had}(E)/E = 0.50/\sqrt{E[\text{GeV}]} \oplus 0.02$ , respectively.

### 4.5 The Forward Detectors

#### 4.5.1 The Forward Muon Detector

The Forward Muon Detector (FMD) consists of two sets of three double-layers of drift chambers that are separated by a toroidal magnet, as can be seen in Fig. 4.6. Four of the double-layers are designed to measure the polar angle  $\theta$  and have their wires strung tangentially to the beam-pipe. Two double-layers have their wires in a radial direction and enable a  $\phi$  measurement. The FMD has an angular acceptance of  $3^\circ < \theta < 18^\circ$ . The presence of the toroidal magnet allows for a momentum reconstruction in the range between 5 GeV and 100 GeV. The post-toroidal layers are inherently noisier than the pre-toroidal ones because of the amount of the dead material and synchrotron radiation.

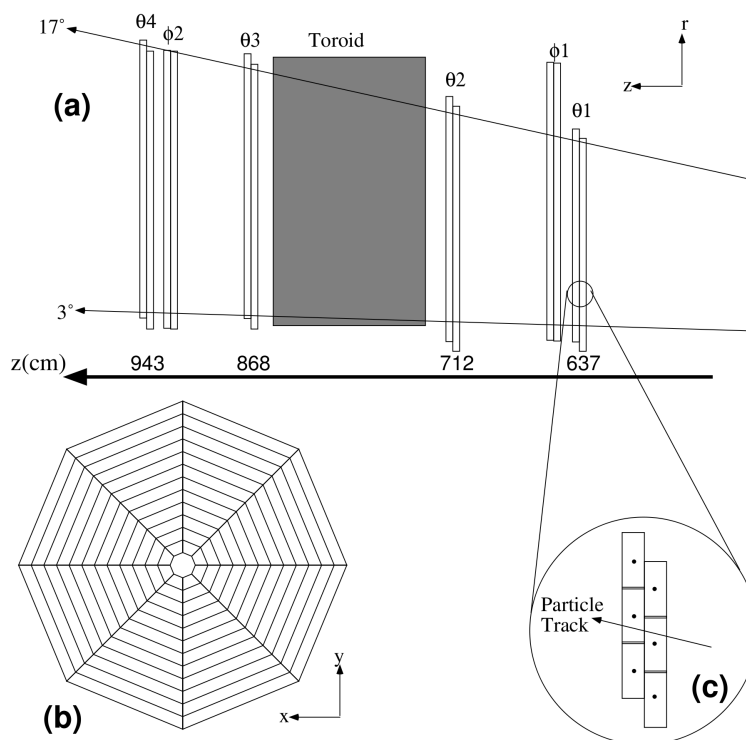


Figure 4.6: The forward muon detector. Six sets of double-layers separated by a toroidal magnet are shown (a), each layer having an octagonal structure. A particle producing a hit-pair in a double-layer is illustrated in (c).

### 4.5.2 The Forward Tagger System

The Forward Tagger System (FTS) includes 4 planes of scintillating counters. They are located at 26, 28, 53 and 92 m from the interaction point in the proton direction. Each layer consists of four counters that surround the proton beampipe. Each counter at 53 and 92 m is formed by two scintillators separated by a 1.5 mm steel layer. Each counter at 26 and 28 m has only one scintillator plate. All counters are protected against synchrotron radiation by 1 mm thick layer of lead.

The FTS allows detection of the proton fragments at very large rapidity with a good efficiency due to secondary interactions of hadrons with the collimators, beam-pipe, magnets and adjunct material.

## 4.6 The Time of Flight System

The Time of Flight (TOF) system is used to reject background from beam-wall and beam-gas interactions. It consists of scintillator layers placed at various distances from the interaction point. They are the BToF (backward ToF) at  $z = -275$  cm, the PToF (Plug ToF) at  $z = +540$  cm and the FToF (forward ToF) at  $z = +790$  cm. In addition there are two layers of Veto scintillator walls located at  $z = -650$  cm and  $z = -810$  cm. These are used to compare the time of arrival of the signal. The background processes occur at different times than the actual  $ep$  interaction and can thus be rejected. The ToF resolution is 1 ns and defines the region of the primary interaction vertex at  $-35 \text{ cm} < z_{\text{vtx}} < +35 \text{ cm}$ .

## 4.7 The Luminosity System

The cross section  $\sigma$  of a specific process can be extracted from the number of events  $N$  in a data sample with an integrated luminosity  $L$  using the relation

$$N = \sigma L. \quad (4.1)$$

The integrated luminosity is obtained from  $L = \int \mathcal{L} dt$ , where  $\mathcal{L}$  is the instantaneous luminosity measured in units of  $\text{cm}^{-2}\text{s}^{-1}$ . At HERA the instantaneous luminosity is determined from the measured rate of Bethe-Heitler events  $ep \rightarrow ep\gamma$ . The cross section of the Bethe-Heitler process is accurately calculable within QED. The H1 luminosity system is depicted in Fig. 4.7 and consists of the electron tagger (ET) located at  $z = -40$  m, and the photon detector (PD) which is placed at  $z = -102$  m.

## 4.8 Data Acquisition and Triggering

The time between consecutive  $ep$  interactions in the H1 detector is 96 ns, and it is determined by the bunch spacing in the HERA accelerator. It is not possible to record all the collisions at this rate. Therefore, there is a multi-stage triggering system that is able to take almost immediate decision, and thus reject background events and keep as many  $ep$  interactions as possible. The H1 trigger system consists of four levels, which reduce the incoming rate of 10.4 MHz determined by the HERA bunch spacing down to about 20 Hz. It is schematically shown in Fig. 4.8.

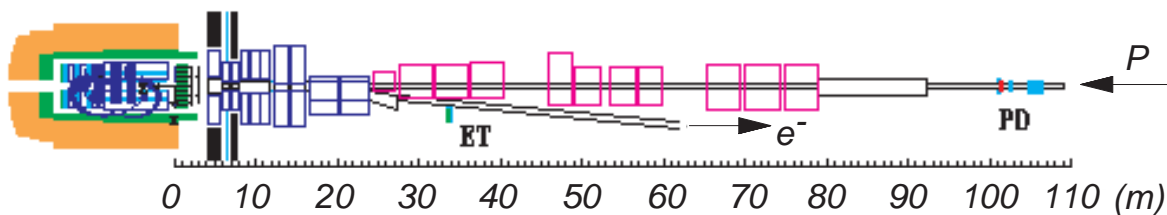


Figure 4.7: The Luminosity System.

Most H1 subdetectors provide binary signals which can be used for triggering and are stored in an array. Based on this information, so-called trigger elements (TE) are constructed, consisting of single as well as multiple bits. Not all subdetectors are able to provide an information within 96 ns. Level 1 operates at the rate of  $2.1 \mu\text{s}$  which corresponds to the time needed by the LAr calorimeter to deliver the trigger information. The full detector information is therefore sent into pipelines where it is stored until all subdetectors provided their TE. The TE serve as an input to the Central Trigger Logic (CTL) where they are combined and form so-called subtriggers (ST). When the CTL finds that the event fulfills any of the subtrigger conditions, then the corresponding event is read from the pipeline and passed onto the next trigger level. The L1 trigger level is deadtime free since any rejected events are simply overwritten in the pipeline.

The next trigger level, L2, operates at the rate of  $20 \mu\text{s}$ . Given the amount of time available, more complicated decisions can be taken. L2 incorporates neural network algorithms as well as topological conditions. Again, if the event passes any of the selection criteria it is passed onto the next level in the chain. According to the plans, this would be L3 with the rate of 2 ms. However, L3 has never been implemented.

The next level is therefore L4 where the full event information is available and a partial event reconstruction is performed. L4 runs asynchronously to the HERA accelerator on a processor farm consisting of 32 CPU's. Each event accepted at lower trigger levels is verified again with a higher precision. At L4, still  $\sim 50\%$  of events are rejected. According to the L4 finders, events are classified and either kept or downscaled, i.e. kept at reduced rate. This applies to obvious backgrounds as well as soft physics with high event rates. The events are written to a Data Summary Tape (DST) in  $\sim 100$  ms.

In order to reduce the rate of particular subtriggers, integer **prescales** are applied on run-by-run basis.

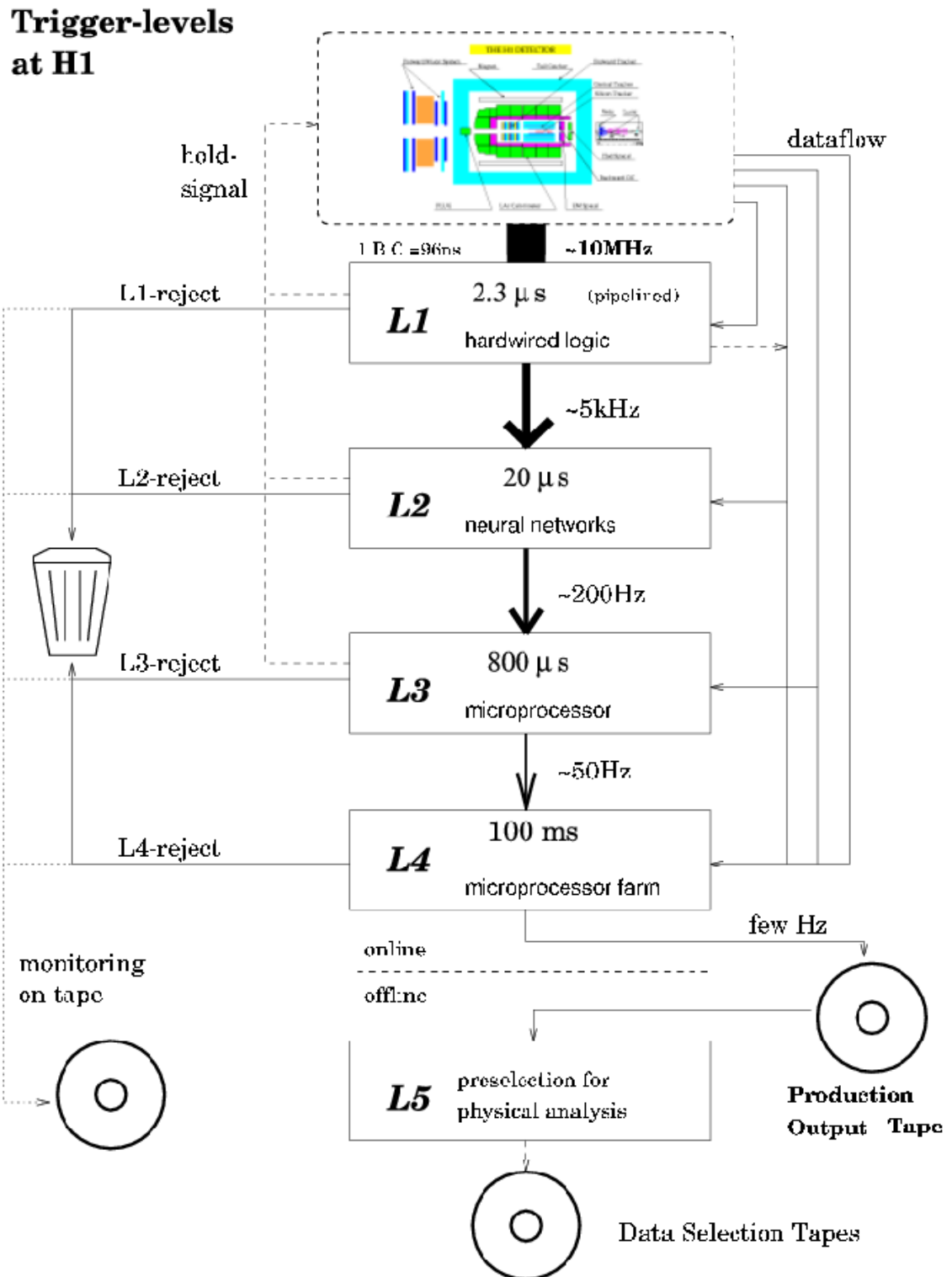


Figure 4.8: The H1 Trigger System.



# Chapter 5

## Measurement Strategy

### 5.1 Extraction of the Longitudinal Proton Structure Functions

#### 5.1.1 Extraction of $F_L$

The inclusive deep inelastic  $ep$  scattering cross section at low  $Q^2$ , written in reduced form as

$$\sigma_r(x, Q^2, y) = \frac{d^2\sigma}{dx dQ^2} \cdot \frac{Q^4 x}{2\pi\alpha^2 Y_+} = F_2(x, Q^2) - \frac{y^2}{Y_+} \cdot F_L(x, Q^2), \quad (5.1)$$

is determined by two structure functions,  $F_2$  and  $F_L$ . The longitudinal structure function  $F_L$  is scaled by a kinematical factor  $\frac{y^2}{Y_+}$ , where  $Y_+ = 1 + (1 - y)^2$ . Therefore, this kinematical factor is proportional to  $y^2$  and the sensitivity to  $F_L$  is largest at high  $y$ . The two structure functions  $F_2$  and  $F_L$  can be separated only if at least two cross section measurements at fixed  $Q^2$  and  $x$  are available for different values of inelasticity  $y$ .

As mentioned in Section 2.1.1, there are two independent kinematic variables describing an inelastic scattering process. This implies that there is no way to vary the inelasticity  $y$  for fixed  $Q^2$  and  $x$ , as it is needed to separate  $F_2$  and  $F_L$ , if only one measurement of  $\sigma_r$  is available. The kinematic variables are bound by

$$Q^2 = xys, \quad (5.2)$$

where  $s$  is the squared centre-of-mass energy of the collision which can be calculated from the beam energies as

$$s = 4E_e E_p. \quad (5.3)$$

Combining two or more  $\sigma_r$  measurements at fixed  $Q^2$  and  $x$  and different  $s$  makes it possible to extract  $F_2$  and  $F_L$  separately.

Fig. 5.1 illustrates how the two structure functions are determined in the so-called **Rosenbluth plot** which shows the reduced cross section as a function of  $\frac{y^2}{Y_+}$ , which is the kinematic factor shielding the contribution of  $F_L$  in Eq. 5.1. All the available  $\sigma_r$  measurements at a given  $Q^2$  and  $x$  are combined in a single Rosenbluth plot. In an ideal case, all such points sit on a single line, where the two structure functions can be

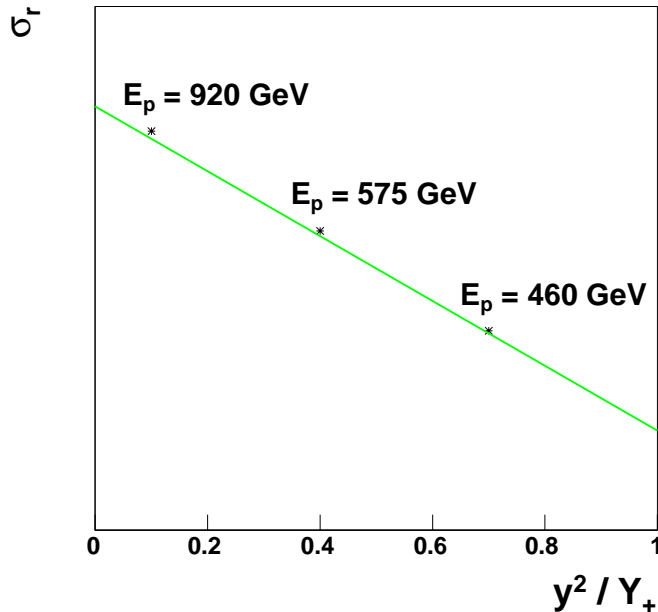


Figure 5.1: A sketch of the extraction of the proton structure functions  $F_2$  and  $F_L$  in the Rosenbluth plot. The reduced cross sections at the same  $Q^2$  and  $x$  from collisions at different centre-of-mass energies (denoted by the different energies of the proton beam) are plotted as a function of the suppression factor  $y^2/Y_+$ . The cross sections are expected to form a line, where the intercept at  $y^2/Y_+ = 0$  gives the structure function  $F_2$  and the intercept at  $y^2/Y_+ = 1$  gives the combination  $F_2 - F_L$ .

read off in the following way

$$\sigma_r\left(\frac{y^2}{Y_+} = 0\right) = F_2, \quad (5.4)$$

$$\sigma_r\left(\frac{y^2}{Y_+} = 1\right) = F_2 - F_L. \quad (5.5)$$

### 5.1.2 Extraction of $F_L^D$

The extraction of  $F_L^D$  is analogous. The diffractive reduced cross section  $\sigma_r^D$ , defined in Eq. 2.40, has the same structure as  $\sigma_r$ . It is expressed as a function of three kinematic variables  $\beta$ ,  $Q^2$  and  $x_P$ . Equally, three different variables can be used. The  $F_L^D$  analysis described here evaluates the diffractive reduced cross sections in  $y$ ,  $Q^2$  and  $x_P$ . The diffractive kinematics is bound by

$$Q^2 = x_P \beta y s = x y s. \quad (5.6)$$

Again, it is necessary to change  $y$  for fixed  $\beta$ ,  $Q^2$  and  $x_P$  in order to separate the structure functions  $F_2^D$  and  $F_L^D$ . The only way to do it is to change the centre-of-mass energy of the collision. Therefore, the procedure described in the Rosenbluth plot in Fig. 5.1 holds for diffraction as well.

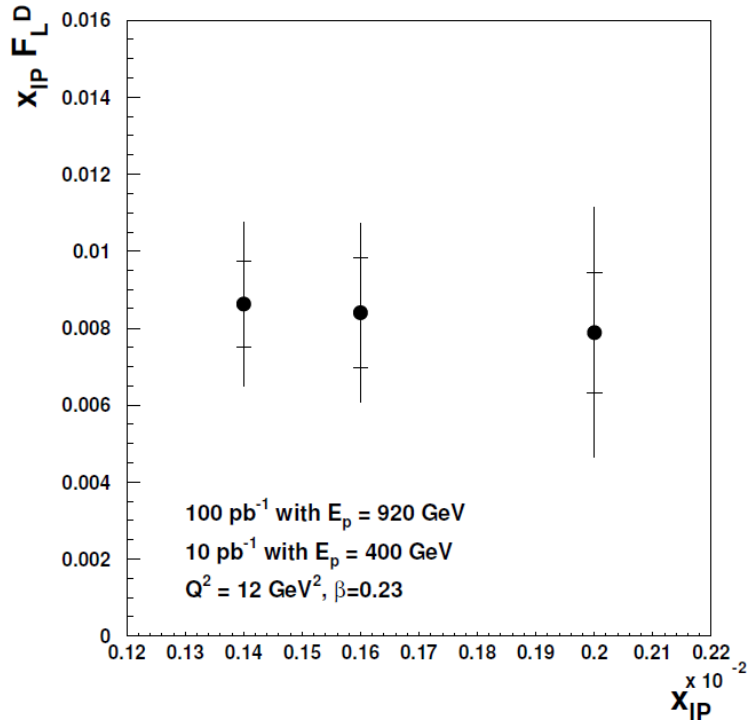


Figure 5.2: Simulation of a measurement of the diffractive longitudinal structure function  $F_L^D(x_P, Q^2, \beta)$  based on data at  $E_p = 920$  GeV ( $100 \text{ pb}^{-1}$ ) and  $E_p = 400$  GeV ( $10 \text{ pb}^{-1}$ ). The inner error bars show the statistical accuracy and the total error bars represent the total uncertainty taking into account correlations of systematic effects and adding both uncertainties in quadrature. [50]

## 5.2 Running at Low Proton Beam Energies

Changing the centre-of-mass energy  $\sqrt{s}$  of collisions requires different setups of the accelerator so that it is able to provide beams at different energies.

For 13 years HERA operated at the highest accessible centre-of-mass energy  $\sqrt{s}$  above 300 GeV in order to explore the region of highest momentum transfers  $Q^2$  and high transverse scales. Towards the end of data taking, H1 decided to express its firm interest in a run with lowered proton beam energies [50, 32]. This run was meant to be devoted to a complementary measurement at low  $x$  and thus provide the important information on theory of a high density gluon dominated systems of partons. In particular, two main physics subjects were foreseen: a measurement of the longitudinal proton structure function  $F_L$  and its diffractive counterpart  $F_L^D$ .

Simulations of these measurements revealed that with  $\sim 10 \text{ pb}^{-1}$  of data, an  $F_L$  measurement with an accuracy of 5-6 standard deviations, and an  $F_L^D$  measurement with an accuracy of 3 standard deviations can be expected (see Fig. 5.2) [50, 32]. This accuracy was considered as good enough to distinguish between different theoretical predictions for  $F_L$ . It was estimated that in order to acquire  $10 \text{ pb}^{-1}$  of data three months are needed, including the set-up time.

At the end of HERA operation in 2007, the proton beam energy was reduced first to  $E_p = 460$  GeV, and then also to  $E_p = 575$  GeV. Fig. 5.3 shows the H1 integrated luminosity for the whole period of its operation, with a closer look at the reduced

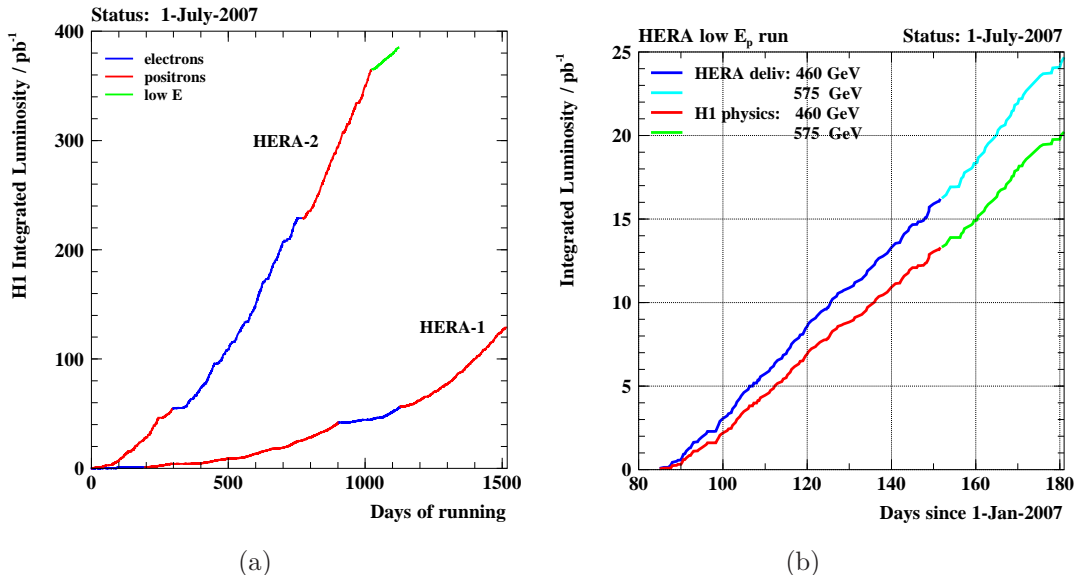


Figure 5.3: Acquired luminosity of data as a function of time. Data-taking periods HERA-I and HERA-II are compared in (a) where the effect of the luminosity upgrade is seen. The runs at reduced proton beam energy are shown as a green line at the end of HERA-II data-taking, and they are viewed in detail in (b).

proton beam energy runs at the end of data-taking. 13 pb<sup>-1</sup> of data at  $E_p = 460$  GeV, and 7 pb<sup>-1</sup> of data at  $E_p = 575$  GeV were taken by the H1 detector.

The proton beam energies also roughly determine the  $y$  range that needs to be analysed in the  $F_L$  and  $F_L^D$  analyses. A certain  $y$  value at  $E_p = 460$  GeV corresponds to a twice smaller  $y$  value at  $E_p = 920$  GeV for fixed  $x$  and  $Q^2$  (see Eq. 5.2). Therefore, the upper limit of the  $y$  range in the analysis of the  $E_p = 920$  GeV data does not need to be larger than a half of the upper  $y$  limit in the  $E_p = 460$  GeV data analysis.

### 5.3 Overview of the $F_L^D$ Analysis

The  $F_L^D$  analysis is a complex measurement that requires understanding of three data sets at different centre-of-mass energies at diffractive as well as inclusive level. It also requires a perfect understanding of the H1 detector which makes it possible to measure at high values of inelasticity  $y$  and separate the signal from background which is dominant there.

In order to do that the analysis involves a complex set of selection criteria when searching for the scattered positron. The cuts are motivated by the ability to properly identify the scattered positron and reduce the background from mis-identified hadrons. The background at high  $y$  cannot be fully excluded by the cuts and has to be quantified and subtracted from the data.

It is a challenging task to measure DIS events at high  $y$ . The Monte Carlo simulations are not fully tuned to reproduce the detector effects correctly and the efficiencies of particular cuts have to be studied in data and Monte Carlo in order to adjust the simulation.

In the first step, the  $F_L^D$  analysis copies the approach of the  $F_L$  analysis and makes sure that the official H1  $F_L$  results can be reproduced. As a second step, the diffractive selection is applied. This means that the data sample for the  $F_L^D$  analysis is a sub-sample of the data used in the  $F_L$  analysis. Using the measurement strategy adopted from the  $F_L$  analysis, the diffractive structure function  $F_2^D$  has to be reproduced from all three data sets as a cross-check. In the final step, the diffractive longitudinal proton structure function  $F_L^D$  is extracted.



# Chapter 6

## Longitudinal Proton Structure Function

### 6.1 Data

The  $F_L$  analysis uses three data sets that differ by the proton beam energy.

- $E_p = 920 \text{ GeV}$ : The last HERA data at the nominal proton beam energies are analysed. These are the so-called 2007  $e^+$  data and will be denoted as the 'high energy data' in this text.
- $E_p = 460 \text{ GeV}$ : The first data set from the runs at reduced proton beam energy. These runs were dedicated to the  $F_L$  and  $F_L^D$  analyses. The full data set is used and it will be denoted as the 'low energy data' here.
- $E_p = 575 \text{ GeV}$ : The last run period at the HERA accelerator. Again, the full data set is used and it will be denoted as the 'medium energy data'.

All three data sets contain  $e^+p$  collisions.

Obviously the full set of low and medium energy data are used in the official H1  $F_L$  analysis as well. However, it uses different data set at  $E_p = 920 \text{ GeV}$ . The  $F_L^D$  analysis chooses to use the latest high energy data. Since the  $F_L$  analysis described here serves as a starting point for the  $F_L^D$  analysis, the same data sets will be used there as well. Only the high energy data set will be extended in the  $F_L^D$  analysis, since the 2007  $e^+$  data alone do not have the desired statistics of diffractive events. Therefore, the 2006  $e^+$  data will be used in addition.

### 6.2 Monte Carlo

Monte Carlo simulations are used to correct data for the detector effects of acceptance, inefficiencies and migrations between measurement intervals. The  $F_L$  analysis uses the DJANGO [69] Monte Carlo to describe data. The DJANGO model fully generates inclusive final states for the neutral current processes, and no other Monte Carlo is needed in the analysis.

Higher order QCD radiation is modelled using initial and final state parton showers in the leading  $\log(Q^2)$  approximation [70]. Hadronisation is simulated using the Lund

string model [71] as implemented in JETSET [72]. The generated events are passed through a full GEANT simulation of the H1 detector [73]. The simulated events are subjected to the same reconstruction and analysis chain as the data. As described in the following sections, the data are used to provide more accurate estimates of important reconstruction efficiencies and the Monte Carlo responses are tuned accordingly.

It is possible to choose from different parametrisations of parton distribution functions. The DJANGO model used for the high energy data is generated with the GRV in LO set<sup>1</sup> [74]. DJANGO for the low and medium energy data uses the CTEQ 6L LO set<sup>2</sup> [75]. All three Monte Carlo samples are reweighted so that the parton distributions correspond to the H1 PDF 2009 set in NLO. This is reached by using the QCD weight at the generator level which is simply defined as

$$w(QCD) = \frac{(\sigma_r)_{outputPDF}}{(\sigma_r)_{inputPDF}} \quad (6.1)$$

where the input and output reduced cross sections  $(\sigma_r)_{inputPDF}$  and  $(\sigma_r)_{outputPDF}$  are calculated from the corresponding parametrisations.

The longitudinal proton structure function in  $(\sigma_r)_{inputPDF}$  is calculated from the structure function  $F_2$  using the quantity  $R$  defined in Eq. 2.30

$$F_L = \frac{R}{1+R} F_2. \quad (6.2)$$

As seen in Fig. 3.5(c),  $R$  can be taken as constant, to a good approximation. The value  $R = 0.25$  is used in the  $F_L$  analysis<sup>3</sup>.

## 6.3 Selection of NC DIS Events

### 6.3.1 Run Selection

The first stage of selecting data for the analysis before studying actual events is the run selection. Only the runs that contain relevant information for the analysis are taken.

Each data taking period has a specific run range that is required in the run selection. The analysis relies on several sub-detectors that are required to be turned on during the data acquisition. For the  $F_L$  analysis, these are the CIP, CJC and BST trackers, the LAr and SPACAL calorimeters, the time of flight and the luminosity system. The minimum luminosity per run should be at least  $1 \text{ nb}^{-1}$  for events with the interaction point at  $-35 < z_{vtx} < 35 \text{ cm}$ . For low and medium energy runs, the sub-triggers ST0, ST7 and ST8, which are used in the actual analysis (see Section 6.3.2), are requested. There were no prescales applied in the low and medium energy runs, i.e. the event rate for a particular sub-trigger was not reduced. For safety reasons, a maximum prescale limit of 1 is introduced. All the run selection criteria are listed in Table 6.1.

---

<sup>1</sup>PDF set number 5004 in PDFLIB

<sup>2</sup>PDF set number 10041 in LHAPDF

<sup>3</sup> The value of  $R = 0.25$  does not correspond to the results of the  $\lambda$  fit presented in Section 3.1.2, where  $R = 0.5$  is quoted. However, the results of the latest QCD fits are consistent with  $R \sim 0.25$  which is illustrated in Fig. 7.39(d). The plot shows the ratio  $R$  in data and the H1 PDF 2009 parametrisation.

Run period	2007 $e^+$ $E_p = 920$ GeV	$E_p = 460$ GeV	$E_p = 575$ GeV
Run range	492559 – 500611	500919 – 507824	507843 – 511079
Sub-triggers	ST0, ST7, ST8		
Minimal luminosity	1 nb <sup>-1</sup>		
Prescale limit	1		
Sub-detectors	CJC1, CJC2, LAR, TOF, LUMI, CIP, BST, SPAC		
Vertex	$-35 < z_{vtx} < 35$ cm		

Table 6.1: Run selection.

Run period	Run Range	Luminosity
2007 $e^+$ $E_p = 920$ GeV	492559 – 500611	46.3 pb <sup>-1</sup>
$E_p = 460$ GeV	500919 – 507824	12.1 pb <sup>-1</sup>
$E_p = 575$ GeV	507843 – 511079	5.9 pb <sup>-1</sup>

Table 6.2: Run ranges and luminosity.

The selected amount of data used in the  $F_L$  measurement presented here is given in Table 6.2. It is 45.7 pb<sup>-1</sup> for the high energy data, 11.0 pb<sup>-1</sup> for the low energy data and 6.0 pb<sup>-1</sup> for the medium energy data.

### 6.3.2 The Trigger Selection

The  $F_L$  measurement is an inclusive analysis, i.e. it does not require any specific hadronic final state and uses all the DIS processes. The inclusive DIS processes in general require a good reconstruction of the scattered positron. This basic characteristics of the processes considered in this analysis define also the preselection of the events using the triggering system. The expected topology of the events is such that the scattered positron is detected in the SPACAL calorimeter. Therefore, only the so-called SPACAL sub-triggers are used in the trigger selection. No other triggers are required because of the inclusive nature of the analysed events.

The high energy data analysis requires sub-triggers S0, S2 and S3. All these sub-triggers demand an energy deposit in SPACAL. S0 and S2 cover region of radial distance  $r_{SPACAL} > 20$  cm, and S3 is sensitive only to higher  $r_{SPACAL}$  above 30 cm. The sub-triggers in high energy data-taking periods are prescaled, i.e. the rate of keeping the triggered events is reduced by a prescale factor. The number of analysed events has to be multiplied by the prescale factor in order to calculate the luminosity of the analysed data sample correctly. The smaller the prescale number the larger the number of analysed events is, and thus the better the statistical precision is. Table 6.3 shows the average prescale numbers for 2006  $e^+$  and 2007  $e^+$  data-taking periods. The 2006

Sub-trigger	Average prescale	
	2006 $e^+$	2007 $e^+$
ST0	21.69	2.13
ST2	1.14	4.15
ST3	1.00	1.00

Table 6.3: Sub-trigger prescale factors in 2006  $e^+$  and 2007  $e^+$  high energy data.

Run period	Trigger selection
2006 $e^+$	$r_{SPACAL} < 29$ cm : ST2
$E_p = 920$ GeV	$r_{SPACAL} > 29$ cm : ST3
2007 $e^+$	$r_{SPACAL} < 29$ cm : ST0
$E_p = 920$ GeV	$r_{SPACAL} > 29$ cm : ST3
$E_p = 460$ GeV	$y < 0.6$ : ST0
	$y > 0.6$ : ST7 or ST8
$E_p = 575$ GeV	$y < 0.56$ : ST0
	$y > 0.56$ : ST7 or ST8

Table 6.4: Trigger selection.

$e^+$  data set is not used in the  $F_L$  analysis, as 2007  $e^+$  data contain enough statistics for the inclusive measurement. It is discussed here because it is analysed in the  $F_L^D$  measurement where the final data sample is a sub-sample of the events selected in the  $F_L$  analysis. Based on the low prescale numbers, the 2006  $e^+$  data requires sub-triggers S2 and S3 at  $r_{SPACAL} < 29$  cm and  $r_{SPACAL} > 29$  cm, respectively. The 2006  $e^+$  data use sub-triggers S0 and S3 at  $r_{SPACAL} < 29$  cm and  $r_{SPACAL} > 29$  cm, respectively.

As already discussed in Section 5.2, the lower the proton beam energy is the higher  $y$  data need to be analysed. The high  $y$  events are more likely to fall within the acceptance of the BST detector. Therefore, BST is also used in the trigger for the low and medium energy data. At  $y > 0.6$  ( $y > 0.56$ ) for low (medium) energy data, a combination of ST7 or ST8 sub-triggers (so-called 'high  $y$ ' sub-triggers) is required. Otherwise, ST0 is used. The low and medium energy data are not prescaled.

The sub-triggers used in the analysis and the corresponding regions are listed in Table 6.4.

### 6.3.3 Vertex Requirement

The Central Jet Chamber (CJC) tracker is used for the reconstruction of the primary vertex. In standard HERA run conditions, the proton and the lepton beams are aimed

to collide in the centre of the H1 detector at  $z = 0$  cm (in the H1 coordinate system). The distribution of the  $z$ -position of the primary vertex follows a Gaussian distribution and standardly, a cut at  $-35 < z < 35$  cm is required.

### 6.3.4 The Scattered Positron Finder

The inclusive measurements crucially depend on a perfect understanding of the scattered lepton. The topology of the inclusive NC DIS processes naturally leads to the requirement of the existence of the primary vertex, a cluster in the calorimeter corresponding to the energy deposition of the scattered positron. A track linking the primary vertex and the cluster can also be considered.

The scattered positron finder is going to be described in detail in the following lines.

#### Cluster Requirement

The scattered positron can be reconstructed in the backward ( $-z$ ) direction in the SPACAL calorimeter or, for larger scattering angles, in the LAr calorimeter. The  $F_L$  analysis described here looks at data at  $2.5 < Q^2 < 100 \text{ GeV}^2$  which corresponds to scattering angles such that the LAr calorimeter can be excluded from the scattered positron selection. The first requirement on the scattered positron candidate is to have its energy deposited in a cluster in the SPACAL calorimeter.

As already mentioned in Sections 5.1 and 2.1.6, the highest sensitivity to the  $F_L$  structure function is at high values of inelasticity  $y$ . In order to extract  $F_L$ , one has to combine measurements at fixed values of  $Q^2$  and  $x$ , and different  $y$  (see Eq. 5.1). Data sets with the proton beam energy of 920, 460 and 575 are analysed. The collisions in these data sets correspond to centre-of-mass energies  $\sqrt{s}$  of 319, 225 and 252 GeV, respectively. The fact that the low proton beam energy ( $E_p = 460 \text{ GeV}$ ) is exactly half of the nominal proton beam energy ( $E_p = 920 \text{ GeV}$ ) leads to the following. The kinematical variables are constrained by  $Q^2 = xys$ , therefore the highest value of  $y$  in the high energy data set ( $\sqrt{s} = 319 \text{ GeV}$ ) suitable for  $F_L$  extraction equals to the half of the highest accessible value of  $y$  in the low energy data set ( $\sqrt{s} = 225 \text{ GeV}$ ). The  $F_L$  analysis described here takes the challenge to describe the low and the medium energy data sets by a Monte Carlo simulation in a wide range of inelasticity spanning up to values of  $y < 0.9$ , which corresponds to  $E'_e \sim 2.8 \text{ GeV}$ . For the high energy data set, data up to  $y < 0.56$ , corresponding to  $E'_e \sim 12 \text{ GeV}$ , are analysed. The high  $y$  edges in the high and medium energy data sets exceed the actual range needed for the  $F_L$  extraction. Nevertheless, the fact that data are described by the simulation even beyond the region of interest serves as an important check of understanding data.

The inelasticity  $y$  can be approximated by  $y \sim 1 - \frac{E'_e}{E_e}$  (which follows from Eq. 6.27; the ways of reconstructing kinematics are discussed in detail in Section 6.3.5). The upper cuts on the inelasticity  $y$  are also accompanied by similar cuts on the cluster energy of the scattered lepton candidate.  $E'_e > 3.4 \text{ GeV}$  is used for the low and medium energy data sets,  $E'_e > 12 \text{ GeV}$  is used for the high energy data set.

The position of the cluster is reconstructed in H1 coordinates. In order to properly reconstruct the scattering angle  $\theta_e$ , the following inputs are needed: the position of the cluster of the scattered positron, the position of the primary vertex and the trajectory

of the beam. The  $\theta$  and  $\varphi$  angles are first calculated as

$$\tan \theta = \frac{\sqrt{(x_{clus}^{H1} - x_{vtx})^2 + (y_{clus}^{H1} - y_{vtx})^2}}{z_{clus}^{H1} - z_{vtx}} \quad (6.3)$$

$$\tan \varphi = \frac{y_{clus}^{H1} - y_{vtx}}{x_{clus}^{H1} - x_{vtx}} \quad (6.4)$$

where  $x_{clus}^{H1}$ ,  $y_{clus}^{H1}$ ,  $z_{clus}^{H1}$  define the position of the cluster and  $x_{vtx}$ ,  $y_{vtx}$ ,  $z_{vtx}$  define the position of the vertex in the H1 coordinates. The angles  $\theta$  and  $\varphi$  are then corrected for the actual direction of the beam in the following way. First, a direction vector of the beam is defined

$$s_x = \frac{x'}{\sqrt{x'^2 + y'^2 + 1}}, \quad s_y = \frac{y'}{\sqrt{x'^2 + y'^2 + 1}}, \quad s_z = \frac{1}{\sqrt{x'^2 + y'^2 + 1}} \quad (6.5)$$

where  $x'$  and  $y'$  denote the beam direction in  $x$  and  $y$ , respectively<sup>4</sup>. The physical scattering angles  $\theta_e$  and  $\varphi_e$  are then calculated as

$$\cos \theta_e = \sin \theta \cos \varphi s_x + \sin \theta \sin \varphi s_y + \cos \theta s_z \quad (6.6)$$

$$\tan \varphi_e = \frac{y_{vtx} - y_0 - y' z_{clus}^{H1}}{x_{vtx} - x_0 - x' z_{clus}^{H1}} \quad (6.7)$$

where  $x_0$  and  $y_0$  stand for the beam position at  $z = 0$  in the H1 coordinate system.

Only clusters in a certain region of the SPACAL calorimeter are considered. Based on the efficiency of data description, clusters have to fall in the radial range of  $18 < r_{SPACAL} < 74$  cm, where the radius  $r_{SPACAL}$  is calculated at  $z = -160$  cm and corrected for the beam tilt

$$r_{SPACAL} = \tan \theta_e (-160 - z_{vtx}). \quad (6.8)$$

The lower cut is driven by the definition of sub-triggers used in the analysis. The upper cut is close to the edge of the SPACAL calorimeter and it makes sure that the full cluster is contained within the SPACAL acceptance. There is a region in the SPACAL calorimeter where L2 triggers are inefficient due to a cabling problems. Therefore, a box defined by  $-16 < x_{clus} < 9$  cm,  $-6 < y_{clus} < 16$  cm is excluded.  $x_{clus}$  and  $y_{clus}$  are the beam tilt corrected cluster positions

$$x_{clus} = r_{SPACAL} \cos \varphi_e, \quad y_{clus} = r_{SPACAL} \sin \varphi_e. \quad (6.9)$$

Fig. 6.1(a) shows the position of SPACAL clusters after the cut on  $r_{SPACAL}$  and the box cut. Table 6.5 gives a list of cuts involved in the SPACAL acceptance cut.

The positron finder requires an electromagnetic cluster to be assigned to the scattered positron candidate. Variable  $r_{log}$ , energy weighted cluster radius, is used to distinguish between electromagnetic and hadronic clusters. It is defined in the following way involving the information from the cells contained in the cluster

$$r_{log} = \frac{\sum_{cells} d_r \max(0, 4.8 + \log(\frac{E_{cell}^i}{E_{cluster}}))}{\sum_{cells} \max(0, 4.8 + \log(\frac{E_{cell}^i}{E_{cluster}}))} \quad (6.10)$$

<sup>4</sup> The beam parameters  $x_0$ ,  $y_0$ ,  $x'$ ,  $y'$  are determined on event-by-event basis from the CST information.

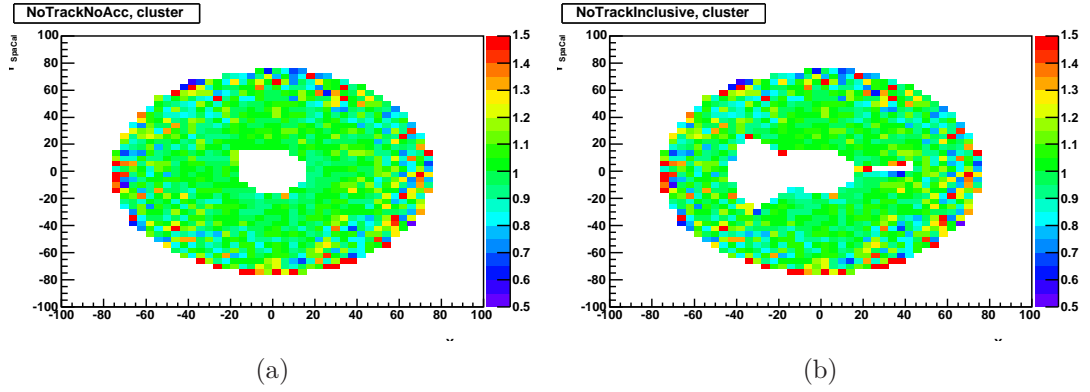


Figure 6.1: SPACAL cluster position. The plots show the ratio of low energy data and Monte Carlo after the analysis selection (see Table 6.10) without a track–cluster link requirement. Only the SPACAL acceptance cut is applied (a), both the SPACAL acceptance and the BST acceptance cuts are applied (b).

Selection Description	Values
Radius cut	$18 < r_{SPACAL} < 74$ cm
Box cut	$-16 < x_{clus} < 9$ cm, $-6 < y_{clus} < 16$ cm

Table 6.5: SPACAL acceptance cuts.

where  $d_r$  is the radial distance between the cell position and the cluster barycentre

$$d_r = \sqrt{(x_{cell}^i - x_{barycentre})^2 + (y_{cell}^i - y_{barycentre})^2} \quad (6.11)$$

and the barycentre is defined as

$$x_{barycentre} = \frac{\sum_{cells} x_{cell}^i \max(0, 4.8 + \log(\frac{E_{cell}^i}{E_{cluster}}))}{\sum_{cells} \max(0, 4.8 + \log(\frac{E_{cell}^i}{E_{cluster}}))}, \quad (6.12)$$

analogously for  $y_{barycentre}$ . A logarithmic energy cutoff of 4.8 is used in the calculation. Electromagnetic showers are in general contained within a cone of smaller radius than hadronic showers. A cut at  $r_{log} < 5$  cm is used in the analysis in order to suppress hadronic particle candidates.

Electromagnetic particles are also expected to deposit their energy in the electromagnetic part of the SPACAL calorimeter. A cut on the fraction of the cluster energy coming from the cells in the hadronic SPACAL  $\frac{E_{had}}{E_{tot}} < 0.15$  is introduced.

### Link between the Track and the Cluster

The vertex and cluster requirements, as described in the previous paragraphs, are considered as the basic selection for the inclusive DIS processes. Such selection is sufficient for analyses that do not probe a region with high levels of photoproduction

background (described and discussed in Section 6.3.8). This background is dominant at low energies of the scattered positron  $E'_e$  and is negligible above an energy of  $\sim 15$  GeV. The low and medium data analyses attempt to understand data down to energies of 3.4 GeV, whereas the high energy data analysis cuts at  $y < 0.56$  which roughly corresponds to an energy of 12 GeV. Additional requirement of a track linking the primary vertex and the cluster helps to reduce the photoproduction background. Therefore, it is used in the selection for the low and medium energy data. In the high energy data, the track-cluster link is not required since the lowest scattered positron energies are not analysed. The following lines describe the procedure of finding a linking track.

Given the geometry of the H1 detector, a track linking the primary vertex and the cluster of the scattered positron can be found in the Central Jet Chamber (CJC) tracker or the Backward Silicon Tracker (BST). The trackers as well as the LAr and SPACAL calorimeters are contained in the 1.15 T homogeneous magnetic field of the H1 detector. Therefore, the charged particles follow helix trajectories. The BCREC routine is used to reconstruct the combined CJC or BST tracks. This routine returns helix parameters  $\kappa$  (the curvature of the helix),  $\phi$  (the azimuthal angle of the helix axis with respect to the pivotal point),  $\theta$  (the pitch angle),  $d_{ca}$  (distance of closest approach of the helix and the pivotal point in the transversal plane), and  $z_0$  (distance of the helix from the pivotal point in  $z$ -direction). The pivotal point is chosen in the origin of the H1 coordinate system. The BCREC routine also returns the number of linked hits in CJC and BST.

The  $\varphi$  structure of the BST detector is such that there is a slice where electronics is located, and therefore particles cannot be detected there. In order to take into account this geometrical acceptance of the BST detector, the position of the track in the BST has to be known. The helix can be reconstructed either from the output of the BCREC routine, or from the position of the cluster and the primary vertex. The BST acceptance cut in this analysis uses the position of the track in the middle of the BST detector at  $z = -50$  cm where the track is reconstructed from the cluster and the vertex position.

In general, the helix can be parametrized in the following way

$$x = x_{pivot} + d_{ca} \cos \phi_0 + \rho(\cos \phi_0 - \cos(\phi_0 + \phi)) \quad (6.13)$$

$$y = y_{pivot} + d_{ca} \sin \phi_0 + \rho(\sin \phi_0 - \sin(\phi_0 + \phi)) \quad (6.14)$$

$$z = z_{pivot} + z_0 - \rho \tan \lambda \phi \quad (6.15)$$

where  $x_{pivot}$ ,  $y_{pivot}$ ,  $z_{pivot}$  specify the position of the pivotal point,  $d_{ca}$  is the distance of the helix from the pivotal point in the transversal plane,  $\phi_0$  is the azimuthal angle that specifies the pivotal point with respect to the helix center,  $\rho$  being the signed radius of the helix,  $z_0$  is the distance of the helix from the pivotal point in the  $z$ -direction, and  $\tan \lambda$  is the dip angle. The deflection angle  $\phi$  is measured from the pivotal point and specifies the position of the charged particle on the helix track. The meanings of these parameters are depicted in Fig. 6.2. Note that a negatively charged particle travels in the increasing  $\phi$  direction, while a positively charged particle travels in the decreasing  $\phi$  direction.

Starting with the vertex position  $x_{vtx}$ ,  $y_{vtx}$ ,  $z_{vtx}$  and the cluster position in the H1 coordinates  $x_{clus}^{H1}$ ,  $y_{clus}^{H1}$ ,  $z_{clus}^{H1}$  one can approximate the transversal momentum of the

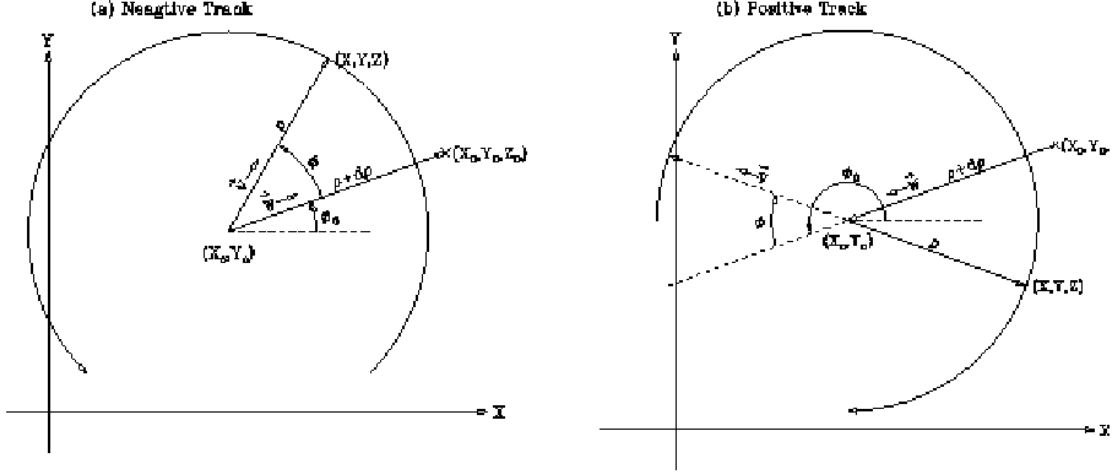


Figure 6.2: A graphical explanation of the helix parameters for (a) negatively charged and (b) positively charged tracks. Notice that the meaning of  $\phi_0$  changes discretely by  $\pi$ , depending on the charge. [76]

scattered lepton as

$$p_T = E'_e \sin \theta \quad (6.16)$$

where

$$\tan \theta = \frac{\sqrt{(x_{clus}^{H1} - x_{vtx})^2 + (y_{clus}^{H1} - y_{vtx})^2}}{z_{clus}^{H1} - z_{vtx}}. \quad (6.17)$$

The signed radius of the helix can be calculated as

$$\rho = \frac{p_T}{cBQ} \quad (6.18)$$

where  $c$  is the speed of light,  $B$  is the size of the magnetic field and  $Q$  is the charge of the scattered lepton. Since the  $e^+p$  scattering data are analysed the charge of the scattered lepton is always taken as positive.

In order to evaluate the helix parameters  $\phi_0$  and  $\tan \lambda$  the following steps are taken. First, the deflection parameter  $\phi$  is calculated for the cluster position

$$\sin \frac{\phi_{clus}}{2} = \frac{\frac{1}{2} \sqrt{(x_{clus}^{H1} - x_{vtx})^2 + (y_{clus}^{H1} - y_{vtx})^2}}{|\rho|}. \quad (6.19)$$

The dip angle can then be evaluated as

$$\tan \lambda = -\frac{z_{clus}^{H1} - z_{vtx}}{\rho \phi_{clus}}. \quad (6.20)$$

The calculation of the helix position in the centre of the BST detector is straightforward now. The deflection parameter  $\phi$  at  $z = -50$  cm is calculated from Eq. 6.15 where we take the vertex position as the pivotal point

$$\phi_{BST} = \frac{-50 - z_{vtx}}{-\rho \tan \lambda}. \quad (6.21)$$

Selection Description	Values
Geometry	$r_{SPACAL} < 45 \text{ cm} : -134^\circ < \varphi_{BST} < 134^\circ$
Problematic $\varphi_{BST}$ slice	$r_{SPACAL} < 45 \text{ cm} : -2^\circ < \varphi_{BST} < 15^\circ$
Box cuts	$-4 < x_{BST} < 4 \text{ cm}, -7 < y_{BST} < -4 \text{ cm}$ $2 < x_{BST} < 7 \text{ cm}, 0 < y_{BST} < 4 \text{ cm}$
Radius cut	$r_{BST} < 6 \text{ cm}$

Table 6.6: BST acceptance cuts.

$\varphi_{BST}$  is then directly used in Eq. 6.14 and 6.15 in order to obtain the  $x_{BST}$  and  $y_{BST}$  positions. Finally, the  $x_{BST}$  and  $y_{BST}$  positions are corrected for the beam tilt

$$x_{BST} \rightarrow x_{BST} - x_0 - x'(-50), \quad y_{BST} \rightarrow y_{BST} - y_0 - y'(-50). \quad (6.22)$$

The radial length of the track in the middle of the BST is calculated using these beam tilt corrected positions as

$$r_{BST} = \sqrt{x_{BST}^2 + (y_{BST} + 0.7)^2} \quad (6.23)$$

$$\tan \varphi_{BST} = \frac{y_{BST} + 0.7}{x_{BST}} \quad (6.24)$$

where 0.7 is an alignment correction.

### The BST Acceptance Cut

The BST acceptance cut consists of the following components. The geometry of the BST detector requires to cut away the  $\varphi_{BST} < -134^\circ$  and  $\varphi_{BST} > 134^\circ$  ranges for  $r_{SPACAL} < 45 \text{ cm}$ . There is also a problematic region at  $\varphi_{BST} \sim 0^\circ$ . Therefore, the range of  $-2^\circ < \varphi_{BST} < 15^\circ$  for  $r_{SPACAL} < 45 \text{ cm}$  is also excluded. Two boxes are removed as well:  $-4 < x_{BST} < 4 \text{ cm}, -7 < y_{BST} < -4 \text{ cm}$  and  $2 < x_{BST} < 7 \text{ cm}, 0 < y_{BST} < 4 \text{ cm}$ . A cut on the radial length of the track  $r_{BST} < 6 \text{ cm}$  takes care of the inner edge acceptance of the BST detector. Table 6.6 gives a list of cuts involved in the BST acceptance cut. Fig. 6.1(b) shows the SPACAL cluster position after the BST acceptance cut.

### The Combined CJC/BST Track Validation

Using the parameters from the BCREC routine, the helix trajectory can be propagated to the  $z$ -position of the cluster. The distance between the propagated helix and the cluster in the transverse plane calculated at  $z = z_{clus}$  is required to be less than 3 cm.

The quality of the reconstructed track is ensured by a cut on the total number of linked hits in the trackers  $N_{CJC} + N_{BST} > 2$ . Depending on the radial length of the track in the middle of the BST detector (at  $z = -50 \text{ cm}$ )  $r_{BST}$  and the radial length of

Selection Description	Values
Track-cluster distance	$d_{track-cluster} < 3 \text{ cm}$
Linked hits in total	$N_{CJC} + N_{BST} > 2$
CJC range	$r_{CJC} > 40 \text{ cm} : N_{CJC} \geq 10$
CJC/BST transition region	$30 < r_{CJC} < 40 \text{ cm} : N_{CJC} > r_{CJC} - 30$
BST range	$20 < r_{CJC} < 30 \text{ cm} : N_{CJC} \leq 15$
	$r_{BST} < 13 \text{ cm} : N_{BST} \geq 2$
Low radius	$r_{CJC} < 20 \text{ cm} : N_{CJC} \leq 4$

Table 6.7: List of cuts in the combined **CJC/BST track validation**.

the track in the middle of the CJC (at  $z = -112.5 \text{ cm}$ )  $r_{CJC}$ , the quality of the track can be studied in more detail.  $r_{CJC}$  is defined in a similar way as  $r_{BST}$

$$r_{CJC} = (-112.5 - z_{vtx}) \tan \theta \quad (6.25)$$

where

$$\tan \theta = \frac{r_{BST}}{-50 - z_{vtx}}. \quad (6.26)$$

Both radial lengths help to decide whether the track falls into the acceptance region of the corresponding detector. The cut on the number of linked hits is then extended by the following set of conditions. These ranges are considered depending on  $r_{CJC}$ :

- CJC range : At least 10 hits in the CJC are expected for  $r_{CJC} > 40 \text{ cm}$ .
- CJC/BST transition region : A linear dependence of the minimum number of hits required in the CJC on the radial length is considered for  $30 < r_{CJC} < 40 \text{ cm}$ . The following cut is applied:  $N_{CJC} > r_{CJC} - 30$ .
- BST range : Not more than 15 hits are expected in the CJC for  $20 < r_{CJC} < 30 \text{ cm}$ .
- Low radius : Almost no hits in the CJC are expected at all. A cut on  $N_{CJC} \leq 4$  is applied for  $r_{CJC} < 20 \text{ cm}$ .

There is only one requirement for a specific range in  $r_{BST}$ .

- At least 2 BST hits are expected in the middle of the BST acceptance at  $r_{BST} < 13 \text{ cm}$ .

The full set of the cuts involved in the combined **CJC/BST track validation** is listed in Table 6.7.

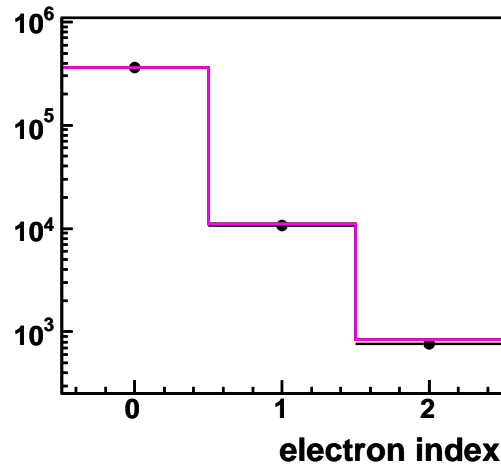


Figure 6.3: Index of the electromagnetic particle candidate that passes the scattered positron selection criteria. The candidates are sorted in energy in decreasing order. The relative amount of the scattered positrons that do not correspond to the highest energy electromagnetic particle is at a percent level.

### Scattered Positron Hunting

Table 6.8 gives the list of all cuts applied in the scattered positron finder. This set of cuts is applied to the three highest energy electromagnetic particle candidates in the SPACAL calorimeter. Fig 6.3 shows the index of the electromagnetic particle candidates that pass the positron finder selection criteria in the final analysis sample for low energy data. The scattered positron candidates found at the second and third place among the electromagnetic particle candidates correspond mostly to low energy scattered positrons where it is more likely to find a hadronic final state particle that mimics an electromagnetic particle and has a larger energy than the real scattered positron. The reason to probe the first three scattered positron candidates is a possible increase of statistics. As the figure shows the relative amount of the scattered positrons that do not correspond to the highest energy electromagnetic particle is at a percent level.

### 6.3.5 Reconstruction of the Inclusive Final State

Ideally, a  $4\pi$  detector gathers the full information about the collision. In reality, it is impossible to detect everything. There are energy losses from the final state particles leaving the detector unseen through the beam pipe or, in general, going outside of the detector acceptance. The accuracy of the gathered information depends on the detector resolution, and on the understanding of the detector and robustness of the reconstruction techniques.

The H1 detector is a  $4\pi$  detector and it attempts to measure the whole final state of the  $ep$  collisions. In NC DIS processes, both the scattered lepton and the hadronic final state are detected (provided it strikes the acceptance region of the detector). Therefore,

Selection Description	Values	
	$E_p = 460, 575 \text{ GeV}$	$E_p = 920 \text{ GeV}$
Cluster type	SPACAL cluster	SPACAL cluster
Energy	$E'_e > 3.4 \text{ GeV}$	$E'_e > 12 \text{ GeV}$
Electromagnetic/hadronic cluster separation	$r_{log} < 5 \text{ cm}$ $\frac{E_{had}}{E_{tot}} < 0.15$	$r_{log} < 5 \text{ cm}$ $\frac{E_{had}}{E_{tot}} < 0.15$
Acceptance	SPACAL acceptance cut BST acceptance cut	SPACAL acceptance cut
Track requirement	CJC/BST track validation cuts	

Table 6.8: List of cuts in the scattered positron finder.

the kinematics of the process is over-constrained and can be reconstructed either from the measured scattered lepton or from the hadronic final state measurement. The following paragraphs describe possible ways of reconstructing kinematics together with their pros and cons.

### The Electron Method

Only the scattered lepton is used to determine the kinematics of the  $ep$  interaction in the Electron method. The scattered lepton energy  $E'_e$  is measured together with the scattering angle  $\theta_e$ . The kinematics is then given by

$$y_e = 1 - \frac{E'_e}{E_e} \sin^2 \frac{\theta}{2}, \quad Q_e^2 = 4E_e E'_e \cos^2 \frac{\theta}{2} \quad (6.27)$$

where  $E_e$  is the energy of the electron beam. The Electron method has especially a good resolution at high  $y$ .

### The Hadron Method

Contrary to the Electron method, the Hadron method uses the information from the hadronic final state. The kinematics is reconstructed from the transverse size of the total hadronic final state momentum  $p_T$  and the difference between the energy and the  $z$ -component of the momentum  $\Sigma = (E - p_z)_h$

$$y_h = \frac{\Sigma}{2E_e}, \quad Q_h^2 = \frac{p_T^2}{1 - y_h} \quad (6.28)$$

The Hadron method is mainly used for processes where no information about the scattered lepton is available (e.g. photoproduction processes). In general, the scattered lepton is reconstructed with a better precision ( $< 1\%$ ) than the hadronic final state. With a good hadronic calibration,  $\sim 2\%$  uncertainty on the energy scale is considered. However, the main reason for a poor resolution of the Hadron method are energy losses in the forward region.

### The Double-Angle Method

The Double-Angle method combines the angular information of both the scattered lepton and the hadronic final state. The polar angle of the hadronic final state is defined by

$$\cos \gamma_h = \frac{p_T^2 - \Sigma^2}{p_T^2 + \Sigma^2} \quad (6.29)$$

The kinematics is then reconstructed as

$$y_{da} = \frac{\sin \theta_e (1 - \cos \gamma_h)}{\sin \gamma_h + \sin \theta_e - \sin(\theta_e + \gamma_h)}, \quad Q_{da}^2 = \frac{4E_e^2 \sin \gamma_h (1 + \cos \theta_e)}{\sin \gamma_h + \sin \theta_e - \sin(\theta_e + \gamma_h)} \quad (6.30)$$

The Double-Angle method has a good resolution at low  $y$ .

### The Average Method

The Average method combines the excellent precision of the Electron method at high  $y$  with the excellent precision of the Double-Angle method at low  $y$ . This method is especially suitable for inclusive diffraction. In diffraction, the hadronic final state is fully contained in the main calorimeter. As there are no energy losses in the forward region, the resolution in the hadronic angle, and therefore the Double-Angle method, is excellent. The Average method is given by

$$y_{av} = y_e^2 + y_{da}(1 - y_{da}), \quad Q_{av}^2 = \frac{4E_e^2(1 - y_{av})}{\tan^2 \frac{\theta}{2}} \quad (6.31)$$

### 6.3.6 Background Rejection

Two background processes are considered for the inclusive NC DIS analysis: photoproduction processes and QED-Compton scattering events.

#### Photoproduction Background

The photoproduction  $\gamma^*p$  processes are processes where the lepton and the proton from the beam exchange a low virtuality photon. These processes are characterised by  $Q^2 \rightarrow 0$  and low scattering angles such as the scattered lepton exits the main detector undetected through the beam pipe.

If one of the hadronic final state particles (pion) deposits energy in the SPACAL calorimeter it can be mis-identified as a lepton, and the event topology can mimic a signal NC DIS process. Therefore it is important to introduce cuts that help to separate electromagnetic and hadronic clusters. Such cuts (on  $r_{log}$ ,  $\frac{E_{had}}{E_{tot}}$ ) were already introduced in Section 6.3.4.

Another important selection criterium that reduces the photoproduction background is based on the conservation of energy and longitudinal momentum. In DIS event, kinematics define that  $E - p_z = 2E_e = 55$  GeV where all final states (including the scattered lepton) contribute to  $E - p_z$ . The event selection requires  $E - p_z > 35$  GeV for all events in the measurement.

There are detectors along the beam pipe in the electron beam direction that can detect the scattered lepton from the photoproduction events (electron and photon taggers). Photoproduction studies using these detectors show that the hadronic final state particles reconstructed in SPACAL can mimic the scattered lepton from DIS processes up to energies of  $\sim 18$  GeV. However, the photoproduction background is mainly an issue at lower energies of the scattered lepton candidate reconstructed in SPACAL. The  $F_L$  and  $F_L^D$  structure functions are extracted from data at high values of inelasticity  $y$  which correspond to low scattered lepton energies. Even after the rejection of background using the selection criteria described here the photoproduction background is still comparable to the signal at high  $y$ . Introducing harder cuts against photoproduction is not desirable since it kills the signal events as well. A large amount of background in the final event selection makes the  $F_L$  and  $F_L^D$  measurements so challenging. The understanding and treatment of the remaining photoproduction background is discussed in Section 6.3.8.

Selection Description	Values
Number of electromagnetic particles in the SPACAL calorimeter	$N_{elmag.}^{SPACAL} \geq 2$
Energy	$E_1 > 4 \text{ GeV}$ $E_2 > 4 \text{ GeV}$ $E_1 + E_2 > 18 \text{ GeV}$
Acoplanarity	$-\cos(\varphi_1 - \varphi_2) > 0.95$

Table 6.9: Selection criteria for the QED-Compton events.

### QED-Compton Events

The QED-Compton scattering events ( $ep \rightarrow ep\gamma$ ) are not part of the deep inelastic scattering signal and have to be excluded from the analysed data sample. The QED-Compton events are identified by the set of cuts in Table 6.9. At least two electromagnetic particles are required in order to have candidates in the opposite  $\varphi$  direction that match the final state lepton and photon.

### 6.3.7 The Final Inclusive NC DIS Selection

This section gives an overview of all the selection criteria used in the analysis, the so-called **analysis selection**.

The low and medium energy data are analysed in the kinematical range  $2.5 < Q^2 < 100 \text{ GeV}^2$  and  $0.1 < y < 0.9$ . The scattered positrons with energies down to  $E'_e = 3.4 \text{ GeV}$  are selected. A track linking the primary vertex with the positron energy cluster is also required.

The high energy data are selected in more restricted kinematical domain of  $7 < Q^2 < 100 \text{ GeV}^2$  and  $0.1 < y < 0.56$ . The lower  $Q^2$  cut is increased on grounds of the trigger efficiency. A track cluster link is not required in this data set.

The analysis selection is summarised in Table 6.10.

### 6.3.8 Photoproduction Background Subtraction

As already mentioned in Section 6.3.6, there is a large amount of photoproduction background in the final data analysis sample. The cuts responsible for background rejection do not succeed in removing all the background events, and introducing harder cuts would lead to further rejection of signal events as well. The amount of remaining photoproduction background at high values of inelasticity  $y$  – which is the most important region for the  $F_L$  and  $F_L^D$  extraction – is comparable to signal. This section describes a way how to subtract the residual photoproduction background.

The photoproduction events that appear as a NC DIS signal in the central detector are of two kinds. Either a positive pion is mis-identified as the scattered positron, or a negative pion mimics the scattered positron. Negative pions can be excluded by the

Selection Description	Values
	$E_p = 460, 575 \text{ GeV}$ $E_p = 920 \text{ GeV}$
Vertex	CJC vertex $-35 < z_{vtx} < 35 \text{ cm}$
Cluster type	SPACAL cluster
Energy	$E'_e > 3.4 \text{ GeV}$ $E'_e > 12 \text{ GeV}$
Inelasticity	$0.1 < y_e < 0.9$ $0.1 < y_e < 0.56$
Electromagnetic/hadronic cluster separation	$r_{log} < 5 \text{ cm}$ $\frac{E_{had}}{E_{tot}} < 0.15$
Acceptance	SPACAL acceptance cut BST acceptance cut
Track requirement	CJC/BST track validation cuts
$Q^2$ region	$Q_e^2 > 2.5 \text{ GeV}^2$ $Q_e^2 > 7 \text{ GeV}^2$
$E - p_z$ cut	$E - p_z > 35 \text{ GeV}$
QED-C events	anti-Compton selection

Table 6.10: Overview of the **analysis selection** criteria.

Selection Description	Values
$E - p_z$ cut	$E - p_z + 2E_{tagger}^{electron} + 2E_{tagger}^{photon} < 80 \text{ GeV}$
Energy in the taggers	$E_{tagger}^{electron} > 2 \text{ GeV}$ $E_{tagger}^{photon} < 2 \text{ GeV}$
Trigger element	L1TE 115 (signal in the tagger)
	$E_{tagger}^{electron} < 6 \text{ GeV} : x_{tagger}^{electron} > -2.8 \text{ cm}$

Table 6.11: Selection criteria for the tagged photoproduction events.

requirement of a positively charged track linking the vertex and the cluster, assuming reliable charge reconstruction.

### Tagged Events Subtraction

The scattered positron from photoproduction events can be detected in the tagger detectors. One way to subtract the residual photoproduction background from the final data analysis sample is to subtract the tagged events multiplied by the geometrical acceptance of the tagger  $acc_{tagger} = 0.2$ . The number of signal events is then equal to

$$N_{signal} = N_{all} - \frac{2}{acc_{tagger}} N_{tagged}^- \quad (6.32)$$

where  $N_{all}$  stands for the number of all events in the final selected data analysis sample, and  $N_{tagged}^-$  is the number of events that pass the analysis selection criteria as well as the tagger selection and have a negatively charged track associated to the scattered positron candidate. The amount of  $\pi^+$  and  $\pi^-$  mis-identified as scattered leptons is similar, hence the factor of 2.

The **tagger selection** involves two tagger detectors: the 6 m electron tagger station and the photon tagger. There is a cut on the total  $E - p_z$  from the central detector, the electron tagger and the photon tagger

$$(E - p_z)_{total} = E - p_z + 2E_{tagger}^{electron} + 2E_{tagger}^{photon}. \quad (6.33)$$

This quantity is required to be less than 80 GeV which should reject the events with the scattered positron detected in the central detector and a beam halo measured in the taggers. In order to reject Bethe-Heitler processes, cuts on  $E_{tagger}^{electron} > 2 \text{ GeV}$  and  $E_{tagger}^{photon} < 2 \text{ GeV}$  are considered. The tagger selection is listed in Table 6.11.

The charge requirement in  $N_{tagged}^-$  does not depend on the charge reconstruction efficiency since the number of positive mis-reconstructed charges is the same as the number of negative mis-reconstructed charges. Therefore, the number of subtracted events in Eq. 6.32 is correct. The reason for the charge requirement is the presence of the background from Bethe-Heitler processes. Especially at  $E_p = 920 \text{ GeV}$ , there is a significant fraction of events with overlap of DIS and Bethe-Heitler processes due to higher instantaneous luminosity. Requiring a negative charge of the scattered positron candidate naturally removes this background.

The charge is reconstructed from the track curvature. Since there is no track–cluster link requirement in the high energy data analysis, the charge information is not used for the tagged event subtraction, and the background is removed as

$$N_{signal} = N_{all} - \frac{1}{acc_{tagger}} N_{tagged} \quad (6.34)$$

where  $N_{tagged}$  denotes all events that pass the tagger selection. The number of tagged events is corrected just by the tagger acceptance  $acc_{tagger}$  and the factor of 2 as in Eq. 6.32 is missing.

### Charge Asymmetry

As already said, the amount of  $\pi^+$  and  $\pi^-$  mis-identified as scattered leptons (referred to as  $N^+$  and  $N^-$ , respectively) is similar and can be accurately studied with the tagger detectors. The **background charge asymmetry**

$$asym = \frac{N^+}{N^-} \quad (6.35)$$

is determined in an independent analysis. Since the tagger detectors have limited acceptance the analysis looks at the whole HERA-II data set. The analysis gives the charge asymmetry both for data and Monte Carlo

$$asym_{data} = 0.98, \quad asym_{MC} = 0.94. \quad (6.36)$$

### Wrong Charge Background Subtraction

In the low and medium energy data analyses, there is a requirement of a track linking the primary vertex and the cluster of the scattered lepton candidate in the scattered positron finder. Therefore, a charge measurement from the curvature of the track is also available. The larger the curvature the higher the charge measurement precision is, and vice versa. Fig. 6.4 shows the  $Q \frac{E'_e}{p}$  distribution in the final selection of events from the low energy data. Here, the energy  $E'_e$  is measured in the calorimeter and the track momentum  $p$  comes from the track and the charge  $Q$  from its curvature. The black points are data, the magenta line is the Monte Carlo simulation of the  $e^+p$  NC DIS events. Therefore, the Monte Carlo events seen with a negative charge correspond only to the events where the charge is mis-reconstructed. There are significantly more negative events in data. Assuming the charge reconstruction is well simulated by the Monte Carlo (the charge reconstruction efficiency is discussed in detail in Section 6.4.4), the difference in negative events seen between data and Monte Carlo has to correspond to the photoproduction background ( $e^+p$  collisions are analysed in data). Since there is also a certain amount of signal events in the data with negative reconstructed charge (charge mis-reconstruction), these events are referred to as the wrong charge background (rather than just the photoproduction background).

In order to subtract the full photoproduction background from the final selected data sample, also the  $\pi^+$  photoproduction events have to be identified. The amount of these events can be estimated using the charge asymmetry (6.35) and the number of the  $\pi^-$  photoproduction events  $N^-$ . Signal events can then be obtained as

$$N_{signal} = N_{all} - (1 + asym)N^- = N^+ - asymN^-. \quad (6.37)$$

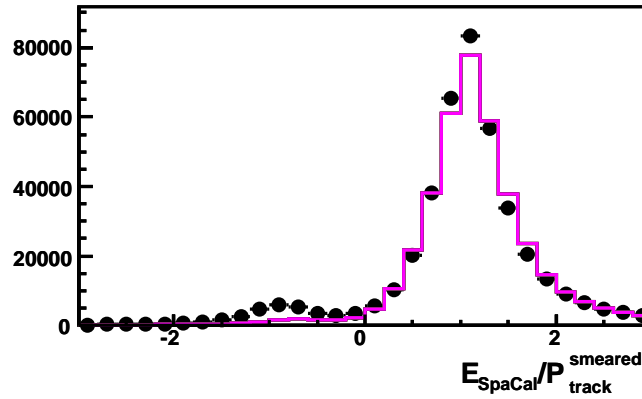


Figure 6.4: A distribution of  $Q \frac{E_e'}{p}$  in the final selection of events from the low energy data. The black points are data, the magenta line is the Monte Carlo simulation.

As already mentioned above,  $N^-$  in the analysis consists not only of the  $\pi^-$  photoproduction events but also from the charge mis-reconstructed signal. Therefore, the wrong charge background subtraction (6.37) is performed for both data and Monte Carlo in order to account for the presence of the mis-reconstructed signal events. The mistake made by using different charge asymmetry factors for data and Monte Carlo (6.36) for these events is negligible and covered by the systematic uncertainty on the charge reconstruction.

### Background Subtraction Summary

In the low and medium energy data analysis, the wrong charge background subtraction relies on precise charge measurement and accurate charge reconstruction simulation in the Monte Carlo. Since the charge reconstruction is most precise for low  $p_T$  tracks, the following strategy for the background subtraction is chosen for the low and medium energy data:

- The wrong charge background subtraction is performed for  $y > y_{trans}$ . High  $y$  region corresponds to low energy, low  $p_T$  scattered leptons. As already mentioned above, the precision of the charge reconstruction improves with decreasing  $p_T$  (increasing curvature of the track).
- The tagged events subtraction based on Eq. 6.32, where the negative charge of the tagged background is required, is done in the remaining region of the inelasticity  $y < y_{trans}$ .

The transition values  $y_{trans}$  are chosen as

$$y_{trans}^{575} = 0.56, \quad y_{trans}^{460} = 0.6. \quad (6.38)$$

In the analysis of high energy data, the background is subtracted using the tagged events in the whole  $y$  range according to Eq. 6.34. No charge is required here. The background subtraction strategy is also summarised in Table 6.12.

$y$ range	Background subtraction technique
$E_p = 460, 575 \text{ GeV}$	
$y > y_{trans}$	wrong charge background subtraction $N_{signal} = N_{all} - (1 + asym)N^- = N^+ - asymN^-$
$y < y_{trans}$	tagged events subtraction $N_{signal} = N_{all} - \frac{2}{acc_{tagger}}N_{tagged}^-$
$y_{trans}^{575} = 0.56, \quad y_{trans}^{460} = 0.6$	
$E_p = 920 \text{ GeV}$	
all $y$	tagged events subtraction $N_{signal} = N_{all} - \frac{1}{acc_{tagger}}N_{tagged}$

Table 6.12: Photoproduction background subtraction strategy.

Fig. 6.5 shows the wrong charge background and the tagged event background in the final selected low energy data sample. Fig. 6.6 then shows the description of the positron energy in the same data sample. Data are well described by the Monte Carlo simulation after the wrong charge background subtraction.

Fig. 6.7 shows the tagged background in the electron energy distribution. Since the overlap of the DIS signal with the Bethe-Heitler processes is not reduced by the charge requirement, the tagged background appears even at higher positron energies as a constant fraction of the signal events. Around  $\sim 1\%$  of the signal events also pass the tagger selection because of the overlap with Bethe-Heitler processes. These events are not background events. Real photoproduction background appears in addition only at lower positron energies. Since the tagged events are corrected by the tagger acceptance  $acc_{tagger} = 0.2$ , there is  $\sim 5\%$  fraction of events that should not be subtracted. This has to be taken into account when normalising the control plots from data and Monte Carlo and extracting cross sections.

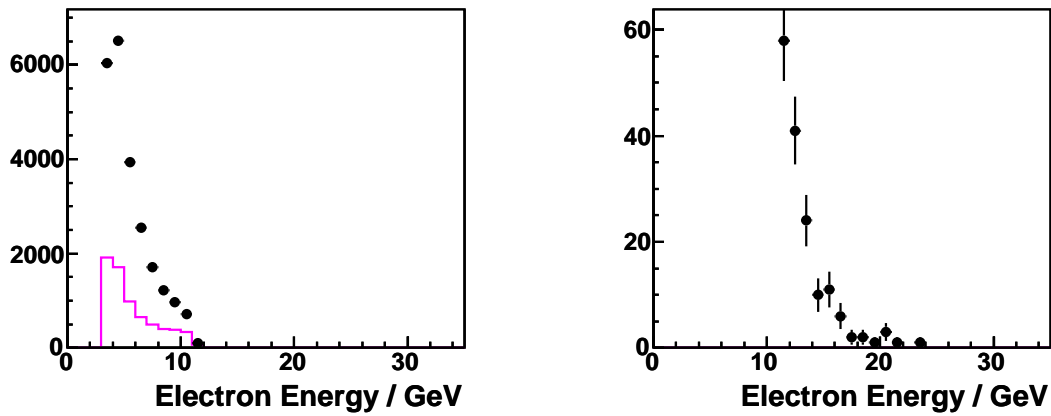
## 6.4 Efficiency of the Selection and Accuracy of the Simulation

The efficiency of particular selection cuts is not necessarily the same in data and Monte Carlo. The efficiencies of the cuts have to be monitored both in data and the simulation, and possible differences have to be taken into account in the corrections applied to data or Monte Carlo or both at the analysis level.

The efficiency of the cuts is usually monitored in the following way

$$\varepsilon(cut) = \frac{monitor \ \& \ cut}{monitor} \quad (6.39)$$

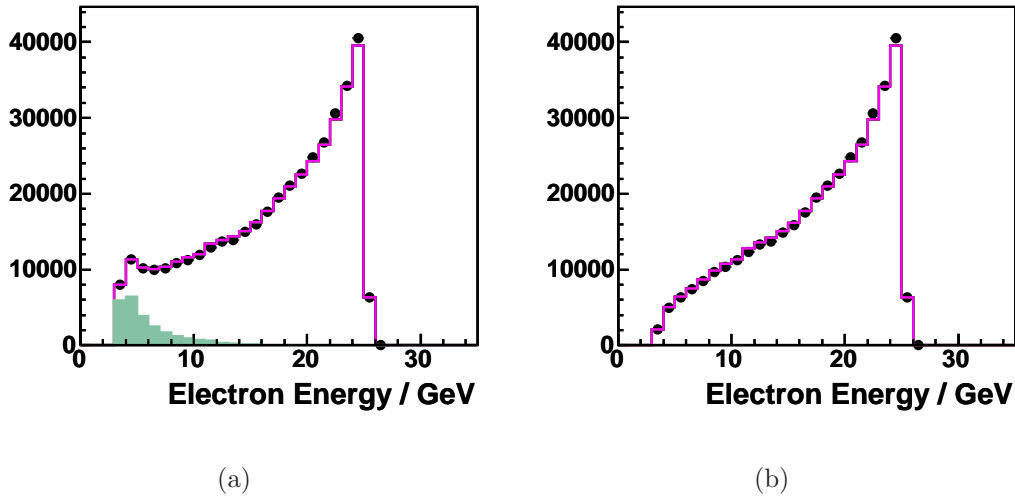
where *monitor* stands for the number of events in the monitoring sample, and *monitor & cut*



(a) Wrong charge background at  $y > 0.6$ . The background seen in Monte Carlo (magenta line) contains only the charge misreconstructed signal events. The difference between data and Monte Carlo shows the amount of photoproduction background. However, the wrong charge background is subtracted as a whole (for both data and Monte Carlo).

(b) Tagged events with the negative charge in data at  $y < 0.6$  multiplied by the factor of  $\frac{2}{acc_{tagger}}$ . The photoproduction background for the scattered lepton energy above  $\sim 18$  GeV is negligible.

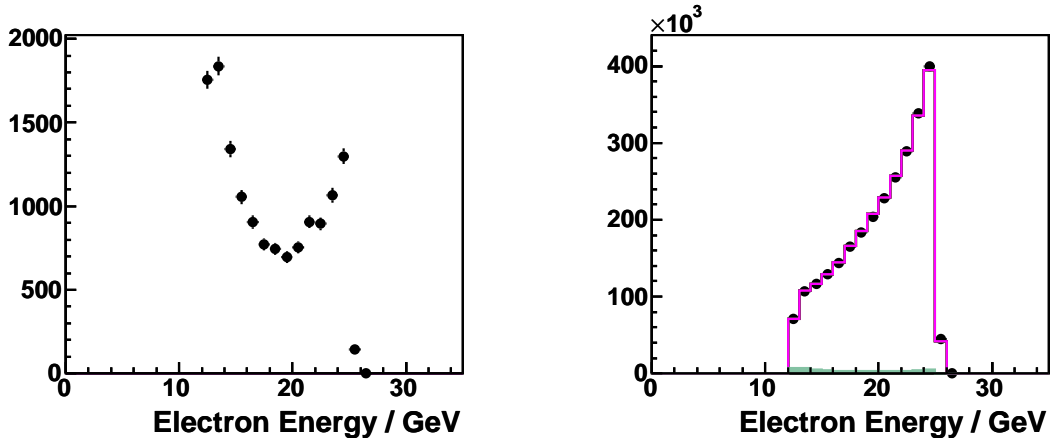
Figure 6.5: Background in the low energy data sample.



(a)

(b)

Figure 6.6: Positron energy description before (a) and after (b) the background subtraction in the low energy data. Black points are the selected data, green area is the background determined from data. Monte Carlo (magenta line) describes the signal data well.



(a) Tagged events without any charge requirement. The charge requirement (used in the low and middle energy data) removes the Bethe-Heitler overlap events. Therefore, the tagged events are seen even at high  $E'_e$ . Only the low  $E'_e$  events are the photoproduction background.

(b) Positron energy description. Black points are data, green area is the tagged background and the magenta line is the Monte Carlo. The tagged background is seen even at high  $E'_e$  and it is a constant fraction of the signal events there.

Figure 6.7: Background in the high energy data sample.

is the number of events that pass the monitoring sample selection together with the monitored cut. The monitoring sample has to be defined as independently on the monitored cut as possible. Table 6.13 lists the so-called **basic selection** that is used for several efficiency monitorings described in this section. It is a simple NC DIS event selection in a similar kinematical domain as the **analysis selection** (see Table 6.10). The basic selection consists of an positron cluster requirement where a stronger  $r_{log}$  cut is used in order to suppress the photoproduction background even harder (the signal is suppressed as well, which is not desirable for the final analysis selection). There are the SPACAL and BST acceptance cuts, the  $E - p_z$  cut and anti-Compton selection.

The requirement of a primary vertex is missing and it will be specified in each of the sections below where the basic selection is used.

There is also no trigger selection in the basic selection. Again, the trigger selection will be specified in the following sections depending on the efficiency studied.

The efficiency corrections in Monte Carlo can be applied in two ways. Either an efficiency weight is assigned to each event, or a corresponding fraction of events is rejected on random basis.

### 6.4.1 Trigger Efficiency

This sections describes the efficiency of the sub-triggers used in the analysis. Details on the efficiency monitoring are given here, and possible sources of inefficiencies are discussed.

Selection Description	Values
	$E_p = 460, 575 \text{ GeV}$ $E_p = 920 \text{ GeV}$
Cluster type	SPACAL cluster
Energy	$E'_e > 3.4 \text{ GeV}$ $E'_e > 11 \text{ GeV}$
Inelasticity	$0.1 < y_e < 0.9$ $0.1 < y_e < 0.56$
Electromagnetic/hadronic cluster separation	$r_{log} < 4 \text{ cm}$ $\frac{E_{had}}{E_{tot}} < 0.15$
Acceptance	SPACAL acceptance cut BST acceptance cut
$Q^2$ region	$Q_e^2 > 2.5 \text{ GeV}^2$ $Q_e^2 > 7 \text{ GeV}^2$
$E - p_z$ cut	$E - p_z > 35 \text{ GeV}$
QED-C events	anti-Compton selection

Table 6.13: Overview of the **basic selection** criteria used in the efficiency studies.

### Trigger Efficiency in the High Energy Data

In order to monitor a sub-trigger efficiency, it is necessary to find an independent sample for the monitoring. Sub-triggers consist of trigger elements. The monitoring sample has to be defined by sub-triggers that have different trigger elements in their definition. The sub-triggers used in the analysis fall into a category of so-called SPACAL sub-triggers. Table 6.14 lists non-SPACAL sub-triggers that are used for the monitoring<sup>5</sup>.

As already mentioned in Section 6.3.2, sub-triggers used in the high energy analysis are prescaled. Suppression by prescales is done at the trigger level 3. Since the sub-triggers ST0, ST2 and ST3 do not use any level 3 trigger elements, the efficiency of L1\*L2 raw sub-triggers can be monitored. No prescale suppression means higher statistics which leads to better precision of the monitoring. At least one of the actual non-SPACAL sub-triggers is required in the monitoring sample. To summarize, the sub-trigger efficiency is monitored as

$$\varepsilon(\text{sub-trigger}) = \frac{top}{bottom} \quad (6.40)$$

where the *bottom* = *monitor* and *top* = *monitor* & *cut* selections are defined as:

- **bottom**

<sup>5</sup>The list is generated from

<https://www-h1.desy.de/h1/iww/ittrigger/TrigSetup/tdl.subtriggers>

via the following command:

```
cat tdl.subtriggers |grep -v "C\[2\]" |grep -v "\\\\"* |
sed "s/^(^s)\(...)\(.*\)/\2,/g"
```

10 , 12 , 13 , 14 , 16 , 18 , 19 , 20 , 23 , 24 , 25 , 29 , 30 , 32 ,  
 34 , 45 , 47 , 48 , 50 , 51 , 52 , 53 , 54 , 55 , 56 , 57 , 58 , 59 ,  
 60 , 62 , 64 , 65 , 66 , 67 , 68 , 71 , 72 , 73 , 74 , 75 , 76 , 77 ,  
 78 , 79 , 80 , 81 , 82 , 84 , 85 , 86 , 87 , 89 , 91 , 92 , 93 , 94 ,  
 95 , 96 , 99 , 101 , 102 , 103 , 104 , 105 , 107 , 108 , 109 , 110 , 111 ,  
 113 , 114 , 116 , 117 , 118 , 119 , 120 , 122 , 123 , 124 , 126 , 127

Table 6.14: List of non-SPACAL sub-triggers. These sub-triggers contain no trigger elements requiring any information from SPACAL. Therefore, they can be used as independent monitors for the SPACAL trigger elements used in this analysis.

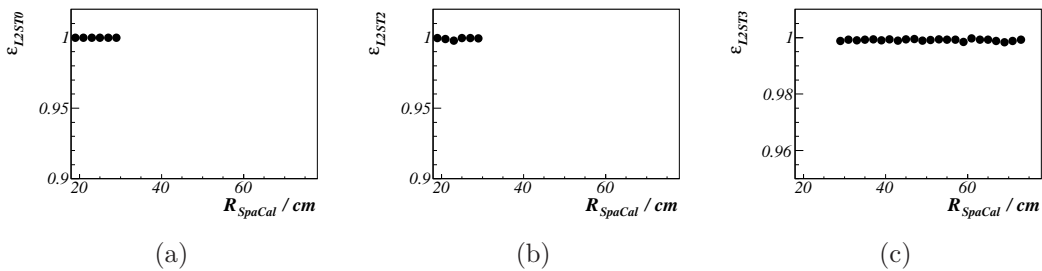


Figure 6.8: Efficiency of ST0 (a) and ST2 (b) sub-triggers at  $r_{SPACAL} < 29$  cm, and ST3 (c) sub-trigger at  $r_{SPACAL} > 29$  cm.

basic selection

CJC vertex ( $-35 < z_{vtx}^{CJC} < 35$  cm)

at least one non-SPACAL actual sub-trigger

$r_{SPACAL}$  cut

- top

bottom

L1\*L2 raw sub-trigger

Fig. 6.8 shows the efficiency of sub-triggers in the region where they are used: ST0, ST2 at  $r_{SPACAL} < 29$  cm and ST3 at  $r_{SPACAL} > 29$  cm. No correction is needed.

The sub-trigger ST3 uses hadronic SPACAL trigger elements `!SPCLh_ATof_E_!` && `!SPCLh_ToF_E_2` in its definition. Therefore, it is desirable to check the efficiency of the sub-trigger as a function of a variable sensitive to the hadronic SPACAL. Fig. 6.9(a) shows the efficiency in bins of  $(E - p_z)_{SPACAL}^{had}$  and reveals a rapid drop of the efficiency above  $\sim 30$  GeV. However, a detailed study of the efficiency in bins of  $E'_e$  and  $r_{SPACAL}$  reveals that no correction is needed because the statistics at  $(E - p_z)_{SPACAL}^{had} > 30$  GeV is very limited. The inefficiency propagates only to the lowest  $E'_e$  and high  $r_{SPACAL}$  where it is observed at the level of  $\sim 0.5\%$ . Therefore, no correction is needed.

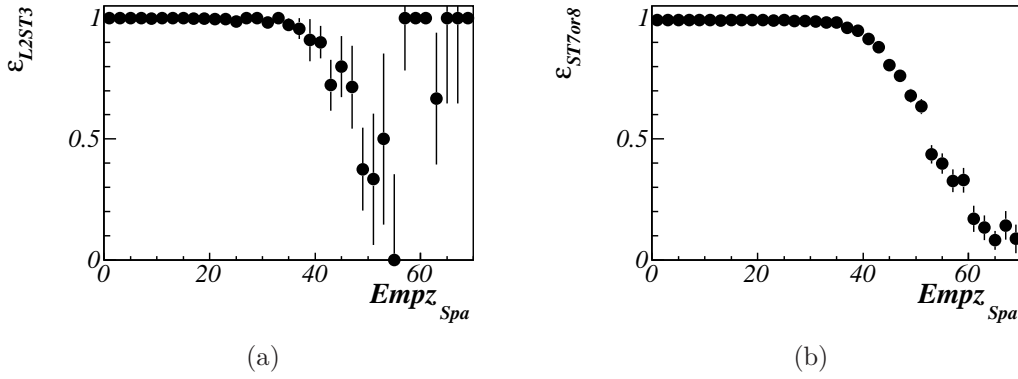


Figure 6.9: Efficiency of ST3 and a combination of ST7 or ST8 sub-triggers as a function of  $(E - p_z)_{SPACAL}^{had}$ .

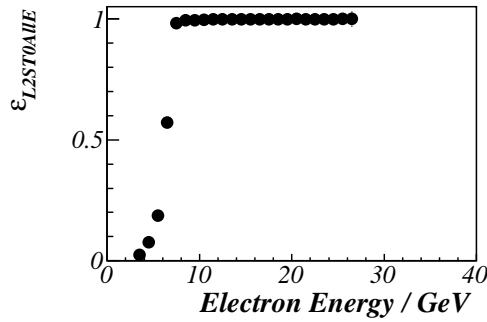


Figure 6.10: Efficiency of ST0 monitored by the non-SPACAL sub-triggers in the low energy data. The efficiency is steeply falling at  $E'_e < 7$  GeV.

### Trigger Efficiency in the Low and Medium Energy Data

The efficiency of the sub-trigger ST0 is monitored in the same way as described above for the high energy data. Fig. 6.10 shows the efficiency of ST0 monitored by the non-SPACAL sub-triggers as a function of  $E'_e$ . There is no efficiency correction needed in the region where ST0 is used, i.e. at  $y < 0.6$  and  $y < 0.56$  for the low energy and medium energy data, respectively (which corresponds roughly to  $E'_e > 11$  GeV and  $E'_e > 12$  GeV, respectively).

The figure also points out that the efficiency is steeply falling at  $E'_e < 7$  GeV. ST0 will be used in the monitoring samples for other efficiencies, and it is clear that in these cases the efficiencies cannot be studied at  $E'_e < 7$  GeV.

The combination of ST7 or ST8 is used at  $y > 0.6$  and  $y > 0.56$  in the low energy and medium energy data, respectively. The efficiency of this sub-trigger combination can be monitored by the ST0 sub-trigger, but only for  $E'_e > 7$  GeV. Since the ST7 and ST8 sub-triggers are used only at high  $y$ , a cut on  $y_e > 0.38$  is used in the monitoring. The efficiency is monitored as

$$\varepsilon(\text{ST7 or ST8}) = \frac{top}{bottom} \quad (6.41)$$

where the *bottom* = *monitor* and *top* = *monitor* & *cut* selections are defined as:

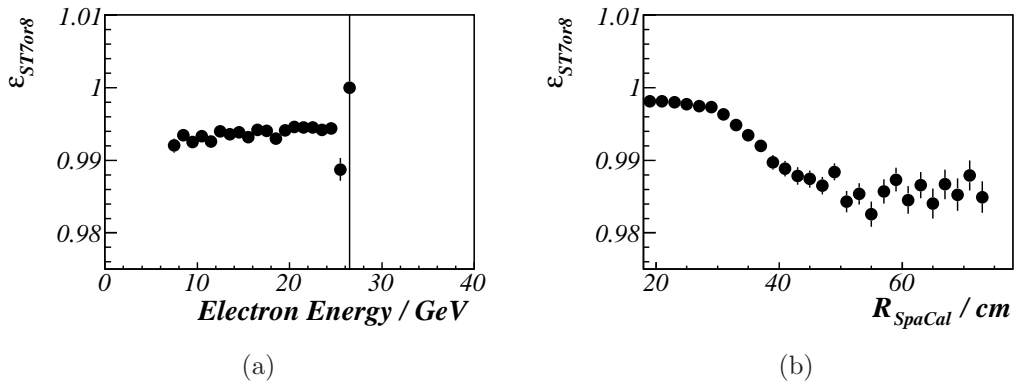


Figure 6.11: Efficiency of ST7 or ST8 sub-triggers for  $(E - p_z)_{SPACAL}^{had} < 32$  GeV.

- **bottom**

basic selection

CJC vertex ( $-35 < z_{vtx}^{CJC} < 35$  cm)

$E'_e > 7$  GeV

$y_e > 0.38$

ST0 actual sub-trigger

- **top**

bottom

ST7 or ST8 actual sub-triggers

The sub-triggers ST7 and ST8 contain also the hadronic SPACAL trigger elements `!SPCLh_ATof_E_!` && `!SPCLh_ToF_E_2` in their definitions. Similarly as in the case of ST3, they are sources of an inefficiency (see Fig. 6.9(b)). The figure shows the efficiency of ST7 or ST8 as a function of  $(E - p_z)_{SPACAL}^{had}$  where the efficiency rapidly drops above  $(E - p_z)_{SPACAL}^{had} > 32$  GeV.

Cutting on  $(E - p_z)_{SPACAL}^{had} < 32$  GeV in the monitoring sample removes the inefficiency caused by the hadronic SPACAL trigger elements and makes it possible to monitor other sources of inefficiency. Fig. 6.11 shows the ST7 or ST8 efficiency after the cut on  $(E - p_z)_{SPACAL}^{had}$ . The plot showing the trigger efficiency as a function of  $r_{SPACAL}$  is used to determine the efficiency correction for ST7 or ST8 sub-triggers. The correction is 0.3% at  $r_{SPACAL} < 30$  cm, 1.3% at  $r_{SPACAL} > 45$  cm, and linear in-between.

Fig. 6.12 displays the ST7 or ST8 efficiency after the  $r_{SPACAL}$  dependent correction is applied. There is no longer an inefficiency as a function of  $E'_e$  or  $r_{SPACAL}$  observed. However, there is still the inefficiency coming from the hadronic SPACAL trigger elements that needs to be treated.

After applying the correction described above, the hadronic SPACAL trigger element inefficiency can be studied simply by removing the  $(E - p_z)_{SPACAL}^{had} < 32$  GeV cut from the monitoring sample. Although the plot in Fig. 6.9(b) shows a clear dependence of the efficiency on  $(E - p_z)_{SPACAL}^{had}$ , the correction is not evaluated as a function of this

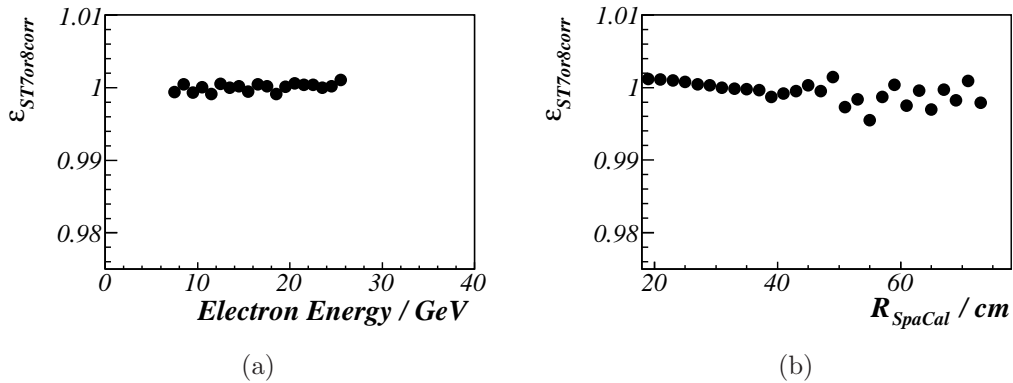


Figure 6.12: Efficiency of ST7 or ST8 sub-triggers after  $(E - p_z)_{SPACAL}^{had} < 32$  GeV the  $r_{SPACAL}$  dependent correction.

variable. The reason for that is the following. The efficiency drops close to 0 at higher values of  $(E - p_z)_{SPACAL}^{had}$  and it is not desirable to apply extremely large weights to the corresponding data events in order to correct for such a low efficiency. Therefore, the correction is evaluated in bins of different variables. The scattered positron energy  $E'_e$  and  $r_{SPACAL}$  are chosen for that. Since the SPACAL calorimeter is situated in the backward direction, the inefficiency should be visible at low  $E'_e$ , i.e. high values of inelasticity  $y$  (which directly follows from the prescription for hadronic reconstruction method for  $y$  in Eq. 6.28). Fig. 6.13(a) shows the efficiency evaluated in three slices of  $r_{SPACAL}$ . The inefficiency arises only at  $E'_e < 16$  GeV and is fitted by a line with a fixed point  $\varepsilon(E'_e = 16 \text{ GeV}) = 1$ . The correction at  $E'_e = 7$  GeV, which is the lower limit for a monitoring with sub-trigger ST0, is  $\sim 2\%$ . An extrapolation of the correction to lower  $E'_e$  is used in the analysis.

## 6.4.2 Vertex Reconstruction Efficiency

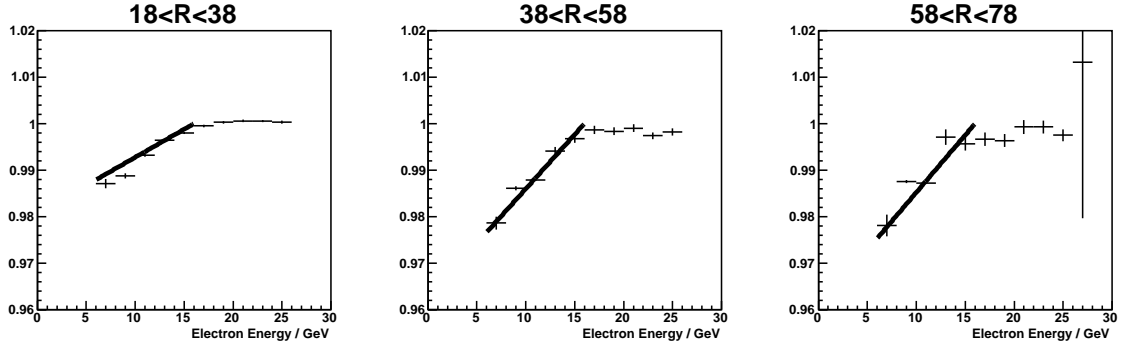
This section discusses the efficiency of the primary vertex reconstruction in the CJC tracker. Two ways of monitoring the CJC vertex reconstruction efficiency are considered. The efficiency can be monitored by a vertex reconstructed in the CIP detector or by a track reconstructed with the BCREC routine.

In the monitoring with the CIP vertex, more than 3 hits in the CIP detector are required as a quality check of the reconstructed vertex. The acceptance of the CIP detector restricts the monitoring to a region of  $r_{SPACAL} > 23$  cm. The lower  $r_{SPACAL}$  region (the analysis uses a lower  $r_{SPACAL} > 18$  cm cut) is out of acceptance and cannot be monitored by the CIP vertex. The way of CJC vertex reconstruction efficiency monitoring is summarized here.

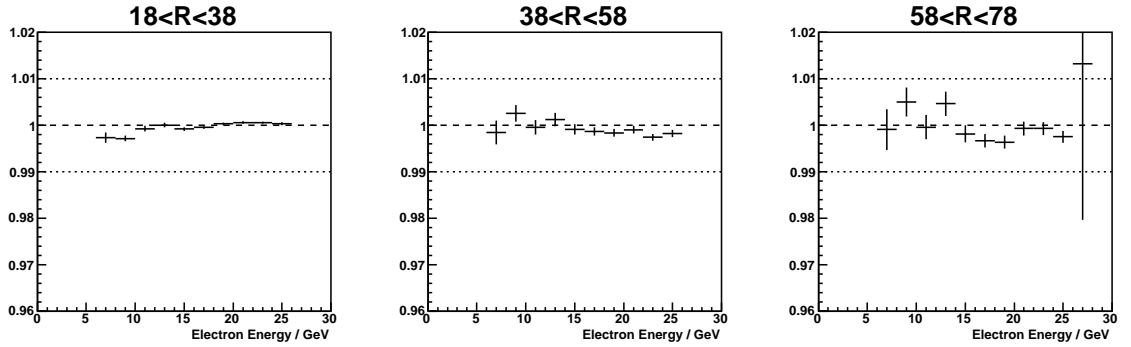
$$\varepsilon(\text{CJC vertex}) = \frac{top}{bottom} \quad (6.42)$$

where the *bottom* = *monitor* and *top* = *monitor* & *cut* selections are defined as:

- **bottom**  
basic selection



(a) The efficiency of ST7 or ST8 sub-triggers as a function of  $E'_e$  after the  $r_{SPACAL}$  dependent correction in three bins of  $r_{SPACAL}$ . A combined efficiency from the low and medium energy data is shown. The cut on  $(E - p_z)_{SPACAL}^{had} < 32$  GeV is not applied here. Therefore, the plots show the residual inefficiency coming from the hadronic SPACAL trigger elements. The correction for this inefficiency is obtained as a linear fit and is displayed as a line.



(b) The efficiency of ST7 or ST8 sub-triggers after all corrections. The trigger efficiency is well understood within 1%.

Figure 6.13: ST7 or ST8 sub-trigger efficiency.

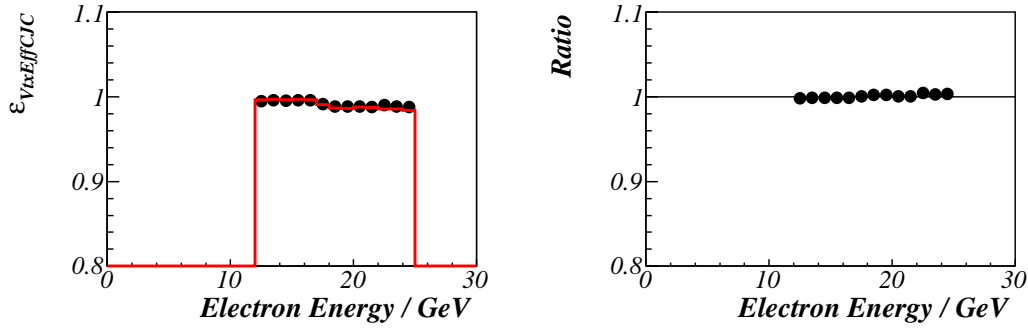


Figure 6.14: CJC vertex reconstruction efficiency as a function of  $E'_e$  in the high energy data analysis. The efficiency in data (black points) is well described by Monte Carlo (red line).

ST0

CIP vertex ( $-30 < z_{vtx}^{CIP} < 30$  cm,  $N_{hits}^{CIP} > 3$ )

- **top**

bottom

analysis trigger

CJC vertex ( $-35 < z_{vtx}^{CJC} < 35$  cm)

Another way of monitoring the CJC vertex reconstruction efficiency is by using the BCREC track, i.e. requiring the CJC/BST validation cut in the monitoring sample. If there is a CJC vertex found in the monitoring sample then it is required to lie between  $-35$  cm and  $35$  cm. The *bottom = monitor* and *top = monitor & cut* selections are chosen as:

- **bottom**

basic selection

ST0

CJC/BST validation

if CJC vertex exists :  $-35 < z_{vtx}^{CJC} < 35$  cm

- **top**

bottom

analysis trigger

CJC vertex ( $-35 < z_{vtx}^{CJC} < 35$  cm)

### Vertex Reconstruction Efficiency in the High Energy Data

Fig 6.14 shows the CJC vertex reconstruction efficiency as a function of  $E'_e$  for data and Monte Carlo. The efficiencies agree well and no correction is needed.

### Vertex Reconstruction Efficiency in the Low and Medium Energy Data

In the monitoring described at the beginning of this section, the sub-trigger ST0 is required in the monitor sample and the analysis trigger is required in the sample that is monitored. In Section 6.4.1, where the trigger efficiency is discussed, the combination of ST7 or ST8 is also monitored by the sub-trigger ST0. Therefore, the monitoring described here can be considered as a monitoring of a combined trigger and vertex reconstruction efficiency, and the combined CJC vertex and trigger efficiency can be written as a product of the trigger and the CJC vertex efficiency

$$\varepsilon(\text{CJC vertex and trigger}) = \varepsilon(\text{ST7 or ST8}) \times \varepsilon(\text{CJC vertex}). \quad (6.43)$$

The efficiency monitoring is displayed in Fig. 6.15.

- **combined CJC vertex and trigger efficiency:** The upper row of plots shows the combined CJC vertex and trigger efficiency  $\varepsilon(\text{CJC vertex and trigger})$  in bins of  $E'_e$  and  $r_{SPACAL}$ . The observed inefficiency at low  $E'_e$  and  $r_{SPACAL}$  will be partially corrected by the trigger efficiency correction  $\varepsilon(\text{ST7 or ST8})$  (see Section 6.4.1).
- **CJC vertex efficiency alone:** The plots in the middle row show the same  $\varepsilon(\text{CJC vertex and trigger}) = \frac{top}{bottom}$  efficiency where the events in the numerator are corrected for the trigger efficiency correction for ST7 or ST8. In other words, the plots show the CJC vertex efficiency alone. The CJC vertex efficiency correction is evaluated for  $E'_e < 16$  GeV and  $r_{SPACAL} < 43$  cm in 5 cm  $r_{SPACAL}$  slices. For each slice, the efficiency is evaluated as a linear fit to the  $E'_e$  dependence<sup>6</sup>. Up to 4% correction is needed in the simulation.
- **after the efficiency corrections:** The bottom row of plots show the  $\varepsilon(\text{CJC vertex and trigger})$  efficiency after both the trigger and the CJC vertex efficiency corrections.

### 6.4.3 Track–Cluster Link Efficiency

The efficiency of finding a track linking the primary vertex with the cluster of the scattered lepton is not the same in data and Monte Carlo, therefore a correction of the simulation is needed. The efficiency can be monitored in the following way

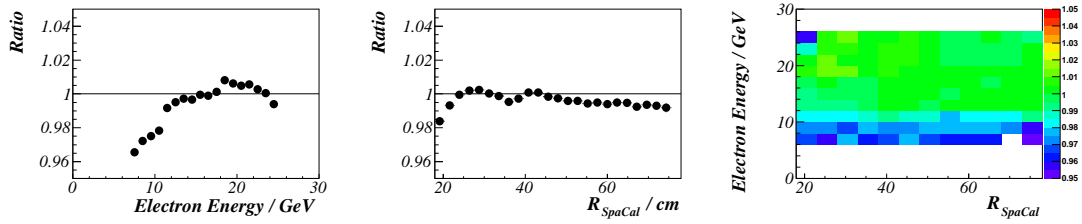
$$\varepsilon(\text{track–cluster link}) = \frac{top}{bottom} \quad (6.44)$$

where the *bottom* = *monitor* and *top* = *monitor & cut* selections are defined as:

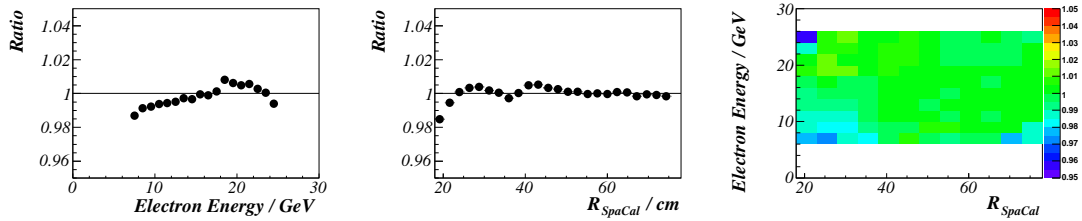
- **bottom**
  - basic selection
  - analysis trigger
  - CJC vertex
  - $15 < E'_e < 25$  GeV

---

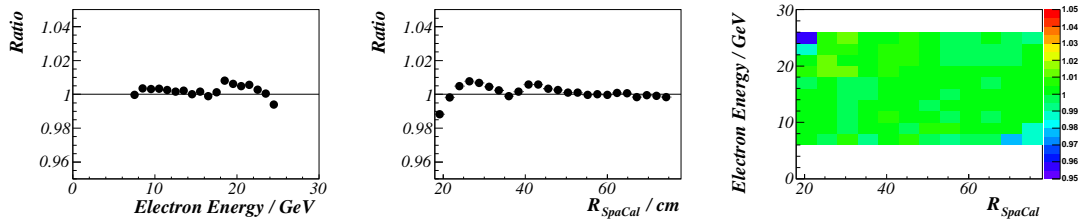
<sup>6</sup>The CJC vertex efficiency alone can be consistently monitored with ST7 or ST8 sub-triggers in the monitoring sample (instead of ST0). In this way, the efficiency can be evaluated even at  $E'_e < 7$  GeV.



(a) Combined CJC vertex and trigger efficiency as monitored by the BCREC vertex and the ST0 sub-trigger.



(b) The above corrected for the trigger efficiency. The plots show the CJC vertex efficiency alone. An inefficiency is seen at low  $E_e^l$  and low  $r_{SPACAL}$ .



(c) After the trigger and the CJC vertex efficiency corrections, the efficiency is understood within 2%.

Figure 6.15: Combined CJC vertex and trigger efficiency in the low energy data. The plots show the ratio of the efficiency in data and Monte Carlo.

- top
  - bottom
  - CJC/BST track validation

The lower cut on the energy of the scattered lepton candidate is there to reduce the photoproduction background. Fig 6.16 shows the track–cluster link efficiency in the low energy data analysis. There is up to 10% difference seen between data and the simulation at lower  $r_{SPACAL}$ . Therefore a correction is needed. The efficiency correction factors are evaluated in bins of  $r_{SPACAL}$  and  $\varphi_e$ . The analysed region of  $18 < r_{SPACAL} < 74$  cm can be divided into 3 regions with respect to the acceptance of the tracking detectors:

- $18 < r_{SPACAL} < 30$  cm : BST only region
- $30 < r_{SPACAL} < 54$  cm : CJC/BST overlap
- $54 < r_{SPACAL} < 78$  cm : CJC only region

$r_{SPACAL}$  slices of 2 cm are considered for the track–link efficiency correction. Based on the geometry of the BST detector, 7 equidistant slices in  $\varphi_e$  are considered for  $r_{SPACAL} < 54$  cm. No bins in  $\varphi_e$  are defined in the CJC region since it has no complicated  $\varphi$  structure.

The obtained correction factors are applied to the monitored events in order to check the performance of the correction. Fig. 6.17 compares the track–link efficiency in the low energy data with the corrected efficiency in the Monte Carlo. The correction works perfectly as a function of  $r_{SPACAL}$  and  $\varphi_e$ . However, there is a discrepancy at low  $E'_e$  in Fig. 6.17(d).

This difference in efficiency is attributed to the photoproduction background in data. The track–link requirement helps to reduce this background. However, the cut is not present in the monitoring sample selection. Therefore, the amount of photoproduction background in the monitoring sample is not negligible, and has an effect on the monitored efficiency. The photoproduction background can be subtracted in a similar way as in the analysis of the high energy data (see Section 6.3.8), and the signal events are obtained as

$$N_{signal} = N_{all} - \frac{1}{acc_{tagger}} N_{tagged} \quad (6.45)$$

where  $N_{tagger}$  is the number of events that passed the tagger selection described in Table 6.11 and  $acc_{tagger} = 0.2$  is the tagger acceptance. Fig 6.18 shows the track–cluster link efficiency as a function of  $E'_e$  where the tagged event subtraction is performed in the monitoring sample. No dependence on  $E'_e$  is seen.

The  $F_L$  and  $F_L^D$  analysis requires a good understanding of data down to  $E'_e$  of 3.4 GeV. Because of the photoproduction background, it is not possible to measure the track–link efficiency at low  $E'_e$ . However, being able to show that there is no energy dependence of the efficiency for  $E'_e > 10$  GeV only hints that the derived correction can be trusted in the whole range of  $E'_e$ . Validity of the correction at low  $E'_e$  was checked in an independent analysis using radiative events. The track-cluster link efficiency is related to the performance of the tracking detectors, and it is natural to assume that the correction factors should depend only on geometrical quantities (such as  $r_{SPACAL}$  and  $\varphi_e$ ) and not  $E'_e$ .

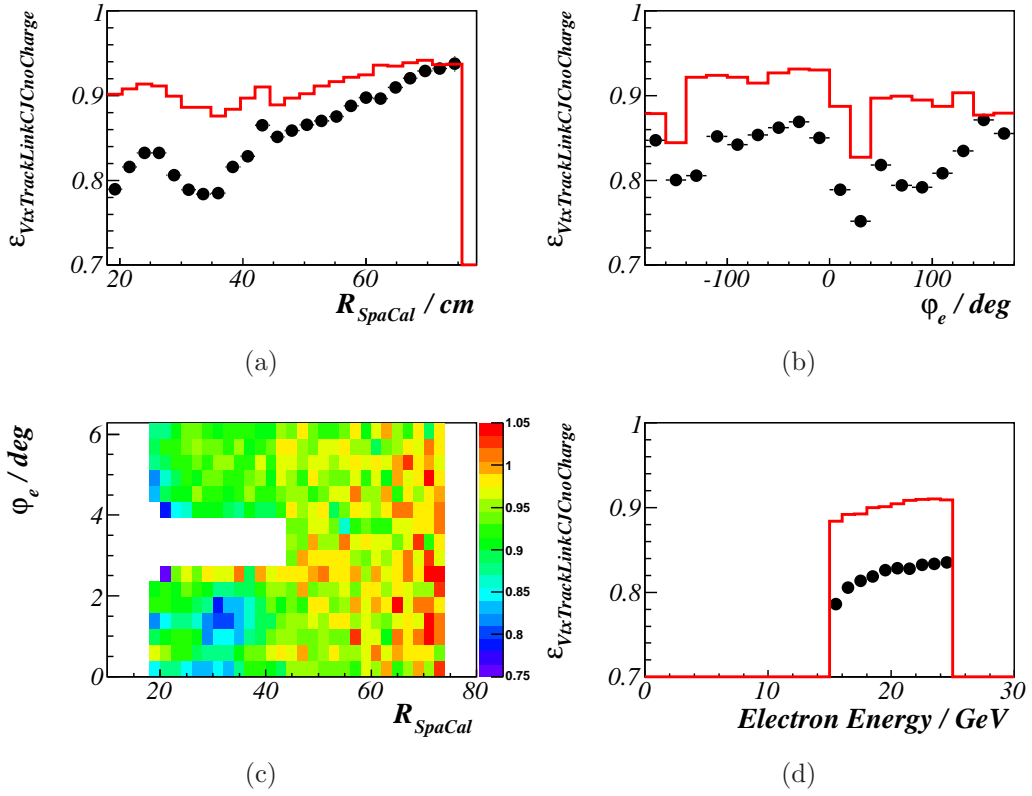


Figure 6.16: Track-cluster link efficiency in the low energy data (black points) and Monte Carlo (red line) as a function of  $r_{SPACAL}$ ,  $\phi_e$ , and  $E'_e$ . The 2-dimensional plot shows the efficiency double-ratio in bins of  $r_{SPACAL}$  and  $\phi_e$ .

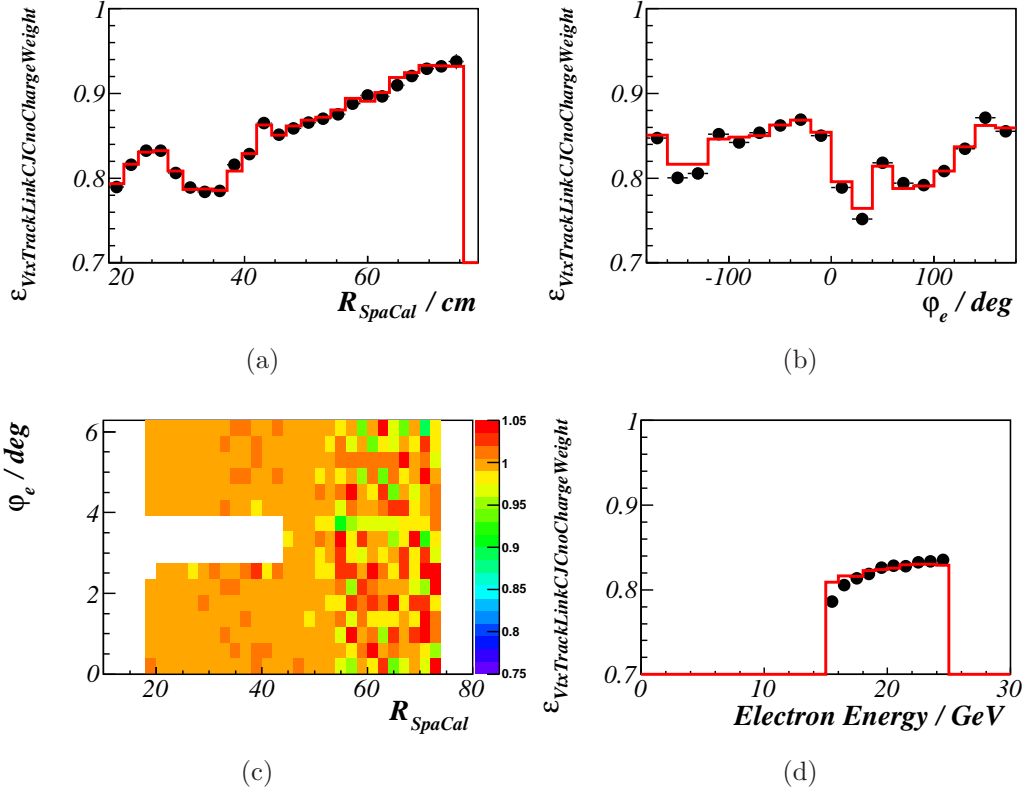


Figure 6.17: Track-cluster link efficiency in the low energy data (black points) and Monte Carlo (red line) as a function of  $r_{SPACAL}$ ,  $\varphi_e$ , and  $E'_e$ . The 2-dimensional plot shows the efficiency double-ratio in bins of  $r_{SPACAL}$  and  $\varphi_e$ . The track-cluster link efficiency correction is applied in the Monte Carlo. The remaining discrepancy at low  $E'_e$  is attributed to the photoproduction background in the monitoring sample.

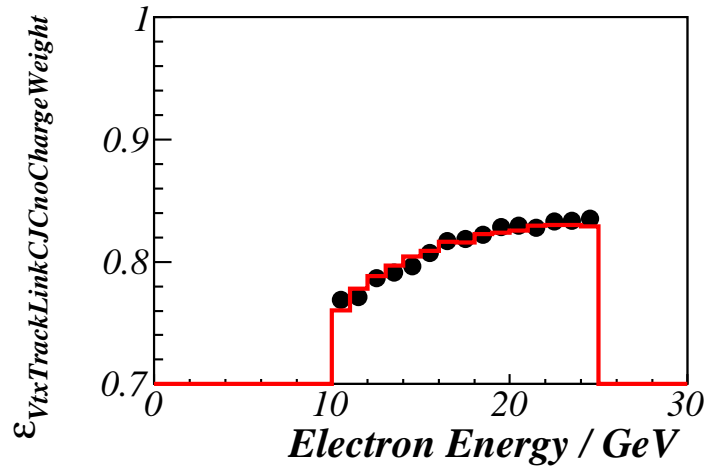


Figure 6.18: Track-cluster link efficiency in the low energy data (black points) and Monte Carlo (red line) as a function of  $E'_e$ . The track-cluster link efficiency correction is applied in the Monte Carlo. Photoproduction background is subtracted from the monitoring sample using tagged events.

The correction factors are evaluated separately for the low energy, medium energy and high energy analyses.

#### 6.4.4 Charge Reconstruction Efficiency

The LAr and the SPACAL calorimeters as well as the inner tracking detectors are situated within the 1.15 T homogeneous magnetic field. This allows to reconstruct the charge of a particle from a curvature of the corresponding reconstructed track. The selection criteria for the scattered positron used in this analysis contain a track-cluster link requirement where the cluster from SPACAL calorimeter has to be linked with a track reconstructed by the BCREC routine. One of the parameters returned by this routine,  $\kappa$ , gives the signed inverse transversal momentum of the track. The sign of  $\kappa$  can be directly transformed into a charge.

The wrong charge background subtraction described in Section 6.3.8 crucially depends on the correct simulation of the charge reconstruction efficiency in the Monte Carlo. Fig. 6.19(a) shows the  $Q \frac{E'_e}{p}$  distribution in the final selection of events from the low energy data. The energy  $E'_e$  comes from the calorimeter measurement, and it is well described by the Monte Carlo. The momentum  $p$  and charge  $Q$  are reconstructed in the tracker. The data (black points) are not well described by Monte Carlo (magenta line) where no correction to the simulated momentum is applied. The  $\frac{E'_e}{p}$  peak in data is broader than in Monte Carlo which means the momentum reconstruction in Monte Carlo is too efficient. Since the charge is reconstructed from the curvature of the track, it is important to get the track momentum reconstruction efficiency in Monte Carlo at the same level as it is in data. Therefore, a **momentum smearing correction** is introduced.

The momentum smearing corrects the shape of the  $\frac{E'_e}{p}$  distribution in Monte Carlo. The  $\frac{E'_e}{p}$  peak is fitted by a Gaussian distribution in bins of  $E'_e$  (1 GeV slices) and  $r_{SPACAL}$  (5 cm slices). The resulting  $\mu$  and  $\sigma$  of the fit to data and Monte Carlo is then combined

$$M = \frac{\mu_{data}}{\mu_{MC}}, \quad S = \sqrt{\sigma_{data}^2 - \sigma_{MC}^2} \quad (6.46)$$

and used to calculate the smeared momentum of the track

$$\frac{E'_e}{p_{smeared}} = M \times \frac{E'_e}{p} + S \times \text{RANDOM} \quad (6.47)$$

where RANDOM is a random number from the Gaussian distribution with  $\mu = 0$  and  $\sigma = 1$ .

Fig. 6.19(b) shows the fraction of the cluster energy and the smeared track momentum multiplied by the track charge  $Q \frac{E'_e}{p_{smeared}}$ . The effect of the **momentum smearing correction** is clearly visible in the side-by-side comparison. The description of the fraction improves after the correction, however there is still place for improvement. Therefore, an additional correction is going to be discussed in the following text.

In order to check the charge reconstruction efficiency it is useful to study the amount of positive and negative charge events. Fig. 6.20 shows the asymmetry  $\frac{N^+ - N^-}{N^+ + N^-}$  in the low energy data sample. Only events that pass the **analysis selection** with  $15 < E'_e < 25$  GeV are considered. The events with  $E'_e$  below 15 GeV are excluded in order to reject the photoproduction background. The figure shows the dependence of

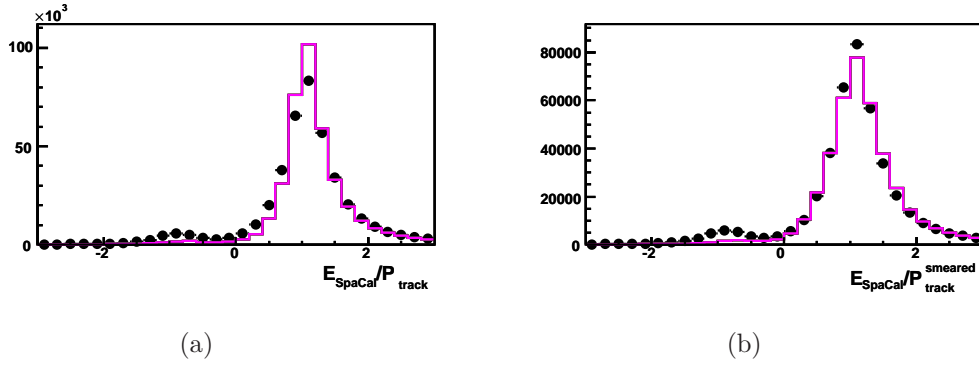


Figure 6.19: Distribution of  $Q \frac{E'_e}{p}$  in the final selection of events from the low energy data. The black points are data, the magenta line is the Monte Carlo simulation before (a) and after (b) the momentum smearing correction.

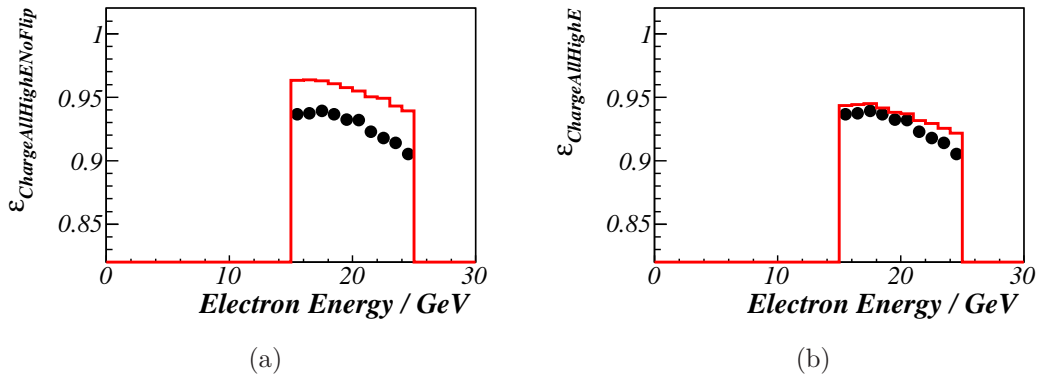


Figure 6.20: Asymmetry of the selected events  $\frac{N^+ - N^-}{N^+ + N^-}$  in low energy data sample. Data (black points) as described by Monte Carlo (red line) after the momentum smearing correction (a), and after both the momentum smearing as well as the charge flip corrections (b).

the asymmetry on  $E'_e$  and  $r_{SPACAL}$  in data and Monte Carlo where the **momentum smearing correction** is applied. The plots suggest that an additional correction to the Monte Carlo is needed. The charge reconstruction efficiency can also be modified by artificially changing the amount of positive and negative charge events, regardless what the track curvature implies. Based on Fig. 6.20(a), an additional **charge flip correction** is introduced. The correction flips the reconstructed charge with the probability of 1%.

The asymmetry of events after the **momentum smearing correction** and the additional **charge flip correction** is displayed in Fig. 6.20(b). The 1% overall charge flip correction describes the low  $E'_e$  region well<sup>7</sup>. The remaining discrepancy at high  $E'_e$  proves that a simple overall correction is not sufficient to describe the whole  $E'_e$  range. However, the charge measurement in the analysis is required only at high  $y$

<sup>7</sup>The description at lower energies was checked in an independent study.

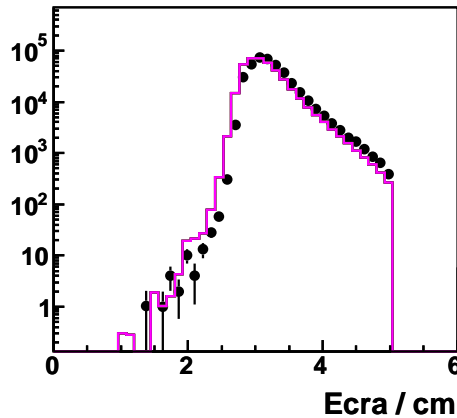


Figure 6.21:  $r_{log}$  distribution in the low energy data (points) and Monte Carlo (magenta line). The quantity is not well described by the simulation.

(low  $E'_e$ ). The performance of the correction at low  $E'_e$  was checked in an independent study using radiative events. The  $\frac{E'_e}{p}$  distribution after both corrections is shown in Fig. 6.4.

The momentum smearing correction is evaluated separately for the low energy, medium energy and high energy data analyses. The 1% charge flip correction holds for all three analyses.

#### 6.4.5 Efficiency of the $r_{log}$ Cut

Fig. 6.21 shows the quality of description of the  $r_{log}$  variable. The peak position in data and Monte Carlo is different and also the tail, where the cut on  $r_{log} < 5$  cm is applied, is not well described. Therefore, it is necessary to check of the efficiency of the  $r_{log}$  cut used in the analysis.

The efficiency of the  $r_{log}$  cut is monitored together with the cut on  $\frac{E_{had}}{E_{tot}} < 0.15$ . These two cuts are removed in the monitoring sample. Since the DJANGO Monte Carlo does not contain photoproduction background events it is important to remove this background from data. This is achieved by the wrong charge background subtraction. It is important to mention that the charge asymmetry changes with the  $r_{log}$  cut which makes the monitoring more complicated. The asymmetry for the corresponding  $r_{log}$  and  $\frac{E_{had}}{E_{tot}}$  cuts is checked using tagged events.

The efficiency correction is up to 5% at high  $y$  and it is given in Table 6.15.

#### 6.4.6 Hadronic Final State Calibration

The  $F_L$  and  $F_L^D$  analyses use the **iterative calibration method** for the calibration of hadronic final state particles. The method is described in detail in Part A. The introduction to hadronic final state calibrations, the explanation of how the **iterative calibration method** works and how the calibration constants are derived together with the problems encountered during the extraction of the constants can be found

$y$ range	correction
$y > 0.8$	$0.95 \pm 0.03$
$0.7 < y < 0.8$	$0.965 \pm 0.015$
$0.6 < y < 0.7$	$0.989 \pm 0.005$

Table 6.15:  $r_{log}$  efficiency correction.

there. In this section, only the performance of the calibration in the  $F_L$  analysis is discussed.

The **iterative calibration method** is designed as a low  $p_T$  calibration suitable for hadronic final states with total transverse momenta below 10 GeV. This  $p_T$  range is compatible with the analysis described here. Inclusive final states were used to derive the calibration constants for this method which makes it in particular suitable for inclusive measurements.

There are 20 calibration constants used in the **iterative calibration method**. They correspond to 10 slices in the polar angle  $\theta$  that roughly correspond to the calorimeter wheels<sup>8</sup>. Each wheel  $i$  has a separate calibration constant for its electromagnetic and hadronic part denoted as  $\alpha_{em}^i$  and  $\alpha_{had}^i$ , respectively. Tracks are excluded from the calibration. Therefore, the hadronic final state particles that take the energy measurement from the tracker and not from the calorimeter are not calibrated. Momentum of every other hadronic final state particle detected within the  $\theta$  range corresponding to the calorimeter wheel  $i$  is scaled by a factor of  $(1 + \alpha_{em}^i)$  or  $(1 + \alpha_{had}^i)$ , depending on whether its cluster comes from an electromagnetic or hadronic part of the calorimeter. The calibration constants for the **iterative calibration method** are derived separately for all data taking periods, every time independently for data and three Monte Carlo models. The  $F_L$  analysis uses the constants derived for 06/07  $e^+$  period for data and DJANGO(CDM) model. The same constants are used for all high energy, low energy and medium energy data taking periods. There are no separate calibration constants available for the runs with reduced proton beam energy.

There is one important issue of the **iterative calibration method** that has to be stressed here. The method does not deliver a calibration constant for the hadronic SPACAL  $\alpha_{SPACAL}^{had}$ . The hadronic SPACAL has only one radiation length and therefore it is extremely hard to calibrate. However, the hadronic SPACAL calibration constant can be tuned directly in the analysis.

### Calibration of the Hadronic SPACAL

In order to tune the hadronic SPACAL calibration constant  $\alpha_{SPACAL}^{had}$ , it is useful to look at events where the hadronic final state goes in the backward ( $-z$ ) direction. The prescription for hadronic method of kinematics reconstruction (see Eq. 6.28) tells that the inelasticity  $y_h$  is proportional to  $E - p_z$  of the hadronic final state. This implies

---

<sup>8</sup>There are 8 separate wheels in the LAr calorimeter (see Fig 4.5). Another  $\theta$  range corresponds to the SPACAL calorimeter. One additional wheel is considered in the forward part of the LAr calorimeter.

Run period	$1 + (\alpha_{SPACAL}^{had})_{data}$	$1 + (\alpha_{SPACAL}^{had})_{MC}$
07 $e^+$ $E_p = 920$ GeV	1.25	1.55
$E_p = 460$ GeV	1.25	1.55
$E_p = 575$ GeV	1.25	1.55

Table 6.16: Calibration of the hadronic SPACAL.

that events with hadronic final state going in the backward direction have high values of inelasticity. Therefore, the high  $y$  events are in particular important for setting  $\alpha_{SPACAL}^{had}$ , and  $E - p_z$  is going to be used for its determination.

As already mentioned in Section 6.4.1, the sub-triggers ST3 and ST8 contain hadronic SPACAL trigger elements that are sources of the trigger inefficiency. Therefore, it is desirable not to use these sub-triggers in the studies described here. Only the sub-trigger ST0 is required in the data samples. The samples are selected with the **analysis selection** where the cut on  $E - p_z$  is removed in order to see the lower tails of the  $E - p_z$  distributions as well.

First, the  $E - p_z$  distribution is studied in the sample where all the calibration constants are applied except for  $\alpha_{SPACAL}^{had}$  which is set to 0. The top row of plots in Fig. 6.22 shows such distributions in the low energy data and Monte Carlo. The left plot displays  $E - p_z$  in the whole  $y$  range and there is no significant disagreement between data and Monte Carlo visible there. On the contrary, the right plot shows the  $E - p_z$  distribution only at  $y > 0.38$  which is a region more sensitive to the hadronic SPACAL. This plot is used to determine the value of  $\alpha_{SPACAL}^{had}$ . The momentum conservation law implies that the correct  $E - p_z$  value is 55 GeV. Therefore,  $(\alpha_{SPACAL}^{had})_{data}$  and  $(\alpha_{SPACAL}^{had})_{MC}$  are set such that the mean of the  $E - p_z$  peak in the plot is shifted to 55 GeV. The derived calibration factors are  $(\alpha_{SPACAL}^{had})_{data} = 0.25$  and  $(\alpha_{SPACAL}^{had})_{MC} = 0.55$  and hold for all three data taking periods. The bottom row of the plots in Fig. 6.22 show the  $E - p_z$  distributions after the final calibration.

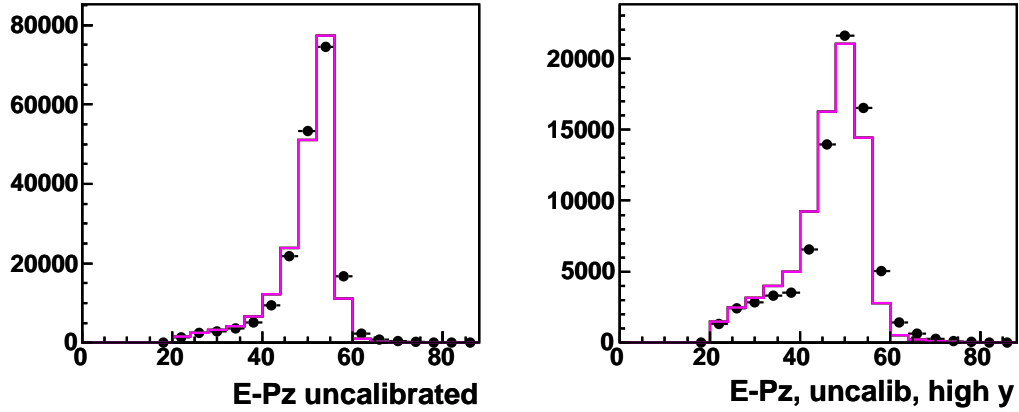
## Performance of the Calibration

The **iterative calibration method** makes use of the transverse momentum balance  $p_T^{bal}$  in order to derive the calibration constants. The balance is defined as

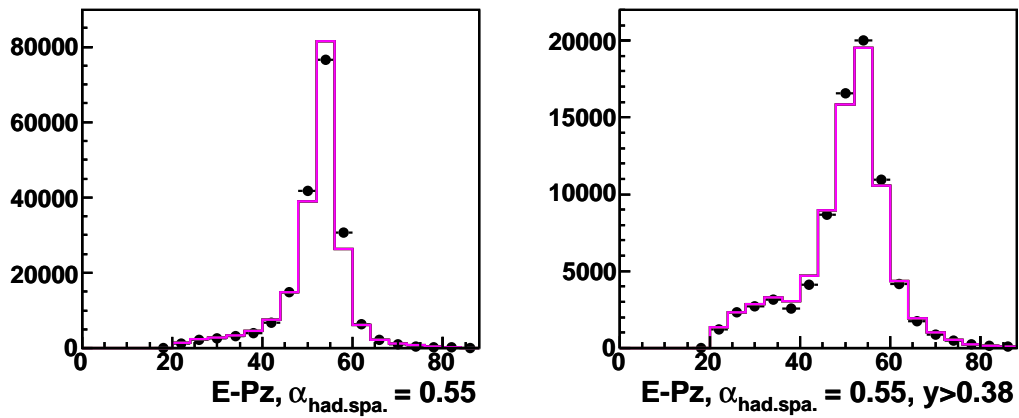
$$p_T^{bal} = \frac{p_T^{HFS}}{p_T^e} \quad (6.48)$$

where  $p_T^{HFS}$  is the transverse component of the total momentum of the hadronic final state and  $p_T^e$  denotes the transverse momentum of the scattered lepton. The balance  $p_T^{bal}$  can be used to check the performance of hadronic calibration methods in general. The aim of the hadronic calibrations in first place is an agreement of the transverse momentum balance between data and Monte Carlo, the so-called hadronic energy scale. The agreement of  $p_T^{bal}$  is usually evaluated as a double-ratio

$$DR(p_T^{bal}) = \frac{\langle p_T^{bal} \rangle_{data}}{\langle p_T^{bal} \rangle_{MC}}, \quad (6.49)$$



(a)  $E - p_z$  after the iterative calibration without any calibration of hadronic SPACAL. The quality of the description at high  $y$  (right) is used to determine the hadronic SPACAL calibration factor  $\alpha_{SPACAL}^{had}$ .



(b)  $E - p_z$  after the iterative calibration with tuned hadronic SPACAL calibration factor. The  $E - p_z$  peak is at 55 GeV and it is well described by the simulation.

Figure 6.22: The  $E - p_z$  distribution in the low energy data (points) and Monte Carlo (magenta line) for all events in the analysis sample (left) and  $y > 0.38$  (right). At high  $y$ , the hadronic final state is expected to occupy the SPACAL calorimeter.

that is the ratio of the mean values of the  $p_T^{bal}$  distributions in data and Monte Carlo. The mean values are obtained in Gaussian fits. The **iterative calibration method** claims to reach an agreement between data and Monte Carlo better than 2%. The calibration is also expected to bring the  $p_T^{bal}$  in data and Monte Carlo closer to unity, i.e. improve the absolute calibration. A good calibration should also conserve the width of the  $p_T^{bal}$  peak, or even better, it can make the  $p_T^{bal}$  peak more narrow. To check this, the width  $\sigma$  of the  $p_T^{bal}$  peak scaled by its mean position  $\mu$  can be compared before and after the calibration. A good calibration should not increase the quantity  $\frac{\sigma}{\mu}$ .

The performance of the calibration is checked in the following way. The  $p_T$  balance is studied as a function of the transverse momentum of the scattered lepton  $p_T^e$ ,  $Q_e^2$ , the polar angle of the hadronic final state  $\theta_h^e$  and the inelasticity  $y_e$ . All these quantities are calculated from the information of the scattered positron only, and thus are independent of the hadronic final state. The angle  $\theta_h^e$  reconstructed by the electron method is defined as

$$\tan \theta_h^e = \frac{2E_e - E'_e + p_z^e}{p_T^e}. \quad (6.50)$$

As quoted above, the double ratio  $DR(p_T^{bal})$  should lie within 2% around unity.

Fig. 6.23 compares the absolute and the relative calibration between data and Monte Carlo for the low energy data taking period. The first row of the plots show the  $p_T^{bal}$  in data and Monte Carlo, the second row compares  $\frac{\sigma}{\mu}$  of the  $p_T^{bal}$  peaks in data and Monte Carlo. The third row shows the double ratio  $DR(p_T^{bal})$ , where the fit error on  $\mu$  of the corresponding peak in the numerator and denominator is used in order to calculate the error of the ratio. The different columns show these quantities studied as a function of  $p_T^e$ ,  $Q_e^2$ ,  $\theta_h^e$  and  $y_e$ . All these plots prove a good consistency between data and Monte Carlo. The double ratios agree within 2% which corresponds to the expected performance of the **iterative calibration method**.

Figures 6.24, 6.25, 6.26 and 6.27 show the Gaussian fits to the  $p_T^{bal}$  peaks in bins of  $p_T^e$ ,  $Q_e^2$ ,  $\theta_h^e$  and  $y_e$ , respectively. The parameters of these fits are used in the previous Fig. 6.23. However, not all bins are considered there. The first two  $p_T^e$  bins do not reveal the mean position of the distribution properly (see Fig. 6.24) and therefore are excluded from the comparison in Fig. 6.23. The same holds for the lowest  $Q_e^2$  bin and the highest non-empty  $y_e$  bin (see Fig. 6.25 and 6.27). The lowest non-empty bin in  $\theta_h^e$  is removed on grounds of low statistics.

So far, the calibration performance was described in terms of the transverse component of the 4-momentum. The performance can also be independently checked with  $\Sigma = (E - p_z)_h$  which uses the remaining two components of the 4-momentum,  $E$  and  $p_z$ . The variable  $\Sigma$  is directly related to the inelasticity  $y_h$  calculated from the hadron reconstruction method (see Eq. 6.28). In order to check the performance of the calibration,  $y_h$  should be compared to the inelasticity  $y$  reconstructed in an independent way from the hadronic final state. The electron reconstruction gives a completely independent inelasticity (see Eq. 6.27). However, the electron method has a poor resolution at low  $y$  where the dominant portion of statistics is. The inelasticity reconstructed using the double-angle method  $y_{da}$  (see Eq. 6.30) has a good resolution even at low  $y$  and therefore is used to balance the  $y_h$ .  $y_{da}$  is not completely independent of the hadronic final state but it relies on the independent information from the scattered electron as

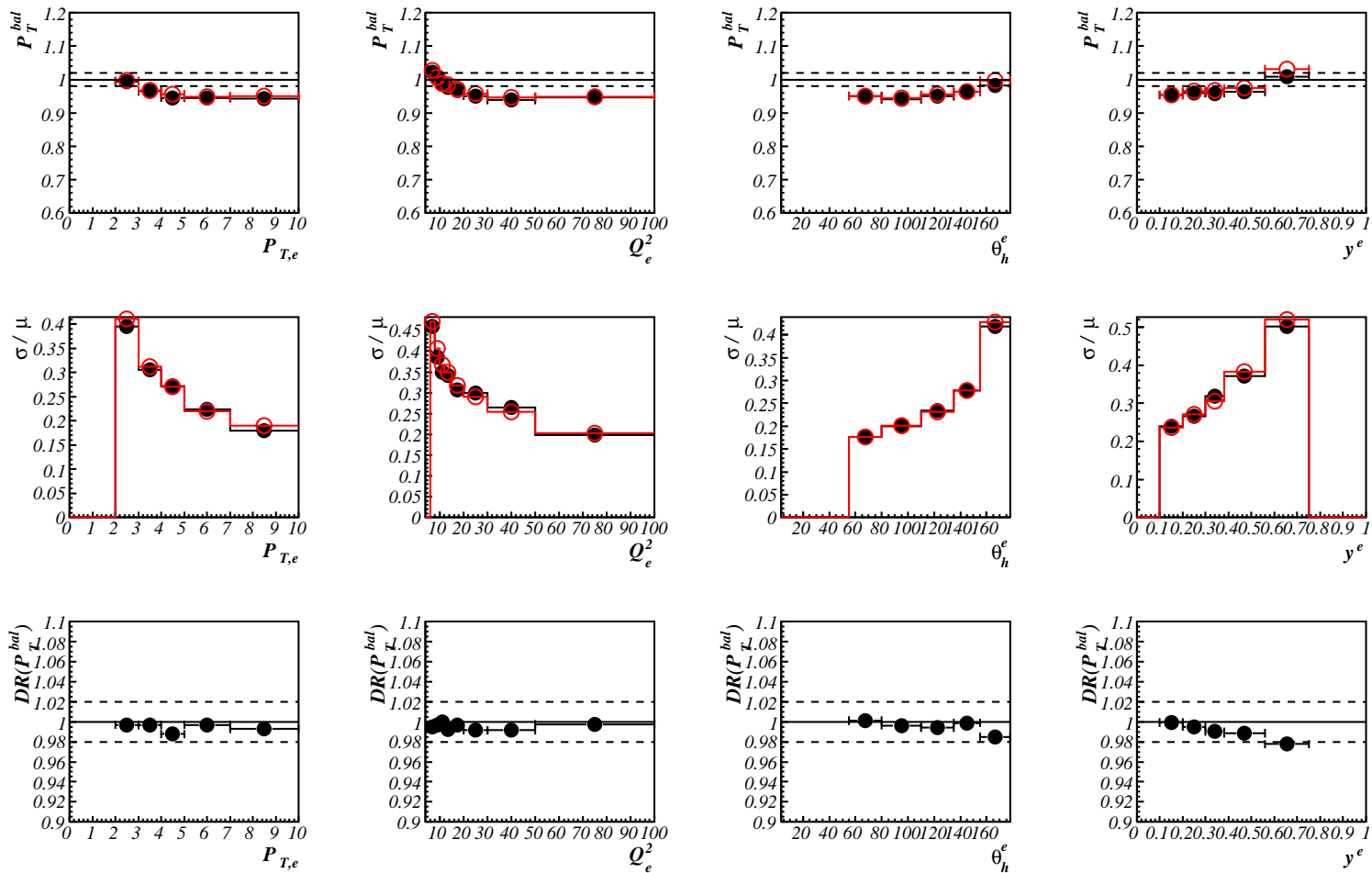


Figure 6.23:  $p_T^{bal}$  (top row) and  $\frac{\sigma}{\mu}$  (middle row) in data (black) and Monte Carlo (red) together with  $DR(p_T^{bal})$  after the iterative calibration shown in bins of  $p_{T,e}^e$ ,  $Q_e^2$ ,  $\theta_h^e$  and  $y_e^e$ . The low energy data are shown. The calibration successfully pushes the hadronic energy scale uncertainty down to 2%.

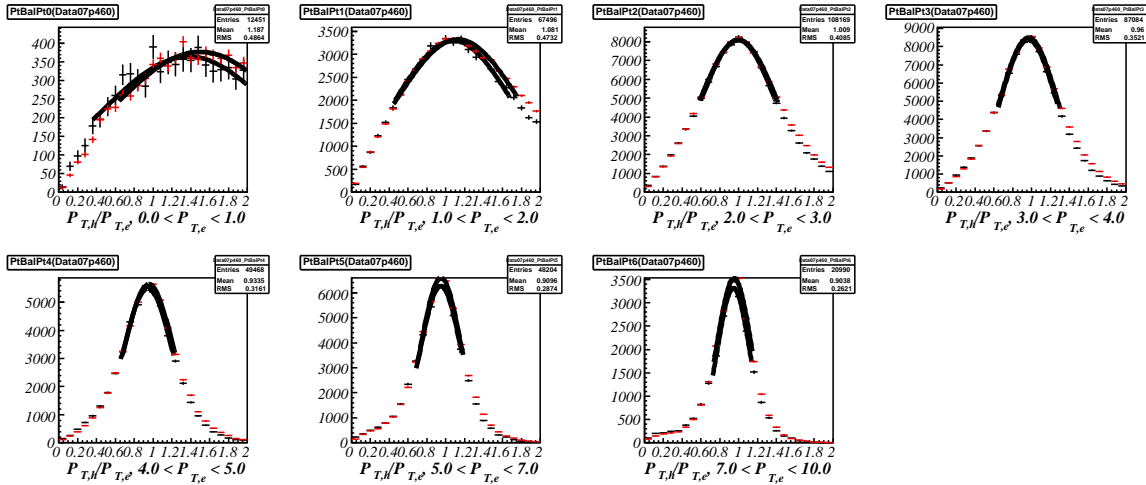


Figure 6.24: Fits to the  $p_T^{bal}$  in data (black) and Monte Carlo (red) in bins of  $p_T^e$ . In the lowest two  $p_T^e$  bins, the fits do not reproduce the peak position properly because of the large tails at higher values.

well. Analogously to the  $p_T^{bal}$  and  $DR(p_T^{bal})$  variables, a  $y$ -balance

$$y^{bal} = \frac{y_h}{y_{da}} \quad (6.51)$$

and its double ratio

$$DR(y^{bal}) = \frac{\langle y^{bal} \rangle_{data}}{\langle y^{bal} \rangle_{MC}} \quad (6.52)$$

are introduced.

Fig. 6.28 shows  $y^{bal}$  in bins of  $p_T^e$ ,  $Q_e^2$ ,  $\theta_h^e$  and  $y_e$  after the calibration. Again, the agreement between data and Monte Carlo is within 2%.

## 6.5 Description of Data

Fig. 6.29, 6.30 and 6.31 show the control plots for the high energy, low energy and medium energy data, respectively. The distributions of  $y_e$ ,  $Q^2$ ,  $E - p_z$ ,  $r_{SPACAL}$  and  $z_{vtx}$  are shown in the figures. In all cases data (points) are well described by the sum of the simulation (magenta line) and the background determined from data (green area).

In the low and medium energy data, the background at  $y > y_{trans}$  is determined using the wrong charged events. Data at  $y > y_{trans}$  in the plots are only the events with positive reconstructed charge of the scattered positron  $N^+$ . The green histogram in this  $y$  region corresponds to the events with negative reconstructed charge of the scattered positron candidate. These events are corrected for the background charge

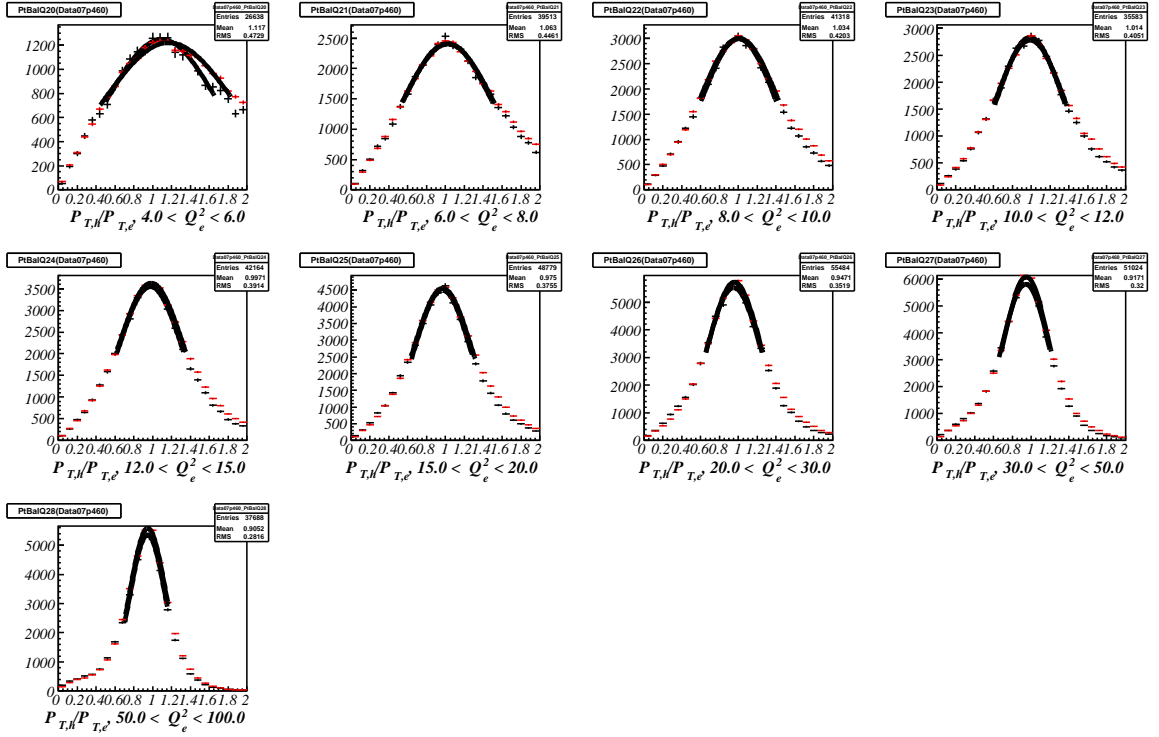


Figure 6.25: Fits to the  $p_T^{bal}$  in data (black) and Monte Carlo (red) in bins of  $Q^2$ . In the lowest  $Q^2$  bin, the fits do not reproduce the peak position properly because of the large tails at higher values.

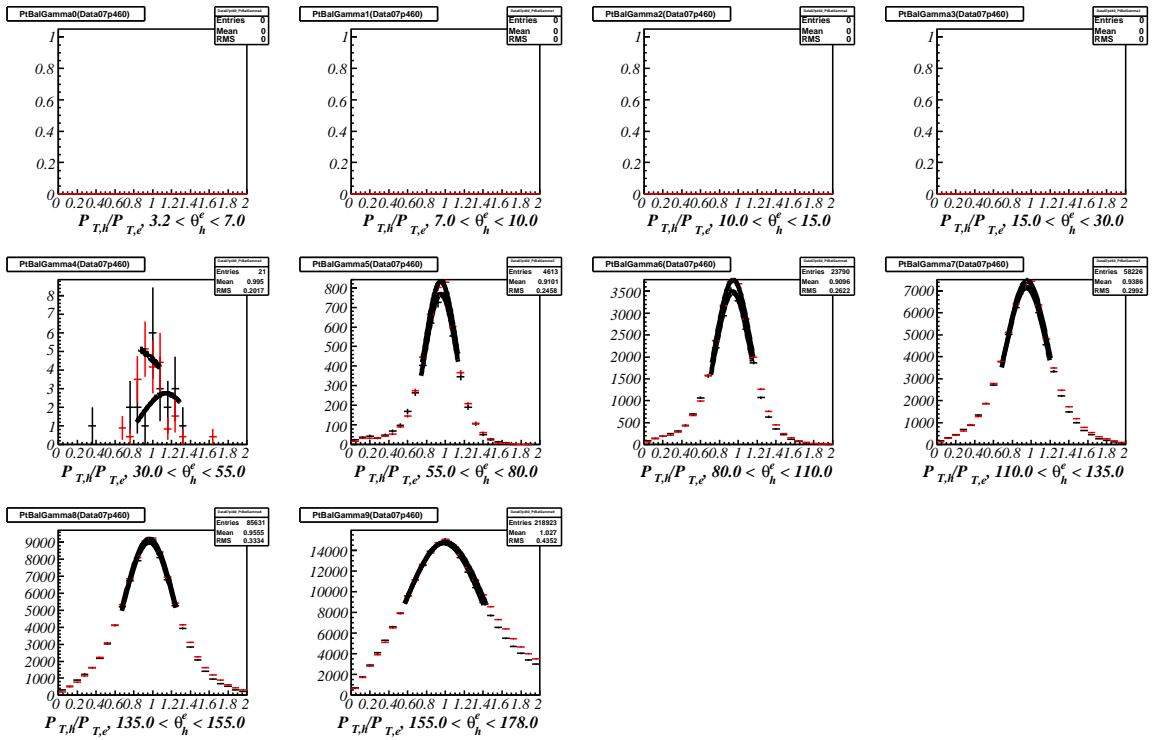


Figure 6.26: Fits to the  $p_T^{bal}$  in data (black) and Monte Carlo (red) in bins of  $\theta_h^e$ .

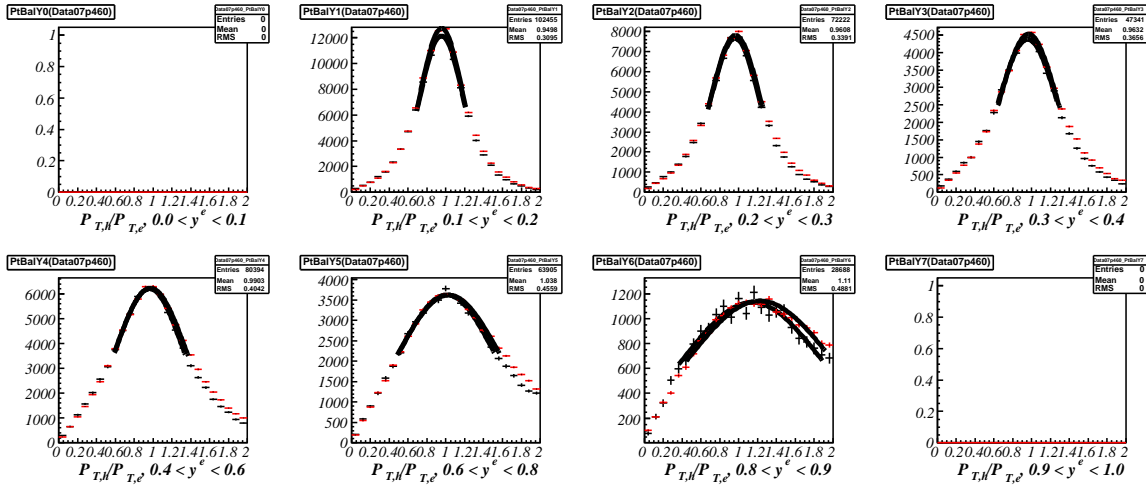


Figure 6.27: Fits to the  $p_T^{bal}$  in data (black) and Monte Carlo (red) in bins of  $y_e$ . In the highest non-empty  $y_e$  bin, the fits do not reproduce the peak position properly because of the large tails at higher values.

asymmetry as described in Section 6.3.8. The plotted background events therefore correspond to  $asymN^-$ .

The remaining  $y$  region,  $y < y_{trans}$ , display events regardless of the charge measurement. The background events here are determined from the tagged events.

The high energy data show the tagged background in the whole  $y$  range.

The DJANGO simulation based on the H1 2009 PDF set with  $R = 0.25$  gives very good description of data.

## 6.6 Extraction of the Reduced Cross Section

The reduced cross section in this  $F_L$  analysis is measured in bins of  $Q^2$  and  $y$ , and it is related to the double differential cross section in the following way

$$\sigma_r = \frac{d\sigma}{dx dQ^2} \cdot \frac{Q^4 x}{2\pi\alpha^2 Y_+}. \quad (6.53)$$

The following paragraphs give detailed description of how the differential cross section is extracted from the data.

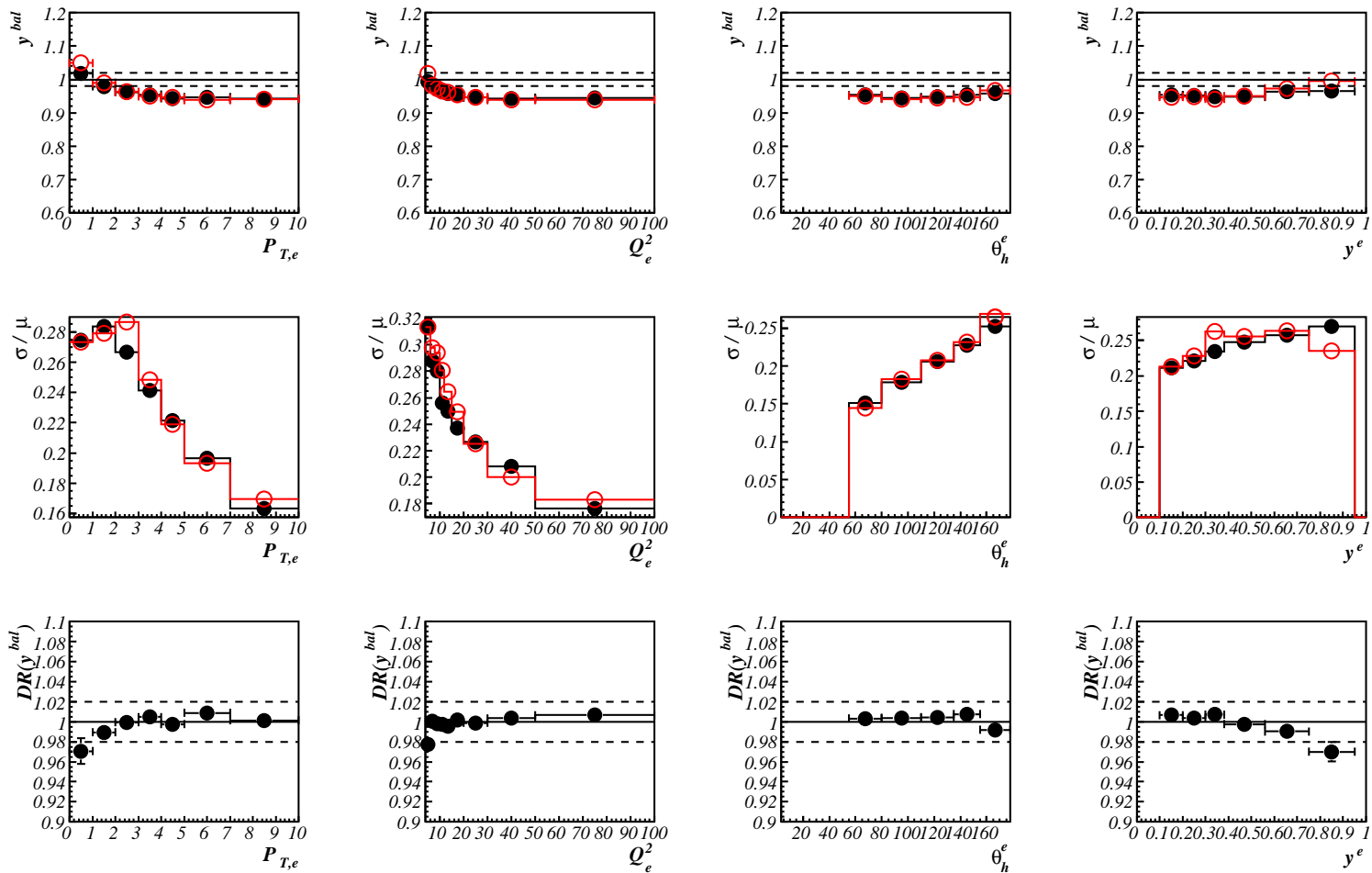


Figure 6.28:  $y^{bal}$  (top row) and  $\frac{\sigma}{\mu}$  (middle row) in data (black) and Monte Carlo (red) together with  $DR(y^{bal})$  after the iterative calibration shown in bins of  $p_{T,e}^e$ ,  $Q_e^2$ ,  $\theta_h^e$  and  $y_e$ . The low energy data are shown. The  $y^{bal}$  agrees within 2%.

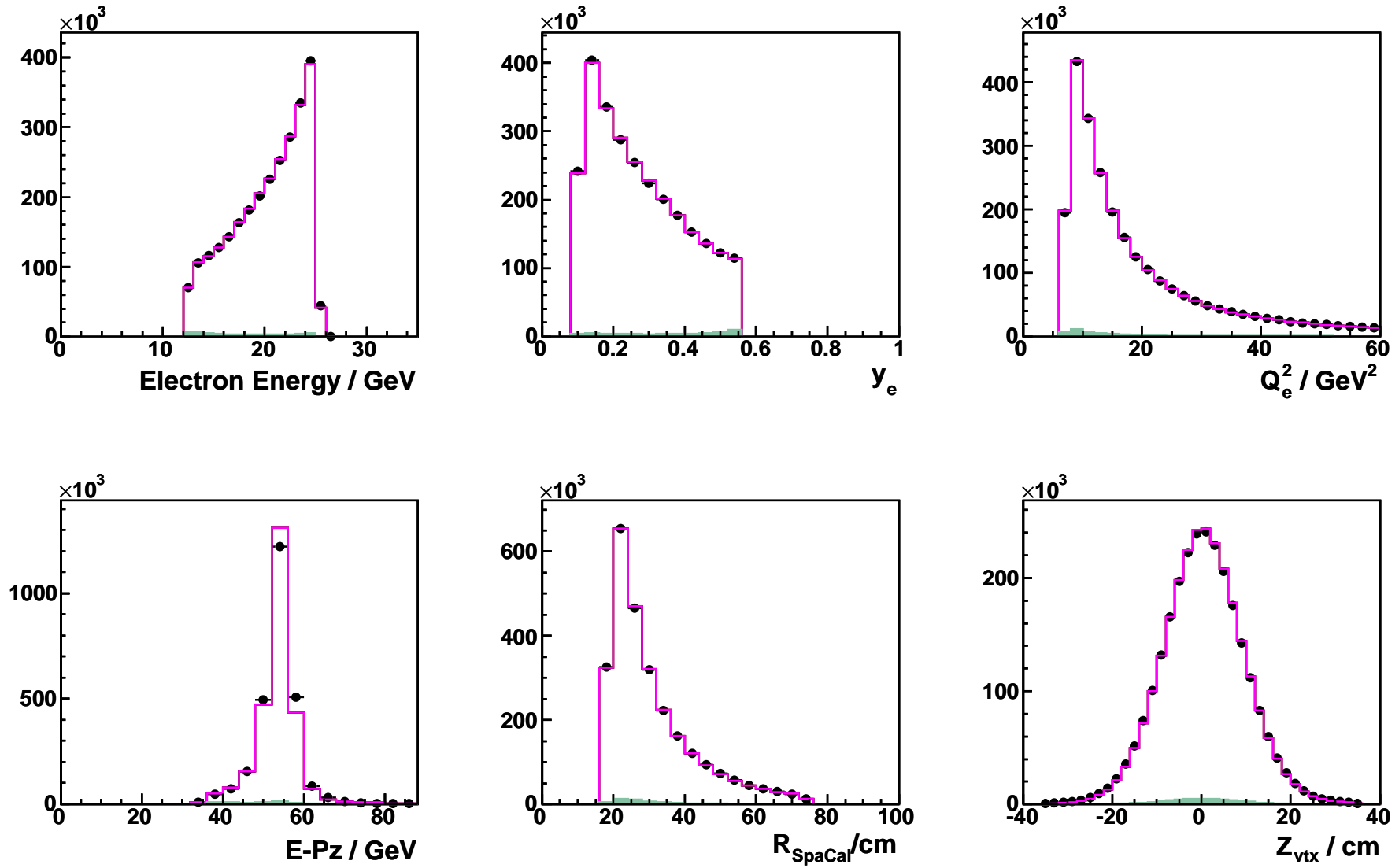


Figure 6.29: Description of the positron energy,  $y_e$ ,  $Q^2$ ,  $E - p_z$ ,  $r_{\text{SPACAL}}$  and  $z_{\text{vtx}}$  in the high energy data sample. Data (points) are well described by the sum of the signal Monte Carlo (magenta line) and background (green area) which is determined from data.

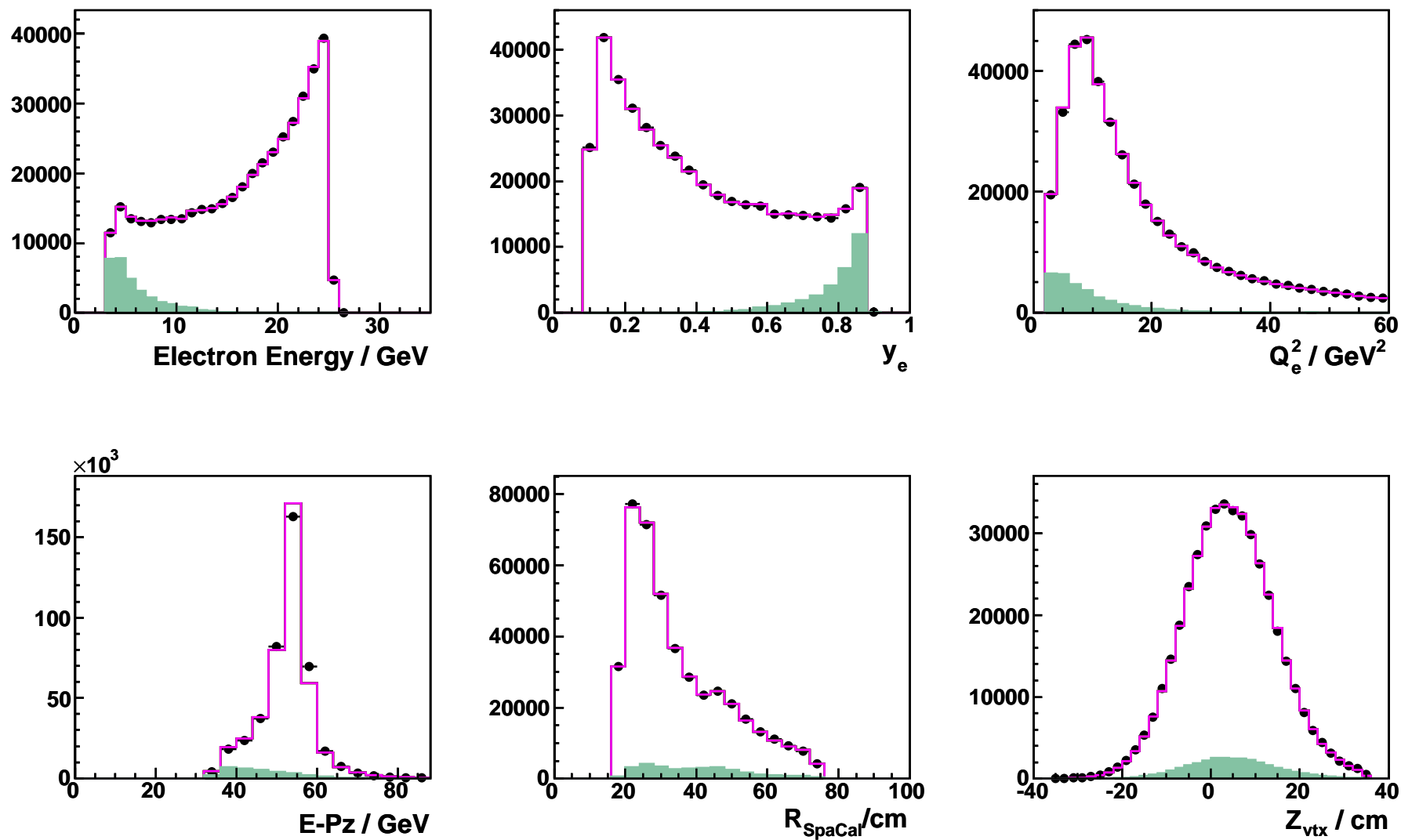


Figure 6.30: Description of the positron energy,  $y_e$ ,  $Q^2$ ,  $E - p_z$ ,  $r_{\text{SPACAL}}$  and  $z_{\text{vtx}}$  in the low energy data sample. Data (points) are well described by the sum of the signal Monte Carlo (magenta line) and background (green area) which is determined from data.

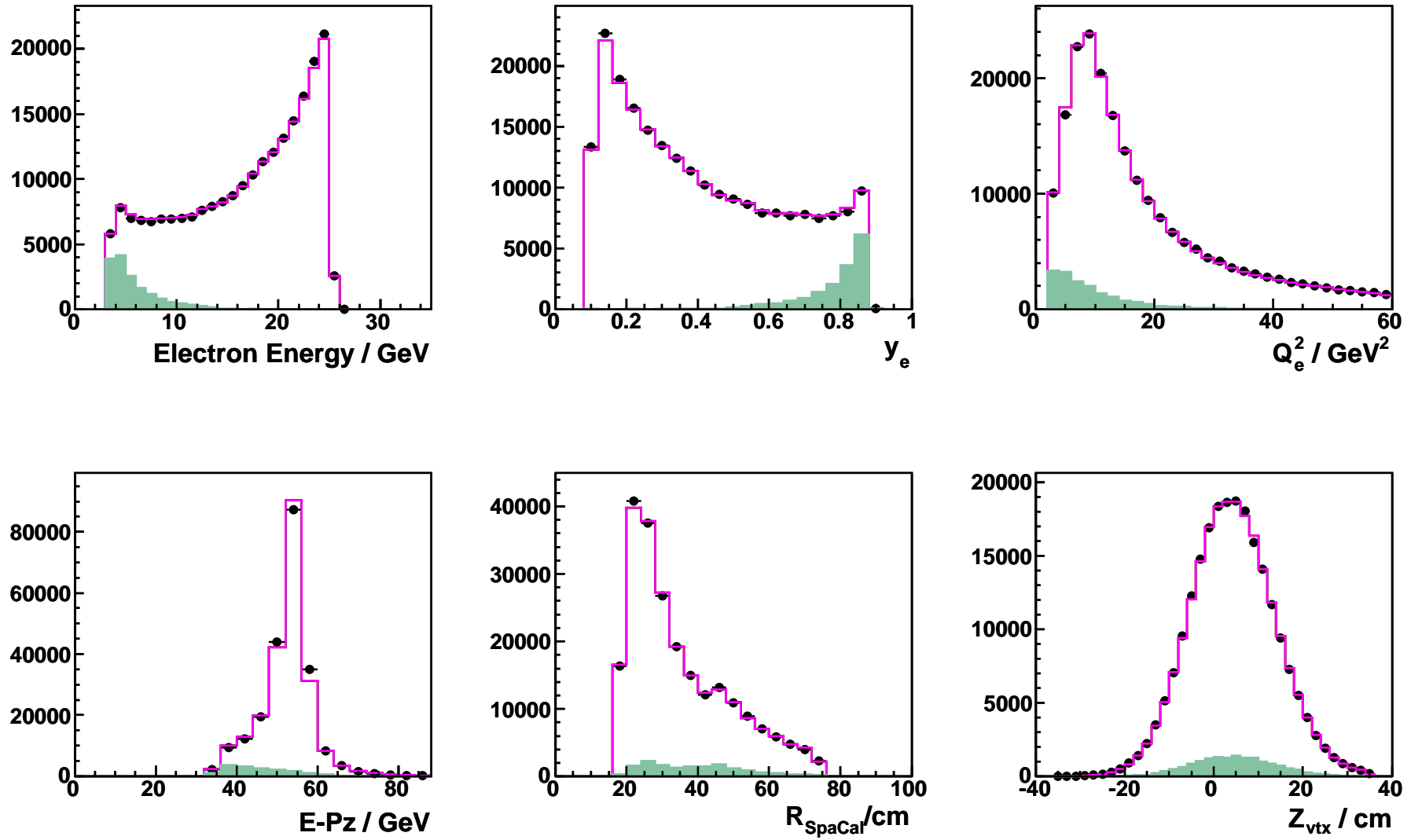


Figure 6.31: Description of the positron energy,  $y_e$ ,  $Q^2$ ,  $E - p_z$ ,  $r_{\text{SPaCal}}$  and  $z_{\text{vtx}}$  in the middle energy data sample. Data (points) are well described by the sum of the signal Monte Carlo (magenta line) and background (green area) which is determined from data.

### 6.6.1 Cross-Section Definition

The differential cross section is standardly defined by the following equation

$$\frac{d\sigma^{data}}{dx dQ^2} = \frac{N^{data} - N_{bg}}{A \cdot L \cdot B} \cdot \frac{\sigma_{gen}^{nrad}}{\sigma_{gen}^{rad}} \quad (6.54)$$

where  $B$  is the bin centre correction,  $A$  is the smeared acceptance and  $L$  is the luminosity. In order to measure the cross section, one first has to make sure that the analysed data sample is properly described by Monte Carlo. Monte Carlo not only reflects our knowledge of the studied process, but it also accounts for hadronisation, detector effects and initial and final state radiation. In order to measure the cross section of the process only, all these effects have to be taken out.

The acceptance correction  $A$  corrects from the cross section measured at the reconstructed level in the radiative Monte Carlo (with the initial and final state radiation turned on) to the cross section at the generator level.

$$A = \frac{N_{rec}^{rad}}{N_{gen}^{rad}} \quad (6.55)$$

The bin centre correction  $B$  accounts for the difference between the actual cross section at the chosen central values of  $Q^2$  and  $x$  with respect to the average cross section in the phase space of the bin.

$$B = \frac{\sigma_{gen}^{nrad}}{\frac{d\sigma_{gen}^{nrad}}{dx dQ^2}} \quad (6.56)$$

where non-radiative Monte Carlo (with the initial and final state radiation turned off) is used in the calculation.

The difference between the cross section in the radiative and non-radiative Monte Carlo is accounted for in the radiative correction which corresponds to the last term in Eq. 6.54.

Inserting the definitions of the acceptance correction and bin centre corrections into Eq. 6.54 leads to

$$\frac{d\sigma^{data}}{dx dQ^2} = \frac{(N^{data} - N_{bg}) \cdot N_{gen}^{rad}}{N_{rec}^{rad} \cdot L \cdot \sigma_{gen}^{nrad}} \cdot \frac{d\sigma_{gen}^{nrad}}{dx dQ^2} \cdot \frac{\sigma_{gen}^{nrad}}{\sigma_{gen}^{rad}} \quad (6.57)$$

which can be simplified by using  $N = \sigma L$  to

$$\frac{d\sigma^{data}}{dx dQ^2} = \frac{(N^{data} - N_{bg})}{N_{rec}^{rad}} \cdot \frac{d\sigma_{gen}^{nrad}}{dx dQ^2} \quad (6.58)$$

Therefore the cross section measurement requires just the number of events in a given bin in data and at the reconstructed level of the radiative Monte Carlo (used to describe the data set). The last term in Eq. 6.58 corresponds to the differential cross section at the generator level in the non-radiative Monte Carlo. It is actually an analytical cross section of the studied process that has been plugged into the Monte Carlo.

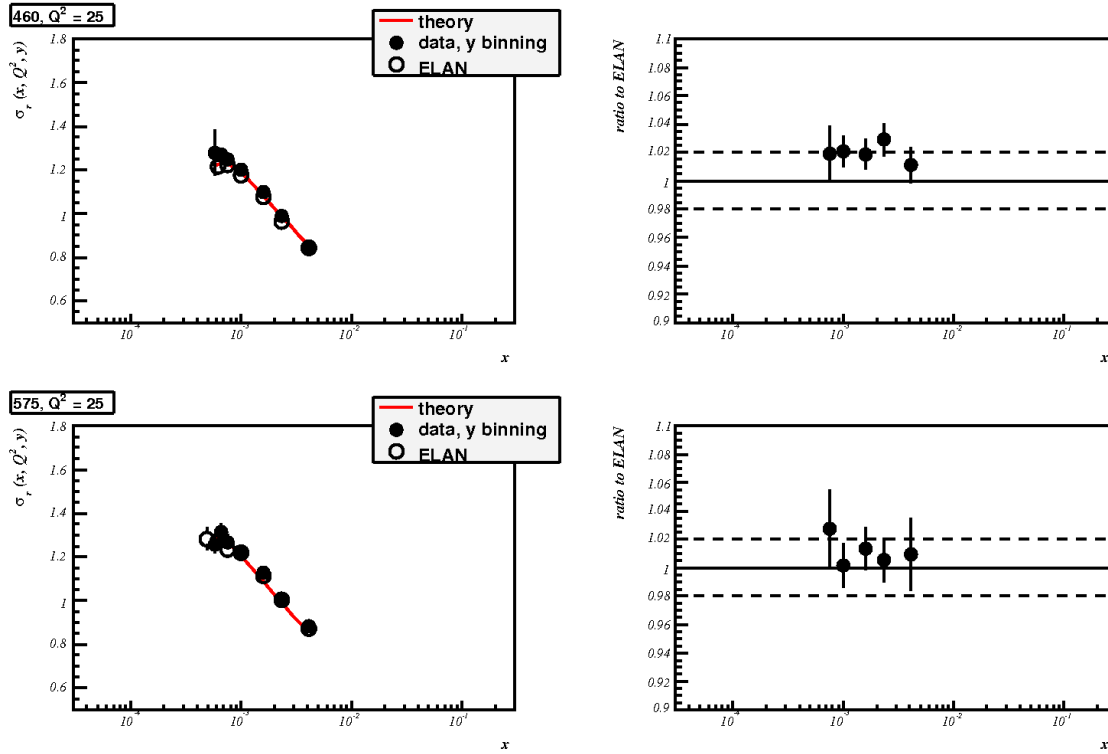


Figure 6.32: Reduced cross sections from low (top) and medium (bottom) energy data at  $24 < Q^2 < 32$  GeV<sup>2</sup>. Data from this analysis (black points) are compared to the results from the official H1 measurement (open points) and the prediction from H1 2009 PDF (red line). The ratio plots (right) show the agreement between the results from the two analyses.

## 6.6.2 Cross Section

At the level of control plots, the data are well described by the DJANGO simulation based on the H1 2009 PDF set with  $R = 0.25$ . Therefore, the same quality is expected in the cross section description, since the cross section extraction method simplifies just to comparing number of reconstructed events (see Eq. 6.58).

In order to demonstrate the agreement of this analysis with the official H1 measurement, the cross section for one bin in  $Q^2$  is shown in Fig. 6.32. Only the low and medium energy data are compared since the high energy data sets are not the same in the two analyses. The cross sections from these two independent measurements agree well with each other.

## 6.7 Summary of the $F_L$ Analysis

The  $F_L$  analysis presented here follows the measurement strategy of the official H1  $F_L$  analysis. The cross sections and  $F_L$  results are not shown here as the aim of this work is the  $F_L^D$  measurement. However, the results of the two analyses are in a very good agreement and the level of understanding data has been shown in Section 6.5 in the control plots. As the analysis is robust and consistent with the official H1 measurement (see the cross section comparison in Section 6.6.2), it can be used as a solid basis for the

diffractive measurement. The data sample is further restricted by a diffractive selection and the diffractive proton structure functions can be measured. The description of the diffractive part of the analysis is described in the following chapter.



# Chapter 7

## Longitudinal Proton Structure Function in Diffraction

### 7.1 Data

The diffractive  $F_L^D$  analysis utilises the same data sets as the inclusive  $F_L$  analysis. The final analysis data are selected in such a way that they are a sub-sample of the data used for the  $F_L$  measurement.

Since the diffractive events form only  $\sim 10\%$  of all DIS processes, more data at  $E_p = 920$  GeV are used in the  $F_L^D$  analysis than in the  $F_L$  analysis in order to increase the statistical precision of the measurement. The high energy data sample consists of two run periods here: 2006  $e^+$  and 2007  $e^+$  data.

The high energy data sets are analysed only at  $Q^2 > 7$  GeV<sup>2</sup> because of the trigger efficiency. The low and medium energy data do not have such limitation and can be analysed down to  $Q^2 = 2.5$  GeV<sup>2</sup>. However, the low and medium energy data by themselves are not sufficient to measure  $F_L^D$  at  $2.5 < Q^2 < 7$  GeV because of low statistics. Therefore, the published cross sections from the HERA-I data analysis at  $E_p = 820$  GeV are used as well to make the  $F_L^D$  measurement at low  $Q^2$  possible.

### 7.2 Monte Carlo

The  $F_L^D$  analysis involves several Monte Carlo models for the event simulation.

#### 7.2.1 Simulation of Signal Processes

The signal diffractive events are generated using the RAPGAP [77] generator. It returns the events in three samples. The first one corresponds to the Pomeron exchange with light quarks  $u$ ,  $d$ ,  $s$ , the second one gives the Pomeron exchange with the  $c$  quark and the third one generates the Reggeon exchange.

The RAPGAP generator is based on the H1 2006 DPDF Fit B and uses only the structure function  $F_2^D$  as the input reduced cross section, i.e. there is no  $F_L^D$  in this Monte Carlo. Therefore, the Monte Carlo cannot be expected to describe data at high  $y$  where the longitudinal structure function contributes. This is a good approximation for all analyses that do not attempt to study high inelasticities  $y$ . However, the high

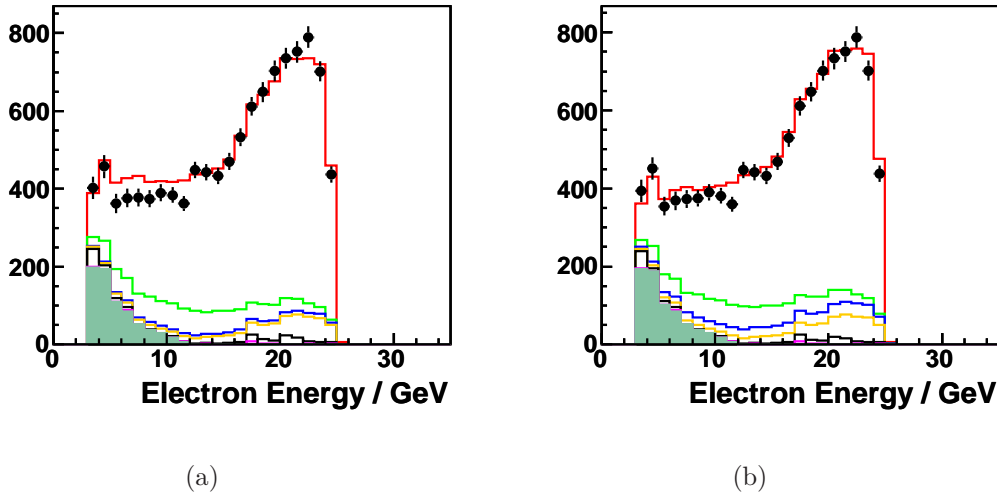


Figure 7.1: Description of the scattered positron energy in the low energy data (points) by the sum of the signal Monte Carlo and background contributions. RAPGAP contains only the  $F_2^D$  structure function and therefore does not describe the data well at high  $y$  (low  $E'_e$ ) where the reduced cross section is suppressed by  $F_L^D$  (a). The low  $E'_e$  region is described better when RAPGAP is reweighted to the full reduced cross section from H1 2006 DPDF Fit B (b). The Monte Carlo is normalised to the area (not to the luminosity).

$y$  region is in particular important for the  $F_L^D$  analysis, and it is desirable to use the best knowledge of the high  $y$  region that is available. Therefore, the following weight is applied to RAPGAP at generator level

$$w(\sigma_r^D) = \frac{\sigma_r^D(\text{Fit B})}{F_2^D(\text{Fit B})} \quad (7.1)$$

that changes the input  $F_2^D$  to  $\sigma_r^D$ . Fig. 7.1 illustrates the effect of the weight. It is clear that RAPGAP with  $F_2^D$  only overestimates the real cross section at high  $y$ .

RAPGAP attempts to describe the whole phase space of inclusive diffractive events. However, it is observed that the low  $M_X$  states are poorly simulated since the vector meson resonances are not well described by RAPGAP. Therefore, the RAPGAP Monte Carlo is used together with the DIFFVM [78] Monte Carlo that generates diffractive events for a particular vector meson resonance in the final state. There are four separate DIFFVM event samples used in the  $F_L^D$  analysis that correspond to the  $\rho$ ,  $J/\Psi$ ,  $\phi$  and  $\omega$  resonances.

All signal Monte Carlo samples are listed in Table 7.1.

## 7.2.2 Simulation of Background Processes

There are four major sources of background in the  $F_L^D$  analysis: photoproduction, QED-Compton events, lepton pair production and smearing of the non-diffractive events into the final selected diffractive sample.

Description	Monte Carlo Generator
Signal	
Pomeron exchange (light quarks)	RAPGAP
Pomeron exchange ( $c$ quark)	RAPGAP
Reggeon exchange	RAPGAP
$\rho$ meson	DIFFVM
$J/\Psi$ meson	DIFFVM
$\phi$ meson	DIFFVM
$\omega$ meson	DIFFVM
Background	
QED-Compton events	COMPTON
non-diffractive events	DJANGO

Table 7.1: Monte Carlo used in the  $F_L^D$  analysis.

The photoproduction events represent the dominant background contribution. However, they do not need to be simulated since a data driven procedure to remove this background from the analysis sample is used. It is described in detail in Sections 6.3.8 and 7.3.6.

The QED-Compton events  $ep \rightarrow ep\gamma$  do not belong to deep inelastic scattering sample. They form a background in both the  $F_L$  and  $F_L^D$  analyses. However, this background is negligible in the  $F_L$  analysis, and it is further reduced by the anti-Compton selection listed in Table 6.9. In the diffractive sample, the QED-Compton background cannot be neglected. Since there is no hadronic final state in these events, the background contributes only at the region of  $M_X \sim 0$  GeV. The events are simulated with the COMPTON [79] Monte Carlo model.

Another class of background events that occupy the lowest  $M_X$  region is the lepton pair production. These events can be generated with the dedicated LPAIR [80] Monte Carlo model. In the  $F_L^D$  analysis, the background coming from QED-Compton events and lepton pairs is modelled only by the COMPTON Monte Carlo where the normalisation of the Monte Carlo sample is modified so that the total background is described. This approach is sufficient because both types of background have less than three final state particles and contribute only at small  $M_X$  to the final analysis sample.

As shown in Fig. 2.6, there is no sharp border between diffractive and standard DIS events in the  $\eta_{max}$  plot.  $\eta_{max}$  is exactly the quantity used to select diffractive sample. Details on the selection are given in Section 7.3.1. Therefore, the background from non-diffractive events is expected at high values of  $\eta_{max}$ . The standard DIS events are generated using the DJANGO Monte Carlo. However, the DJANGO used in the  $F_L$  analysis also generates diffractive events. In the  $F_L^D$  analysis, the DJANGO generator is used only to provide a non-diffractive sample. In order to avoid double-counting

Monte Carlo	Allowed phase space
DJANGO	$x_{\mathcal{P}} > 0.15$ or $M_Y > 5.0 \text{ GeV}$
RAPGAP	$x_{\mathcal{P}} < 0.15$ or $M_Y \leq M_{\text{proton}}$

Table 7.2: Combination of the DJANGO and RAPGAP simulations.

RAPGAP and DJANGO are combined using the cuts listed in Table 7.2.

### 7.2.3 Simulation of Proton Dissociation

The RAPGAP Monte Carlo generates only events with elastic proton. However, there is also a class of diffractive events where the proton does not stay intact and dissociates into the final state  $Y$ , as indicated in Fig. 2.7. The difference between the diffractive cross section of events with elastic proton and a proton that dissociates is studied in Section 7.6.4. The DIFFVM Monte Carlo is used for these studies.

## 7.3 Selection of Diffractive DIS Events

Diffractive events in this analysis are selected on the basis of a large rapidity gap that separates two distinct final state systems: the proton system  $Y$  going in the direction of the proton beam, and the rest of the hadronic final state  $X$ . The rapidity gap is a result of the exchange of a colour singlet.

The large rapidity gap selection asks for a hadronic final state  $X$  contained in the main detector and looks for a rapidity gap that is reflected in absence of activity in the forward region, close to the proton beam pipe. Therefore, the forward parts of the H1 detector that are sensitive to the energy flow are involved in the diffractive event selection.

It is experimentally possible to measure the scattered proton in the diffractive processes with the Forward Proton Spectrometer (FPS) or the Very Forward Proton Spectrometer (VFPS). These tracking detectors can either be used only as a tagger of the scattered protons, or they can reconstruct  $M_Y$  and  $t$  as well. The large rapidity method does not allow that because the scattered proton is not detected. The method of detecting the leading proton is very limited in statistics by the acceptance of the forward spectrometers. Therefore, the analysis presented here uses the large rapidity gap selection method. This technique relies on indirect detection of the scattered proton by demanding no activity in the forward parts of the H1 detector. Due to the acceptance of the detector around the beam pipe in the forward region, the large rapidity gap method not only selects events where the proton remains intact but also keeps events where the proton dissociates into a system with  $M_Y < 1.6 \text{ GeV}$ . Therefore, the diffractive cross section measured by the large rapidity gap method is defined for the kinematic range

$$M_Y < 1.6 \text{ GeV}, \quad |t| < 1.0 \text{ GeV}^2. \quad (7.2)$$

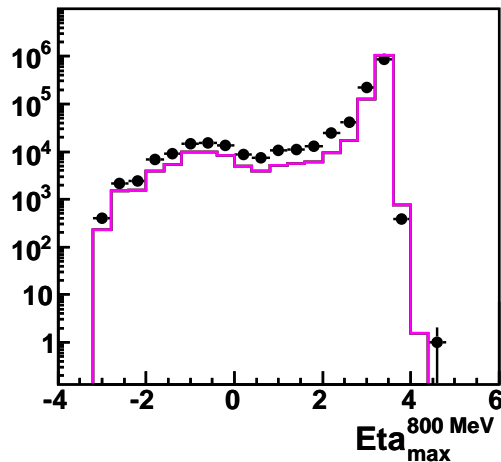


Figure 7.2: Distribution of the  $\eta_{max}$  variable in the inclusive high energy data (black points). The DJANGO Monte Carlo used in the  $F_L$  analysis (magenta line) does not simulate diffractive events.

### 7.3.1 $\eta_{max}$ Selection

First of all, a rapidity gap is required in the forward part of the LAr calorimeter. Rapidity is defined as

$$y = \frac{1}{2} \log \frac{E + p_z}{E - p_z} = \frac{1}{2} \log \frac{(E + p_z)^2}{m^2 + p_T^2}. \quad (7.3)$$

For a massless particle, rapidity is directly related to the polar angle  $\theta$ . Pseudorapidity, a  $m = 0$  GeV limit of the rapidity, reads

$$\eta = y|_{m=0} = \log \frac{E + p_z}{p_T} = -\log(\tan \frac{\theta}{2}). \quad (7.4)$$

The definition implies that the forward region corresponds to the higher values of pseudorapidity.

The  $\eta_{max}$  variable is used in order to require the rapidity gap.  $\eta_{max}$  corresponds to the pseudorapidity of the most forward cluster found in the LAr calorimeter that has an energy higher than a certain threshold which cuts away the calorimeter noise. Fig. 7.2 shows the  $\eta_{max}$  distribution in the high energy data in the  $F_L$  analysis. The peak at the highest values of  $\eta_{max}$  corresponds to the non-diffractive events and contains approximately one order of magnitude more events than the plateau seen at lower  $\eta_{max}$ . The events in the plateau do not show any forward activity and therefore are likely to be diffractive events. As a rapidity gap selection for diffractive events, a cut on  $\eta_{max} < 3.3$  is introduced. The right edge of the distribution corresponds to the forward acceptance of the LAr calorimeter. The DJANGO Monte Carlo used in the  $F_L$  analysis does not simulate diffractive events correctly. Therefore the plateau in the Monte Carlo is significantly lower than in data.

In order to use the  $\eta_{max}$  selection, it is important to be able to distinguish the signal from a hadronic final state particle and a calorimeter noise. Fig. 7.3 shows the

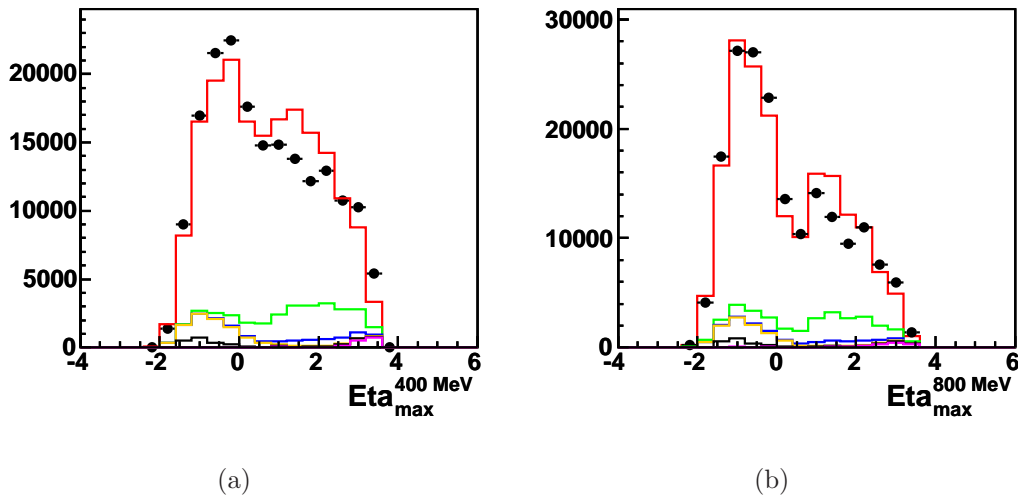


Figure 7.3: Description of the  $\eta_{max}$  variable using the cluster energy noise threshold of 400 MeV (a) and 800 MeV (b). Diffractive high energy data are plotted.

$\eta_{max}$  distribution in the high energy diffractive analysis using an energy threshold of 400 MeV and 800 MeV. Since the  $\eta_{max}^{800MeV}$  variable is described better by the simulation, the 800 MeV threshold is used for the  $\eta_{max}$  cut.

### 7.3.2 Forward Detector Selection

#### Forward Detectors

The principle component of the forward detector selection is the forward muon detector. It was originally designed to measure high energy muons but it was also found to be sensitive to secondary particles from proton dissociation decay products interacting with the beam pipe. Therefore, it is efficient in rejecting proton dissociation events. It has an acceptance in the region of  $5.0 < \eta < 6.5$ . Only the three pre-toroid layers of FMD are used in the selection as they are shielded by synchrotron radiation by the toroidal magnet unlike the noisier post-toroidal layers. The demand on no activity in FMD is such that at most 1 hit pair is detected in the first two double-layers and at most 2 hit pairs are in the three pre-toroid double-layers.

The large rapidity gap requirement also involves the Plug calorimeter. It covers the rapidity range  $3.5 < \eta < 5.5$  which fills the area between the FMD and LAr acceptances. No activity in the Plug detector is ensured by the request on the reconstructed energy  $E_{Plug} < 3 \text{ GeV}$ .

The last detector taking part in the forward detector selection is the forward tagger system station located 28 m away from the central detector. It allows to detect the secondary hadrons from proton dissociation at very large rapidities around the proton direction. The presence of zero hits in this detector is required.

The forward detector selection is listed in Table 7.3.

Selection Description	Values
Hit pairs in the first 2 FMD layers	$N_{1+2}^{FMD} \leq 1$
Hit pairs in the first 3 FMD layers	$N_{1+2+3}^{FMD} \leq 2$
Energy in the Plug	$E_{Plug} < 3 \text{ GeV}$
Hits in the FTS 28m station	$N_{28m}^{FTS} = 0$

Table 7.3: The forward detector selection.

### Run Selection

The run selection for the  $F_L^D$  analysis is similar as in the  $F_L$  analysis. The only difference is in an additional requirement on forward sub-detectors. The forward muon detector and the Plug calorimeter are demanded to be turned on since it is crucial for the large rapidity gap selection. All run selection criteria for the diffractive analysis are listed in Table 7.4.

After the run selection, there are  $82.1 \text{ pb}^{-1}$  of 2006  $e^+$  data with  $E_p = 920 \text{ GeV}$ ,  $45.7 \text{ pb}^{-1}$  2007  $e^+$  data with  $E_p = 920 \text{ GeV}$ ,  $10.9 \text{ pb}^{-1}$  of the low energy data ( $E_p = 460 \text{ GeV}$ ) and  $5.9 \text{ pb}^{-1}$  of the medium energy data ( $E_p = 575 \text{ GeV}$ ). These data samples are further reduced by rejection of noisy runs which is in particular strong in the low and medium energy data.

### Rejection of Noisy Runs

The forward detectors are situated close to the beam pipe and may suffer from high level of noise caused by synchrotron radiation. The synchrotron radiation was an issue especially at the beginning of the low energy data taking. The beam was not well focused and the beam halo produced a constant signal in the forward detectors.

In order to study the noise in the forward detectors an unbiased selection of events is needed. The events from so-called random trigger files can be used. Random trigger files contain events that are randomly triggered and therefore no physical process is preferred there. They can be used as an independent sample in order to study the noise in the forward detectors.

The noise level is studied in the following way. In every run, events that pass the rapidity gap requirement in the LAr calorimeter  $\eta_{max} < 3.3$  are selected. These are events with no forward activity in the central detector, and therefore it is expected to observe no activity in the forward detectors as well. Therefore, the noise is evaluated as a fraction of events that fail the forward detector selection in the  $\eta_{max} < 3.3$  sample.

$$noise = \frac{\eta_{max} < 3.3 \ \& \ \text{activity in the forward detectors}}{\eta_{max} < 3.3}. \quad (7.5)$$

This quantity is evaluated for every run in the random trigger files. Different forward detectors can be considered in the selection.

Fig. 7.4(a) shows the *noise* distribution in the low energy random trigger files. A combination of the FMD and Plug selections is taken into account. An activity in at

Run period	2006 $e^+$ $E_p = 920$ GeV	2007 $e^+$ $E_p = 920$ GeV	$E_p = 460$ GeV	$E_p = 575$ GeV
Run range	468531 – 492541	492559 – 500611	500919 – 507824	507843 – 511079
Sub-triggers			ST0, ST7, ST8	
Minimal luminosity	1 nb <sup>-1</sup>			
Prescale limit			1	
Sub-detectors	CJC1, CJC2, LAR, TOF, LUMI, CIP, BST, SPAC FMD, Plug			
Vertex	$-35 < z_{vtx} < 35$ cm			

Table 7.4: Run selection.

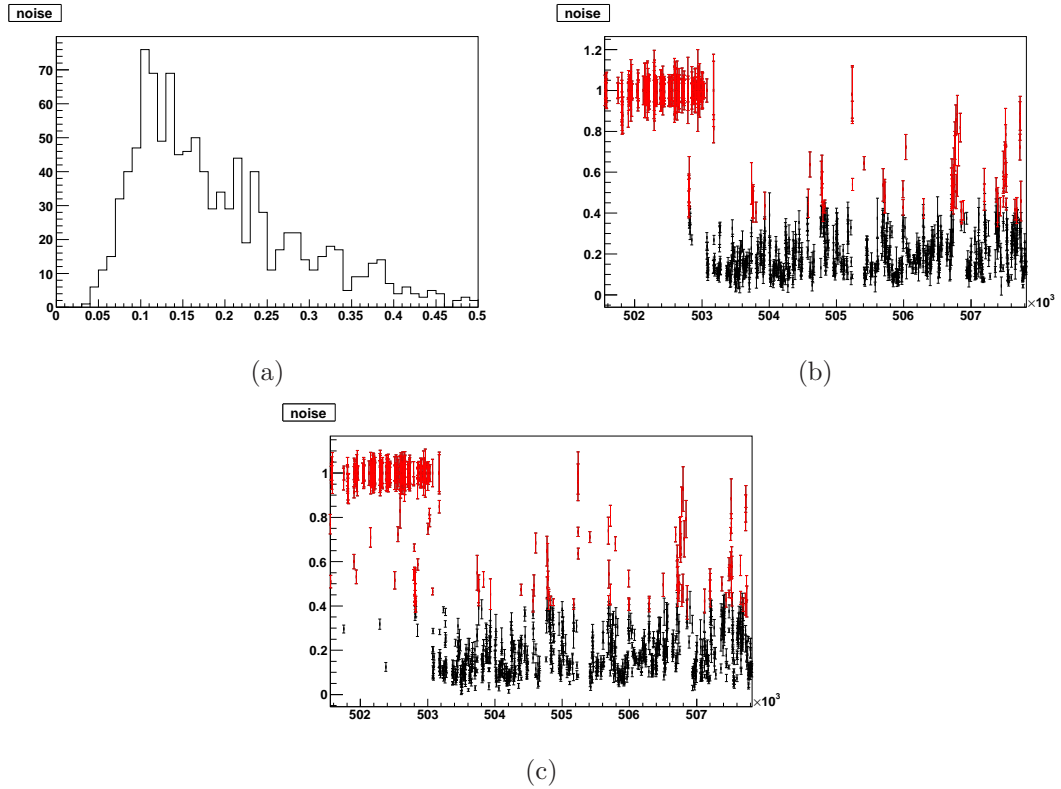


Figure 7.4: Fraction of events in a run that fail the FMD and Plug selection (a). Random trigger files for low energy data are analysed. A 40% noise threshold is considered in the selection (noisy runs are plotted in red). The run dependence of the noise levels in data (b) is well simulated in the Monte Carlo (c).

least one of these detectors has to be seen in order to contribute to the numerator of Eq. 7.5. The noise fraction is plotted also in Fig. 7.4(b) and 7.4(c) as a function of run number in data and Monte Carlo, respectively. The noise simulation in Monte Carlo describes the run dependence well, therefore only the runs with extreme noise levels are rejected. A cut on  $noise < 40\%$  is chosen and the excluded runs are plotted in red. The noisy period at the beginning of the low energy data taking is clearly visible in the plot and removed by the selection. Fig. 7.5 shows the distribution of  $noise$  in the medium energy random trigger files. The amount of noisy runs there is smaller than in the low energy data.

The FTS 28m station is not considered in the study of the noisy runs. It is not sensitive to the forward noise caused by beam halo and the noise levels there are negligible. The  $noise$  quantity where only the FTS 28m station is studied is plotted in Fig. 7.6. This detector is in general quiet and not very efficient in detecting forward activity (see Section 7.4.1). However, it can be used in addition to the FMD and Plug detectors in order to slightly increase their tagging efficiency.

The rejection of the noisy runs results in significant reduction of statistics in the low and medium energy data. Nevertheless, it is crucial to retain low levels of noise in the forward detectors in order to ensure a high efficiency of the large rapidity gap selection. Table 7.5 shows the luminosity before and after the rejection of noisy runs

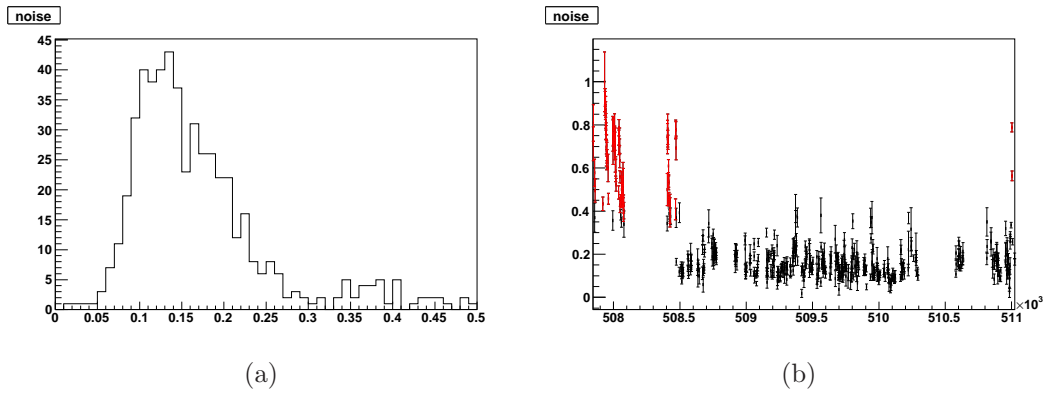


Figure 7.5: Fraction of events in a run that fail the FMD and Plug selection (a). Random trigger files for medium energy data are analysed. A 40% noise threshold is considered in the run selection (noisy runs are plotted in red). The run dependence of the noise levels in data is shown (b).

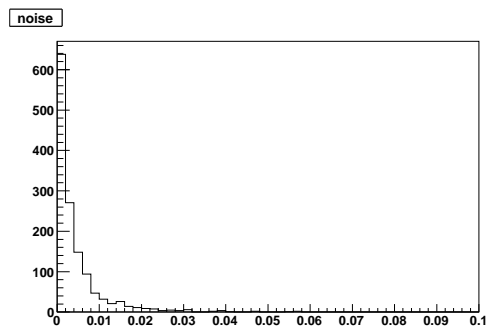


Figure 7.6: Fraction of events in a run that fail the FTS 28m station selection. Random trigger files for low energy data are analysed.

Run period	Run Range	Luminosity		
		all runs	40% noise	20% noise
2006 $e^+$ $E_p = 920$ GeV	468531 – 492541	81.7 pb <sup>-1</sup>	81.3 pb <sup>-1</sup>	72.8 pb <sup>-1</sup>
2007 $e^+$ $E_p = 920$ GeV	492559 – 500611	45.7 pb <sup>-1</sup>	45.5 pb <sup>-1</sup>	43.8 pb <sup>-1</sup>
$E_p = 460$ GeV	500919 – 507824	10.7 pb <sup>-1</sup>	8.5 pb <sup>-1</sup>	5.9 pb <sup>-1</sup>
$E_p = 575$ GeV	507843 – 511079	5.9 pb <sup>-1</sup>	5.2 pb <sup>-1</sup>	4.2 pb <sup>-1</sup>

Table 7.5: Run ranges and luminosity. The 40% noise cut is used in the analysis. The H1  $F_L^D$  preliminary results (see Appendix E) were obtained with the harder cut on 20%.

in all analysed data sets in the  $F_L^D$  analysis. The analysis uses the 40% noise cut.

### 7.3.3 Reconstruction of Diffractive Kinematics

The diffractive event kinematics are reconstructed using the mass of the system  $X$ . Standardly,  $M_X$  is obtained from

$$M_X^2 = (E^2 - p^2)_h \frac{y_e}{y_h}. \quad (7.6)$$

Neglecting the transverse momentum of the hadrons and using the definition of  $y_h$  in Eq. 6.28, this method of reconstructing  $M_X^2$  reduces to  $2E_e(E + p_z)_h y_e$ , which improves the resolution.

Furthermore, an additional correction to the reconstruction of  $M_X$  is applied in the Monte Carlo based on the study of  $\frac{M_{X,gen}^2}{M_{X,rec}^2}$ . Fig. 7.7 shows the fraction of generated and reconstructed  $M_X^2$  in bins of  $\eta_{max}$ . The entries in the plot were obtained from Gaussian fits to the  $\frac{M_{X,gen}^2}{M_{X,rec}^2}$  distributions in corresponding  $\eta_{max}$  bins. The plot shows an overall under-reconstruction of  $M_X$  which slightly increases for high values of  $\eta_{max}$ . The following correction to the reconstructed  $M_X$  is derived from the linear fit to the displayed dependence

$$\delta(M_X^2) = 1.18 + 0.004\eta_{max}. \quad (7.7)$$

The correction is applied to both data and simulation in order to accurately reconstruct  $M_X$ . The final reconstruction of  $M_X$  is then

$$M_X^2 = (E^2 - p^2)_h \frac{y_e}{y_h} \delta(M_X^2). \quad (7.8)$$

As  $t$  cannot be measured in a diffractive sample selected by the large rapidity gap method, the diffractive kinematics are reconstructed in the following way (compare to Eq. 2.37 and 2.38)

$$\beta = \frac{Q^2}{Q^2 + M_X^2}, \quad x_P = \frac{x}{\beta}. \quad (7.9)$$

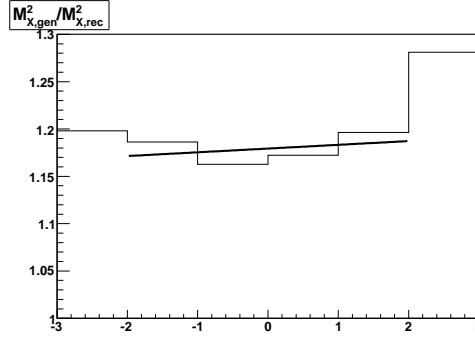


Figure 7.7: Mean values of the Gaussian fits to the  $\frac{M_{X,gen}^2}{M_{X,rec}^2}$  distribution in bins of  $\eta_{max}$ . The linear fit to this plot gives the correction applied to the reconstructed  $M_X^2$  as a function of  $\eta_{max}$ . The bins at the edges are statistically limited and therefore are not involved in the fit.

Selection Description	Values
Box cut	$\eta_{max} < -1.7, r_{SPACAL} < 40$ cm

Table 7.6: CJC acceptance cut.

### 7.3.4 Vertex Requirement

#### CJC Vertex

The topology of the diffractive events can be a source of an inefficiency of vertex reconstruction using the tracks in the CJC detector. The large rapidity gap separating the final states  $X$  and  $Y$  can lead to a lack of CJC tracks coming from the hadronic final state. There is a requirement of a track–cluster link for the scattered positron, where the track can be reconstructed either in the CJC or the BST detector. This means that there are diffractive events with no or very limited activity in CJC where a very low efficiency of the CJC vertex reconstruction has to be expected. The efficiency of such events will be discussed in detail in Section 7.4.2. These events are excluded from the analysis sample. The problematic region is identified with  $\eta_{max} < -1.7$  and  $r_{SPACAL} < 40$  cm, where the value of  $\eta_{max}$  corresponds to the polar angle of  $160^\circ$  which is the backward edge of the CJC detector. The range of  $r_{SPACAL} \sim 40$  cm roughly corresponds to the region where the BST acceptance takes over the acceptance of the CJC tracker. The CJC acceptance cut is shown in Table 7.6. The topology of an event is highly correlated with its kinematics. Therefore, such a geometrical cut has an influence on a certain part of phase space. It will be shown that mainly the low  $x_P$  events are affected by the cut.

### 7.3.5 The Final Diffractive Selection

The  $F_L^D$  analysis uses the large rapidity gap selection method. All the cuts described above ensure there is no activity in the forward region, i.e. there is a gap separating the proton final state  $Y$  from the hadronic final system  $X$ . In order to make sure that the

Selection Description	Values
Rapidity gap	$\eta_{max}^{800MeV} < 3.3$
Hit pairs in the first 2 FMD layers	$n_{1+2}^{FMD} \leq 1$
Hit pairs in the first 3 FMD layers	$n_{1+2+3}^{FMD} \leq 2$
Energy in the Plug	$E_{Plug} < 3 \text{ GeV}$
Hits in the FTS 28m station	$N_{28m}^{FTS} = 0$
$x_P$ cut	$0.0001 < x_P < 0.01$
Final state $X$ exists	$N_{particles}^{HFS} \geq 1$
Acceptance	CJC acceptance cut
Inelasticity	$y_{av} > 0.1$

Table 7.7: The diffractive selection.

final system  $X$  exists, at least one reconstructed hadronic final state particle is required. The analysis attempts to measure  $F_L^D$  in the kinematical range of  $0.0001 < x_P < 0.01$ , therefore a cut on  $x_P$  is applied as well.

A cut on  $y_{av} > 0.1$  is also introduced to accompany the lower cut on  $y_e$  in the **analysis selection**. The electron reconstruction method has poor resolution at low  $y$ . The average reconstruction method has better resolution there since it also involves hadronic final state in the reconstruction. The  $F_L$  analysis does not require a specific final state, it is a fully inclusive analysis. The  $F_L^D$  analysis is also an inclusive analysis, but it uses the hadronic final state in the diffractive kinematic reconstruction and in the large rapidity gap selection. Therefore, it makes sense to take the advantage of the better low  $y$  resolution of the average reconstruction method.

### 7.3.6 Photoproduction Background Subtraction

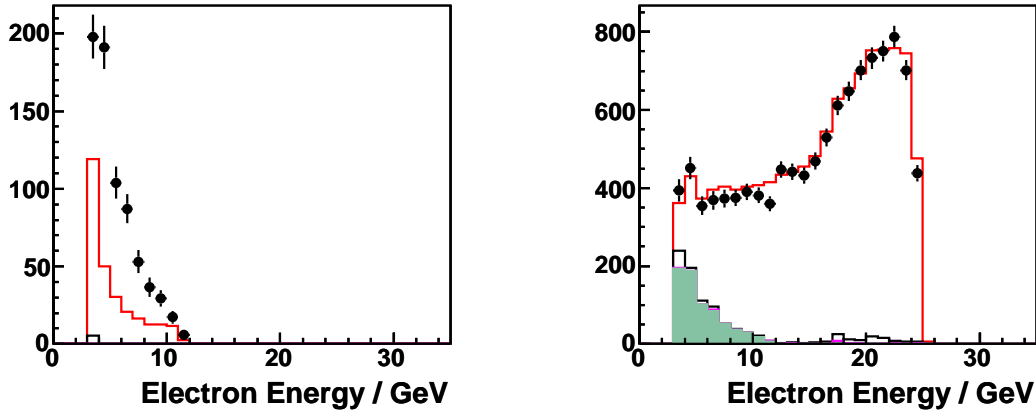
The background subtraction strategy in the  $F_L$  analysis combines both the wrong charge background subtraction at  $y > y_{trans}$  and the tagged events subtraction at  $y < y_{trans}$ . The negative charged tagged events are scaled by  $\frac{2}{acc_{tagger}}$  in Eq. 6.32 where  $acc_{tagger} = 0.2$  is the tagger acceptance.

In the  $F_L^D$  analysis, the statistics of the tagged events is very limited, and the large correction would therefore lead to big statistical fluctuations in the signal sample, after the background subtraction. Therefore, the tagged background is not used.

The wrong charge background subtraction could be used instead of the tagged event subtraction at lower  $E'_e$ . However, it strongly relies on the charge reconstruction which is poorly modelled at lower  $E'_e$  in the simulation (see Fig. 6.20(b)). The amount of mis-reconstructed charges in data and Monte Carlo is different at lower  $E'_e$  which makes the wrong charge background subtraction technique unreliable there.

The decision is taken to perform the wrong charge background subtraction only at

$y$ range	Background subtraction technique
$y > 0.6$	wrong charge background subtraction $N_{signal} = N_{all} - (1 + asym)N^- = N^+ - asymN^-$

Table 7.8: Photoproduction background subtraction strategy in the  $F_L^D$  analysis.

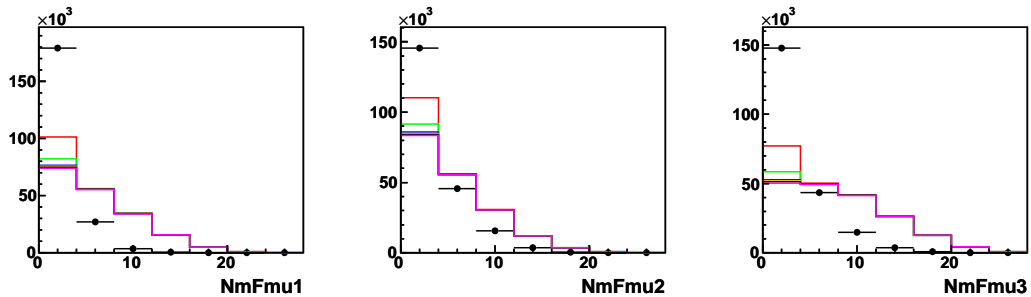
(a) Wrong charge background at  $y > 0.6$ . The background seen in Monte Carlo (red line) contains only the charge mis-reconstructed signal events. The difference between data and Monte Carlo shows the amount of photoproduction background. However, the wrong charge background is subtracted as a whole (for both data and Monte Carlo).

(b) Positron energy in data (points) is shown summed with the wrong charge background determined from data (green area) and compared to the Monte Carlo signal (red line) that is also summed with the wrong charge background from data.

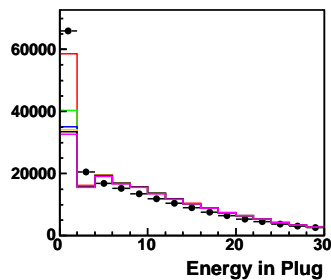
Figure 7.8: Background in the low energy data sample.

$y > 0.6$  for all data sets<sup>1</sup>. The expected amount of photoproduction background at lower  $y$  is negligible with respect to the statistical precision of the diffractive analysis. Any attempt to remove this background either by using tagged events or wrong charge events is not reliable because of the reasons given above. No background is subtracted in the remaining region. The photoproduction background subtraction strategy is also given in Table 7.8, and the amount of wrong charge background in the low energy data sample is illustrated in Fig. 7.8.

<sup>1</sup>This means that no background is subtracted in the high energy data since they are analysed only in the region of  $0.1 < y < 0.56$ .



(a) Number of hit pairs in the first three FMD double-layers.



(b) Energy in the Plug calorimeter.

Figure 7.9: Simulation of the FMD and Plug response. The non-diffractive Monte Carlo (magenta) dominates at higher values and clearly denotes the difference between diffractive and non-diffractive processes.

## 7.4 Efficiency of the Selection and Accuracy of the Simulation

### 7.4.1 Efficiency of the Forward Detector Selection

The large rapidity gap selection requires an empty forward region of the H1 detector. It involves a forward detector selection where no activity above certain noise threshold is required. The noise in the forward detectors is simulated in the Monte Carlo and the simulation reflects the time dependence of the noise levels as it is seen in data. Fig. 7.9 shows the number of hit pairs in the first three layers of the FMD detector and the energy measured in the Plug calorimeter. Data after the analysis selection (without the diffractive selection applied) are compared to the combination of non-diffractive and diffractive Monte Carlo models. The simulation is not accurate and gives rather poor description of data. Therefore, the activity of the forward detector selection has to be monitored and a correction has to be evaluated, if needed.

The efficiency of forward activity tagging for a particular forward detector is studied using a data sample where a forward activity is required. It is ensured by an anti-diffractive cut on  $\eta_{max} > 3.3$ . The  $\eta_{max}$  variable is defined only within the LAr calorimeter, therefore it can be used to independently check the performance of the

Detectors	Efficiency		Correction
	Data	Monte Carlo	
FMD	$0.771 \pm 0.001$	$0.953 \pm 0.004$	$0.809 \pm 0.003$
Plug	$0.852 \pm 0.001$	$0.874 \pm 0.004$	$0.975 \pm 0.004$
FTS 28m	$0.193 \pm 0.001$	$0.256 \pm 0.002$	$0.754 \pm 0.006$
FMD + Plug	$0.933 \pm 0.001$	$0.981 \pm 0.004$	$0.952 \pm 0.004$
FMD + Plug + FTS 28m	$0.946 \pm 0.001$	$0.986 \pm 0.004$	$0.959 \pm 0.004$

Table 7.9: Forward activity tagging efficiency of the forward detectors in the 2006  $e^+$  data. The efficiency in Monte Carlo is higher and needs to be corrected.

forward detectors. The efficiency is simply monitored in the following way

$$\varepsilon(\text{forward detector}) = \frac{\text{top}}{\text{bottom}} \quad (7.10)$$

where the *bottom* = *monitor* and *top* = *monitor* & *cut* selections are defined as:

- **bottom**

analysis selection

$$\eta_{max} > 3.3$$

- **top**

bottom

activity in the forward detector

The activity in the forward detector means that the event fails to pass a requirement of an empty detector listed in Table 7.3. The non-diffractive DJANGO Monte Carlo model is used for this study. This model does not generate diffractive events, therefore the events with a large rapidity gap are missing which makes this Monte Carlo suitable to study the forward activity tagging.

Tables 7.9, 7.10, 7.11 and 7.12 list the efficiencies of the FMD, Plug, and FTS 28 m detectors separately and in combination for data and Monte Carlo. The tables correspond to  $06e^+$ ,  $07e^+$  at  $E_p = 920$  GeV,  $E_p = 460$  GeV and  $E_p = 575$  GeV run periods, respectively. The study reveals that the Plug detector has the highest efficiency in data and is simulated with the best precision. According to the simulation, FMD is the most efficient one. The FTS 28m station alone has  $< 20\%$  efficiency in data and it brings  $\sim 1\%$  improvement to the combined efficiency of the FMD and Plug detectors. In all cases, the Monte Carlo efficiency is larger than in data and has to be corrected. The absolute efficiencies differ among the run periods. However, the correction factors needed for Monte Carlo remain the same. Therefore, all data sets are combined together in order to achieve the best precision possible for the determination of the Monte Carlo efficiency correction.

Detectors	Efficiency		Correction
	Data	Monte Carlo	
FMD	$0.760 \pm 0.002$	$0.954 \pm 0.005$	$0.797 \pm 0.004$
Plug	$0.853 \pm 0.002$	$0.872 \pm 0.005$	$0.978 \pm 0.006$
FTS 28m	$0.182 \pm 0.001$	$0.251 \pm 0.003$	$0.727 \pm 0.008$
FMD + Plug	$0.932 \pm 0.002$	$0.980 \pm 0.005$	$0.951 \pm 0.005$
FMD + Plug + FTS 28m	$0.944 \pm 0.002$	$0.985 \pm 0.005$	$0.958 \pm 0.005$

Table 7.10: Forward activity tagging efficiency of the forward detectors in the 2007  $e^+$  data. The efficiency in Monte Carlo is higher and needs to be corrected.

Detectors	Efficiency		Correction
	Data	Monte Carlo	
FMD	$0.728 \pm 0.003$	$0.912 \pm 0.004$	$0.799 \pm 0.005$
Plug	$0.809 \pm 0.003$	$0.821 \pm 0.003$	$0.986 \pm 0.006$
FTS 28m	$0.075 \pm 0.001$	$0.106 \pm 0.001$	$0.707 \pm 0.013$
FMD + Plug	$0.913 \pm 0.004$	$0.959 \pm 0.004$	$0.952 \pm 0.005$
FMD + Plug + FTS 28m	$0.922 \pm 0.004$	$0.965 \pm 0.004$	$0.956 \pm 0.005$

Table 7.11: Forward activity tagging efficiency of the forward detectors in the low energy data. The efficiency in Monte Carlo is higher and needs to be corrected.

Detectors	Efficiency		Correction
	Data	Monte Carlo	
FMD	$0.764 \pm 0.004$	$0.932 \pm 0.003$	$0.819 \pm 0.005$
Plug	$0.825 \pm 0.004$	$0.840 \pm 0.003$	$0.983 \pm 0.006$
FTS 28m	$0.107 \pm 0.001$	$0.148 \pm 0.001$	$0.723 \pm 0.011$
FMD + Plug	$0.924 \pm 0.004$	$0.969 \pm 0.003$	$0.953 \pm 0.005$
FMD + Plug + FTS 28m	$0.934 \pm 0.004$	$0.975 \pm 0.003$	$0.958 \pm 0.005$

Table 7.12: Forward activity tagging efficiency of the forward detectors in the medium energy data. The efficiency in Monte Carlo is higher and needs to be corrected.

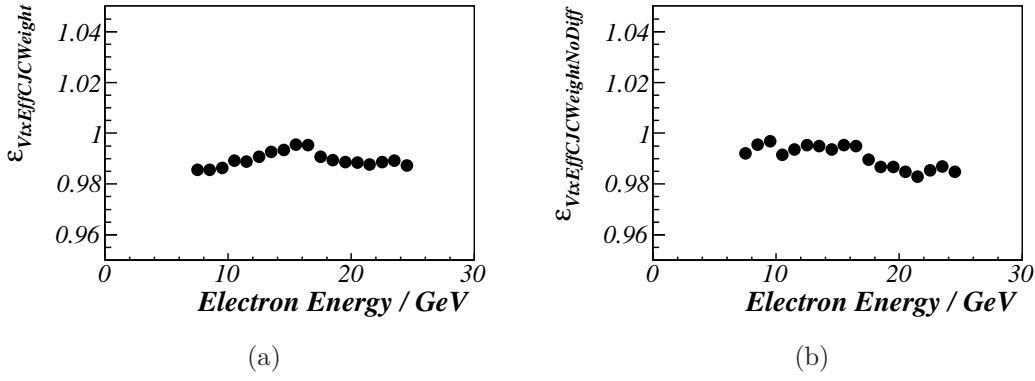


Figure 7.10: CJC vertex reconstruction efficiency in low energy data. The efficiency is monitored with (a) and without (b) an anti-diffractive selection applied in the monitoring sample. The CIP vertex is used for the monitoring.

## 7.4.2 Vertex Reconstruction Efficiency

The following text explains the CJC vertex reconstruction efficiency monitoring and motivates the CJC acceptance cut introduced in Section 7.3.4.

### CJC Vertex Reconstruction Efficiency

The vertex reconstruction efficiency in the diffractive analysis is monitored in a similar way as in the inclusive  $F_L$  analysis. The only difference is the presence of the diffractive selection. The efficiency can be monitored by a CIP vertex or by a BCREC track. For more details, see Section 6.4.2.

Possible sources of the CJC vertex reconstruction inefficiency are diffractive events due to a lack of activity in the forward region. No forward activity naturally leads to smaller amount of tracks that define a vertex. In order to study this effect, the CJC vertex reconstruction efficiency can be monitored in an inclusive sample (as in the case of the  $F_L$  analysis) and compared to the efficiency monitored in the anti-diffractive sample. The anti-diffractive selection can be defined by the  $\eta_{max} > 3.3$  cut and a requirement of an activity in the forward detectors, i.e. failure to pass the forward detector selection listed in Table 7.3. Fig. 7.10(a) shows the CJC vertex efficiency in the low energy data monitored in the inclusive sample. Fig. 7.10(b) shows the CJC vertex efficiency monitored in the anti-diffractive sample. Indeed, the efficiency in the anti-diffractive sample is better than in the inclusive sample and diffractive events are a source of the CJC vertex inefficiency.

The diffractive selection uses the CJC acceptance cut (see Table 7.6) that cuts away the events with a poor CJC vertex reconstruction efficiency. The cut is motivated by the fact that some diffractive events exist such that the final state misses the CJC detector. The scattered lepton in these events has a track reconstructed in BST and the hadronic final state  $X$  goes in the backward direction beyond the acceptance of CJC. Therefore, it makes sense to study the vertex reconstruction efficiency in bins of  $\eta_{max}$ , which is the pseudorapidity of the most forward cluster of the final state  $X$ , and  $r_{SPACAL}$ . The  $r_{SPACAL}$  variable is sensitive to the position of the track, and three regions of the CJC and BST detectors are considered:

- $18 < r_{SPACAL} < 30$  cm : BST only region
- $30 < r_{SPACAL} < 54$  cm : CJC/BST overlap
- $54 < r_{SPACAL} < 78$  cm : CJC only region

The problematic region is expected for low  $r_{SPACAL}$  where no CJC track of the scattered lepton is available, and  $\eta_{max} < -1.7$  which is the pseudorapidity value corresponding to the polar angle of  $160^\circ$  that defines the backward acceptance of the CJC detector. The poor efficiency should be mainly visible for high  $y$  events and low  $x_{\mathcal{P}}$  events. Since the high  $y$  (low  $E'_e$ ) and low  $r_{SPACAL}$  regions are in particular important for this study, the CIP vertex is not suitable for the efficiency monitoring. The CIP acceptance puts a lower limit on  $r_{SPACAL}$  at  $\sim 23$  cm. The monitoring with the BCREC track does not have such limitation. The study is done for the low and medium energy data where the low  $E'_e$  cut of 3.4 GeV is used. The combination of ST7 or ST8 sub-trigger is required for the monitoring. The way of CJC vertex reconstruction efficiency monitoring is summarized here.

$$\varepsilon(\text{CJC vertex}) = \frac{top}{bottom} \quad (7.11)$$

where the *bottom* = *monitor* and *top* = *monitor* & *cut* selections are defined as:

- **bottom**

basic selection

diffractive selection

ST7 or ST8

CJC/BST validation

if CJC vertex exists :  $-35 < z_{vtx}^{CJC} < 35$  cm

- **top**

bottom

CJC vertex ( $-35 < z_{vtx}^{CJC} < 35$  cm)

Fig. 7.11 shows the CJC vertex reconstruction efficiency at  $0.0001 < x_{\mathcal{P}} < 0.001$ ,  $E'_e < 15$  GeV in bins of  $\eta_{max}$  as a function of  $r_{SPACAL}$ . As expected, the efficiency is poor especially at low  $\eta_{max}$ , low  $r_{SPACAL}$  and low  $x_{\mathcal{P}}$ . The efficiency for data at  $E'_e < 15$  GeV,  $\eta_{max} < -2.3$ ,  $r_{SPACAL} < 33$  cm and  $0.0001 < x_{\mathcal{P}} < 0.001$  is only around 30% and is not well described by the simulation. For  $\eta_{max} > -1.7$ , the efficiency in data is above 80% and it is in agreement with the simulation within 5%. The plots are used to derive the CJC acceptance cut which removes the region at  $\eta_{max} < -1.7$  and  $r_{SPACAL} < 40$  cm.

The CJC vertex reconstruction efficiency in the diffractive analysis in a wider  $E'_e$  and  $r_{SPACAL}$  range and for  $0.0001 < x_{\mathcal{P}} < 0.01$  is shown in Fig. 7.12. The figure displays the effect of the CJC acceptance cut on both the absolute efficiency and the agreement between data and the simulation.

Fig. 7.13 shows in detail the efficiency after the CJC acceptance cut is applied separately for  $0.001 < x_{\mathcal{P}} < 0.01$  and  $0.0001 < x_{\mathcal{P}} < 0.001$ . The data efficiency in the higher  $x_{\mathcal{P}}$  region is described within 2% by the simulation. The description in lower

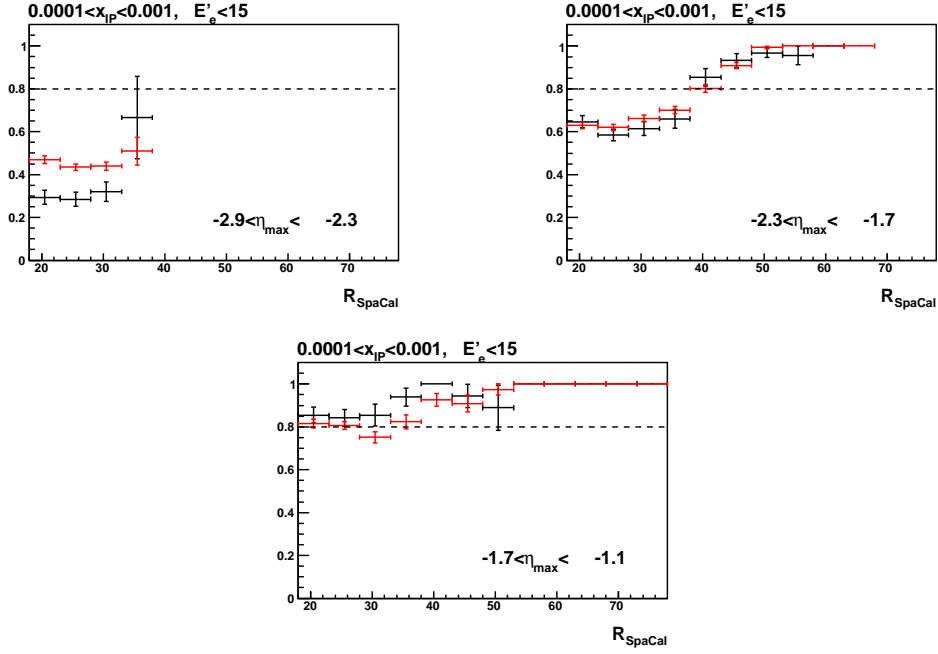
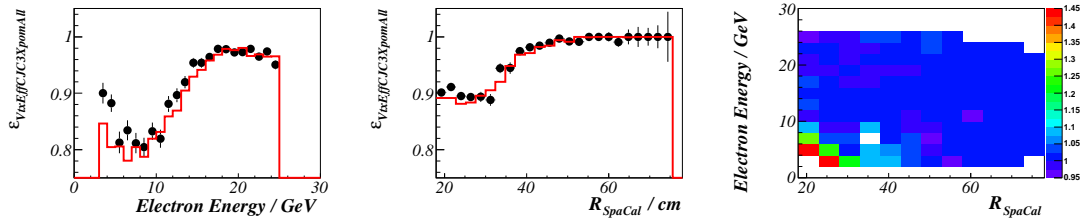
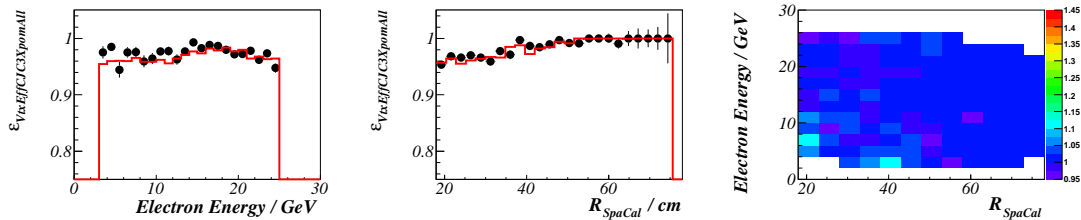


Figure 7.11: CJC vertex efficiency in the low energy data at  $0.0001 < x_P < 0.001$ ,  $E'_e < 15$  GeV and low  $\eta_{max}$ . The efficiency is shown as a function of  $r_{SPACAL}$  in three bins of  $\eta_{max}$ . Data efficiency (black) is not described by the simulation (red) at low  $\eta_{max}$  where it drops below 30%. The region where the efficiency is below  $\sim 80\%$  is excluded by the CJC acceptance cut of  $\eta_{max} < -1.7$  and  $r_{SPACAL} < 40$  cm.

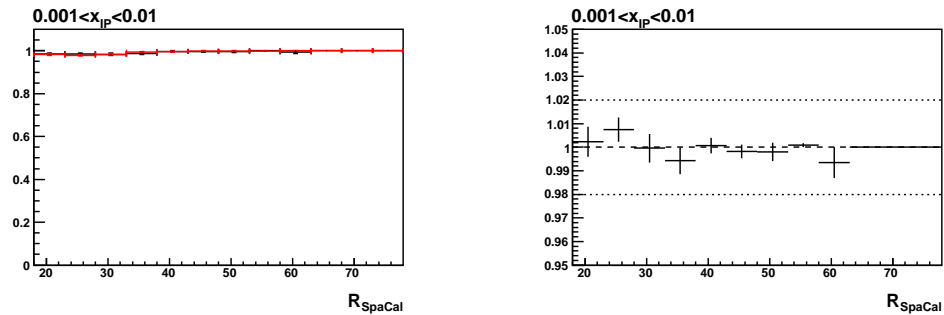


(a) The efficiency is low and not described by the simulation before the CJC acceptance cut is applied.

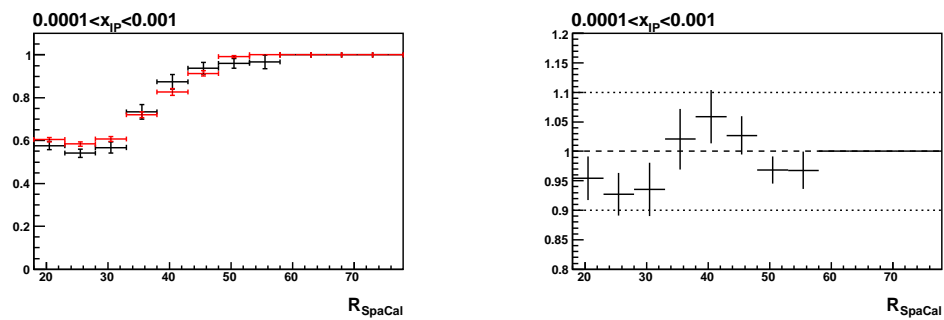


(b) RAPGAP gives a good description of the CJC vertex reconstruction after the CJC acceptance cut.

Figure 7.12: CJC vertex reconstruction efficiency in the low energy data (black) as described by the simulation (red) in the full analysis  $x_P$  range of  $0.0001 < x_P < 0.01$ .



(a) The efficiency at  $0.001 < x_P < 0.01$  is well modelled within 2%.



(b) The efficiency at  $0.0001 < x_P < 0.001$  is modelled within 10%.

Figure 7.13: CJC vertex reconstruction efficiency in the low energy data after the CJC acceptance cut in two bins of  $x_P$ . The left plots show the efficiency in data (black) and Monte Carlo (red), the right plots show the ratio of the efficiencies.

$x_{\mathcal{P}}$  is worse and an agreement within 10% is claimed. This level of agreement is taken as a systematic uncertainty. No efficiency correction in the simulation is needed.

Contrary to the  $F_L$  analysis, there is no CJC vertex efficiency correction applied in the  $F_L^D$  analysis.

### 7.4.3 Track–Cluster Link Efficiency

The  $F_L^D$  analysis uses the same track–cluster link efficiency correction as the  $F_L$  analysis. Finding a link between a reconstructed track and a cluster associated to the scattered positron does not depend on hadronic final state and therefore there is no difference between the efficiency correction for diffractive and non-diffractive events expected. The efficiency is monitored in a similar way as described in Section 6.4.3. The **diffractive selection** is used in addition, and different Monte Carlo models are studied.

Fig. 7.14 compares the efficiency for the high energy data sample as it is seen in the inclusive and the diffractive sample. In the diffractive analysis, the monitored efficiency in data is seen to be lower than in the inclusive case. A more detailed study reveals that this extra inefficiency comes from the QED-Compton and/or lepton pair background in the monitoring sample, and that the COMPTON Monte Carlo does not model the track–cluster link efficiency well. This background is also present in the inclusive analysis but it is negligible there. Fig. 7.15 shows the ratio of the track–cluster link efficiency in data and Monte Carlo with a cut on  $M_X > 1$  GeV applied in the monitoring sample. The cut significantly reduces background from QED-Compton and lepton pair production processes. Indeed, the efficiency both in data and Monte Carlo is larger than without using the  $M_X$  cut as shown in Fig. 7.14(b), and it is consistent with the efficiency seen in the inclusive analysis as displayed in Fig. 7.14(a). The efficiency is well modelled by the signal Monte Carlo. The remaining discrepancy observed at the highest  $r_{SPACAL}$  comes from the poor modelling of the background by the COMPTON Monte Carlo.

The diffractive analysis uses the same track–cluster link efficiency correction as the  $F_L$  analysis.

### 7.4.4 Hadronic Final State Calibration

Hadronic final states in the  $F_L^D$  analysis are calibrated with the **iterative calibration method** which is briefly introduced in Section 6.4.6. The constants derived for 06/07  $e^+$  period for data and RAPGAP model are applied here. The same constants are used for all high energy, low energy and medium energy data since there is no separate calibration constants available for the runs with reduced proton beam energy.

#### Calibration of the Hadronic SPACAL

The **iterative calibration method** does not provide calibration constants for the hadronic SPACAL. Similarly as in the  $F_L$  analysis, the corresponding calibration constant is derived from the description of  $E - p_z$  at high values of inelasticity  $y$  where a backward activity is expected.

The momentum conservation law implies that  $E - p_z$  of the whole final state is equal to 55 GeV. In the  $F_L$  analysis, the  $(\alpha_{SPACAL}^{had})_{data} = 0.25$  factor is used for all

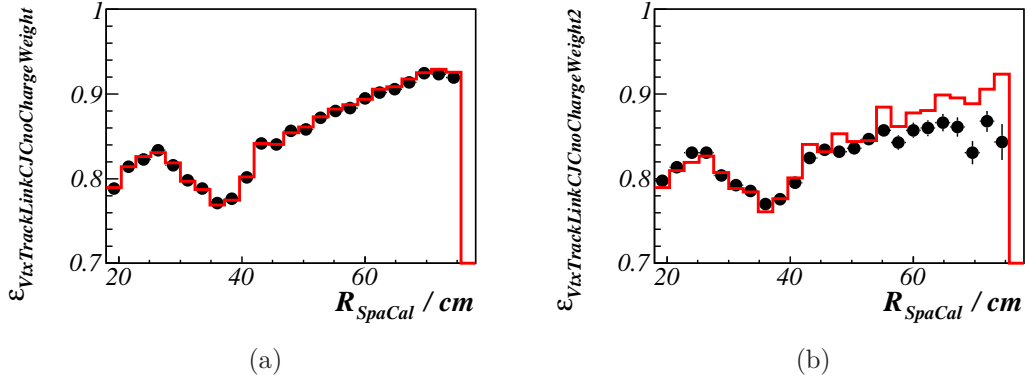


Figure 7.14: Track-cluster link efficiency in the high energy data (black) compared to the simulation (red) after the efficiency correction derived in the inclusive analysis. Therefore, the efficiency is well described by DJANGO in the inclusive analysis (a). The efficiency in the diffractive analysis (b) is not well described by the combination of RAGPAP, DIFFVM and COMPTON Monte Carlo models. A more detailed study reveals that the description is spoiled just by the COMPTON Monte Carlo.

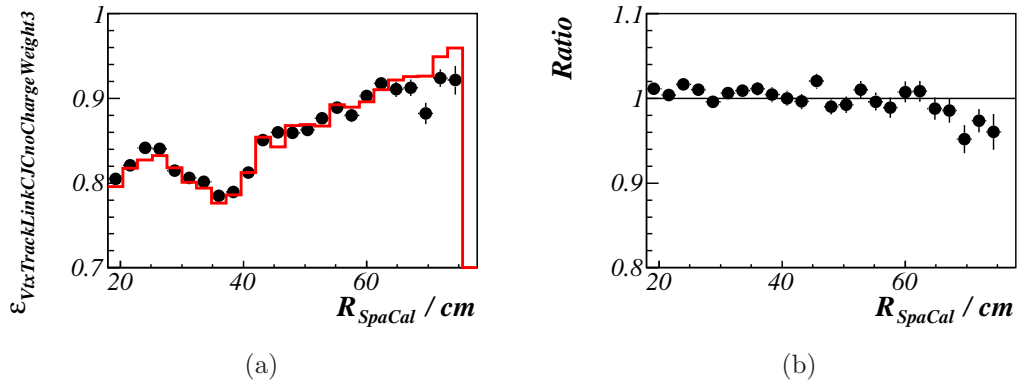


Figure 7.15: Track-cluster link efficiency in the diffractive high energy data (black) as described by the combination of RAGPAP, DIFFVM and COMPTON Monte Carlo models (red) at  $M_X > 1$  GeV (a). The ratio of the efficiencies is shown in (b). The cut reduces the COMPTON Monte Carlo contribution that produces low mass final states, and data are well described by Monte Carlo after this cut. The remaining discrepancy observed at the highest  $r_{SPACAL}$  comes from the poor modelling of the background by the COMPTON Monte Carlo.

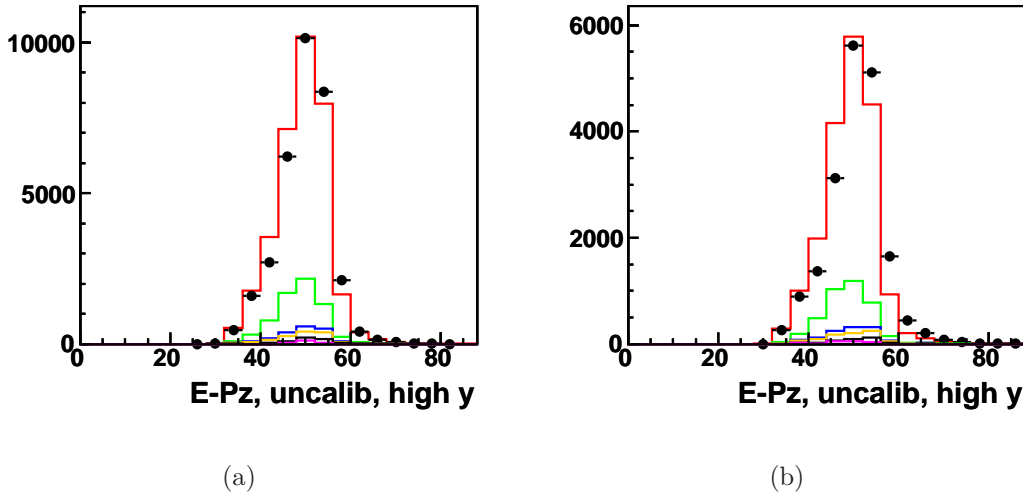


Figure 7.16:  $E - p_z$  distribution in 2006  $e^+$  (a) and 2007  $e^+$  (b) data before the calibration of hadronic SPACAL. The peak position in data is different between the two periods. Therefore, different  $(\alpha_{SPACAL}^{had})_{data}$  calibration factors are needed.

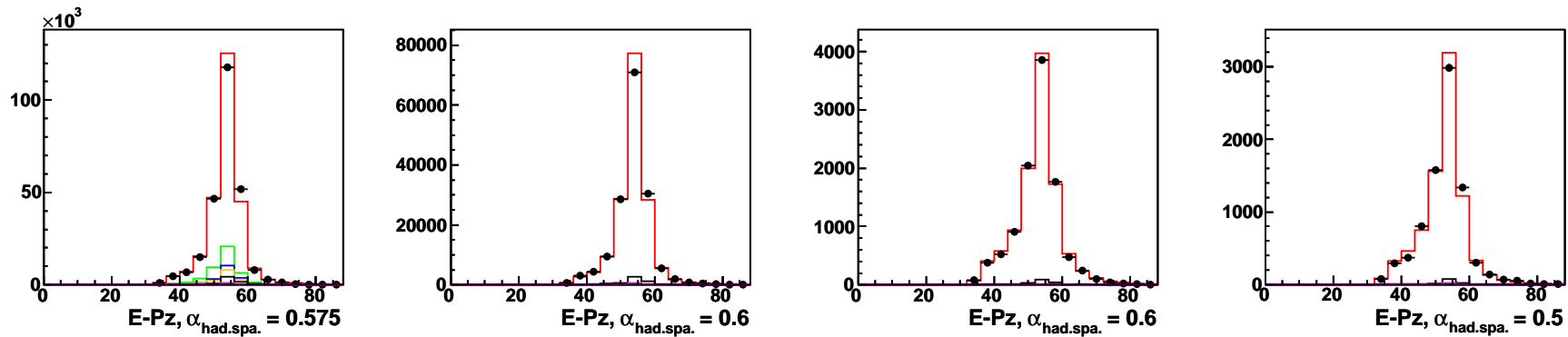
data sets. The same set of calibration constants for data is used in the diffractive analysis and there is no reason to expect any difference in the calibration performance in the diffractive sample. Fig. 7.16(b) shows the  $E - p_z$  distribution at  $y > 0.38$  for 2007  $e^+$  period. All calibration factors except for  $\alpha_{SPACAL}^{had}$  are applied in these plots for both data and Monte Carlo. The mean value of the peak position in data determines the calibration factor  $(\alpha_{SPACAL}^{had})_{data} = 0.25$  which corresponds to the one used in the  $F_L$  analysis. The  $F_L^D$  analysis also looks at the 2006  $e^+$  data. Fig. 7.16(a) reveals that the  $E - p_z$  peak position in data before the hadronic SPACAL calibration is different than in the 2007  $e^+$  data. A higher calibration factor is needed for the 2006  $e^+$  data and it is set to  $(\alpha_{SPACAL}^{had})_{data} = 0.35$ .

The RAPGAP Monte Carlo does not use the same set of calibration constants as the DJANGO model in the  $F_L$  analysis. There are also constants for the RAPGAP model available from the **iterative calibration method**. They were derived for an inclusive version of RAPGAP. Therefore, the hadronic SPACAL calibration factors derived here do not have to fully agree with the ones determined for DJANGO.

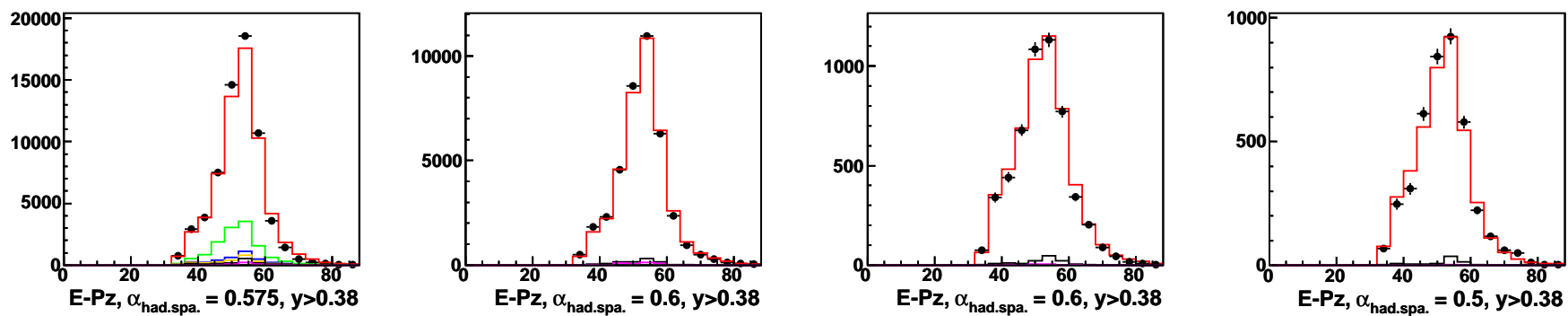
Fig. 7.17 displays the  $E - p_z$  distributions after the final calibration for 2006  $e^+$ , 2007  $e^+$  at  $E_p = 920$  GeV,  $E_p = 460$  GeV and  $E_p = 575$  GeV periods. The corresponding hadronic SPACAL calibration constants for Monte Carlo  $(\alpha_{SPACAL}^{had})_{MC}$  are 0.575, 0.6, 0.6 and 0.5, respectively. They are similar to  $(\alpha_{SPACAL}^{had})_{MC} = 0.55$  derived for DJANGO. The constants for both data and Monte Carlo are given in Table 7.13.

## Performance of the Calibration

Fig. 7.18 compares the absolute and the relative calibration between data and Monte Carlo for the low energy data taking period. The first row of the plots shows the  $p_T^{bal}$  in data and Monte Carlo after the calibration, the second row compares  $\frac{\sigma}{\mu}$  of the



(a)



(b)

Figure 7.17:  $E - p_z$  after the iterative calibration with the tuned calibration of hadronic SPACAL for all  $y$  (a) and  $y > 0.38$  (b). The high  $y$  plots were used to fix the  $\alpha_{SPACAL}^{had}$  calibration constant. The plots show the data-taking periods 06  $e^+$ , 07  $e^+$ , low energy and medium energy data, from left to right.

Run period	$1 + (\alpha_{SPACAL}^{had})_{data}$	$1 + (\alpha_{SPACAL}^{had})_{MC}$
06 $e^+$ $E_p = 920$ GeV	1.35	1.575
07 $e^+$ $E_p = 920$ GeV	1.25	1.6
$E_p = 460$ GeV	1.25	1.6
$E_p = 575$ GeV	1.25	1.5

Table 7.13: Calibration of the hadronic SPACAL.

$p_T^{bal}$  peaks in data and Monte Carlo after the calibration.  $\mu$  and  $\sigma$  are the standard Gaussian parameters, The third row shows the double ratio  $DR(p_T^{bal})$ , where the fit error on  $\mu$  of the corresponding peak in the numerator and denominator is used in order to calculate the error on the ratio. The different columns show these quantities studied as a function of  $p_T^e$ ,  $Q_e^2$ ,  $\theta_h^e$  and  $y_e$ . All these plots prove a good consistency between data and Monte Carlo. The double ratios agree within 2% which corresponds to the expected performance of the **iterative calibration method**. Fig. 7.19 summarises a similar study done for  $y_{bal}$ . Again, the data and Monte Carlo agreement is within 2%.

## 7.5 Description of Data

### 7.5.1 RAPGAP components

RAPGAP has three components: the pomeron exchange with light quarks ( $u, d, s$ ), the pomeron exchange with the charm quark  $c$ , and the reggeon exchange. All three components are normalised so that they give consistent cross sections with the analytical prediction from H1 2006 DPDF Fit B. After the proton dissociation acceptance correction (described in Section 7.6.4), data and Monte Carlo agree within 3% in terms of normalisation.

### 7.5.2 Normalization of the DIFFVM Simulation

The RAPGAP simulation does not describe the low  $M_X$  final states well. It is the region occupied by vector meson resonances that are clearly visible in the  $M_X$  distribution in data. RAPGAP also produces low  $M_X$  final states but it does not give satisfactory description of data. Therefore, the DIFFVM model is used to generate events with  $\rho$ ,  $\omega$ ,  $\phi$  and  $J/\Psi$  vector meson resonances which are then added to RAPGAP in order to improve the data description.

The cross sections of vector meson production follow the SU(4) relations

$$\rho : \omega : \phi : J/\Psi = 9 : 1 : 2 : 8 \quad (7.12)$$

The luminosity of the DIFFVM components is modified so that the cross sections obey these relations.

The absolute normalisation of the DIFFVM contributions is determined directly from control plots. There is a dedicated selection, referred to as **vector meson selection**, that chooses events where only the scattered lepton and two particles from

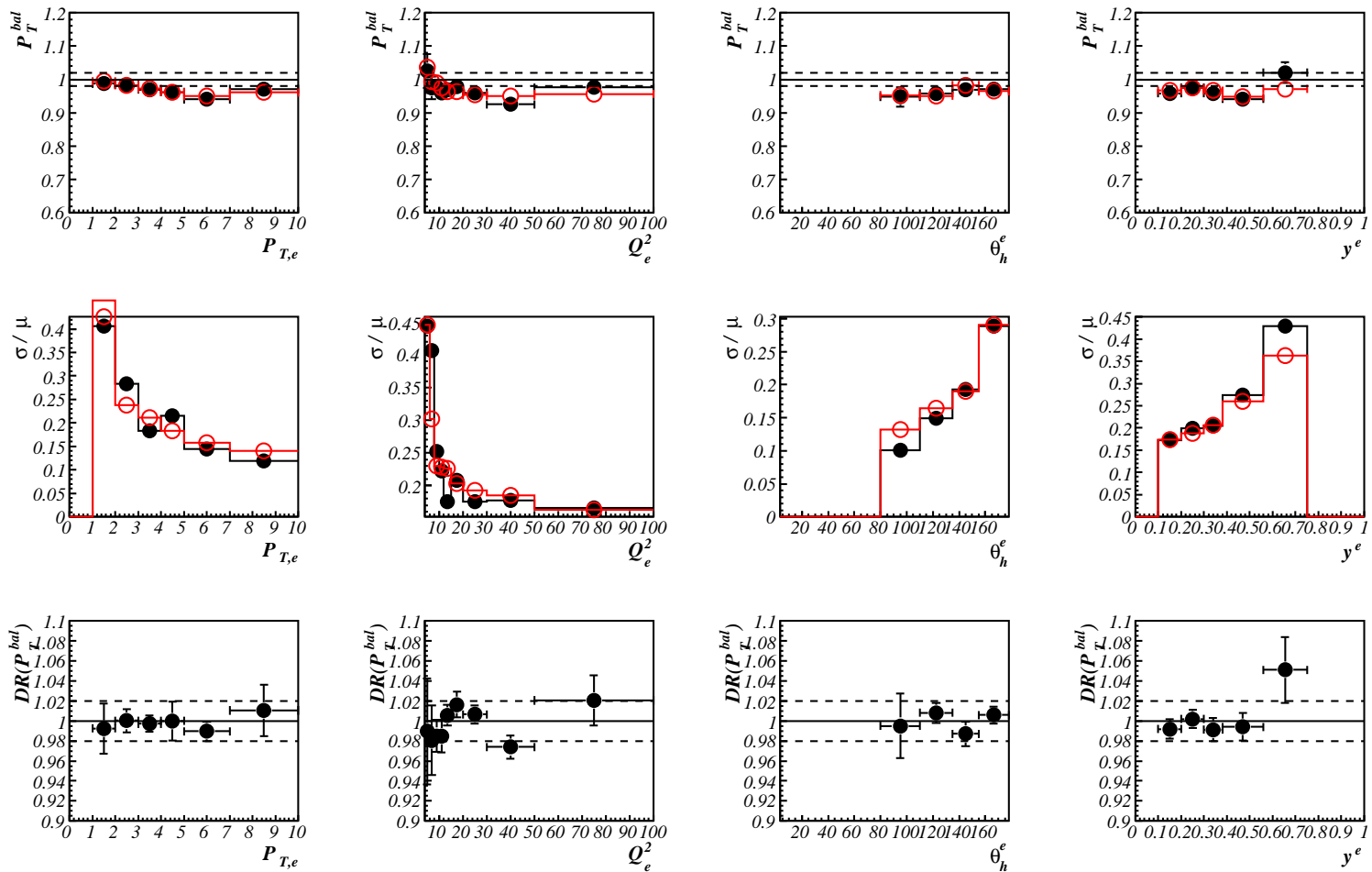


Figure 7.18:  $p_T^{bal}$  (top row) and  $\frac{\sigma}{\mu}$  (middle row) in data (black) and Monte Carlo (red) together with the  $DR(p_T^{bal})$  after the iterative calibration shown in bins of  $p_{T,e}^e$ ,  $Q_e^2$ ,  $\theta_h^e$  and  $y_e^e$ . The low energy data are shown. The calibration successfully pushes the hadronic energy scale uncertainty down to 2%.

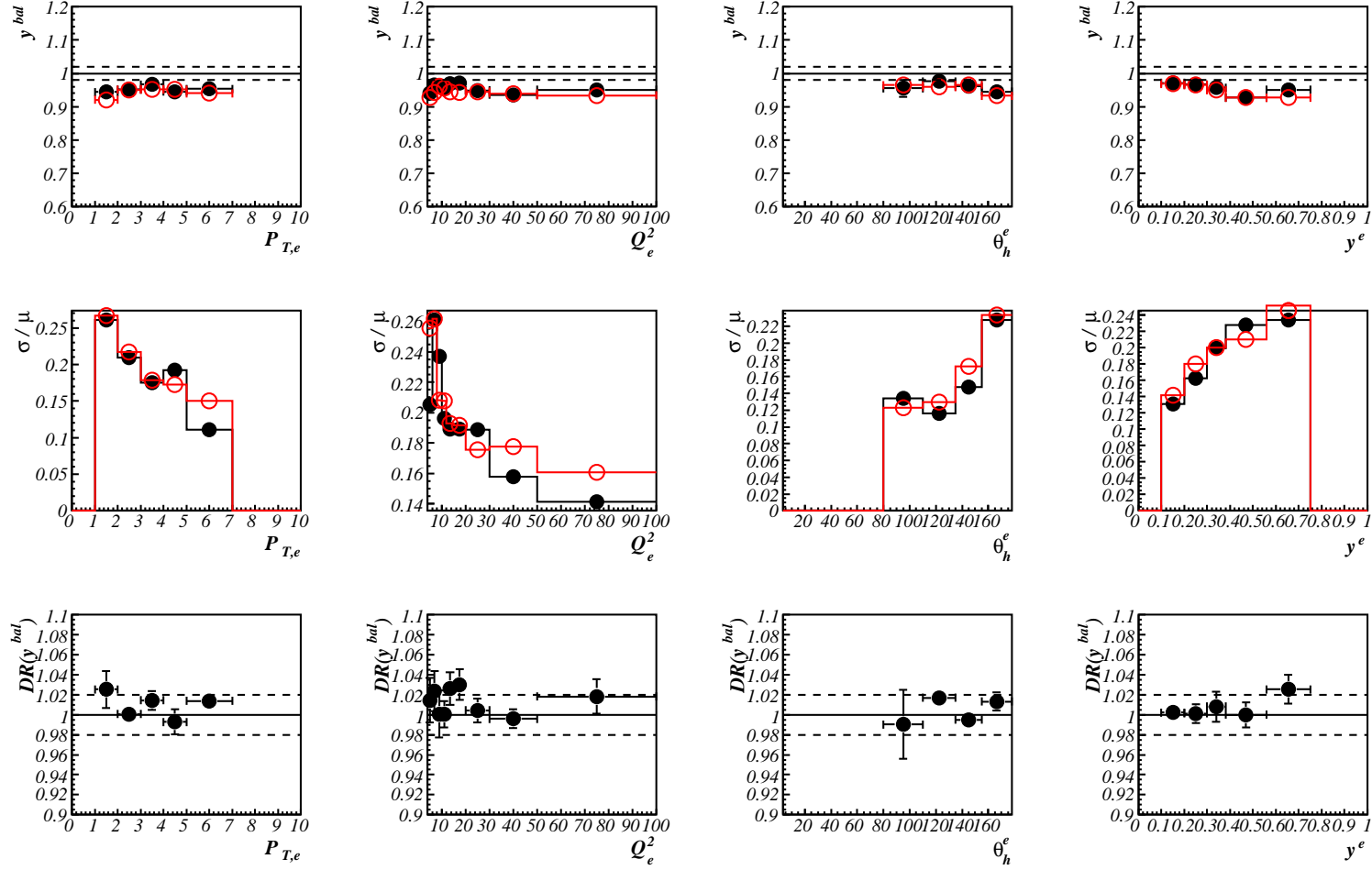


Figure 7.19:  $y^{bal}$  (top row) and  $\frac{\sigma}{\mu}$  (middle row) in data (black) and Monte Carlo (red) together with the  $DR(y^{bal})$  after the iterative calibration shown in bins of  $p_{T,e}^e$ ,  $Q_e^2$ ,  $\theta_h^e$  and  $y^e$ . The low energy data are shown. The  $y^{bal}$  agrees within 2%.

Selection Description	Values
Number of final state particles	$N_{particles}^{FS} = 3$
Central tracks	
$\pi^+\pi^-$ topology	$N_{tracks}^{central} = 2, \quad Q_1 + Q_2 = 0$
or	
$\pi^+\pi^-e^+$ topology	$N_{tracks}^{central} = 3, \quad Q_1 + Q_2 + Q_3 = 1$

Table 7.14: Vector meson selection.

the hadronic final state are detected. It is a simple topology cut that uses the central tracks, and selects either two opposite charged central tracks (the scattered positron is assumed to have a track outside the central region) or three central tracks with a total positive charge. In the second case, one of the central tracks is assumed to correspond to the scattered positron, therefore the requirement on the total charge translates into a selection of two particles from the final state  $X$  with an opposite charge. The **vector meson selection** in addition to the **analysis selection** and the **diffractive selection** is used in order to fix the normalisation of the DIFFVM Monte Carlo components. The selection criteria are listed in Table 7.14.

The selection is suitable especially for  $\rho$  resonances that decay into  $\pi^+\pi^-$  with almost 100% branching ratio, and  $\phi$  resonance where the main decay channel is the  $K^+K^-$  production. On the other hand,  $\omega$  resonances dominantly decay into  $\pi^+\pi^-\pi^0$  with 89.1% probability, and the branching ratio of the decay into  $\pi^+\pi^-$  is only 1.7%. Therefore, only a limited sensitivity of this selection to the  $\omega$  resonances can be expected. The same holds for  $J/\Psi$  which is too heavy to expect a decay only into two hadrons. Therefore the normalisation of the DIFFVM components is also cross checked by looking at the description of data at low  $M_X$  after the **analysis selection** and the **diffractive selection** only.

Fig. 7.20(a) shows the description of  $E'_e$  in the final analysis sample of  $E_p = 920$  GeV data using the **vector meson selection** as well. Fig. 7.20(b) displays the low  $M_X$  region in the same data set in the final analysis sample without the **vector meson selection**. This level of description is achieved by an appropriate normalisation of the DIFFVM components. The SU(4) relations 7.12 have to be violated in order to give a satisfactory description of data as seen in the figure. The  $J/\Psi$  cross section needs to be reduced by a half. Otherwise, there is an excess of events around the  $J/\Psi$  mass in Monte Carlo. This is not considered as a problem since there is already some model of low mass states in RAPGAP.

The same normalisation factor for DIFFVM models is used for all data sets in the analysis. The normalisation is not well constrained. The uncertainty coming from the DIFFVM normalisation is discussed in Section 7.6.5.

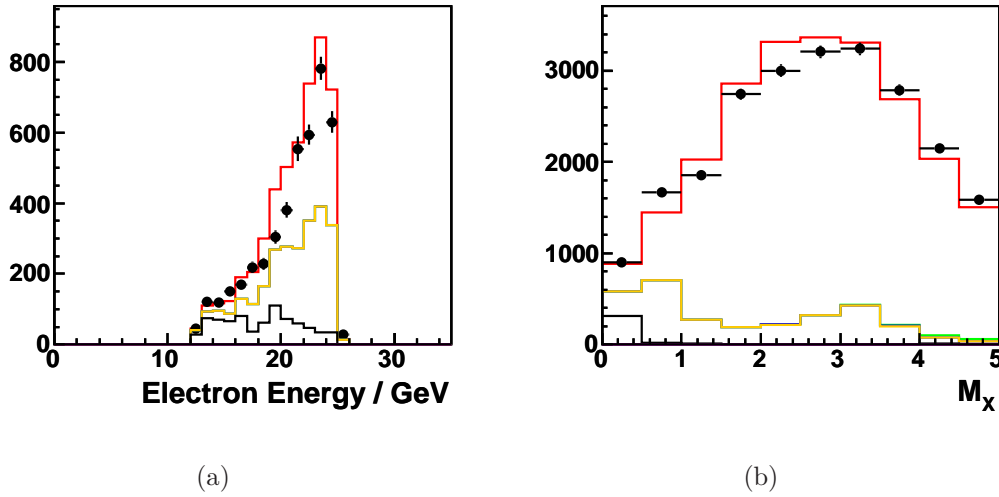


Figure 7.20: High energy data (black points) as described by the sum of Monte Carlo (red). The normalisation of the DIFFVM contribution (yellow) is determined using the dedicated vector meson selection (a) and the low  $M_X$  region in the analysis data sample (b). High energy data sample is shown.

### 7.5.3 Normalisation of the COMPTON Simulation

The COMPTON Monte Carlo model is used to describe background processes from QED-Compton events as well as from the lepton pair production. The **anti-Compton selection** is used in the analysis in order to reduce this background. The remaining events have to be modeled by Monte Carlo and then subtracted from the data using the simulation.

The COMPTON Monte Carlo simulates the QED-Compton events only. However, it is sufficient to use this model also to describe the background from the lepton pair production. Both processes appear as events with the hadronic final state mass  $M_X \sim 0$  GeV. Since the events from the COMPTON Monte Carlo are used to describe both these processes, its luminosity has to be modified. A dedicated selection is used to set the normalisation of the COMPTON Monte Carlo. It requires no hadronic final states by cutting on  $M_X < 0.1$  GeV. It also requires 2 final state particles and 2 tracks at most. The selection criteria of this **Compton selection** are listed in Table 7.15, and they are used together with the **analysis selection** and the **diffractive selection** in order to set the COMPTON Monte Carlo normalisation.

Fig. 7.21 shows the 460 data in the analysis sample after the **Compton selection** as described by the simulation after fixing the normalisation of the COMPTON Monte Carlo. The normalisation factors needed in each data set differ by 30% which is also taken as a systematic uncertainty.

### 7.5.4 Control Plots

Fig. 7.22, 7.23, 7.24 and 7.25 show the control plots for the 2006  $e^+$ , 2007  $e^+$ , low energy and medium energy data, respectively. The distributions of  $y_e$ ,  $Q^2$ ,  $E - p_z$ ,

Selection Description	Values
$M_X$ cut	$M_X < 0.1$ GeV
Number of final state particles	$N_{particles}^{FS} = 2$
Number of central tracks	$N^{central} \leq 2$

Table 7.15: The Compton selection.

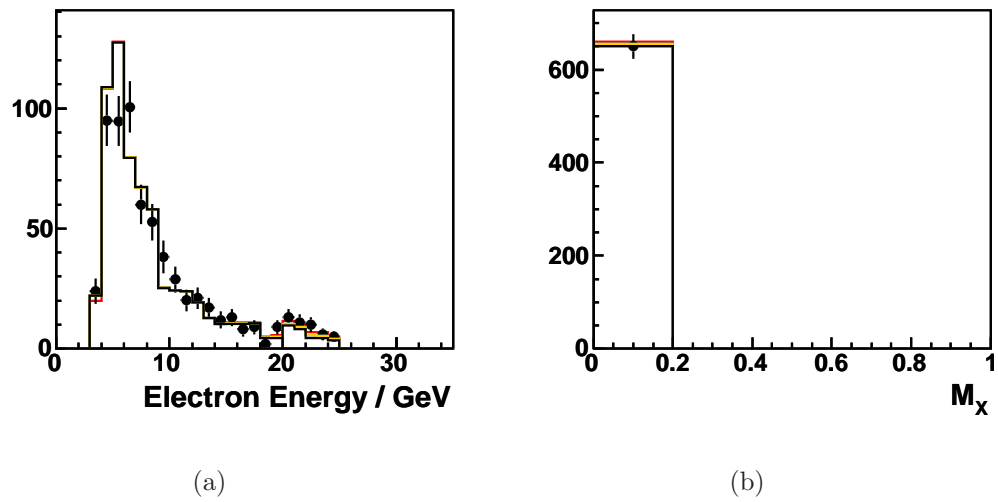


Figure 7.21: Positron energy (a) and  $M_X$  (b) in the low energy data (points) using the dedicated Compton selection as described by the COMPTON Monte Carlo (black line) after fixing its normalisation.

$r_{SPACAL}$  and  $z_{vtx}$  are shown together with the diffractive variables  $\eta_{max}$ ,  $M_X$ ,  $\beta$  and  $x_{\mathcal{P}}$ . In all cases data (points) are well described by the sum of the simulation (red line) and the background estimates.

The signal Monte Carlo models are depicted using different colours, and the individual contributions are stacked on top of each other. The largest contribution comes from the RAPGAP pomeron exchange with light quarks (red line). The second largest contributions is the RAPGAP pomeron exchange with charmed quarks (green line). The reggeon exchange RAPGAP (blue line) contributes only at high  $x_{\mathcal{P}}$ . The vector meson resonances simulated by the DIFFVM Monte Carlo (yellow line) are seen at the low  $M_X$  region, and correspondingly at high  $\beta$ .

There are two background Monte Carlo simulations. The COMPTON Monte Carlo (black line) is visible only at the highest  $\beta$  bins since the reconstructed  $M_X$  in these events is close to 0 GeV. The non-diffractive DJANGO (magenta line) simulates smearing of inclusive processes into the diffractive sample. Therefore, it is visible at high  $\eta_{max}$  and high  $x_{\mathcal{P}}$ .

In the low and medium energy data, a photoproduction background at  $y > y_{trans}$  is determined from data using the wrong charged events. Data at  $y > y_{trans}$  in the plots are only the events with positive reconstructed charge of the scattered positron  $N^+$ . The green histogram corresponds to the events with negative reconstructed charge of the scattered positron candidate. These events are corrected for the background charge asymmetry as described in section 6.3.8. The plotted background events therefore correspond to  $asymN^-$ .

There is no photoproduction background evaluated in the remaining  $y$  region. The high energy data do not consider any photoproduction background at all.

The RAPGAP Monte Carlo here is tuned to generate events according to the diffractive deduced cross section based on the prediction from H1 2006 DPDF Fit B. The DIFFVM and COMPTON Monte Carlo samples are normalised using a dedicated selection.

In all data sets, the simulation gives good description of data.

## 7.6 Extraction of the Diffractive Reduced Cross Section

### 7.6.1 Cross Section Definition

The diffractive reduced cross section in this analysis is measured in bins of  $x_{\mathcal{P}}$ ,  $Q^2$  and  $y$ , and it is related to the triple differential cross section in the following way

$$\sigma_r^D(y, Q^2, x_{\mathcal{P}}) = \frac{Q^4 y}{2\pi\alpha^2 Y_+} \cdot \frac{d\sigma}{dydQ^2dx_{\mathcal{P}}}. \quad (7.13)$$

The following paragraphs give detailed description of how the differential cross section is extracted from the data.

### 7.6.2 Bin Selection

The bin grid (in  $x_{\mathcal{P}}$ ,  $Q^2$  and  $y$ ) for the differential cross section measurement for all three proton beam energies is given in Table 7.16. The measurement in each bin is

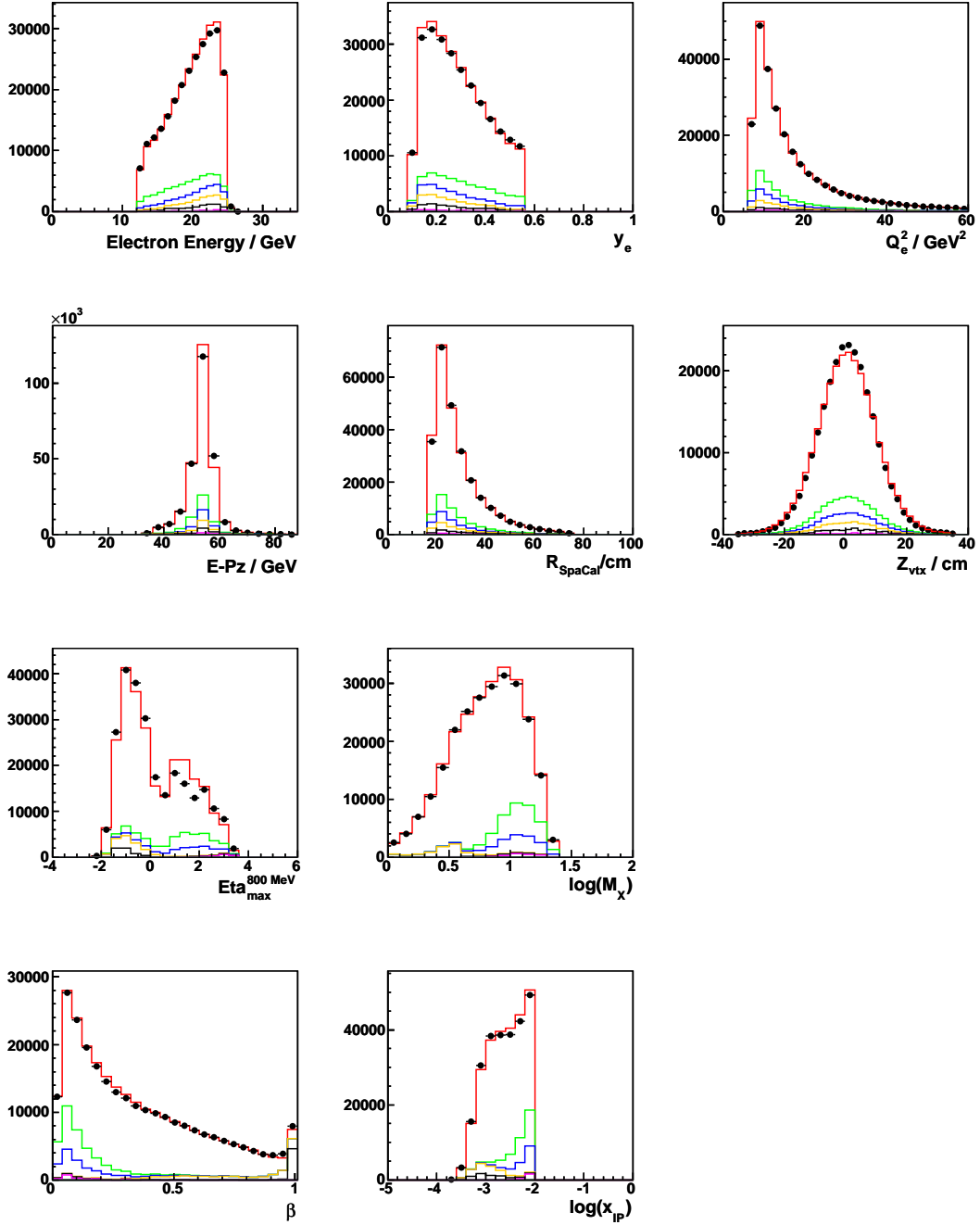


Figure 7.22: Description of the positron energy,  $y_e$ ,  $Q^2$ ,  $E - p_z$ ,  $r_{SPACAL}$ ,  $z_{vtx}$ ,  $\eta_{max}$ ,  $M_X$ ,  $\beta$  and  $x_{IP}$  in the 2006  $e^+$  data sample. The data (points) are shown compared to the sum of the Monte Carlo simulations and background estimates (red line). The solid green histogram shows the data with negatively charged linked tracks. The individual Monte Carlo contributions are: RAPGAP pomeron exchange with light quarks (red) and charm quark (green), RAPGAP reggeon exchange (blue), DIFFVM (yellow), COMPTON (black), and non-diffractive DJANGO (magenta).

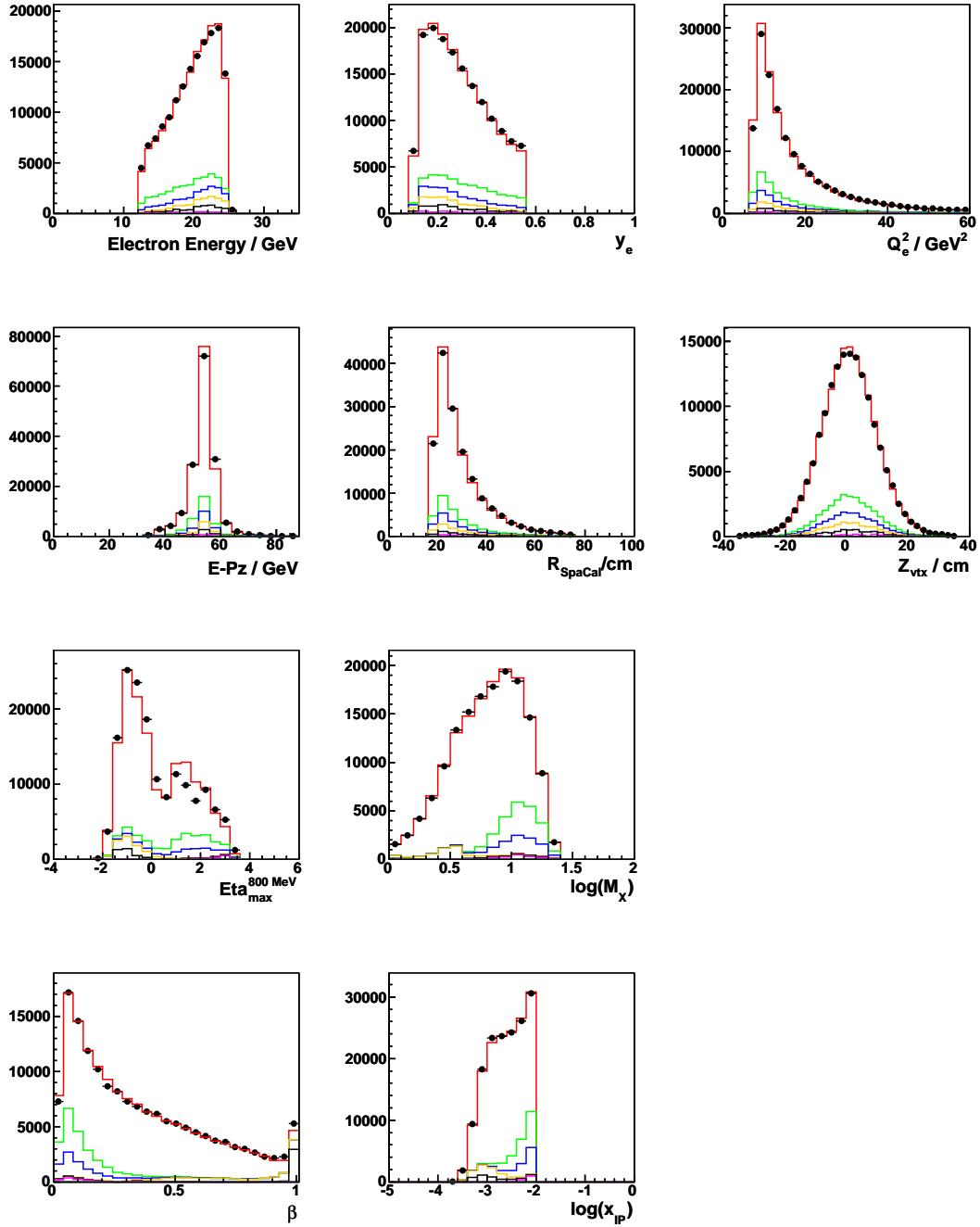


Figure 7.23: Description of the positron energy,  $y_e$ ,  $Q^2$ ,  $E - p_z$ ,  $r_{\text{SPACAL}}$ ,  $z_{\text{vtx}}$ ,  $\eta_{\text{max}}$ ,  $M_X$ ,  $\beta$  and  $x_{\text{IP}}$  in the 2007  $e^+$  data sample. The data (points) are shown compared to the sum of the Monte Carlo simulations and background estimates (red line). The solid green histogram shows the data with negatively charged linked tracks. The individual Monte Carlo contributions are: RAPGAP pomeron exchange with light quarks (red) and charm quark (green), RAPGAP reggeon exchange (blue), DIFFVM (yellow), COMPTON (black), and non-diffractive DJANGO (magenta).

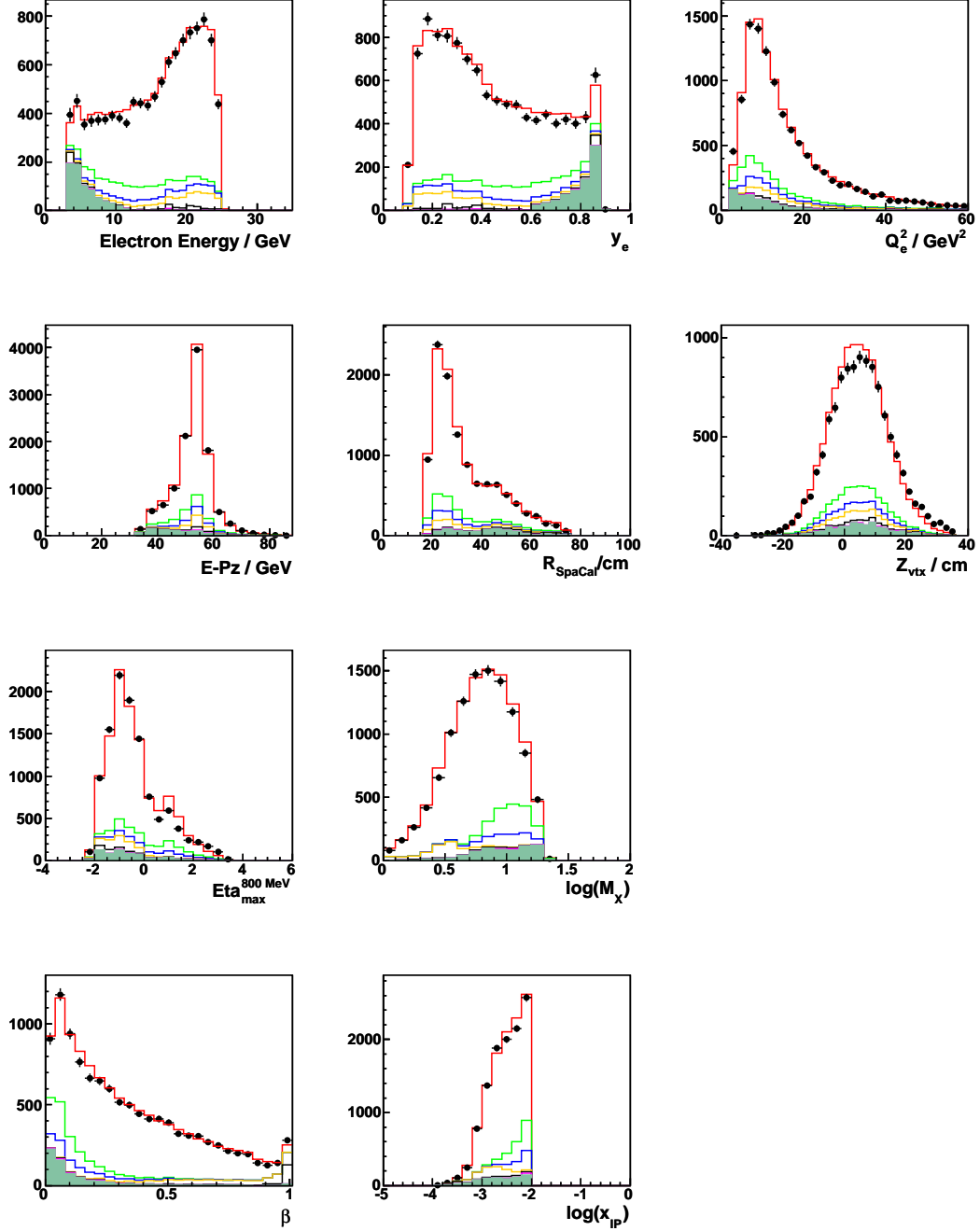


Figure 7.24: Description of the positron energy,  $y_e$ ,  $Q^2$ ,  $E - p_z$ ,  $r_{\text{SPACAL}}$ ,  $z_{\text{vtx}}$ ,  $\eta_{\text{max}}$ ,  $M_X$ ,  $\beta$  and  $x_{\text{IP}}$  in the low energy data sample. The data (points) are shown compared to the sum of the Monte Carlo simulations and background estimates (red line). The solid green histogram shows the data with negatively charged linked tracks. The individual Monte Carlo contributions are: RAPGAP pomeron exchange with light quarks (red) and charm quark (green), RAPGAP reggeon exchange (blue), DIFFVM (yellow), COMPTON (black), and non-diffractive DJANGO (magenta).

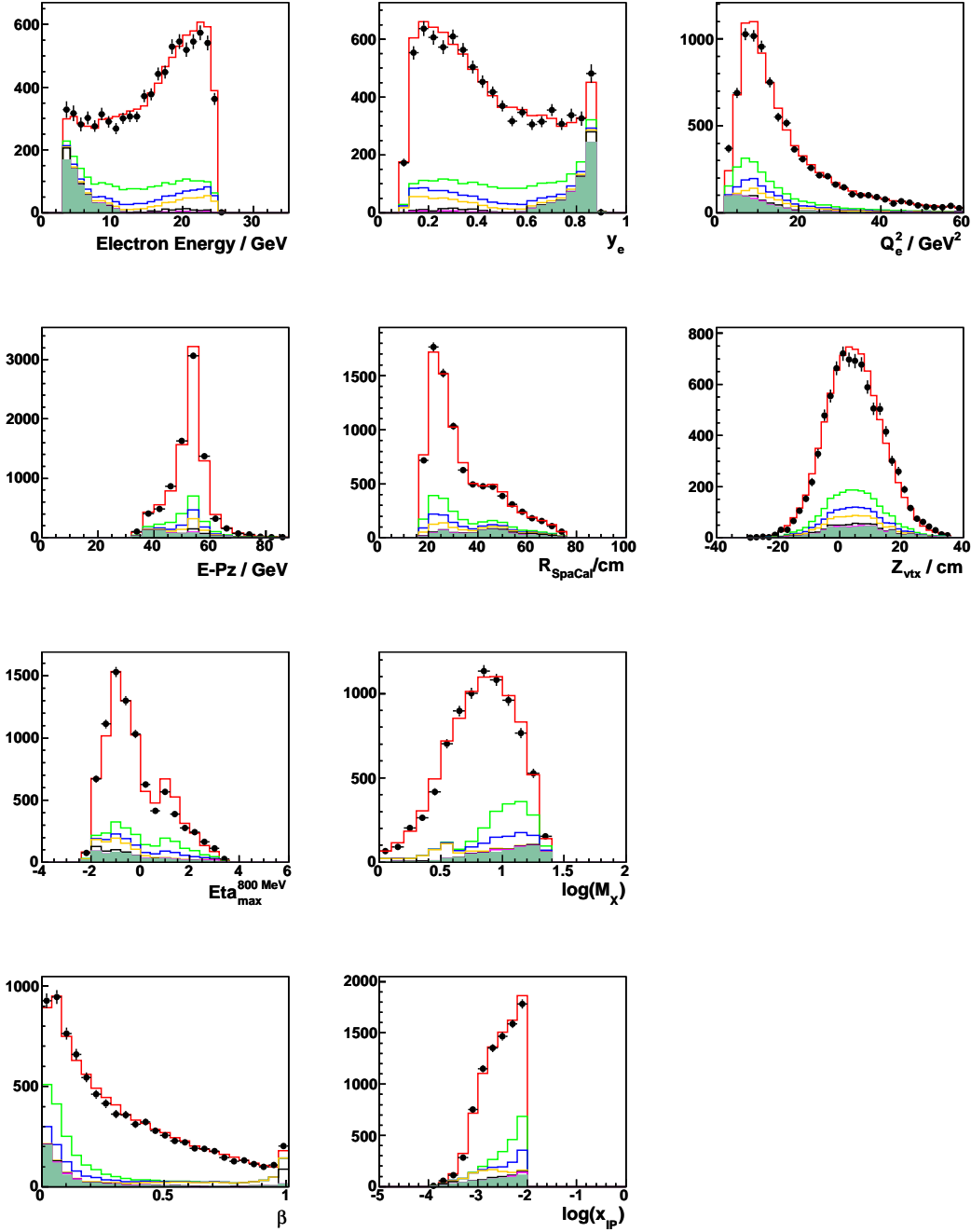


Figure 7.25: Description of the positron energy,  $y_e$ ,  $Q^2$ ,  $E-p_z$ ,  $r_{SPACAL}$ ,  $z_{vtx}$ ,  $\eta_{max}$ ,  $M_X$ ,  $\beta$  and  $x_{IP}$  in the middle energy data sample. The data (points) are shown compared to the sum of the Monte Carlo simulations and background estimates (red line). The solid green histogram shows the data with negatively charged linked tracks. The individual Monte Carlo contributions are: RAPGAP pomeron exchange with light quarks (red) and charm quark (green), RAPGAP reggeon exchange (blue), DIFFVM (yellow), COMPTON (black), and non-diffractive DJANGO (magenta).

Variable	Bin edges
$E_p = 920$ GeV	0.045, 0.075, 0.12, 0.19, 0.3, 0.35, 0.4, 0.45
$y$ $E_p = 575$ GeV	0.072, 0.12, 0.2, 0.304, 0.48, 0.56, 0.64, 0.72
$E_p = 460$ GeV	0.09, 0.15, 0.24, 0.38, 0.6, 0.7, 0.8, 0.9
$Q^2$	2.5, 7, 19, 100
$x_{\mathcal{P}}$	0.0001, 0.001, 0.01

Table 7.16: Bin edges. The  $y$  values are chosen in such a way that the  $\beta$  value is the same for all three proton beam energies (following the relation  $Q^2 = xys = x_{\mathcal{P}}\beta ys$ ).

Variable	Bin centres
$E_p = 920$ GeV	0.06, 0.105, 0.155, 0.245, 0.325, 0.375, 0.425
$y$ $E_p = 575$ GeV	0.096, 0.168, 0.248, 0.392, 0.52, 0.6, 0.68
$E_p = 460$ GeV	0.12, 0.21, 0.31, 0.49, 0.65, 0.75, 0.85
$Q^2$	4, 11.5, 44
$x_{\mathcal{P}}$	0.0005, 0.003

Table 7.17: Bin centres. The  $y$  values are chosen in such a way that the  $\beta$  value is the same for all three proton beam energies (following the relation  $Q^2 = xys = x_{\mathcal{P}}\beta ys$ ).

corrected to the central values listed in Table 7.17. The bins are optimised for the  $F_L^D$  measurement. Note that the  $y$  edges and the  $y$  centres are chosen such that the same value of  $\beta$  is received for all three proton beam energies.

Since the low and medium energy data probe high  $y$  the electron reconstruction method is used to define the bin centres and edges, as it has the best resolution there. On the other hand, the highest  $y$  bin edge is at 0.45 in the high energy data analysis. Therefore the average reconstruction method is chosen.

### 7.6.3 Acceptance, Purity, Stability

The three variables acceptance  $A$ , purity  $P$  and stability  $S$  quantify the relationship between the generator (GEN) and reconstructed (REC) level. Cuts are placed on a simulated event at both the GEN and REC level and possible migrations between the bins defined for the differential cross section measurement are studied. There are four scenarios for a given bin  $i$  that are recorded in the following variables:

- $N_{STAY}$  = The number of events that fall into bin  $i$  at both the GEN and REC levels.
- $N_{SMEARIN}$  = The number of events in bin  $i$  at the REC level that fall into a different bin at the GEN level.

- $N_{SMEAROUT}$  = The number of events in bin  $i$  at the GEN level that fall into a different bin at the REC level.
- $N_{LOST}$  = The number of events in bin  $i$  at the GEN level that do not pass the selection cuts at the REC level.

The total number of reconstructed and generated events in bin  $i$  is then given by

$$N_{REC} = N_{STAY} + N_{SMEARIN} \quad (7.14)$$

$$N_{GEN} = N_{STAY} + N_{SMEAROUT}. \quad (7.15)$$

Acceptance, purity and stability are defined as

$$A = \frac{N_{REC}}{N_{GEN}} \quad (7.16)$$

$$P = \frac{N_{STAY}}{N_{REC}} \quad (7.17)$$

$$S = \frac{N_{STAY}}{N_{GEN} - N_{LOST}}. \quad (7.18)$$

The acceptance  $A$  is the ratio of the reconstructed and generated events in bin  $i$ , and therefore is used to correct data for the detector effects. The other two variables, purity  $P$  and stability  $S$ , account for smearing between different bins.  $P$  quantifies the fraction of events at the GEN and REC levels that fall into the same bin.  $S$  quantifies the fraction of events at the GEN and REC level that have the same bin, without taking into account events that are lost (as this is taken into account by the acceptance).

The values of acceptance, purity and stability for each measurement bin must satisfy

$$A > 20\% \quad (7.19)$$

$$P > 50\% \quad (7.20)$$

$$S > 50\% \quad (7.21)$$

in order to ensure that the contents of the bin are well understood. Since there are three variables used to define the cross section grid, then  $1 \sigma$  corresponds to a value of  $(68\%)^3 \approx 30\%$ .

#### 7.6.4 Correcting Data using Simulations

The differential cross section in the diffractive analysis using the large rapidity gap selection is given by

$$\frac{d\sigma^{data}}{dydQ^2dx_P} = \frac{N^{data} - N_{bg}}{A \cdot L \cdot B} \cdot \frac{\sigma_{gen}^{nrad}}{\sigma_{gen}^{rad}} \cdot PDAC \quad (7.22)$$

where  $PDAC$  is the proton dissociation acceptance correction which will be described further on. All other corrections in Eq. 7.22 were already introduced in Section 6.6.1. It was shown that none of the corrections is explicitly needed (they cancel out), and that the number of signal events in data and Monte Carlo, together with the prediction for the cross section of the signal process, is sufficient in order to measure the cross

section. However, this statement is true only if the model used in the Monte Carlo is fully compatible with the model used for the prediction.

In the  $F_L^D$  analysis, the original RAPGAP Monte Carlo is based only on the  $F_2^D$  structure function from H1 2006 DPDF Fit B. The  $F_L^D$  structure function is missing and is added by hand, as explained in Section 7.2.1. Therefore, all the corrections have to be explicitly calculated.

### The Acceptance Correction

The acceptance correction is calculated only from the RAPGAP Monte Carlo. The DIFFVM Monte Carlo is not used in the calculation and its effect on the acceptance correction is taken into account as a systematic uncertainty.

### Bin Centre Corrections

The bin centre corrections are calculated using the prediction from H1 2006 DPDF Fit B.

### Radiative Corrections

The radiative corrections are calculated using RAGPAP with the initial and final state radiation turned on and off.

### The Proton Dissociation Acceptance Correction

The acceptance of the forward parts of the H1 detector determine the range in  $M_Y$  and  $t$  that is measured in a diffractive analysis using the large rapidity gap selection method (see Eq. 7.2). The RAPGAP Monte Carlo simulates only elastic processes where the scattered protons remain intact and does not account for the proton dissociation within these kinematic boundaries. Therefore, the cross section given by the RAPGAP simulation has to be corrected for proton dissociation. The proton dissociation acceptance correction is given by

$$PDAC = \frac{N_{rec}^{PD}(M_Y < 1.6 \text{ GeV}, |t| < 1 \text{ GeV}^2) + N_{gen}^{elastic}}{N_{gen}^{PD}(M_Y < 1.6 \text{ GeV}, |t| < 1 \text{ GeV}^2) + N_{gen}^{elastic}} \quad (7.23)$$

where  $N_{rec}^{PD}(M_Y < 1.6 \text{ GeV}, |t| < 1 \text{ GeV}^2)$  is the number of proton dissociative events reconstructed within the given kinematic range that defines the acceptance of the large rapidity gap selection method,  $N_{gen}^{PD}(M_Y < 1.6 \text{ GeV}, |t| < 1 \text{ GeV}^2)$  is the number of proton dissociative events generated within the same kinematic range, and  $N_{gen}^{elastic}$  is the number of generated elastic processes. The number of generated (not reconstructed) elastic processes is taken in the numerator since the acceptance correction defined in Eq. 7.17 already corrects the elastic processes. The proton dissociation acceptance correction corrects only for the effect of the proton dissociation.

The DIFFVM Monte Carlo is used to simulate proton dissociative processes in order to estimate this acceptance correction. It does not simulate elastic processes, therefore Eq. 7.23 is transformed to

$$PDAC = \frac{N_{rec}^{PD}(M_Y < 1.6 \text{ GeV}, |t| < 1 \text{ GeV}^2) + R_{PD}^{elastic} N_{gen}^{PD}}{N_{gen}^{PD}(M_Y < 1.6 \text{ GeV}, |t| < 1 \text{ GeV}^2) + R_{PD}^{elastic} N_{gen}^{PD}} \quad (7.24)$$

Run period	PDAC
$E_p = 920$ GeV	$1.150 \pm 0.003$
$E_p = 460$ GeV	$1.038 \pm 0.002$
$E_p = 575$ GeV	$1.063 \pm 0.002$

Table 7.18: Proton dissociation acceptance correction (with statistical uncertainty).

where  $R_{PD}^{elastic}$  is the ratio of elastic to proton dissociative cross sections. It is experimentally constrained to be in the range  $0.5 < R_{PD}^{elastic} < 2.0$ .  $R_{PD}^{elastic} = 1$  is the generally assumed value. The equation then reduces to

$$PDAC = \frac{N_{rec}^{PD}(M_Y < 1.6 \text{ GeV}, |t| < 1 \text{ GeV}^2) + N_{gen}^{PD}}{N_{gen}^{PD}(M_Y < 1.6 \text{ GeV}, |t| < 1 \text{ GeV}^2) + N_{gen}^{PD}}. \quad (7.25)$$

Only the DIFFVM events at  $x_p^{gen} < 0.01$  and  $M_Y^{gen} < 5$  GeV are analysed. The  $x_p$  cut coincides with the one used in the  $F_L^D$  analysis and  $M_Y < 5$  GeV is wide enough to approximate all proton dissociative processes needed in Eq. 7.25. The reconstructed events entering the equation also have to pass the large rapidity gap selection ( $\eta_{max} < 3.3$  and the forward detector selection).

The proton dissociation acceptance correction is studied separately for all three proton beam energies. The higher the proton beam energy is the larger PDAC correction is expected, since the final states tend to go more in the forward direction. Table 7.18 lists PDAC for all run periods used in the analysis. Only statistical errors are stated. The total uncertainty is  $\sim 7\%^2$ .

## 7.6.5 Correlated Systematics

This section lists the systematics that can be treated as correlated among the three data sets. They are summarised in Table 7.19 and described in detail in the following lines.

### Electron Systematics

The calorimeter energy scale systematics for the scattered lepton measurement is taken as 0.4% for  $E'_e = 27.5$  GeV and 1% for  $E'_e = 0$  GeV. The uncertainty at  $E'_e = 27.5$  GeV is evaluated by studying the kinematic peak. The energy scale in the lower part of the  $E'_e$  spectrum is determined from  $\pi^0 \rightarrow \gamma\gamma$  studies. QED-Compton events and  $J/\Psi \rightarrow e^+e^-$  decays are used as a cross check for the region in between. The results of an independent study are summarised in Fig. 7.26.

An uncertainty on the scattering angle  $\theta_e$  is also considered. It is determined from the difference between the polar angle of the cluster  $\theta_e^{clus}$  and the polar angle of the corresponding BCREC track  $\theta_e^{BCREC}$ . Fig. 7.27 shows the difference for the

<sup>2</sup>Taken from the latest inclusive analysis of diffractive LRG data. The uncertainty takes into account the experimental constraints on  $R_{PD}^{elastic}$  as well as the precision of the  $M_Y$  modelling in the DIFFVM Monte Carlo.

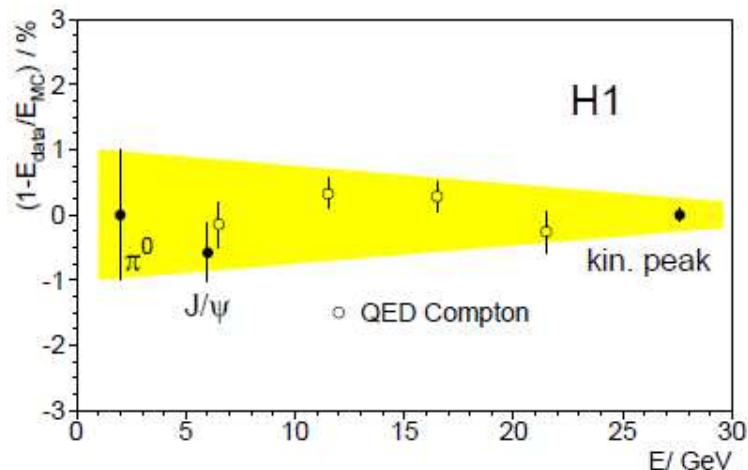


Figure 7.26: Scattered lepton energy scale.

$E_p = 460$  GeV sample. The mean position of the peak in data is described by the RAPGAP simulation within 1 mrad, which is also taken as the systematic uncertainty on  $\theta_e$  determination.

### Hadronic Final State Systematics

The hadronic energy scale systematics of 2% is achieved by the **iterative calibration method**. A separate uncertainty on the calibration of the hadronic SPACAL is considered. The performed studies indicate that the calibration factor  $\alpha_{SPACAL}^{had}$  can be determined with 5% precision which corresponds to the shift of  $\pm 0.075$  (see Fig. 7.28).

Concerning the noise in the LAr calorimeter, an uncertainty of 15% is taken. It is evaluated from the  $\frac{(E-p_z)_{noise}}{(E-p_z)_{total}}$  and  $\frac{(E+p_z)_{noise}}{(E+p_z)_{total}}$  noise fractions (see Fig. 7.29).

### $r_{log}$ Efficiency

The  $r_{log}$  efficiency is described in Section 6.4.5 and has to be corrected for  $y > 0.6$ . The uncertainty on the correction goes from 0.5% to 3% at  $y > 0.8$ . See Table 6.15 for more details.

### Diffraction Systematics

The uncertainties on the  $x_P$  and  $\beta$  distributions used in RAPGAP enters as a model uncertainty and arise from the uncertainties of previous measurements that RAPGAP is based on. The input distributions are reweighted by  $\left(\frac{1}{x_P}\right)^{\pm 0.05}$ ,  $\beta^{\pm 0.05}$  and  $(1 - \beta)^{\pm 0.05}$ .

The  $t$  dependence of the cross section is parametrised as  $e^{Bt}$  where the parameter  $B$  used in RAPGAP is taken from previous H1 measurements. The input distribution is reweighted by  $e^{\pm t}$  in order to reflect the uncertainty on the measured value of  $B$ .

### Vector Meson Monte Carlo

The diffractive production of vector mesons is part of an inclusive diffractive signal. The RAPGAP Monte Carlo does not model the low mass final state well, therefore the

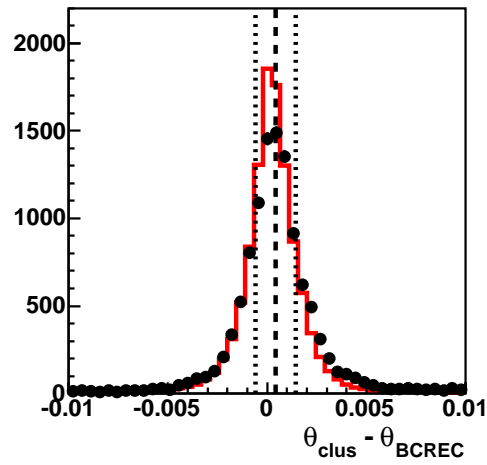


Figure 7.27: The cluster and the BCREC track independently determine the scattering angle  $\theta$ . Data (points) and Monte Carlo (red) peak position of the difference  $\theta_{clus} - \theta_{BCREC}$  agree within 1 mrad (illustrated by dotted lines).

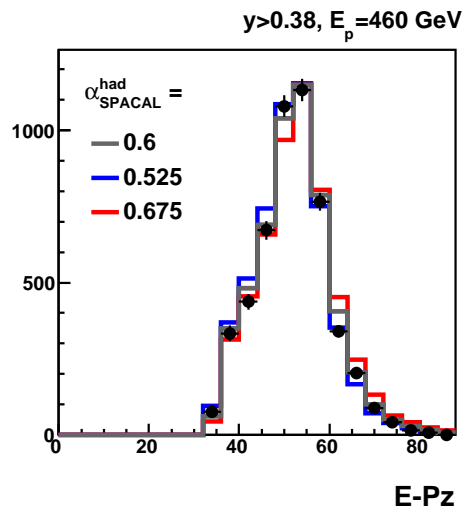


Figure 7.28: Uncertainty on the hadronic SPACAL calibration. The calibration constant is determined from the  $E - p_z$  position at high  $y$ . The data are well described by the simulation within  $\alpha_{SPACAL}^{had} \pm 0.075$ . The low energy data sample is shown.

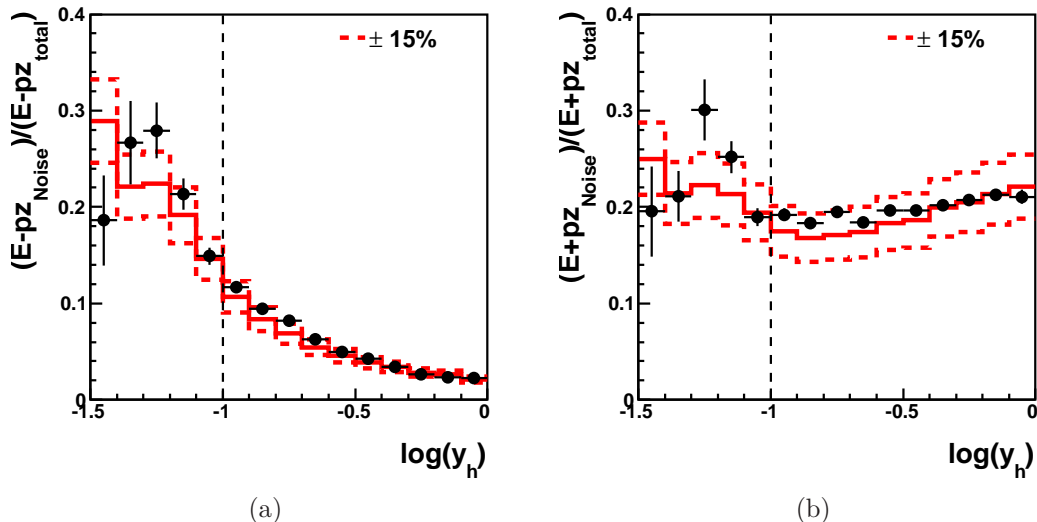


Figure 7.29:  $E - p_z$  and  $E + p_z$  noise fractions in the low energy data. The simulation (red) agrees with the data (points) within 15% (illustrated by dashed red lines). The horizontal line at  $y_h = 0.1$  marks the lower  $y$  cut used in the analysis.

DIFFVM model is used in addition to RAGPAP in order to improve the description of data at low  $M_X$ .

The signal Monte Carlo is used in the calculation of the acceptance correction defined in Eq. 7.17. It is the only place where the DIFFVM simulation can enter the cross section extraction in Eq. 7.22. The relative contribution of the DIFFVM events to the final Monte Carlo signal is not well constrained. The effect of the uncertainty of the DIFFVM normalisation on the cross section is evaluated in the following way. The acceptance correction is calculated once using only the RAGPAP simulation and once using the sum of RAGPAP and DIFFVM. The difference between these two corrections directly relates to the change in cross sections. The effect of adding the DIFFVM Monte Carlo in the acceptance correction is visible only in the resonant low  $M_X$  region.

### QED-Compton Monte Carlo

The COMPTON Monte Carlo is used to simulate background from QED-Compton processes and lepton pair production in this analysis. The normalisation of the COMPTON Monte Carlo sample is constrained within 30%. It is changed up and down by this amount and subtracted from data in order to estimate the effect of this uncertainty on the final cross section.

### Non-Diffractive Monte Carlo

The background from non-diffractive processes is simulated with the DJANGO Monte Carlo. The amount of DJANGO processes passing the final event selection in the  $F_L^D$  analysis is scaled by 2 and divided by 2. The effect of this uncertainty on the cross section is evaluated in a similar way as described above.

### Model Uncertainty

As mentioned in Section 7.2.1, the RAPGAP Monte Carlo used in this analysis is reweighted so that it contains the full diffractive reduced cross section  $\sigma_r^D$  from H1 2006 DPDF Fit B. It reflects our state of art of understanding of the diffractive cross sections based on QCD fits to the inclusive data. The gluon density (important at high  $y$ ) is only weakly constrained from the scaling violations.

The RAPGAP prediction is changed by 50% in order to account for the model uncertainty. This is done by changing the  $w(\sigma_r^D)$  introduced in Eq. 7.1 by 50%.

### Bin Centre Correction

However, the previous model uncertainty changes only the prediction used in RAPGAP and does not affect the prediction used in the calculation of the bin centre corrections. The uncertainty on that is evaluated from the difference between bin centre corrections calculated from H1 2006 DPDF Fit B and H1 2006 DPDF Fit A.

### Charge Asymmetry

The charge asymmetry factors  $asym_{data}$  and  $asym_{MC}$  used in the wrong charge background subtraction (see Eq. 6.36) are determined with 2% precision. In order to account also for the charge reconstruction efficiency, the uncertainty is increased to 4%.

## 7.6.6 Uncorrelated Systematics

This section lists the uncorrelated systematics. They are summarised in Table 7.20 and described in detail in the following lines.

### Trigger Efficiency

A global 1% uncertainty on the trigger efficiency is considered. This systematic uncertainty also covers the correction derived for the inefficiency of the hadronic SPACAL trigger elements (see Fig. 6.13(b)).

### CJC Vertex Reconstruction Efficiency

The CJC Vertex Reconstruction efficiency is modelled with a 2% precision for  $x_P > 0.001$ , and a 10% precision below that (see Fig. 7.13). The corresponding global shifts of the reconstruction efficiency in Monte Carlo are considered.

### Track–Cluster Link Efficiency

A 1.5% global uncertainty on the track–cluster link efficiency is used.

### Forward Detector Efficiency

The efficiency correction for the combined FMD, PLUG and FTS 28m selection is evaluated with a 0.5% statistical precision. The corrections derived for different run periods also agree within 0.5%. It is taken as a global uncertainty.

Description	Shift
Electron energy	$\pm 1\% @ E'_e = 0, \pm 0.4\% @ E'_e = 27.5$
Scattering angle $\theta_e$	$\pm 1$ mrad
LAr energy scale	$\pm 2\%$
LAr noise	$\pm 15\%$
Hadronic SPACAL energy	$\alpha_{SPACAL}^{had} \pm 0.075$
$r_{log}$	up to $3\% @ y > 0.8$
$\beta$	$\beta^{\pm 0.05}$ $(1 - \beta)^{\pm 0.05}$
$x_P$	$1/x_P^{\pm 0.05}$
$t$	$\exp(\pm t)$
Vector meson Monte Carlo	$acc(\text{RAPGAP}), acc(\text{RAPGAP}+\text{VM})$
QED-Compton Monte Carlo	*1.3, /1.3
Non-diffractive Monte Carlo	*2, /2
Model uncertainty	$\frac{\sigma_r^D}{F_2^D} \pm 50\%$
Bin centre corrections	$BCC(\text{Fit A}), BCC(\text{Fit B})$
Charge asymmetry	$\pm 0.04$

Table 7.19: Correlated systematic shifts.

Description	Uncertainty
Trigger efficiency	1%
CJC vertex efficiency	$\pm 2\% @ x_P > 0.001$ , $\pm 10\% @ x_P < 0.001$
Track-cluster link efficiency	1.5%
Forward detector efficiency	0.5%
Relative normalisation	$< 2.5\%$
Monte Carlo statistics	

Table 7.20: Uncorrelated systematics.

### Relative Normalisation

The luminosity of HERA-II data is determined with 2.5% precision. In the diffractive analyses using the large rapidity gap selection method, also the uncertainty on PDAC, which is  $\sim 7\%$ , has to be taken into account. In order to reduce this uncertainty, the three data sets are normalised to the H1 2006 DPDF Fit B prediction at high  $\beta$  where the contribution of  $F_L^D$  to the diffractive reduced cross section is negligible. More information on the normalisation is given in Section 7.7.1. All three data sets then give the same cross section at low  $\beta$  and only an uncertainty on the relative normalisation is considered. It is determined by statistics and reads 0.4%, 1.6% and 2.1% for high, low and medium energy data, respectively.

### Monte Carlo Statistics

In each measurement bin, the statistical error on the number of events at the reconstructed level in Monte Carlo is added in quadrature to the total uncorrelated systematic uncertainty. This uncertainty reflects the statistical precision of the Monte Carlo corrections that are applied to data in order to extract cross sections. This uncertainty should be negligible with respect to the statistical precision of data. Therefore, the statistics in Monte Carlo should be at least three times larger than in data (optimal statistics is ten times larger).

### 7.6.7 Cross Section

The acceptance, purity and stability have to fulfil the requirements of  $A > 20\%$ ,  $P > 50\%$  and  $S > 50\%$  in order to ensure that a cross section measurement in a particular bin is understood (see Section 7.6.3). Only the cross section measurements that fulfil these criteria are considered among the results. Some of the points in the plots of acceptance, purity and stability shown in this section are at  $\beta > 1$ . Values of  $\beta > 1$  result from the choice of the central bin values, and the corresponding cross sections are not shown, since the central values are unphysical.

As the high energy data are analysed only at  $Q^2 > 7 \text{ GeV}^2$ , the  $F_L^D$  measurement uses the results from the published analysis of  $E_p = 820 \text{ GeV}$  data for  $Q^2 < 7 \text{ GeV}^2$ .

The cross section measurements from the publication are moved so that they can be used in the binning chosen for the  $F_L^D$  analysis.

Fig. 7.30 shows the diffractive reduced cross sections and the corresponding acceptance, purity and stability for the  $2.5 < Q^2 < 7 \text{ GeV}^2$  and  $0.0001 < x_P < 0.001$  bin. Based on the low acceptance, only three  $\beta$  bins are kept at  $E_p = 575 \text{ GeV}$ . In the low energy data, there are also three  $\beta$  bins kept although the lowest  $\beta$  cross section point has an acceptance below 20%. Because of the poor statistics, the bin is merged with the following one for the  $F_L^D$  extraction. The average acceptance of the combined bin is then larger than 20%.

Fig. 7.32 shows the diffractive reduced cross sections and the corresponding acceptance, purity and stability for the  $2.5 < Q^2 < 7 \text{ GeV}^2$  and  $0.001 < x_P < 0.01$  bin. The highest  $\beta$  point is excluded on grounds of poor acceptance. The two lowest  $\beta$  bins are merged together for the  $F_L^D$  extraction in order to improve the statistical precision.

At  $Q^2 < 7 \text{ GeV}^2$ , the data cross sections are compared to the low  $Q^2$  extrapolation of the H1 2006 DPDF Fit B as it was extracted only from data at  $Q^2 > 8.5 \text{ GeV}^2$ ,  $\beta < 0.8$  and  $M_X > 2 \text{ GeV}$ . The data are significantly above the prediction which is a known feature of the fit, seen already in the original publication [12].

The diffractive reduced cross sections for  $Q^2 > 7 \text{ GeV}^2$  are shown in Fig. 7.31, 7.32 and 7.34. There are no points excluded because of low acceptance, purity or stability. The two lowest  $\beta$  points in the low  $x_P$  are merged in order to improve the precision of the  $F_L^D$  measurement. There are also two points at  $\beta > 0.8$  that are beyond the range of validity of the H1 2006 DPDF Fit B. These bins also fall into the resonant low  $M_X$  region and the prediction is steeply falling in these bins. Therefore, the bin centre corrections cannot be trusted, and only the bin averaged value for the cross section can be stated, i.e. no bin centre correction is applied.

The data at  $Q^2 > 7 \text{ GeV}^2$  are in a good agreement with the H1 2006 DPDF Fit B and confirm the turn-over of the reduced cross sections at low  $\beta$  that comes from the  $F_L^D$  structure function. The agreement with the prediction is an important cross-check of consistency with the previous H1 results.

All the cross section points used in the  $F_L^D$  analysis are shown in Fig. 7.35. The cross sections that are merged for the actual  $F_L^D$  measurement are merged in this plot as well. The bin averaged cross sections are plotted with a horizontal error bar. The cross sections in this figure are shown before the normalisation to H1 2006 DPDF Fit B. The 2.5% uncertainty on the luminosity determination and 7% uncertainty on PDAC lead to the total 7.4% error on the normalisation. This error is not shown in the plots.

The cross section measurements are predominantly statistically limited, especially at high  $y$ . The dominant sources of systematic uncertainties are:

- The largest uncertainty in the low  $x_P$  bins comes from the LAr noise. The low  $x_P$  bins are also influenced by the uncertainty on the vector meson simulation as these bins fall into the resonant low  $M_X$  region.
- The dominant source of systematic uncertainty in the high  $\beta$  bins comes from the bin centre corrections because of large differences of the cross section predictions inside of the measurement bins.
- At low  $\beta$  (high  $y$ ), where  $F_L^D$  is measured, the largest sources of uncertainties are the photoproduction background subtraction, the  $r_{log}$  efficiency and the model

uncertainty originating in the poor knowledge of the gluon densities obtained in the fits to inclusive data.

## 7.7 Extraction of the Longitudinal Structure Function

### 7.7.1 Sensitivity to $F_L^D$ and Relative Normalisation of the Data Sets

The longitudinal proton structure function is suppressed by the factor  $y^2/Y_+$  in the prescription for the reduced cross section. The higher the  $y$  is the higher the contribution from the longitudinal structure function is. The sensitivity of the low energy data set in the forth highest  $y$  bin with central value of  $y = 0.49$  is  $y^2/Y_+ = 19\%$ , and it is chosen as the lowest acceptable sensitivity that is considered for the  $F_L^D$  extraction. Therefore, only the highest four  $y$  bins in each  $Q^2$  and  $x_P$  bin are used to measure  $F_L^D$ .

The cross sections from all three data sets at lower  $y$  should be compatible since the suppression factor  $y^2/Y_+$  is small and the reduced cross section is dominated by the structure function  $F_2^D$ . After the proton dissociation acceptance correction, the cross sections at low  $y$  are compatible within 3%. However, there is also a 2.5% uncertainty on luminosity, and  $\sim 7\%$  uncertainty on PDAC that should be taken into account in the  $F_L^D$  extraction. Such a large uncorrelated uncertainty would make it impossible to measure  $F_L^D$ . However, the fact that the cross sections should be compatible at low  $y$  can be used for a cross normalisation of the data sets and this uncertainty does not have to be taken into account.

Therefore, the data sets are normalised to the prediction from H1 2006 DPDF Fit B in the range  $Q^2 > 7 \text{ GeV}^2$  and  $y < 0.38$  (0.3 and 0.3) for  $E_p = 460$  (575 and 920) GeV data sets, and the uncertainty of this normalisation is  $< 3\%$ . As the published data at  $E_p = 820 \text{ GeV}$  were included in the analysis of the data used as input to H1 2006 DPDF Fit B, they are already consistently normalised.

Fig. 7.36 shows the cross sections at  $Q^2 = 11.5 \text{ GeV}^2$  and  $x_P = 0.003$  from all three data sets on top of each other in order to illustrate which points are used for the  $F_L^D$  extraction and which are used for the relative normalisation.

### 7.7.2 Extraction of the Structure Functions from the Fits

The strategy of extracting the structure functions  $F_2$  and  $F_L$  from the Rosenbluth plots was already explained in Section 5.1. All three cross section measurements in the same  $x_P, Q^2, \beta$  bins from different proton beam energies are plotted in a single plot with the suppression factor  $y^2/Y_+$  on the horizontal axis. The structure functions correspond to the parameters of a liner fit

$$\sigma_r^D = A + \frac{y^2}{Y_+} B \quad (7.26)$$

as  $A = F_2^D$  and  $B = -F_L^D$ .

The following fits are performed in order to extract the results:

- Fit to the cross sections with statistical errors only in order to obtain the statistical uncertainty on  $F_L^D$ .

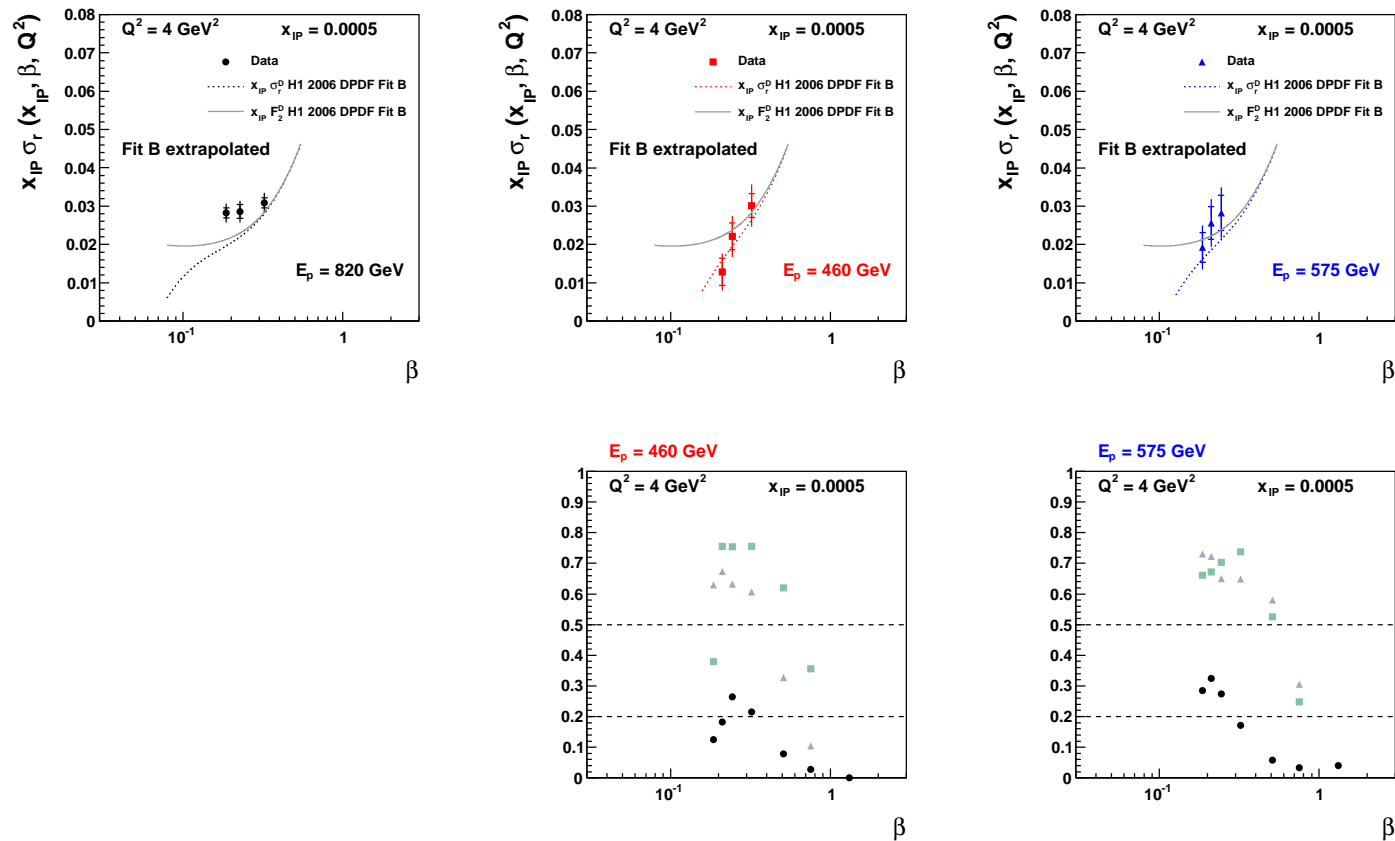


Figure 7.30: Diffractive reduced cross sections multiplied by  $x_P$  and corresponding acceptance, purity and stability for the  $2.5 < Q^2 < 7 \text{ GeV}^2$  and  $0.0001 < x_P < 0.001$  bin as a function of  $\beta$ . In the top row, the data are shown compared to the extrapolation of H1 2006 DPDF Fit B (coloured lines), with the grey line representing the contribution of  $F_2^D$ . Dashed line denote the extrapolation of the fit. The inner error bars represent the statistical uncertainties, the outer error bars show the total error. The cross sections at  $E_p = 820 \text{ GeV}$  are taken from the previous publication. The bottom row shows the acceptance (circles) that is required to be larger than 20%, and the purity (squares) and stability (triangles) that are required to be larger than 50%. Only the cross section measurements that pass these criteria are plotted in the top row.

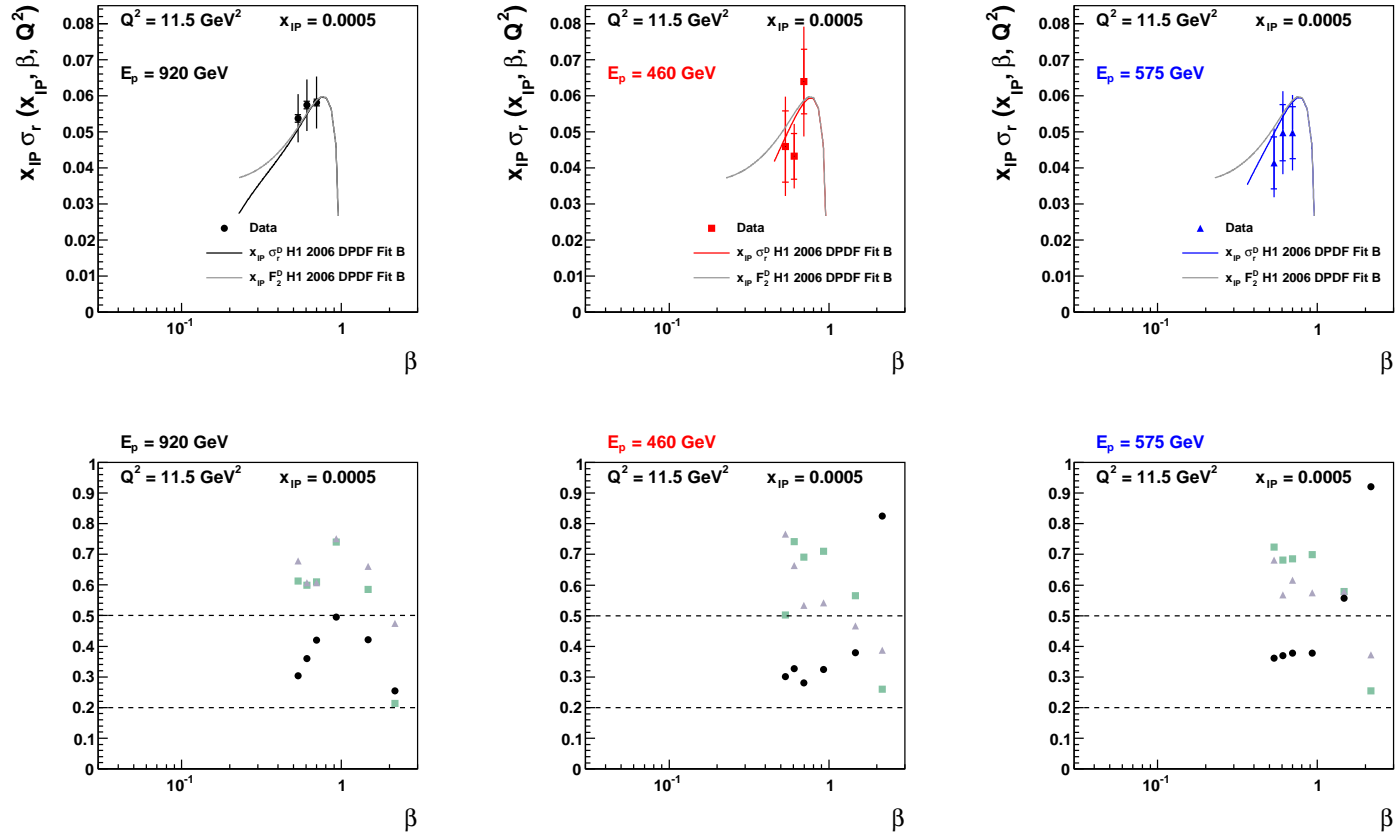


Figure 7.31: Diffractive reduced cross sections multiplied by  $x_{IP}$  and corresponding acceptance, purity and stability for the  $7 < Q^2 < 19 \text{ GeV}^2$  and  $0.0001 < x_{IP} < 0.001$  bin as a function of  $\beta$ . In the top row, the data are shown compared to the extrapolation of H1 2006 DPDF Fit B (coloured lines), with the grey line representing the contribution of  $F_2^D$ . Dashed line denote the extrapolation of the fit. The inner error bars represent the statistical uncertainties, the outer error bars show the total error. The bottom row shows the acceptance (circles) that is required to be larger than 20%, and the purity (squares) and stability (triangles) that are required to be larger than 50%. Only the cross section measurements that pass these criteria are plotted in the top row.

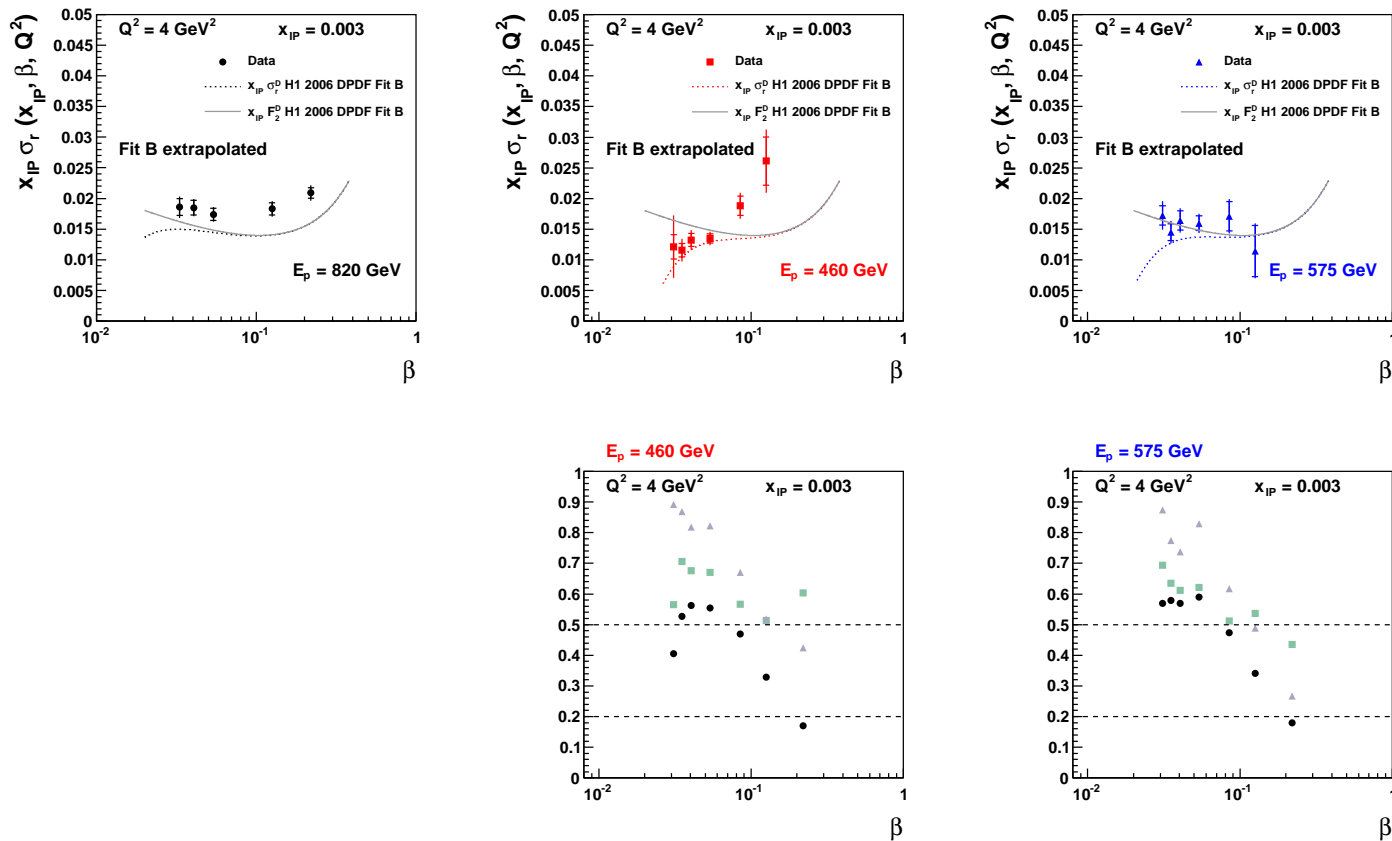


Figure 7.32: Diffractive reduced cross sections multiplied by  $x_{IP}$  and corresponding acceptance, purity and stability for the  $2.5 < Q^2 < 7$  GeV<sup>2</sup> and  $0.001 < x_{IP} < 0.01$  bin as a function of  $\beta$ . In the top row, the data are shown compared to the extrapolation of H1 2006 DPDF Fit B (coloured lines), with the grey line representing the contribution of  $F_2^D$ . Dashed line denote the extrapolation of the fit. The inner error bars represent the statistical uncertainties, the outer error bars show the total error. The cross sections at  $E_p = 820$  GeV are taken from the previous publication. The bottom row shows the acceptance (circles) that is required to be larger than 20%, and the purity (squares) and stability (triangles) that are required to be larger than 50%. Only the cross section measurements that pass these criteria are plotted in the top row.

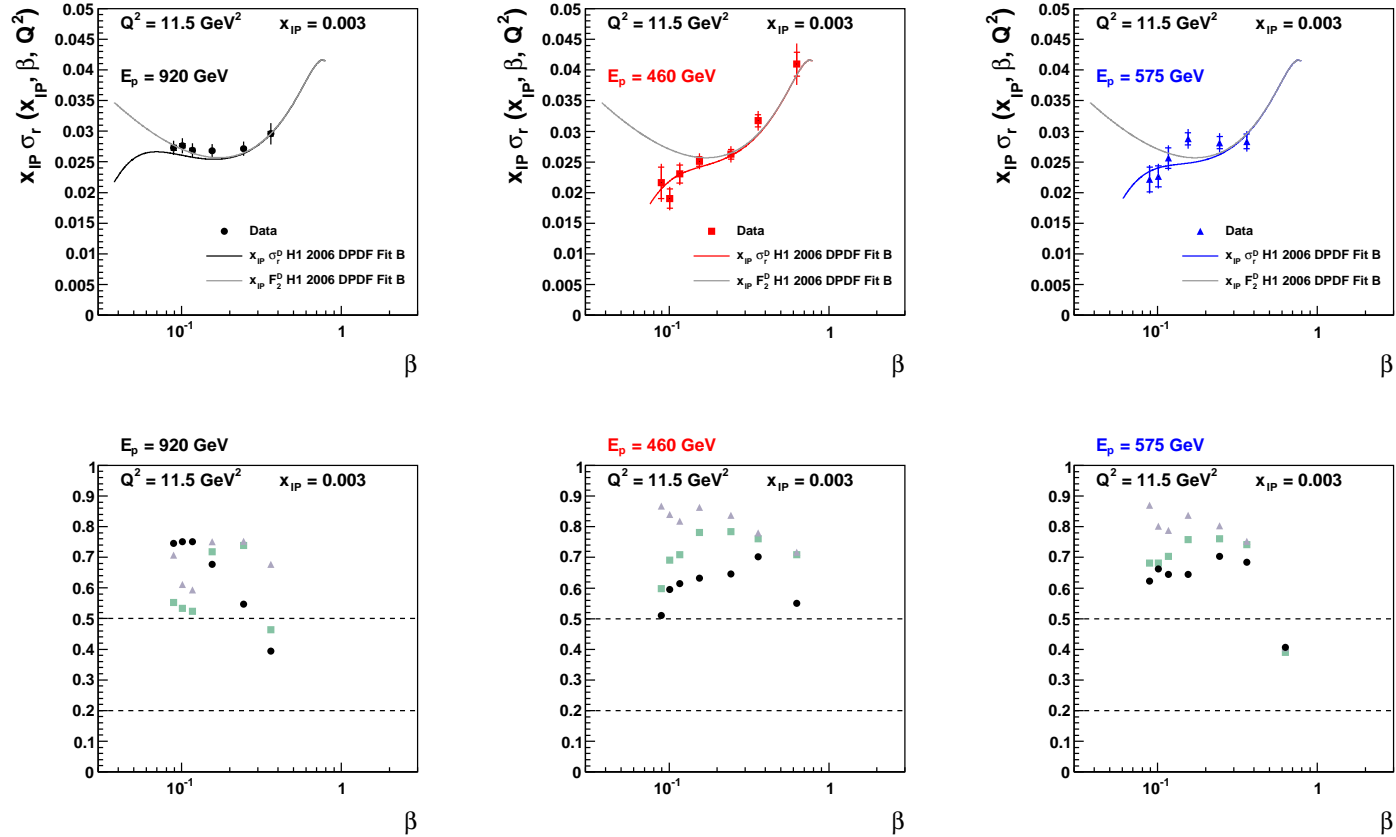


Figure 7.33: Diffractive reduced cross sections multiplied by  $x_{IP}$  and corresponding acceptance, purity and stability for the  $7 < Q^2 < 19 \text{ GeV}^2$  and  $0.001 < x_{IP} < 0.01$  bin as a function of  $\beta$ . In the top row, the data are shown compared to the extrapolation of H1 2006 DPDF Fit B (coloured lines), with the grey line representing the contribution of  $F_2^D$ . Dashed line denote the extrapolation of the fit. The inner error bars represent the statistical uncertainties, the outer error bars show the total error. The bottom row shows the acceptance (circles) that is required to be larger than 20%, and the purity (squares) and stability (triangles) that are required to be larger than 50%. Only the cross section measurements that pass these criteria are plotted in the top row.

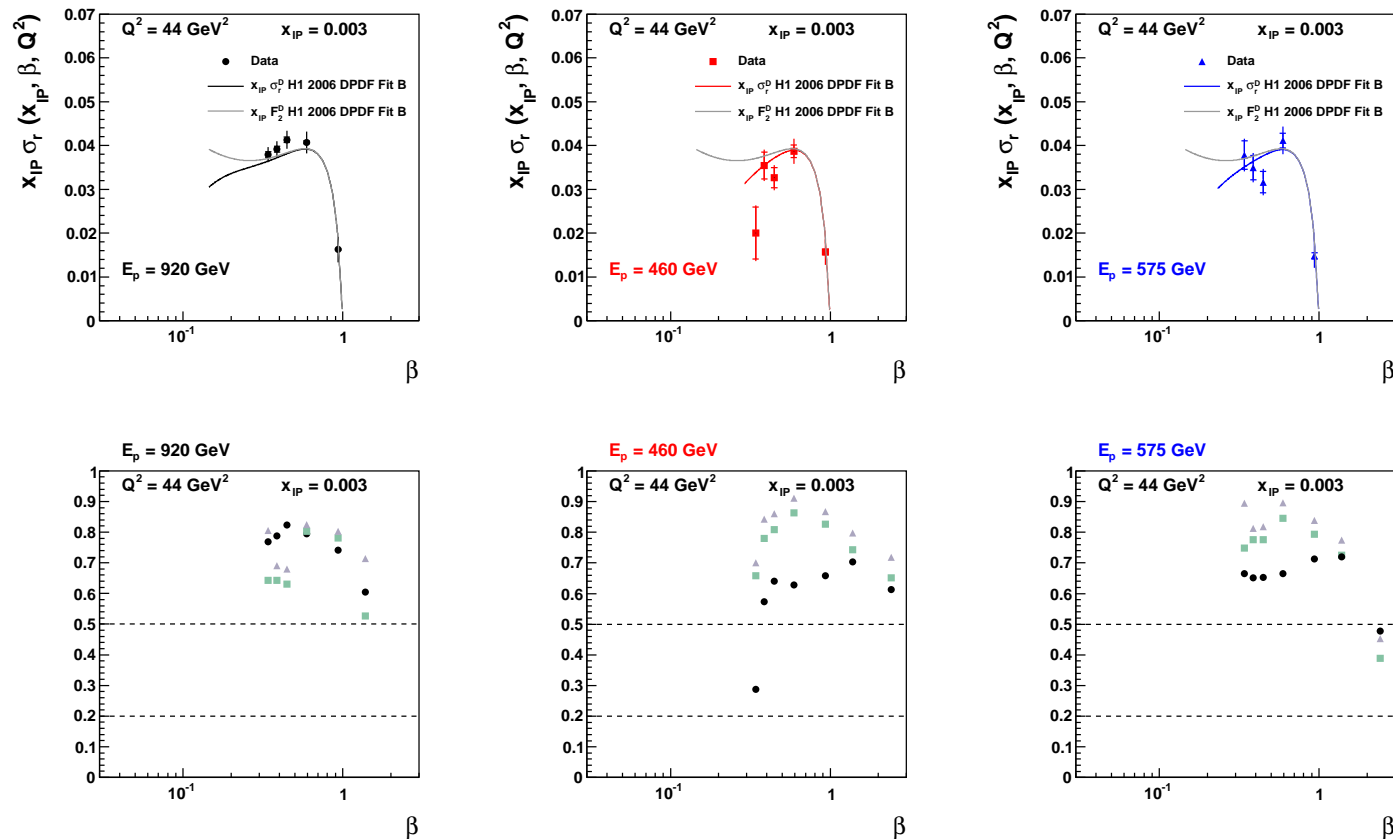


Figure 7.34: Diffractive reduced cross sections multiplied by  $x_{IP}$  and corresponding acceptance, purity and stability for the  $19 < Q^2 < 100 \text{ GeV}^2$  and  $0.001 < x_{IP} < 0.01$  bin as a function of  $\beta$ . In the top row, the data are shown compared to the extrapolation of H1 2006 DPDF Fit B (coloured lines), with the grey line representing the contribution of  $F_2^D$ . Dashed line denote the extrapolation of the fit. The inner error bars represent the statistical uncertainties, the outer error bars show the total error. The bottom row shows the acceptance (circles) that is required to be larger than 20%, and the purity (squares) and stability (triangles) that are required to be larger than 50%. Only the cross section measurements that pass these criteria are plotted in the top row.

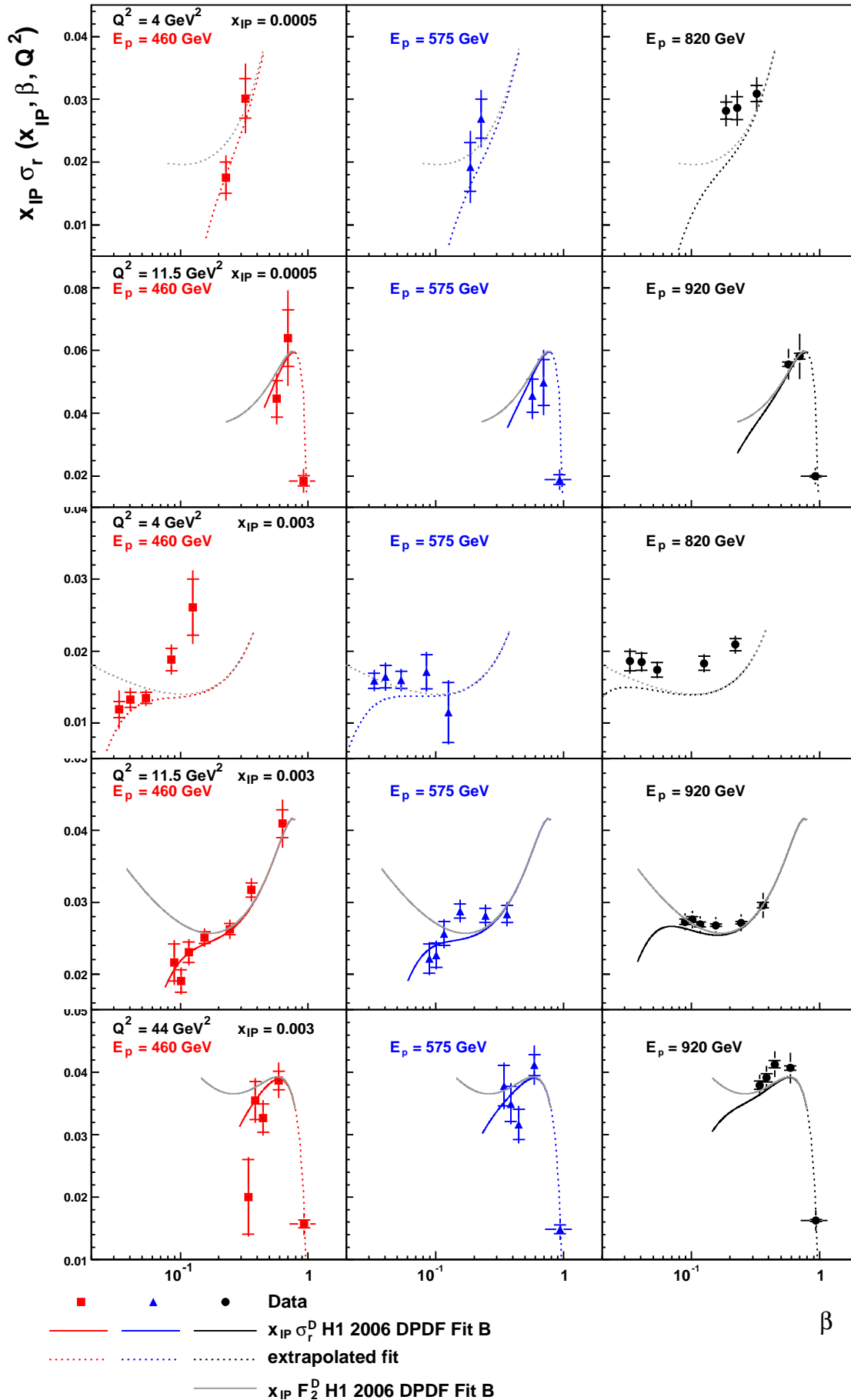


Figure 7.35: Diffractive reduced cross sections multiplied by  $x_P$  compared to the H1 2006 DPDF Fit B prediction. The grey line shows the  $F_2^D$  structure function form the prediction as a reference. The dashed lines represent extrapolations of the fit. The inner error bars represent the statistical uncertainties, the outer error bars show the total error. The data are not normalised to the H1 2006 DPDF Fit B as it is done in

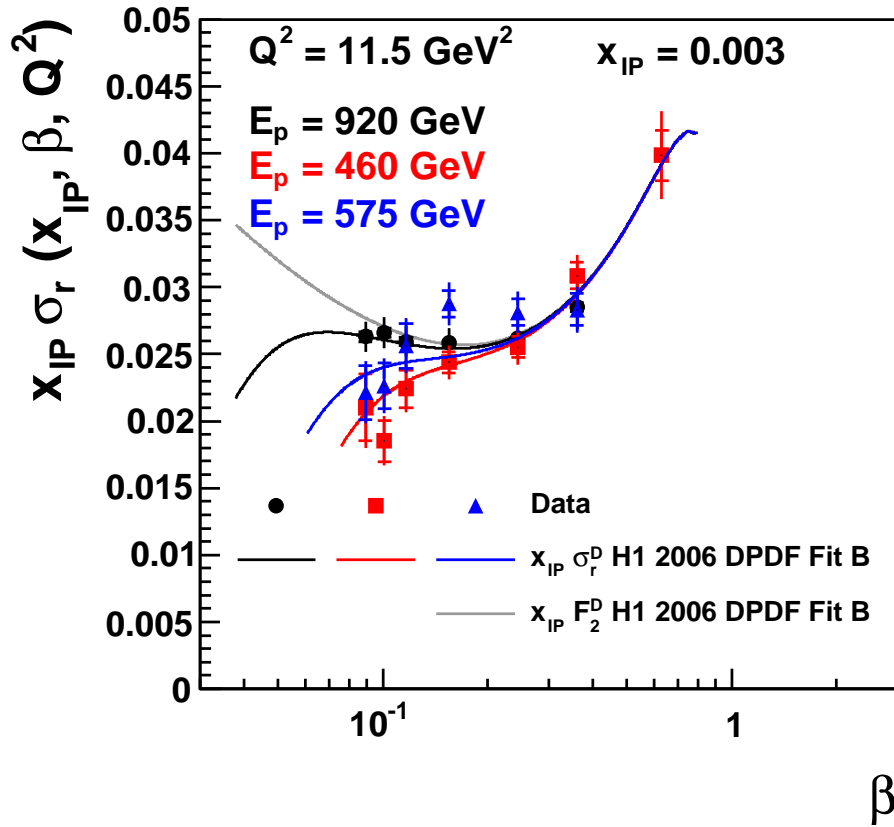


Figure 7.36: Diffractive reduced cross sections multiplied by  $x_{IP}$  measured at  $Q^2 = 11.5 \text{ GeV}^2$  and  $x_{IP} = 0.003$ . The cross sections from different data sets agree well with each other at high  $\beta$  where the contribution from  $F_L^D$  is negligible. The data cross sections are normalised to the prediction from H1 2006 DPDF Fit B there. The cross sections differ at low  $\beta$  where the  $F_L^D$  gives significant contribution. The grey line gives just  $F_2$  as a reference. The high  $\beta$  points are used for the relative normalisation of the data sets and the low  $\beta$  points determine the  $F_L^D$  structure function. The inner error bars represent the statistical error of the measurement, the outer error bars represent the total error.

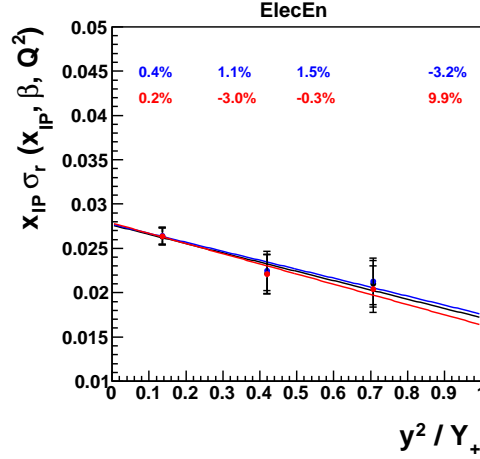


Figure 7.37: Evaluation of the correlated error on  $F_L^D$  from the uncertainty on the positron energy. The black line shows the fit without any shift. The red line is the fit to the points that are shifted up, the blue line is the fit to the points that are shifted down. The changes of the cross section and  $F_L^D$  values are denoted by the corresponding numbers.

- Fit to the cross sections with statistical and uncorrelated errors added in quadrature in order to obtain the  $F_L^D$  value and its statistical and uncorrelated error.
- The correlated uncertainties on  $F_L^D$  are extracted in the following way. The linear fit to the cross sections with statistical and uncorrelated errors is repeated once for the cross sections with the systematic shift up and once for the cross sections with the systematic shift down. The correlated systematic uncertainty is then evaluated as

$$\delta_{cor} = \frac{|(F_L^D)_{shift}^{up} - F_L^D| + |(F_L^D)_{shift}^{down} - F_L^D|}{2F_L^D} \quad (7.27)$$

The procedure is repeated for all correlated systematic shifts and the errors are added in quadrature. Fig.7.37 shows the evaluation of the correlated error for the shift in the positron energy.

Fig. 7.38 shows all the bins used for the  $F_L^D$  measurement. The largest lever arm in  $y^2/Y_+$ , and therefore highest sensitivity to  $F_L^D$ , is evident at the lowest  $\beta$ .

The structure function  $F_2^D$  can be extracted in a similar way.

### 7.7.3 Ratio $R^D$

The ratio  $R^D = \frac{F_L^D}{F_2^D - F_L^D}$  can be simply calculated using the structure functions obtained in the previous fits. However, there is a correlation between the errors on the fit parameters that has to be taken into account when calculating the error on the ratio  $R_D$ . In order to simplify the procedure, the following fit is proposed

$$\sigma_r^D = B + AB\left(1 - \frac{y^2}{Y_+}\right) \quad (7.28)$$

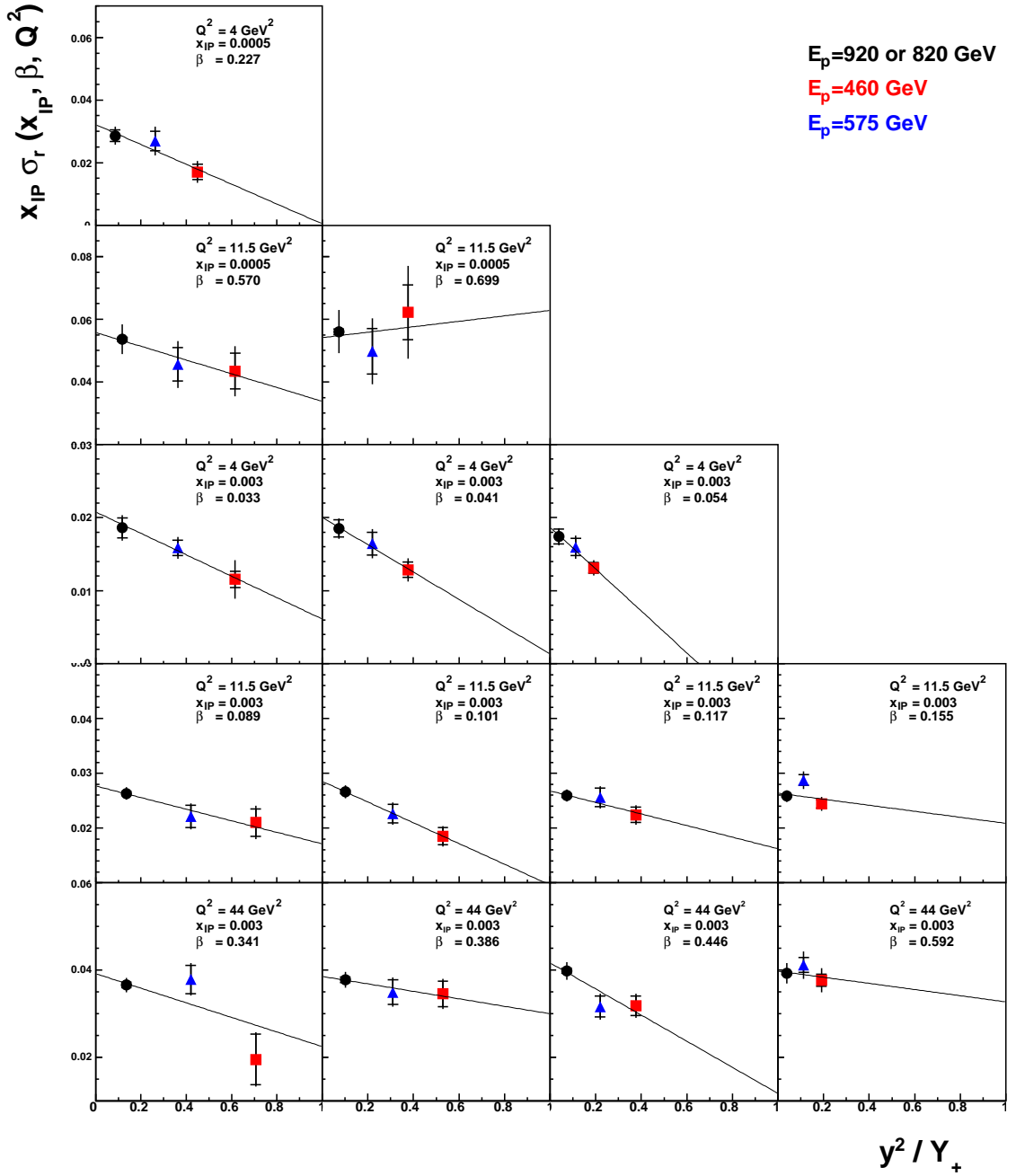


Figure 7.38: Rosenbluth plots. The reduced diffractive cross section  $\sigma_r^D$  multiplied by  $x_{IP}$  as a function of  $y^2/Y_+$  in bins of  $Q^2$ ,  $x_{IP}$  and  $\beta$ . Three beam energies are shown in each bin, where the lowest  $y^2/Y_+$  point is given by the 820 data for  $Q^2 = 4 \text{ GeV}^2$  and by the 920 data at higher  $Q^2$ . The linear fits to the data are also shown, the slope of which gives the value of  $F_L^D$ .

where  $A = R^D$  is directly the ratio  $R_D$  and  $B = F_2^D - F_L^D$ . The statistical, uncorrelated and correlated errors on  $R_D$  are determined in a similar way as in the case of  $F_L^D$  described in the previous section.

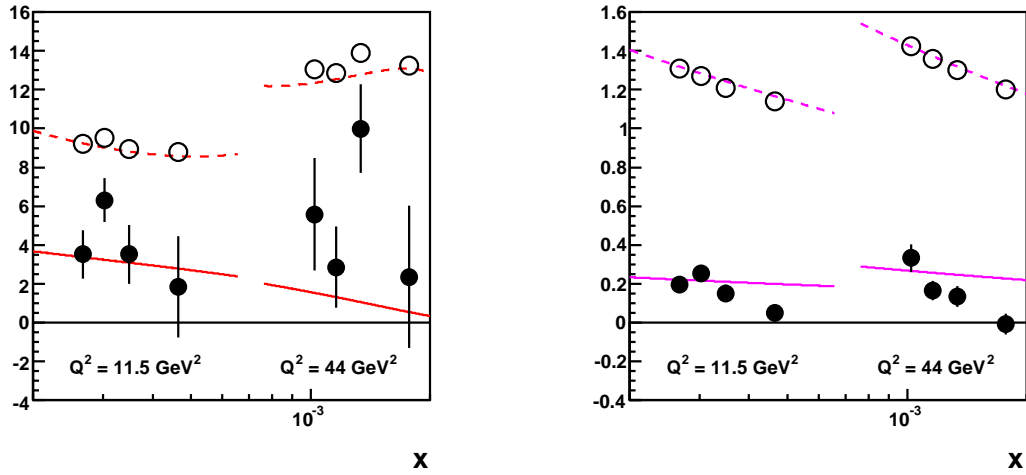
#### 7.7.4 Ratio $R^D/R$

In order to compare the size of the gluon distribution functions in diffractive and inclusive DIS, it is useful to have a look at the fraction  $R^D/R$ . The  $F_L^D$  analysis follows the strategy of the  $F_L$  analysis, and the data sample in the diffractive analysis is a sub-sample of the one used in the inclusive analysis. Therefore, many systematic uncertainties cancel out in the fraction. The ratio is calculated only for  $Q^2 > 7 \text{ GeV}^2$  since there are no high energy data at low  $Q^2$  analysed here. Only the  $R^D$  results from the  $0.001 < x_P < 0.01$  bin are used.

The same  $Q^2$  and  $y$  binning as in the  $F_L^D$  analysis is used for the  $F_L$  analysis in order to calculate the fraction. The inclusive  $F_2$  and  $F_L$  structure functions and the ratio  $R$  are extracted taking into account only the statistical uncertainties. The systematic uncertainties are taken out for the sake of simplicity. This can be justified because the precision of the  $F_L^D$  measurement is largely limited by statistics.

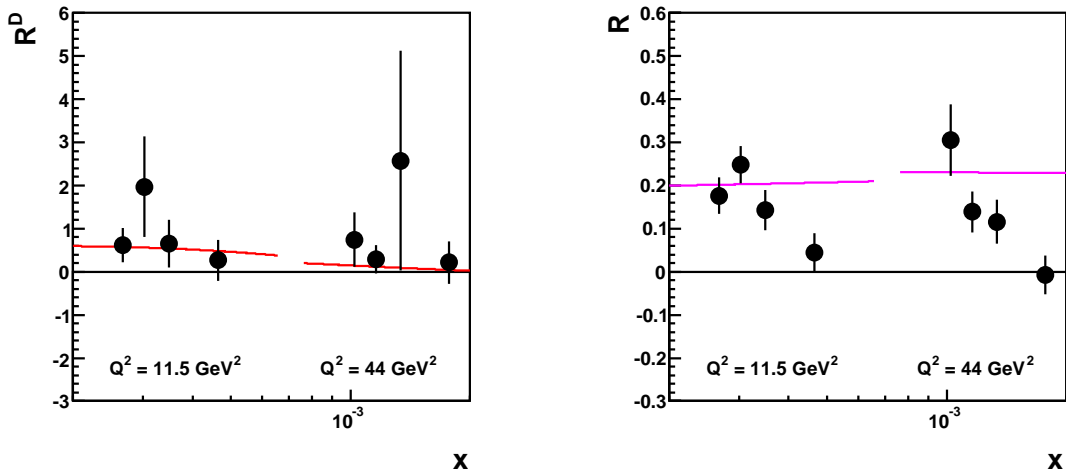
The ratio  $R_D$  is used with the statistical and uncorrelated errors together with the diffractive correlated systematics. All these are added in quadrature. The non-diffractive correlated systematics cancel out in the ratio  $R^D/R$ .

Both the inclusive and diffractive structure functions obtained from the fit with parametrisation in Eq. 7.26 together with the ratios  $R$  and  $R^D$  received from direct fits (using the parametrisation in Eq. 7.28) are shown in Fig. 7.39. The structure functions  $F_L^D$ ,  $F_2^D$  and  $F_L$ ,  $F_2$  agree well with the predictions from H1 2006 DPDF Fit B and H1 2009 PDF. Only the errors used in the  $R^D/R$  calculation are displayed.



(a)  $F_L^D$  (solid circles) and  $F_2^D$  (open circles) as received from the fits compared to the predictions from H1 2006 DPDF Fit B (red lines). The error bars represent the statistical, uncorrelated and diffractive correlated errors added in quadrature. Only the data at  $Q^2 > 7 \text{ GeV}^2$  and  $x_P > 0.001$  are plotted.

(b)  $F_L$  (solid circles) and  $F_2$  (open circles) as received from the fits compared to the predictions from H1 2009 PDF (magenta lines). The error bars represent the statistical error of the measurement.



(c) The ratio  $R^D = \frac{F_L^D}{F_2^D - F_L^D}$  received from the direct fit to the data cross sections (points) are compared to the prediction from H1 2006 DPDF Fit B (red line). The error bars represent the statistical, uncorrelated and diffractive correlated errors added in quadrature.

(d) The ratio  $R = \frac{F_L}{F_2 - F_L}$  received from the direct fit to the data cross sections (points) are compared to the prediction from H1 2009 PDF (magenta line). The error bars represent the statistical error of the measurement.

Figure 7.39: Structure functions  $F_2$  and  $F_L$  and the ratio  $R$ .



# Chapter 8

## Results and Interpretation

### 8.1 Summary of the Results

#### 8.1.1 $F_L^D$

Fig. 8.1 shows all the  $F_L^D$  measurements extracted from the fits. The results are plotted as a function of  $\beta$ , each  $Q^2$  and  $x_{\mathcal{P}}$  value being in a separate plot. Significant, non-zero measurements of  $F_L^D$  are seen in all bins of  $Q^2$  and  $x_{\mathcal{P}}$ . The data are compared to the predictions of the H1 DPDF 2006 Fits A and B and to the Golec-Biernat & Łuszczak model [51]. Although the prediction of Golec-Biernat & Łuszczak lies significantly above both Fit A and Fit B at large  $\beta$ , the precision of the data is insufficient to distinguish between the models. All three models are consistent with the data, although there is a tendency for the measurements to lie above the predictions.

A summary plot of the  $F_L^D$  measurements is given in figure 8.2, where all points from the five  $Q^2$  and  $x_{\mathcal{P}}$  bins are shown as a function of  $\beta$ . In order to remove the significant dependence on  $x_{\mathcal{P}}$ , the  $F_L^D$  points have been divided by a factor  $f_{\mathcal{P}/p}$ , taken from [12], which expressed the measured  $x_{\mathcal{P}}$  dependence of the data, assuming proton vertex factorisation. The  $F_L^D$  data cover a large range in longitudinal fractional momentum  $0.033 < \beta < 0.7$  and the general trend of a slow decrease as a function of  $\beta$  is well reproduced by H1 DPDF 2006 Fit B. The data have a tendency to lie above the prediction, although the precision is limited.

#### 8.1.2 $R^D$

The fits in the Rosenbluth plots allow to extract both structure functions  $F_L^D$  and  $F_2^D$ . The parametrisation of the linear fit can be chosen such that one of the parameters corresponds directly to the ratio  $R^D = \frac{F_L^D}{F_T^D}$  where  $F_T^D = F_2^D - F_L^D$ . The ratio  $R^D$  is extracted for all bins at  $7 < Q^2 < 100 \text{ GeV}^2$ . Fits to the low  $Q^2$  data show no sensitivity to  $R^D$  as the corresponding parameter is returned with large errors. The measured ratios  $R^D$  are shown in Fig. 8.3 and they are consistent with the prediction from H1 2006 DPDF Fit B.

At medium  $Q^2 = 11.5 \text{ GeV}^2$ , the prediction gives  $R^D \sim 0.5$  which means that the longitudinal contribution to the reduced cross section is at the same level as the transversal one (reflecting the fact that there is one longitudinal and two transversal modes). At high  $Q^2 = 44 \text{ GeV}^2$ , data start to lose sensitivity and the prediction from

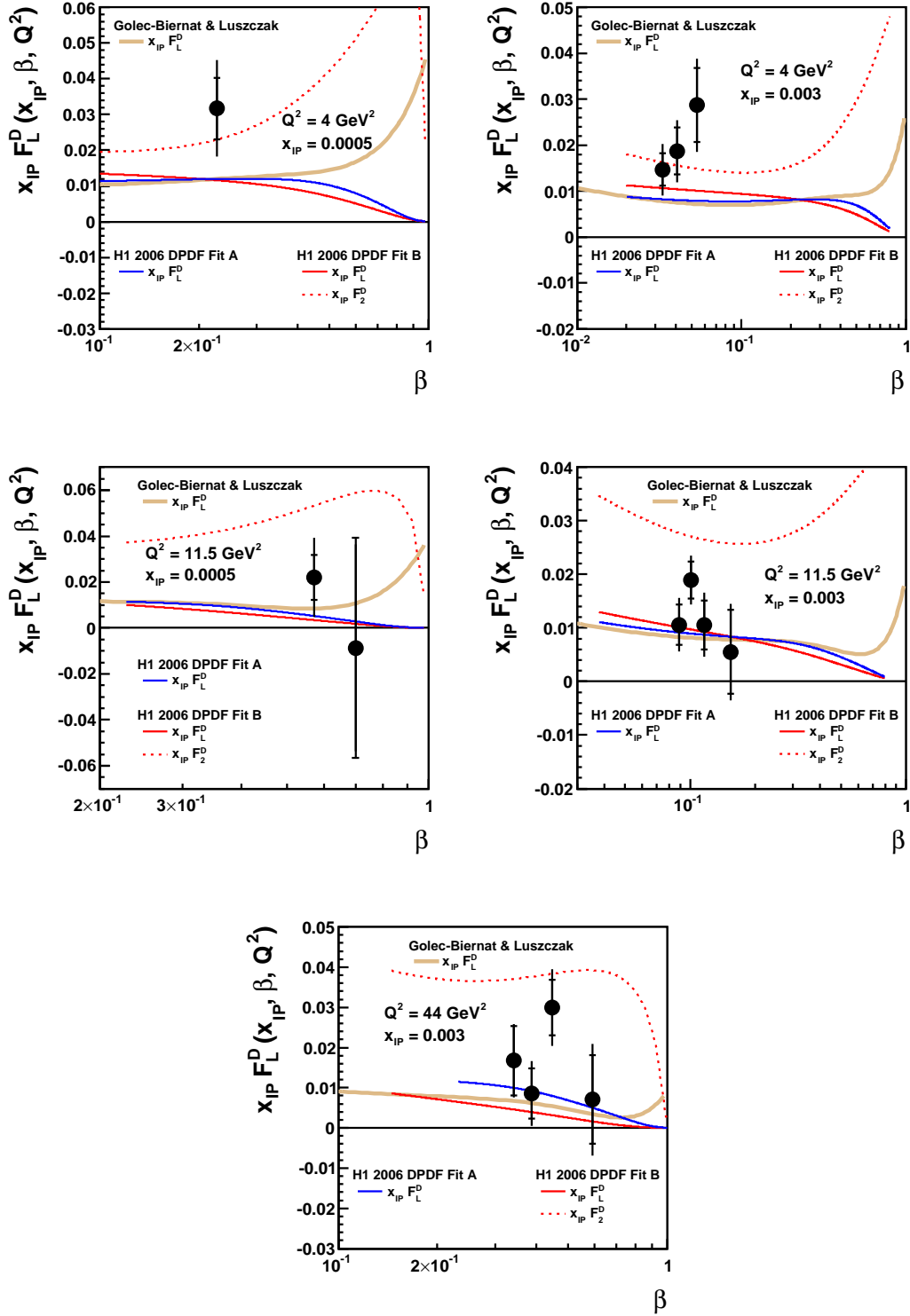


Figure 8.1: The diffractive longitudinal proton structure function  $F_L^D$  multiplied by  $x_{IP}$  in different bins of  $Q^2$  and  $x_{IP}$  plotted as a function of  $\beta$ . The data are shown compared to the predictions of H1 2006 DPDF Fit A (blue line) and Fit B (solid red line). In addition, the value of  $F_2^D$  from Fit B is shown as a red dashed line. The data are also compared to the prediction with a higher twist from the GBW model (solid beige line). The inner error bars represent the statistical error of the measurement, the outer error bars represent the total error.

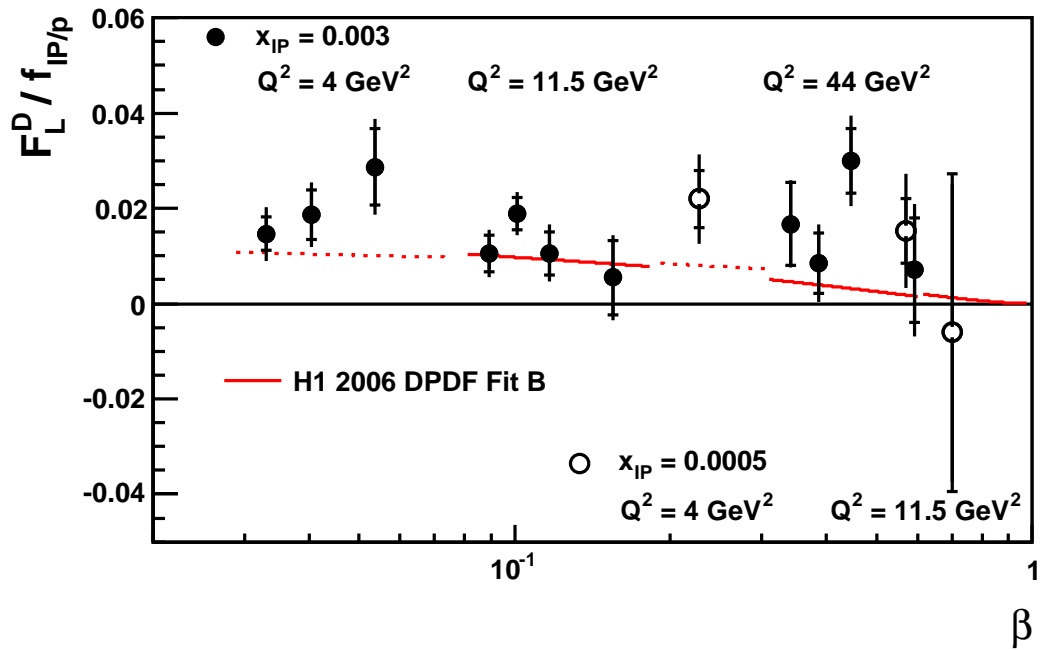


Figure 8.2: The diffractive longitudinal proton structure function  $F_L^D$  divided by the pomeron flux as a function of  $\beta$ . Different  $Q^2$  and  $x_P$  regions are denoted in the plot. The data are shown compared to the predictions of H1 2006 DPDF Fit B. The inner error bars represent the statistical error of the measurement, the outer error bars represent the total error.

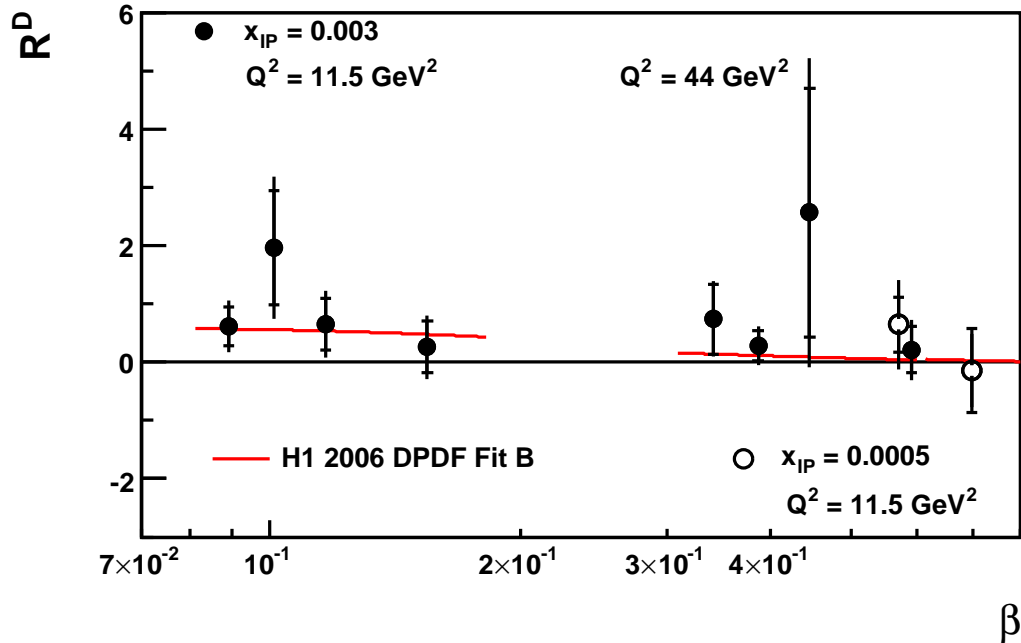


Figure 8.3: The ratio  $R^D = \frac{F_L^D}{F_T^D}$  at  $Q^2 < 7 \text{ GeV}^2$  as a function of  $\beta$ . Different  $Q^2$  and  $x_{IP}$  regions are denoted in the plot. The data are shown compared to the predictions of H1 2006 DPDF Fit B. The inner error bars represent the statistical error, the outer error bars represent the total error.

the leading twist NLO QCD fit falls to 0. At  $Q^2 = 4 \text{ GeV}^2$ , the data have no sensitivity to the ratio.

### 8.1.3 $R^D/R$

The relative importance of the longitudinally polarised photon cross section in diffractive and inclusive scattering can be compared via the ratio  $R^D/R$ . The ratio is extracted for  $Q^2 > 7 \text{ GeV}^2$  and  $10^{-3} < x_{IP} < 10^{-2}$ , and it is shown in Fig. 8.4. The data are compatible with the prediction from H1 2006 DPDF Fit B / H1 2009 PDF. At medium  $Q^2 = 11.5 \text{ GeV}^2$ , the ratio is greater than 1 which means that the gluon density in diffraction is larger than in the inclusive case, with respect to the quark densities. At high  $Q^2 = 44 \text{ GeV}^2$ , the predicted ratio is  $\sim 1$  and falls with increasing  $x$ . The data are not sensitive to the higher  $x$  region.

## 8.2 Conclusions

First measurements of the diffractive reduced cross section at centre of mass energies  $\sqrt{s}$  of 225 and 252 GeV have been presented, together with a new analysis of data at  $\sqrt{s}$  of 319 GeV. These measurements at high inelasticity  $y$  have been used to extract the first measurement of the longitudinal diffractive structure function  $F_L^D$  in the range of

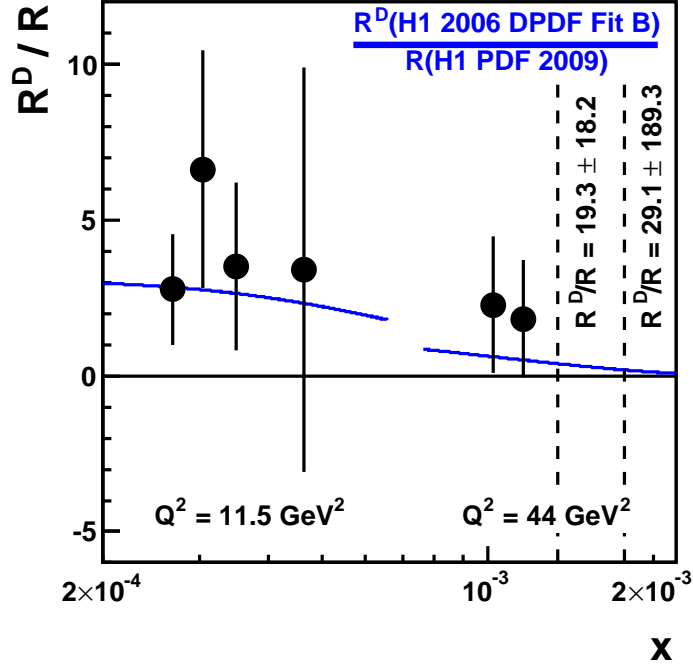


Figure 8.4: The ratio  $R^D/R$  as a function of  $x$ . The data (points) are shown compared to the prediction of H1 2006 DPDF Fit B / H1 2009 PDF (blue line). The ratios with limited precision are shown as dashed lines with the indicated value and error.

photon virtualities  $2.5 < Q^2 < 100 \text{ GeV}^2$  and longitudinal momentum fraction  $10^{-4} < x_P < 10^{-2}$ . The reduced cross section measurements and  $F_L^D$  agree well with the predictions of leading twist NLO QCD fits to previous H1 data [12] throughout the kinematic range. At large fractional momentum  $\beta$ , there is a tendency for the  $F_L^D$  data to overshoot this prediction, but the data are compatible with H1 2006 DPDF Fit A and Fit B as well as a model which includes a higher twist contribution based on a colour dipole approach.

The ratio  $R^D = \frac{F_L^D}{F_T^D} = \frac{F_L^D}{F_2^D - F_L^D}$  have been measured in the same range as  $F_L^D$ . Data agree well with the H1 2006 DPDF Fit B prediction.

Finally, the ratio  $R^D/R$  of the diffractive  $R^D = \frac{F_L^D}{F_T^D}$  to the inclusive  $R = \frac{F_L}{F_T}$  is extracted for  $Q^2 > 7 \text{ GeV}^2$  and  $10^{-3} < x_P < 10^{-2}$ . The data are compatible with the prediction from H1 2006 DPDF Fit B / H1 2009 PDF. The measured ratio indicates that the longitudinally polarised photon contribution plays a larger role in the diffractive than in the inclusive case, which means that the gluon densities are more important in diffractive than in the inclusive DIS.



# Bibliography

- [1] G. Beuf, R. Peschanski, C. Royon and D. Salek, “Systematic Analysis of Scaling Properties in Deep Inelastic Scattering,” *Phys. Rev. D* **78**, 074004 (2008), [arXiv:0803.2186 [hep-ph]].
- [2] S. Osman, D. Salek, “The Low Pt HFS and Jet Energy Calibration,” H1 internal note, H1-IN-631(02/2009).
- [3] D. Salek, “The First Measurement of the Longitudinal Diffractive Structure Function FLD,” *Proc. of XVII Int. Workshop on Deep-Inelastic Scattering and Related Topics*, Madrid, Spain, April 2009.
- [4] C. Royon, G. Beuf, R. Peschanski and D. Salek, “Geometric scaling in deep inelastic scattering,” *AIP Conf. Proc.* **1105**, 274 (2009).
- [5] Z. J. Ajaltouni *et al.*, “Proceedings of the workshop: HERA and the LHC workshop series on the implications of HERA for LHC physics,” [arXiv:0903.3861 [hep-ph]].
- [6] D. Salek, “Measurement of the longitudinal proton structure function in diffraction at the H1 experiment,” *Acta Phys. Polon. B* **39** (2008) 2515.
- [7] J.T. Anderson, K. Byrum, G. Drake, C. Ertley, H.J. Frisch, J.F. Genat, E. May, D. Salek, F. Tang, “New Developments in Fast-Sampling Readout of Micro-Channel Plate Based Large Area Pico-second Time-of-Flight Detectors,” *IEEE NSS/MIC Conference Record* (2008) 2478-2481.
- [8] C. Royon, G. Beuf, R. Peschanski and D. Salek, “Scaling properties in deep inelastic scattering,” arXiv:0811.2257 [hep-ph].
  
- [9] M. Derrick *et al.* [ZEUS Collaboration], “Observation of events with a large rapidity gap in deep inelastic scattering at HERA,” *Phys. Lett. B* **315** (1993) 481; T. Ahmed *et al.* [H1 Collaboration], “Deep inelastic scattering events with a large rapidity gap at HERA,” *Nucl. Phys. B* **429** (1994) 477.
- [10] K. J. Golec-Biernat and M. Wusthoff, “Saturation effects in deep inelastic scattering at low  $Q^2$  and its implications on diffraction,” *Phys. Rev. D* **59** (1998) 014017 [arXiv:hep-ph/9807513];  
K. J. Golec-Biernat and M. Wusthoff, “Saturation in diffractive deep inelastic scattering,” *Phys. Rev. D* **60** (1999) 114023 [arXiv:hep-ph/9903358].

- [11] J. Collins, “Proof of factorization for diffractive hard scattering,” *Phys. Rev. D* **57** (1998) 3051 [Erratum-ibid. *D* **61** (2000) 019902] [hep-ph/9709499].
- [12] A. Aktas *et al.* [H1 Collaboration], “Measurement and QCD analysis of the diffractive deep-inelastic scattering cross-section at HERA,” *Eur. Phys. J. C* **48** (2006) 715 [hep-ex/0606004].
- [13] A. Aktas *et al.* [H1 Collaboration], “Diffractive deep-inelastic scattering with a leading proton at HERA,” *Eur. Phys. J. C* **48** (2006) 749 [hep-ex/0606003].
- [14] S. Chekanov *et al.* [ZEUS Collaboration], “Deep inelastic scattering with leading protons or large rapidity gaps at HERA,” *Nucl. Phys. B* **816** (2009) 1 [arXiv:0812.2003].
- [15] S. Chekanov *et al.* [ZEUS Collaboration], “A QCD analysis of ZEUS diffractive data,” *Nucl. Phys. B* **831** (2010) 1 [arXiv:0911.4119].
- [16] A. Martin, M. Ryskin and G. Watt, “Diffractive parton distributions from perturbative QCD,” *Eur. Phys. J. C* **44** (2005) 69 [hep-ph/0504132].
- [17] A. Aktas *et al.* [H1 Collaboration], “Dijet Cross Sections and Parton Densities in Diffractive DIS at HERA,” *JHEP* **0710** (2007) 042 [arXiv:0708.3217].
- [18] A. Aktas *et al.* [H1 Collaboration], “Diffractive open charm production in deep-inelastic scattering and photoproduction at HERA,” *Eur. Phys. J. C* **50** (2007) 1 [hep-ex/0610076];  
S. Chekanov *et al.* [ZEUS Collaboration], *Nucl. Phys. B* **672** (2003) 3 [hep-ex/0307068].
- [19] A. Zee, F. Wilczek and S. B. Treiman, “Scaling Deviations For Neutrino Reactions In Asymptotically Free Field Theories,” *Phys. Rev. D* **10** (1974) 2881;  
G. Altarelli and G. Martinelli, “Transverse Momentum Of Jets In Electroproduction From Quantum Chromodynamics,” *Phys. Lett. B* **76** (1978) 89.
- [20] L. V. Gribov, E. M. Levin and M. G. Ryskin, “Semihard Processes In QCD,” *Phys. Rept.* **100** (1983) 1;  
A. H. Mueller, “Small x Behavior and Parton Saturation: A QCD Model,” *Nucl. Phys. B* **335** (1990) 115;  
N. N. Nikolaev and B. G. Zakharov, “Colour transparency and scaling properties of nuclear shadowing in deep inelastic scattering,” *Z. Phys. C* **49** (1991) 607.
- [21] E. A. Kuraev, L. N. Lipatov and V. S. Fadin, “Multi - Reggeon Processes In The Yang-Mills Theory,” *Sov. Phys. JETP* **44** (1976) 443 [*Zh. Eksp. Teor. Fiz.* **71** (1976) 840];  
E. A. Kuraev, L. N. Lipatov and V. S. Fadin, “The Pomeranchuk Singularity In Nonabelian Gauge Theories,” *Sov. Phys. JETP* **45** (1977) 199 [*Zh. Eksp. Teor. Fiz.* **72** (1977) 377];  
I. I. Balitsky and L. N. Lipatov, “The Pomeranchuk Singularity In Quantum Chromodynamics,” *Sov. J. Nucl. Phys.* **28** (1978) 822 [*Yad. Fiz.* **28** (1978) 1597].

- [22] M. Ciafaloni, “Coherence Effects In Initial Jets At Small  $Q^2 / S$ ,” Nucl. Phys. B **296** (1988) 49;  
S. Catani, F. Fiorani and G. Marchesini, “QCD Coherence In Initial State Radiation,” Phys. Lett. B **234** (1990) 339;  
S. Catani, F. Fiorani and G. Marchesini, “Small X Behavior Of Initial State Radiation In Perturbative QCD,” Nucl. Phys. B **336** (1990) 18;  
G. Marchesini, “QCD coherence in the structure function and associated distributions at small x,” Nucl. Phys. B **445** (1995) 49 [hep-ph/9412327].
- [23] J. Chyla, “Quarks, Partons and Quantum Chromodynamics,” lecture notes.
- [24] C. Callan and D. Gross, Phys. Rev. Lett. **22** (1969) 156.
- [25] M. Gell-Mann and Y. Ne’eman, “The Eightfold Way,” (Benjamin, New York, 1964).
- [26] Yuri L. Dokshitzer. Calculation of the Structure Functions for Deep Inelastic Scattering and  $e^+ e^-$  Annihilation by Perturbation Theory in Quantum Chromodynamics. (in Russian). *Sov. Phys. JETP*, 46:641–653, 1977.
- [27] V. N. Gribov and L. N. Lipatov.  $e^+ e^-$  Pair Annihilation and Deep Inelastic  $e p$  Scattering in Perturbation Theory. *Yad. Fiz.*, 15:1218–1237, 1972.
- [28] V. N. Gribov and L. N. Lipatov. Deep Inelastic  $e p$  Scattering in Perturbation Theory. *Yad. Fiz.*, 15:781–807, 1972.
- [29] Guido Altarelli and G. Parisi. Asymptotic Freedom in Parton Language. *Nucl. Phys.*, B126:298, 1977.
- [30] R. Keith Ellis, Howard Georgi, Marie Machacek, H. David Politzer, and Graham G. Ross. Factorization and the Parton Model in QCD. *Phys. Lett.*, B78:281, 1978.
- [31] A.M. Cooper-Sarkar *et al.*, HERA Workshop 1987, Vol 1, p.231, ed. R. Peccei; RAL 87-112.
- [32] H1 Collaboration, “Running at Low Proton Beam Energies,” H1-10/05-622, internal note
- [33] T. Regge. Introduction to Complex Orbital Momenta. *Nuovo Cim.*, 14:951, 1959.
- [34] T. Regge. Bound States, Shadow States and Mandelstam Representation. *Nuovo Cim.*, 18:947–956, 1960.
- [35] G. F. Chew and S. C. Frautschi. Principle of Equivalence for all Strongly Interacting Particles Within the  $S$  Matrix Framework. *Phys. Rev. Lett.*, 7:394–397, 1961.
- [36] G. F. Chew and S. C. Frautschi. Regge Trajectories and the Principle of Maximum Strength for Strong Interactions. *Phys. Rev. Lett.*, 8:41–44, 1962.
- [37] A. Levy, “Low- $x$  Physics at HERA,” lecture notes.

- [38] A. Donnachie and P. V. Landshoff. Total Cross-Sections. *Phys. Lett.*, B296:227–232, 1992.
- [39] J. Bartels, *Phys. Lett. B* **298** (1993) 204.
- [40] A. M. Stasto, K. J. Golec-Biernat and J. Kwiecinski, “Geometric scaling for the total  $\gamma^* p$  cross-section in the low  $x$  region,” *Phys. Rev. Lett.* **86**, 596 (2001) [arXiv:hep-ph/0007192].
- [41] F. D. Aaron *et al.* [H1 Collaboration], “A Precision Measurement of the Inclusive  $ep$  Scattering Cross Section at HERA,” *Eur. Phys. J. C* **64** (2009) 561 [arXiv:0904.3513 [hep-ex]].
- [42] F. D. Aaron *et al.* [H1 Collaboration], “Measurement of the Inclusive  $ep$  Scattering Cross Section at Low  $Q^2$  and  $x$  at HERA” *Eur. Phys. J. C* **63** (2009) 625 [arXiv:0904.0929 [hep-ex]].
- [43] P. W. Johnson and W. Tung, *Phys. Rev. D* **16**, 2769 (1977).
- [44] C. Adloff *et al.* [H1 Collaboration], “Measurement and QCD analysis of neutral and charged current cross sections at HERA,” *Eur. Phys. J. C* **30**, 1 (2003) [arXiv:hep-ex/0304003].
- [45] C. Adloff *et al.* [H1 Collaboration], “Measurement and QCD analysis of neutral and charged current cross sections at HERA,” *Eur. Phys. J. C* **30**, 1 (2003) [arXiv:hep-ex/0304003].
- [46] A. Glazov, DIS 2010 conference.
- [47] S. Chekanov *et al.* [ZEUS Collaboration], “Dissociation of virtual photons in events with a leading proton at HERA,” *Eur. Phys. J. C* **38** (2004) 43 [arXiv:hep-ex/0408009].
- [48] M. Diehl, “Azimuthal dependence in diffractive processes,” [arXiv:hep-ph/0509107].
- [49] F. D. Aaron *et al.* [H1 Collaboration], “Measurement of the Proton Structure Function  $F_L$  at Low  $x$ ,” *Phys. Lett. B* **665** (2008) 139 [arXiv:0805.2809 [hep-ex]].
- [50] P. R. Newman, “Prospects for  $F_L^D$  measurements at HERA-II,” [arXiv:hep-ex/0511047].
- [51] K. J. Golec-Biernat and A. Łuszczak, “Diffractive parton distributions from the analysis with higher twist,” *Phys. Rev. D* **76** (2007) 114014 [arXiv:0704.1608 [hep-ph]].
- [52] E. Iancu and R. Venugopalan, “The color glass condensate and high energy scattering in QCD,” [arXiv:hep-ph/0303204].
- [53] I. Balitsky, *Nucl. Phys. B* **463**, 99 (1996);  
Y. V. Kovchegov, *Phys. Rev. D* **60**, 034008 (1999), *D* **61**, 074018 (2000).

- [54] A. B. Kaidalov, V. A. Khoze, A. D. Martin and M. G. Ryskin, “Factorization breaking in diffractive dijet production,” *Phys. Lett. B* **559**, 235 (2003) [arXiv:hep-ph/0302091].
- [55] A. D. Martin, V. A. Khoze and M. G. Ryskin, “Rapidity gap survival probability and total cross sections,” [arXiv:0810.3560 [hep-ph]].
- [56] CDF Collaboration, *Phys. Rev. Lett.* **84** (2000) 5043; *Phys. Rev. Lett.* **87** (2001) 141802.
- [57] F. D. Aaron *et al.* [H1 Collaboration], “Diffractive Dijet Photoproduction in  $ep$  Collisions at HERA,” [arXiv:1006.0946 [hep-ex]].
- [58] T. Aaltonen *et al.* [CDF Collaboration], “Observation of Exclusive Dijet Production at the Fermilab Tevatron  $p^- \bar{p}$  Collider,” *Phys. Rev. D* **77**, 052004 (2008) [arXiv:0712.0604 [hep-ex]].
- [59] B. E. Cox and J. R. Forshaw, *Comput. Phys. Commun.* **144**, 104 (2002) [arXiv:hep-ph/0010303].
- [60] J. Monk and A. Pilkington, *Comput. Phys. Commun.* **175**, 232 (2006) [arXiv:hep-ph/0502077].
- [61] M. Boonekamp and T. Kucs, *Comput. Phys. Commun.* **167**, 217 (2005) [arXiv:hep-ph/0312273].
- [62] M. G. Albrow *et al.* [FP420 R and D Collaboration], “The FP420 R&D Project: Higgs and New Physics with forward protons at the LHC,” *JINST* **4**, T10001 (2009) [arXiv:0806.0302 [hep-ex]]; <http://www.fp420.com>.
- [63] B. E. Cox, F. K. Loebinger and A. D. Pilkington, *JHEP* **0710**, 090 (2007) [arXiv:0709.3035 [hep-ph]].
- [64] C. Royon, R. Staszewski, A. Dechambre and O. Kepka, “Exclusive diffractive Higgs and jet production at the LHC,” [arXiv:1008.0255 [hep-ph]].
- [65] C. Royon, E. Chapon and O. Kepka, “Anomalous quartic and triple gauge couplings in  $\gamma$ -induced processes at the LHC,” [arXiv:1008.0258 [hep-ph]].
- [66] E. Chapon, C. Royon and O. Kepka, “Anomalous quartic  $WW\gamma\gamma$ ,  $ZZ\gamma\gamma$ , and trilinear  $WW\gamma$  couplings in two-photon processes at high luminosity at the LHC,” *Phys. Rev. D* **81**, 074003 (2010) [arXiv:0912.5161 [hep-ph]].
- [67] <http://psec.uchicago.edu/index.php>.
- [68] I. Abt *et al.* [H1 Collaboration], “The H1 detector at HERA,” *Nucl. Instrum. Meth. A* **386** (1997) 310;  
I. Abt *et al.* [H1 Collaboration], “The Tracking, calorimeter and muon detectors of the H1 experiment at HERA,” *Nucl. Instrum. Meth. A* **386** (1997) 348;  
R. Appuhn *et al.* [H1 SPACAL Group], “The H1 lead/scintillating-fibre calorimeter,” *Nucl. Instrum. Meth. A* **386** (1997) 397.

- [69] G. Schüler and H. Spiesberger, Proc. of the Workshop on Physics at HERA, eds. W. Buchmüller, G. Ingelman, Hamburg, DESY (1992) 1419.
- [70] M. Bengtsson and T. Sjöstrand, “Parton Showers In Leptoproduction Events,” Z. Phys. C **37** (1988) 465.
- [71] B. Andersson, G. Gustafson, G. Ingelman and T. Sjöstrand, “Parton Fragmentation And String Dynamics,” Phys. Rept. **97** (1983) 31.
- [72] T. Sjöstrand, “High-energy physics event generation with PYTHIA 5.7 and JETSET 7.4,” Comput. Phys. Commun. **82** (1994) 74.
- [73] R. Brun *et al.*, CERN-DD/EE-84-1 (1987).
- [74] M. Gluck, E. Reya and A. Vogt, “Dynamical parton distributions revisited,” Eur. Phys. J. C **5**, 461 (1998) [arXiv:hep-ph/9806404].
- [75] R. Brock *et al.* [CTEQ Collaboration], “Handbook of perturbative QCD: Version 1.0,” Rev. Mod. Phys. **67** (1995) 157.
- [76] [http://www-jlc.kek.jp/subg/offl/lib/docs/helix\\_manip/node3.html](http://www-jlc.kek.jp/subg/offl/lib/docs/helix_manip/node3.html).
- [77] RAPGAP 3.1: H. Jung, “Hard diffractive scattering in high-energy e p collisions and the Monte Carlo generator RAPGAP,” Comput. Phys. Commun. **86** (1995) 147.
- [78] B. List, A. Mastroberardino, “DIFFVM: A Monte Carlo generator for diffractive processes in *ep* scattering” in A. Doyle *et al.* (eds.), Proceedings of the Workshop on Monte Carlo Generators for HERA Physics, DESY-PROC-1992-02 (1999) 396.
- [79] A. Courau and P. Kessler, “QED Compton scattering in high-energy electron - proton collisions,” Phys. Rev. D **46** (1992) 117.
- [80] S. P. Baranov, O. Duenger, H. Shooshtari, and J. A. M. Vermaseren. LPAIR: A Generator for Lepton Pair Production. In \*Hamburg 1991, Proceedings, Physics at HERA, vol. 3\* 1478-1482. (see High Energy Physics Index 30 (1992) No. 12988).
- [81] Humboldt-Univ, Berlin. V.V.Arkadov *Measurement of the Deep-Inelastic ep Scattering Cross Section using the Backward Silicon tracker at the H1 Detector at HERA*
- [82] Humboldt-Univ, Berlin. A.Glazov *Measurement of the Proton Structure Functions  $F_2(x, Q^2)$  and  $FL(X, Q^2)$  with H1 Detector at HERA*
- [83] M. Jacquet, Z. Zhang, V. Brisson, S. Kermiche, C. Vallee *Absolute hadronic jet calibration of the H1 liquid Argon calorimeter*, H1 internal note, h1-0499-571
- [84] M. Peez, B. Pothault and E. Sauvan, *An Energy Flow Algorithm for Hadronic Reconstruction In OO: Hadroo2*, H1 internal note, h1-0105-616
- [85] D. Lincoln, G. Morrow and P. Kasper, Nucl. Instrum. Meth. A **345**, 449 (1994).
- [86] F. D. Aaron *et al.* [H1 Collaboration], “Jet Production in *ep* Collisions at Low  $Q^2$  and Determination of  $\alpha_s$ ,” Eur. Phys. J. C **67**, 1 (2010) [arXiv:0911.5678 [hep-ex]].

# Appendix A

## Hadronic Final State Calibration

### A.1 Introduction

The energy measurement of hadronic showers suffers from the limited energy fraction of the shower that is measurable (the visible energy) which leads to a systematic deviation from the true value and poor energy resolution. Thus, the measured energy is significantly smaller than the energy carried by the hadron that initiated the shower. The energy measurement has to be corrected for these losses in order to reconstruct, as closely as possible, the energy of the initial hadron. The correction factors are applied in order to bring the measured energy to the correct scale, i.e. the absolute energy scale of the measurement. The absolute scale of track momentum measurement and its uncertainty have been determined to better than 1%, whereas the absolute energy scale for cluster measurements in the hadronic calorimeter is known to substantially worse precision (several percents). The uncertainty in the determination of the absolute energy scale has direct impact on how well the energy of hadronic final state particles (HFS particles) can be measured. The precision in the determination of the energy scale also depends on how well the detector simulation is done. Not only the performance of the calorimeter itself has to be accurately described in the simulation but also the material budget in front of the calorimeter has to be known in detail in order to correctly reproduce the energy measurement of the calorimeter.

Different calibration methods are used by the H1 experiment with the aim of reducing the uncertainty and improving the absolute scale in the measurements of calorimeter cluster energies. The Iterative method [81, 82] and the High Pt Jet Calibration method [84, 83] are the most frequently used ones. The Iterative method provides global calibration of hadronic energy measurements (i.e. it includes all calorimeter clusters in the event), while in the High Pt Jet Calibration method only the clusters belonging to the reconstructed jets are considered. The High Pt Jet Calibration method has been developed for calibrating the energy of the jets with transverse momenta larger than 10 GeV and for high  $Q^2$  events. Recently, the jet calibrations have been enriched by a dedicated Low Pt Jet Calibration [2].

## A.2 Reference for the Hadronic Calibrations

At HERA, the electron and proton beams are colliding head-on, which means that the total transverse momentum of the initial state is zero. Thus, the total transverse momentum of the final state also has to be zero due to momentum conservation. This means that in the laboratory system the transverse momentum of the scattered electron has to be balanced by the transverse momentum of the hadronic final state. However, the experimental measurement suffers from limitations given by the detector, such as the acceptance, the resolutions of energy and momentum measurements, and particles that are escaping detection. One of the reasons of bad resolution and shift in energy measurement using the H1 LAr calorimeter is the non-compensation of the calorimeter, i.e. different response to electromagnetic and hadronic showers. Provided the scattered electron can be measured with high precision, the influence of the detector effects can be studied by using the measured transverse momentum of the scattered electron as reference in comparison with the measured transverse momentum of the hadronic final state. It should be noted that the HADROO II [84] algorithm is used for the reconstruction of hadronic final state (HFS) objects, where isolated electrons and muons are excluded from the HFS. Since the scattered electron is used as reference, all particles in the hadronic final state have to be included (i.e. also isolated electrons and muons).

At high  $Q^2$ , the scattered electron is detected in the LAr calorimeter. In this case the best reconstruction of its transverse momentum is offered by the double angle method, where  $P_T^{da}$  is given by:

$$P_T^{da} = \frac{2E_e}{\tan\frac{\theta_e}{2} + \tan\frac{\theta_h}{2}} \quad (\text{A.1})$$

where

$$\tan\frac{\theta_h}{2} = \frac{\Sigma}{P_{T,h}}. \quad (\text{A.2})$$

The angle  $\theta_h$  is the polar angle of the hadronic system, and  $\Sigma$  and  $P_{T,h}$  are defined as:

$$\Sigma = \sum_i (E_i - P_{z,i}) \quad (\text{A.3})$$

$$P_{T,h} = \sqrt{\left(\sum_i P_{x,i}\right)^2 + \left(\sum_i P_{y,i}\right)^2}. \quad (\text{A.4})$$

Due to its good performance at high  $Q^2$ , the double angle method has been used to calibrate the energy measurements of high  $P_T$  jets [84, 83].

At low  $Q^2$ , the scattered electron is detected in the SPACAL. Here the electron method provides the best determination of its transverse momentum,  $P_{T,e}$ . The performance of the  $P_{T,e}$  reconstruction can be estimated by comparing the reconstructed and generated values from Monte Carlo generated events. Figure A.1 shows the mean value of the ratio between the reconstructed and generated  $P_{T,e}$  distributions,  $\langle P_{T,e}^{rec}/P_{T,e}^{gen} \rangle$ , together with the relative resolution, defined as the standard deviation,  $\sigma$ , of the  $P_{T,e}^{rec}/P_{T,e}^{gen}$  distribution, both plotted as a function of  $P_{T,e}^{gen}$ . A comparison between the electron and double angle method, in the low  $Q^2$  region, demonstrates that the generated  $P_{T,e}$  values are very well reconstructed by the electron method, whereas the

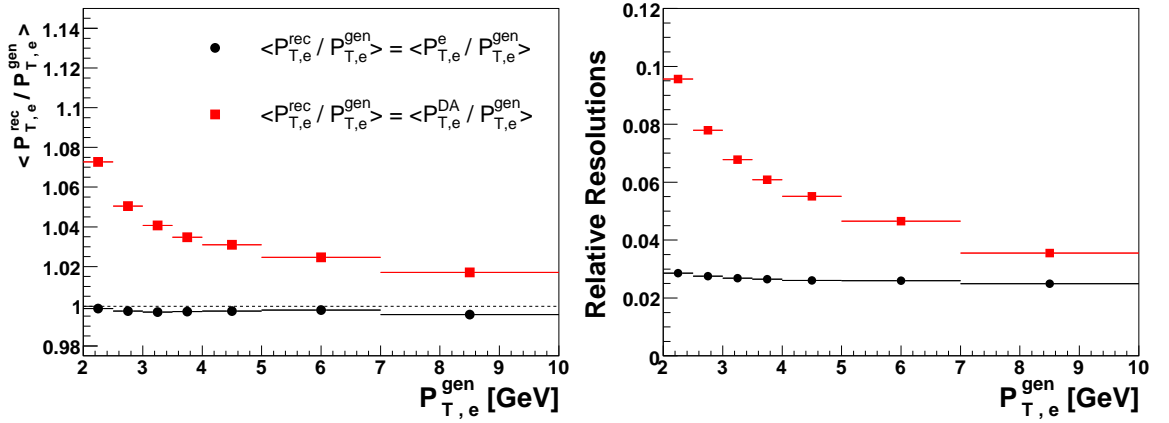


Figure A.1: The mean value of the ratio between the reconstructed and generated  $P_{T,e}$  distributions (top) and the relative resolution, defined as the standard deviation,  $\sigma$ , of the  $P_{T,e}^{rec}/P_{T,e}^{gen}$  distribution (bottom), both plotted as a function of  $P_{T,e}^{gen}$ . A comparison is made between the cases where  $P_{T,e}$  has been reconstructed using the double angle method (DA) and electron method (e), respectively.

double angle method gives much worse reconstruction, especially at low  $P_{T,e}$ . The resolution in the reconstruction is also much better for the electron method compared to the double angle method. However, it should be kept in mind that the  $P_{T,e}$  reconstruction from the electron method also depends on the uncertainty in the absolute energy scale of the SPACAL calorimeter, whereas the error in the absolute energy scale of the LAr calorimeter cancels to first order if the double angle method is applied. Still, the electron method provides by far the most accurate determination due to the high precision in the energy calibration of the electromagnetic SPACAL. Therefore the electron method will be used for the measurement of the balance between the transverse momentum of the scattered electron  $P_{T,e}$  and the total transverse momentum of HFS particles  $P_{T,h}$  defined as

$$P_T^{bal} = \frac{P_{T,h}}{P_{T,e}}. \quad (\text{A.5})$$

The limited resolution of the experimental measurement will lead to Gaussian like  $P_T$  distributions, whereas the losses due to acceptance and non-measurable particles will give a systematic shift of the distributions compared to the  $P_T$  of the scattered electron.

In Figure A.2, the  $P_T^{bal}$  distribution obtained from the low  $Q^2$  DIS data is compared with the detector simulated Monte Carlo data using the RAPGAP(dir) and DJANGO(CDM) programs. As can be seen, the RAPGAP(dir) distribution reproduces the data better than that of DJANGO(CDM). It can also be noticed that the peak value of the distributions is around 0.9, indicating that the average energy loss is around 10%. The calculated mean value of the  $P_T^{bal}$  distributions is used as an indicator of the absolute energy scale, i.e. how well the total  $P_T$  of the hadronic system is reconstructed. In order to gain some knowledge of how well the response of the detector is described by the detector simulation and how well the events are reconstructed, the double ratio of the mean  $P_T^{bal}$  values for data and Monte Carlo events can be studied.

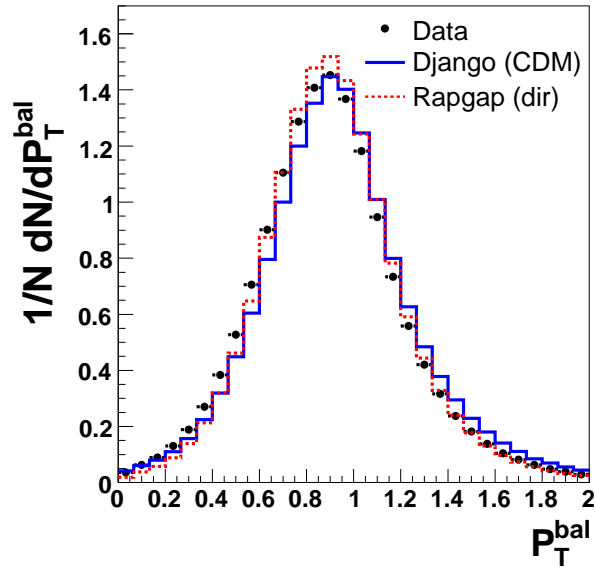


Figure A.2: The  $P_T$  balance distribution,  $P_T^{bal} = P_{T,h}/P_{T,e}$ , shown for data from DIS events, and for the Monte Carlo predictions of RAPGAP(dir) and DJANGO(CDM).

The double ratio is defined as

$$DR(P_T^{bal}) = \langle \frac{P_{T,h}}{P_{T,e}} \rangle_{data} / \langle \frac{P_{T,h}}{P_{T,e}} \rangle_{MC} \quad (\text{A.6})$$

where  $\langle P_{T,h}/P_{T,e} \rangle$  is the mean value of the  $P_T^{bal}$  distributions. If  $DR(P_T^{bal})$  is not equal to unity, different amounts of transverse momentum are reconstructed in the data and Monte Carlo events, suggesting that the knowledge of the detector and/or the event reconstruction is not good enough. Thus, the double ratio,  $DR(P_T^{bal})$ , measures the systematic uncertainty of the HFS transverse momentum. Since  $P_{T,h} \approx E_h \sin(\theta_h)$  and the uncertainty in the  $\theta_h$  reconstruction is expected to be small compared to the  $P_{T,h}$  measurement,  $DR(P_T^{bal})$  is essentially equivalent to the systematic uncertainty in the absolute energy scale.

### A.3 Iterative Calibration Method

The Iterative Calibration method uses the transverse momentum of the scattered electron as a reference and attempts to calibrate complete hadronic final state energy. Therefore this method is suitable for various kinds of inclusive analyses. Using the transverse momentum balance (A.5), the method improves the absolute energy measurement so that the transverse momentum in the whole event is conserved. However, the final goal of calibration procedure is not only to improve the energy measurement. The aim is mainly to reduce the systematic uncertainty in the absolute energy scale. As was already discussed in Section A.2, this requires an improvement of the ratios of  $P_T$  balances in data and Monte Carlo samples (A.6).

In order to achieve an accurate calibration, the Iterative method takes into account segmentation of the calorimeters, such that different calibration constants are assigned

to different parts of calorimeters. Each part of the calorimeters has its own calibration constant that is applied to all energy clusters measured there.

Since the scattered electron serves as a reference for the Iterative Calibration method, the calibration constants are extracted from DIS sample with well measured scattered electron. Selection criteria are introduced in order to reduce the photo-production background, and restrict the sample to the low  $P_T$  region. The Iterative calibration procedure is not meant to correct for the energy losses in the beam pipe in the forward region. However, the energy flow in the forward region can be rather high in standard DIS events. Therefore, the events with significant energy losses in the forward direction are removed from the calibration samples.

## A.4 Calibration Procedure

This section gives detailed information on the Iterative Calibration method. Several different approaches will be described. Calibration constants are extracted for experimental data and for three different Monte Carlo models: DJANGO(CDM), DJANGO(Lepto) and RAPGAP(dir) [69, 77]. The two DJANGO simulations use different hadronisation models. The DJANGO(CDM) Monte Carlo utilize the colour dipole model for radiation in the final state. The DJANGO(Lepto) and RAPGAP(dir) use the so-called MEPS (matrix elements + parton showers) model [70].

### A.4.1 Calibration Constants

The calibration procedure delivers constants for electromagnetic and hadronic sections of the LAr and the SPACAL calorimeters. The calorimeters are segmented into wheels (IF1, IF2, OF, FB, CB3, CB2, CB1, BBE, SPACAL). One additional wheel is added in the forward direction. In order to refer to these wheels the polar angle calculated from the nominal vertex is used. The angular ranges for separate calorimeter wheels are listed in Table A.1. However, one has to bear in mind that the polar angle is only an approximate reference to the calorimeter wheels. There is no one-to-one correspondence between the wheels and the ranges in polar angle; each of the theta bins touches also the neighbouring wheels.

The full hadronic final state is reconstructed from the standard HADROO II algorithm [84], and includes also isolated leptons. The algorithm matches the tracks measured in the tracker and the energy measurement in the calorimeter. Depending on several conditions, either one or the other measurement is preferred. Therefore, the HFS particles are classified either as 'tracks' or 'electromagnetic clusters' or 'hadronic clusters'. For each HFS particle, this classification can be found with the following code:

```
if((!inclHfs[i]->IsSelTrack() || inclHfs[i]->IsHFSClusters())) {
  // cluster
  if(inclHfs[i]->IsHFSEm()) {
    // electromagnetic
  } else {
    // hadronic
  }
}
```

calorimeter wheel	angular range (degrees)	$ \Delta\eta $
additional forward wheel	3.2 – 7	
IF1	7 – 10	0.36
IF2	10 – 15	0.41
OF	15 – 30	0.71
FB	30 – 55	0.68
CB3	55 – 80	0.43
CB2	80 – 110	0.54
CB1	110 – 135	0.53
BBE	135 – 155	0.62
SPACAL	155 – 178	

Table A.1: The different regions in polar angle of the calorimeter wheels as used in calibration and their coverage in  $\eta$ .

```

} else {
  // track
}

```

Since the tracks are assumed to be well measured, only particles in the calorimeter are calibrated. Electromagnetic and hadronic parts of each calorimeter wheel are calibrated separately because the H1 calorimeter is not compensated. There is only one constant per wheel both for the electromagnetic and the hadronic sections of calorimeter. The constants do not depend on  $P_T$  or any other quantity.

#### A.4.2 Data Selection

The selection of events used to determine the calibration constants is listed in Table A.2. These are the standard DIS cuts requiring a primary vertex in the central region, a reconstructed scattered electron, and specifying the  $Q^2$  range. The  $E - P_z$  cut is applied to reduce the photoproduction background. In order to stay in the low  $P_T$  region, a cut on transverse momentum of the scattered electron is imposed. HERA-I data are selected with sub-triggers ST0, ST3 and ST9. HERA-II data, except for the 06/07 data taking period, are selected with subtriggers ST0, ST3 and ST61. In case of the 06/07 data, sub-triggers ST2, ST3 and ST61 are used.

The HFS calibration is based on the momentum conservation in the transverse plane. The transverse momentum of all HFS particles should be balanced by the transverse momentum of the scattered electron. Since some of the HFS particles can exit undetected through the beam-pipe, the detected total 4-momentum of HFS is not always complete. To reduce such losses, only the events with polar angle of the HFS in the range  $5^\circ < \theta_h^e < 150^\circ$  are selected. The polar angle, using the electron

DIS Cuts		
	$ z_{vtx} $	$< 35$ cm
$10 \text{ GeV}^2 <$	$Q_e^2$	
$10 \text{ GeV} <$	$E'_e$	
$0.3 <$	$P_{T,h}/P_{T,e}$	for $E'_e > 24$ GeV
$0.8 <$	$P_{T,e}/P_T^{da}$	
	$R_{cl}$	$< 4$ cm
	$r_{SPACAL}$	$> 9.1$ cm for HERA-I
	$r_{SPACAL}$	$> 23$ cm for HERA-II
$1 \text{ GeV} <$	$P_{T,e}$	$< 10$ GeV
fiducial cuts		
$35 \text{ GeV} <$	$E - P_z$	
$5^\circ <$	$\theta_h^e$	$< 150^\circ$
	ST0\ST3\ST9	for HERA-I (data only)
	ST2\ST3\ST61	
	or	for HERA-II (data only)
	ST0\ST3\ST61	
	run selection	(data only)

Table A.2: A summary of cuts used for the DIS event selection (Iterative Calibration).

reconstruction method, is defined as

$$\tan \theta_h^e = \frac{2 * 27.5 \text{ GeV} - E'_e + P_{z,e}}{P_{T,e}}. \quad (\text{A.7})$$

The Iterative Calibration is not meant to compensate for the particle losses in the forward region.

Three Monte Carlo samples — DJANGO(CDM), DJANGO(Lepto) and RAPGAP(dir) — with full detector simulation are used for the calibration. The simulation contains the ESCL (improved parametrisation of electromagnetic shower shapes). The same selection criteria (except for the trigger selection, and run selection) as for data are applied to the Monte Carlo samples.

For the calibration, it is essential that the electron distributions (energy, angles,  $P_{T,e}$ ) are well described in the simulation, since the transverse momentum of the scattered electron provides the reference for HFS calibration. Then the  $P_T$  balance distributions in data and Monte Carlo can be compared. Other distributions are less relevant for calibrations. In physics analyses, it is usual to improve the agreement between the

simulation and the real data using various reweighting procedures. But in the case of the Iterative Calibration method, the reweighting would not affect resulting calibration constants. All events entering the Iterative method are treated with the same weight. No reweighting or trigger prescale weight plays role in the iterative procedure.

### A.4.3 Iterative Method

The iterative procedure developed to extract the calibration constants is described in this section. As already stated, the Iterative Calibration method delivers calibration constants for the electromagnetic and hadronic calorimeter wheels. For each wheel  $j$ , we denote these constants  $\alpha_{em,j}^{it}$  and  $\alpha_{had,j}^{it}$  respectively. The index  $it$  numbers the iteration steps throughout the whole procedure. As the iteration procedure starts with the uncalibrated HFS, the initial calibration constants  $\alpha_{em,j}^{it=0}$  and  $\alpha_{had,j}^{it=0}$  are set to 0.

The method is based on the idea of using the transverse momentum balance, defined as  $P_T^{bal} = P_{T,h}/P_{T,e}$ , to correct measured momenta of HFS particles.  $P_{T,h}$  stands for the transverse component of the HFS 4-momentum and  $P_{T,e}$  is the transverse momentum of the scattered electron. The deviation of  $P_T^{bal}$  from unity determines corrections to calibration constants in every iteration step. The method is designed to shift the  $P_T$  balance closer to unity.

$P_T$  balance of all selected events in the calibration sample is used to measure how much the calibration constants have to be altered in each iteration step. Since every calorimeter wheel has its own electromagnetic and hadronic constant, each of them has to be modified using the  $P_T$  balance distribution. In order to do so, every event is given a set of weights so that all the electromagnetic and hadronic calorimeter wheels have their own weight. These weights are set for each event quantifying how much do the HFS particles in one particular wheel (electromagnetic or hadronic) contribute to the total  $P_T$  balance distribution in the event. Different definitions of these weights will be discussed in the following section.

Having the method converged for both the data and Monte Carlo samples, the  $P_T^{bal}$  distributions are in better agreement than before the calibration. The agreement of  $P_T^{bal}$  is studied as a function of  $P_{T,e}$ ,  $Q_e^2$  and  $\theta_h^e$ .

### A.4.4 Weighting Schemes

Here, several weighting schemes are discussed along with their pros and cons that lead to the choice of the most suitable one for the Iterative Calibration method. All these schemes are based on the method described in [81]. The original method has been modified in order to improve the performance of the calibration.

**$P$  weighting scheme** In this scheme, the  $P_T^{bal}$  distribution is weighted according to the energy deposited in each calorimeter wheel. Separate calorimeter wheels  $j$  are given weights  $W_{em,j}^{it} = W_j^{it} * F_{em,j}^{it}$  for the electromagnetic and  $W_{had,j}^{it} = W_j^{it} * F_{had,j}^{it}$  for the hadronic part, where the variables are defined as follows.

$$W_j^{it} = P_j^{it} / P_h^{it} \quad (\text{A.8})$$

$$F_{em,j}^{it} = \frac{P_{em,j}^{it}}{P_{em,j}^{it} + P_{had,j}^{it}} \quad (\text{A.9})$$

$$F_{had,j}^{it} = 1 - F_{em,j}^{it} \quad (\text{A.10})$$

The vector  $\vec{P}_{em,j}^{it}$  denotes the total 4-vector of particles contained in the electromagnetic part of the wheel  $j$  using the calibration constant derived in the iteration step  $it$ . Analogously, the 4-vector  $\vec{P}_{had,j}^{it}$  for the hadronic part is defined. The total 4-vector of the particles in both electromagnetic and hadronic parts of the wheel is denoted  $\vec{P}_j^{it}$ , and  $\vec{P}_h^{it}$  is the 4-vector of the full hadronic final state. The previous equations utilize the 3-vector magnitudes of these vectors.

This definition of weights implies the following. For a given wheel, a particular event contributes to the  $P_T^{bal}$  distribution with the weight set as a fraction of the total momentum of the particles in that wheel to the sum of the total momenta from all wheels. In other words, it corresponds to the fraction of energy deposited in the wheel and the total energy of HFS deposited in the whole calorimeter.

The second row of plots in Figure A.3 shows the energy deposited in separate calorimeter wheels scaled by the transverse momentum of the scattered electron in 99/00 data. This quantity is similar to the energy flow. As seen from the plots, most of the energy goes in the forward parts of the calorimeter. On the other hand, particles going in the forward direction have smaller transverse momenta, whereas particles with high transverse momentum are mainly going in the central region (see the third row in Figure A.3). Therefore, the  $P$  weighting scheme is not a good choice for calibrations based on the  $P_T$  balance. It is not sensitive to the high transverse momentum particles and it prefers the forward region, where the particles can leave undetected through the beam-pipe.

**$P_T$  weighting scheme** This scheme weights the  $P_T^{bal}$  distributions with respect to the transverse momentum of all HFS particles in the calorimeter wheels. The electromagnetic  $W_{em,j}^{it} = W_j^{it} * F_{em,j}^{it}$  and hadronic  $W_{had,j}^{it} = W_j^{it} * F_{had,j}^{it}$  weights are defined in the following way.

$$W_j^{it} = (P_j^{it})_T / P_T^{ref} \quad (\text{A.11})$$

$$F_{em,j}^{it} = \frac{(P_{em,j}^{it})_T}{(P_{em,j}^{it})_T + (P_{had,j}^{it})_T} \quad (\text{A.12})$$

$$F_{had,j}^{it} = 1 - F_{em,j}^{it}, \quad (\text{A.13})$$

where  $P_T^{ref}$  stands for a reference transverse momentum. It can be either the transverse component of total HFS 4-vector  $(P^{it})_{T,h}$  or the transverse momentum of the scattered electron  $P_{T,e}$ . Both possibilities will be discussed in Section A.4.6. Here, for a given wheel, one particular event contributes to the  $P_T^{bal}$  distribution with the weight calculated as the ratio of the transverse component of the total momentum of HFS particles in this wheel to that of all HFS particles.

On the contrary to the  $P$  weighting scheme, this scheme is more sensitive to the central region. The plots in the last row in Figure A.3 show the total transverse momentum of HFS particles in separate wheels scaled by the transverse momentum of the scattered electron. This scenario is more suitable for calibrations based on the  $P_T$  balance, since the weights prefer the wheels where the transverse momenta are high and disfavour the forward region where the energy losses take place.

However, there is one shortcoming of the  $P_T$  weighting scheme. It does not accurately ascribe the weight according to the real contribution of the particles

in the wheel to the total transverse momentum in the event. The contribution to the total transverse momentum in the event is not proportional to the total transverse momentum in the wheel. It is proportional to its projection in the direction of the total momentum in the transverse plane. This is fixed in the  $\vec{P}_T$ -projection weighting scheme described below.

**$\vec{P}_T$ -projection weighting scheme** This weighting scheme is sensitive not only to the total transverse momentum (as the  $P_T$  weighting scheme), but also to the direction of the momentum vector in the transverse plane. One can then project the transverse momentum of the HFS particles in the wheel to the direction of the scattered electron, and thus obtain the real contribution of these particles to the total transverse momentum in the event<sup>1</sup>. Here, the  $P_T^{bal}$  distribution is weighted with  $W_{em,j}^{it}$  for the electromagnetic wheels and  $W_{had,j}^{it}$  for the hadronic wheels with the weights defined as

$$W_{em,j}^{it} = (1 + \alpha_{em,j}^{it}) * (P_{em,j})_{proj} / P_T^{ref} \quad (\text{A.14})$$

$$W_{had,j}^{it} = (1 + \alpha_{had,j}^{it}) * (P_{had,j})_{proj} / P_T^{ref}, \quad (\text{A.15})$$

where

$$(P_{em,j})_{proj} = \left| (P_{em,j})_T * \cos(\phi_{em,j}) \right| \quad (\text{A.16})$$

$$\phi_{em,j} = \text{atan}((P_{em,j})_y / (P_{em,j})_x) - \phi^e \quad (\text{A.17})$$

$$(P_{had,j})_{proj} = \left| (P_{had,j})_T * \cos(\phi_{had,j}) \right| \quad (\text{A.18})$$

$$\phi_{had,j} = \text{atan}((P_{had,j})_y / (P_{had,j})_x) - \phi^e \quad (\text{A.19})$$

and  $\phi^e$  is the azimuthal angle of the scattered electron.  $\phi_{em,j}$ , resp.  $\phi_{had,j}$ , is the difference between the azimuthal angle of the total momentum of the uncalibrated particles in the electromagnetic, resp. hadronic, part of the wheel and the azimuthal angle of the scattered electron.  $(P_{em,j})_{proj}$ , resp.  $(P_{had,j})_{proj}$  is then the projected size of the transverse momentum  $(P_{em,j})_T$ , resp.  $(P_{had,j})_T$ , in the wheel in the direction of the scattered electron in the transverse plane.

#### A.4.5 Extraction of the Calibration Constants

The iterative procedure works in the following steps.

- In each iteration, a loop over all events in the calibration sample is performed. For every event, the total 4-momentum of all HFS particles in every calorimeter wheel is calculated as a sum of the three components referring to tracks, electromagnetic and hadronic clusters in the calorimeter.

$$\vec{P}_j^{it} = \vec{P}_{track,j} + \vec{P}_{had,j}^{it} + \vec{P}_{em,j}^{it} \quad (\text{A.20})$$

---

<sup>1</sup>Projecting in the direction of the scattered electron is the same to projecting in the direction of the total HFS momentum vector since these are back-to-back.

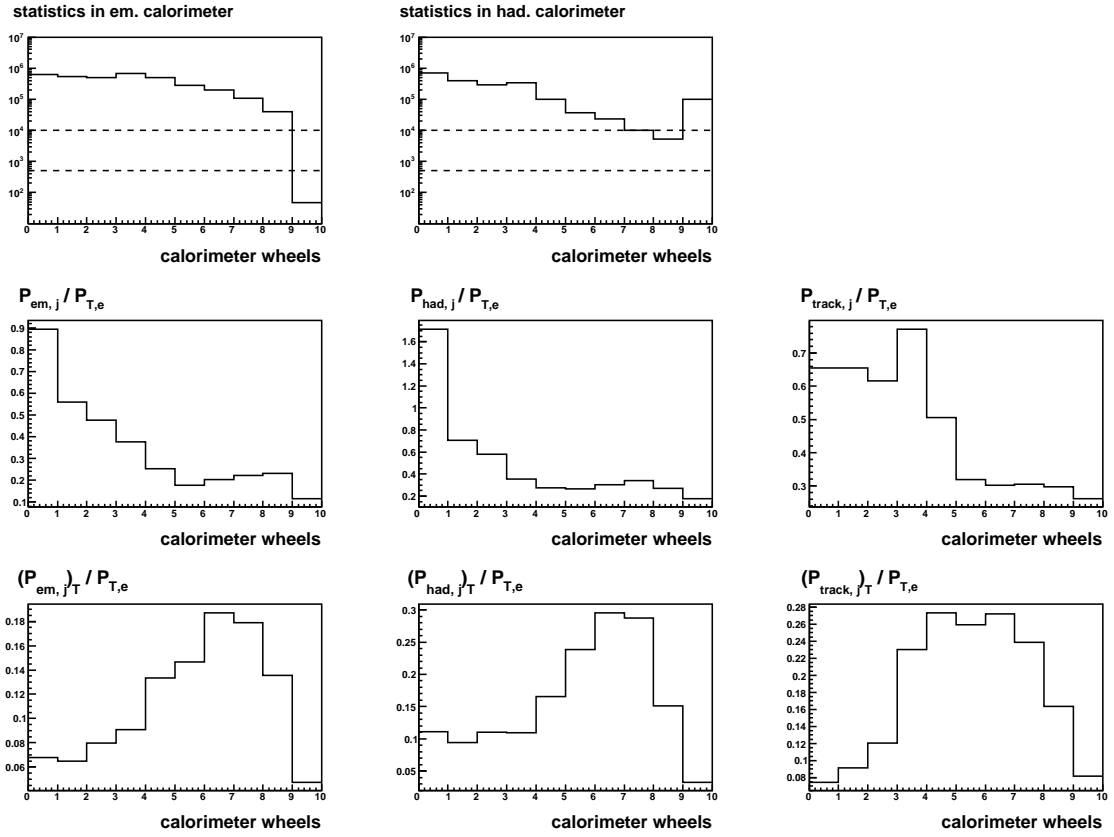


Figure A.3: The first row of histograms shows statistics in separate calorimeter wheels (sum of all particles in all selected events). The second row shows mean values of  $P_{em,j}/P_{T,e}$ ,  $P_{had,j}/P_{T,e}$  and  $P_{track,j}/P_{T,e}$ . The first two are similar to the weights used in  $P$  weighting scheme. The last row displays mean values of  $(P_{em,j})_T/P_{T,e}$ ,  $(P_{had,j})_T/P_{T,e}$  and  $(P_{track,j})_T/P_{T,e}$ . The first two are similar to the weights used in  $P_T$  weighting scheme. The histogram bins correspond to the calorimeter wheels (0 = forward wheel, 9 = SPACAL). 99/00 data sample is used.

Tracks are not being calibrated. Relevant calibration constants are being applied to electromagnetic and hadronic clusters in the following way:

$$\vec{P}_{em,j}^{it} = (1 + \alpha_{em,j}^{it}) * \vec{P}_{em,j} \quad (\text{A.21})$$

$$\vec{P}_{had,j}^{it} = (1 + \alpha_{had,j}^{it}) * \vec{P}_{had,j} \quad (\text{A.22})$$

These constants evolve throughout the calibration process, thus the momenta of electromagnetic and hadronic clusters are modified during the iteration steps.

The total 4-momentum of HFS is given by the sum of 4-momenta in all wheels

$$\vec{P}_h^{it} = \sum_{j \in \text{wheels}} \vec{P}_j^{it}. \quad (\text{A.23})$$

- For each calorimeter wheel, the new calibration constant is calculated using the equation

$$(1 + \alpha_{em,j}^{it+1}) = \frac{(1 + \alpha_{em,j}^{it})}{\langle P_{T,h}^{it}/P_{T,e} \rangle_{W_{em,j}^{it}}} \quad (\text{A.24})$$

$$(1 + \alpha_{had,j}^{it+1}) = \frac{(1 + \alpha_{had,j}^{it})}{\langle P_{T,h}^{it}/P_{T,e} \rangle_{W_{had,j}^{it}}} \quad (\text{A.25})$$

where the  $\langle P_{T,h}^{it}/P_{T,e} \rangle_{W_{em,j}^{it}}$  and  $\langle P_{T,h}^{it}/P_{T,e} \rangle_{W_{had,j}^{it}}$  are the mean values of the  $P_{T,h}^{it}/P_{T,e}$  distributions weighted by the weights  $W_{em,j}^{it}$  and  $W_{had,j}^{it}$ , respectively. Only the weights differ among different wheels in the calibration procedure, all other quantities remain the same. These weights are set in every event for all electromagnetic and hadronic calorimeter wheels, and depend on the contribution of HFS particles in these wheels to the total  $P_T$  balance of the event.

In order to calculate the constants for each wheel, Equations (A.24) and (A.25), one needs to know the mean value of the weighted  $P_T$  balance distributions. Extraction of the mean value depends on statistics (number of events).

- In case there are more than 10000 entries in the histogram, a three step fit is performed. First, the statistical mean value is used to specify the range suitable for Gaussian fit. Then, the first Gaussian fit is performed and the parameters of the fit are used for closer specification of the second Gaussian fit range from  $\mu - \sigma$  to  $\mu + \sigma$ . The mean value of the second fit is taken as the final one.
- In case of smaller statistics, but larger than 500 entries, the statistical mean is used.
- In case of statistics smaller than 500 entries, no calibration is performed at all. The calibration constant for a given wheel is set to 0.

Figure A.3 shows the statistics for all calorimeter wheels in the 99/00 data sample. Dashed lines separate the regions described above, and one can see that only the electromagnetic SPACAL is not calibrated at all. Just one LAr wheel in 99/00 data sample is calibrated using the statistical mean value, and not the Gaussian

fit. Statistics in HERA-II data is generally larger, all the wheels (except of the electromagnetic SPACAL) have sufficient statistics to perform a fit. Similarly, the statistics in the Monte Carlo samples was generated so that there is enough of events for the fits.

- Deviations of  $\langle P_{T,h}^{it}/P_{T,e} \rangle_{W_{em,j}^{it}}$  and  $\langle P_{T,h}^{it}/P_{T,e} \rangle_{W_{had,j}^{it}}$  from unity give a measure of how well the HFS is calibrated in each iteration step. Convergence of the Iterative method can be tracked by the quantity  $\eta$  defined as

$$\eta = \sum_{j \in \text{wheels}} \left( (\langle P_{T,h}^{it}/P_{T,e} \rangle_{W_{em,j}^{it}} - 1)^2 + (\langle P_{T,h}^{it}/P_{T,e} \rangle_{W_{had,j}^{it}} - 1)^2 \right) \quad (\text{A.26})$$

Calibration procedure is stopped when  $\eta$  reaches 0 within a required accuracy.

### A.4.6 Convergence

Although the  $P$  weighting scheme, that defines the weights according to the energy deposited in the calorimeter wheels, reflects the energy flow and number of particles in different regions in the calorimeter, it is not suitable for calibrations based on  $P_T$  balance. The iterative procedure does not converge using the  $P$  projection weighting scheme. It can be attributed either to the energy losses in the forward region, or to the low weights in the central region where the particles with the largest transverse momenta flow. Using the  $\vec{P}_T$ -projection weighting scheme, that sets the weights according to the real contribution of particles in the wheels to the total HFS transverse momentum, the iterative procedure converges. Therefore this is the scheme finally used in the Iterative Calibration method.

Nevertheless, the convergence depends on the choice of the reference variable  $P_T^{ref}$  that acts in Equations (A.11), (A.14) and (A.15). As already stated in Section A.4.4,  $P_T^{ref}$  can either be set equal to  $P_{T,h}$  or  $P_{T,e}$ . Looking at Equations (A.14) and (A.15), the following two observations can be made. In case of  $P_T^{ref} = P_{T,e}$  the weight is sensitive only to the single calibration constant (in the nominator of the equations). Whereas by setting  $P_T^{ref} = P_{T,h}$  the weight is determined by all calibration constants via  $P_{T,h}$  (in the denominator of the equations).

Let us discuss  $P_T^{ref} = P_{T,h}$  first. At the first sight, one may say that the dependence of the weight on all constants is an advantage over the case where  $P_T^{ref} = P_{T,e}$ . But, having the evolving variable  $P_{T,h}$  in the denominator of the weight results in preferring such calibration constants that push  $P_{T,h}$  close to 0. With  $P_T^{ref} = P_{T,h}$  the iteration procedure diverges.

Now, let us set  $P_T^{ref} = P_{T,e}$ . This is the case that will be used to extract the calibration constants. With  $P_{T,e}$  as the reference in the  $\vec{P}_T$ -projection weighting scheme, the iterative procedure converges. However, it converges only in case that the hadronic SPACAL is excluded from the calibration procedure, i.e. the hadronic SPACAL calibration constant is set to 0, and it is not altered throughout the whole iteration process. This can be surprising since the energy deposited in hadronic SPACAL is relatively small in DIS events (see Figure A.3). Calibration of the hadronic part of SPACAL is problematic since it has only one interaction length.

Based on the discussion above, the Iterative method finally uses the  $\vec{P}_T$ -projection weighting scheme (with  $P_T^{ref} = P_{T,e}$ ) and the fully inclusive DIS sample. The cal-

ibration procedure is stopped after 30 iterative steps, which roughly corresponds to  $\eta \sim 10^{-6}$  (see Equation (A.26)). This method is used to extract the calibration constants for 99/00 HERA-I data, and all periods in HERA-II data.

The calibration constants obtained with this Iterative method can be used either alone, or together with the jet calibration to calibrate the particles outside jets only.

## A.5 Results

The aim of the Iterative Calibration is to reach a 2% level agreement between the  $P_T$  balance distributions in data and Monte Carlo. The results of the Iterative Calibration method can be tested with the so called double-ratios  $DR(P_T^{bal}) = \langle P_T^{bal} \rangle_{data} / \langle P_T^{bal} \rangle_{MC}$ . The double-ratios can be plotted as functions of  $Q_e^2$ ,  $P_{T,e}$  and  $\theta_h^e$  to see whether the desired 2% level agreement has been reached. The mean values of  $P_T$  balance are obtained in separate bins of  $Q_e^2$ ,  $P_{T,e}$  and  $\theta_h^e$  using the same method as described in Section A.4.5. Such fits for  $\langle P_T^{bal} \rangle$  versus  $Q_e^2$  in 99/00 period are displayed in Figure A.4. It is also important that the width of  $P_T^{bal}$  distribution is preserved throughout the calibration process. In other words, the value  $\sigma/\mu$  of the Gaussian fit should not increase after the calibration constants are applied. The plots in Figure A.4 show such behaviour, no smearing of the peaks after the calibration is observed.

### A.5.1 HERA-I Data

Figure A.5 shows the performance of the Iterative calibration in the 99/00 period. The calibration constants are extracted using the  $\vec{P}_T$  projection weighting scheme with  $P_T^{ref} = P_{T,e}$ . The performance of the calibration is checked in the same sample that was used for the extraction of the calibration constants. The first (second) row of plots compares  $P_T^{bal}$  before (after) the calibration. The Iterative calibration significantly improves the absolute energy scale, from  $\langle P_T^{bal} \rangle \sim 0.9$  to  $\langle P_T^{bal} \rangle \sim 0.96^2$ . The third (fourth) row of plots show the double-ratio agreement before (after) the calibration. The calibration improves the energy scale agreement as well and reaches the 2% agreement. However, the agreement in the 99/00 period is already good without any calibration.

### A.5.2 HERA-II Data

The agreement of the double-ratios in HERA-II data taking periods is much worse than in the HERA-I period if no calibration is applied. Figure A.6 shows the Iterative calibration performance in the 06/07 period. The first (second) row of plots compares  $P_T^{bal}$  before (after) the calibration. The Iterative calibration significantly improves the absolute energy scale. The mean values of the  $P_T^{bal}$  distributions change from

---

<sup>2</sup>A possible reason why the absolute calibration does not reach 1 is hinted in [85]. This paper describes a bias of calibration methods based on  $\chi^2$  minimization. It gives an explanation why these methods end with the calibration constants that under-calibrate the measurement. It also shows, on a simple example, how to correct for that, so that one receives the expected energy measurement after the calibration. Formula (A.26) has similar structure as  $\chi^2$ , and therefore the Iterative Calibration method is affected by the bias described in [85]. However, the correction of the calibration factors does not simply follow from the formulas in [85]. The authors leave the reference [85] as a possible starting point for future improvement of the Iterative Calibration method.

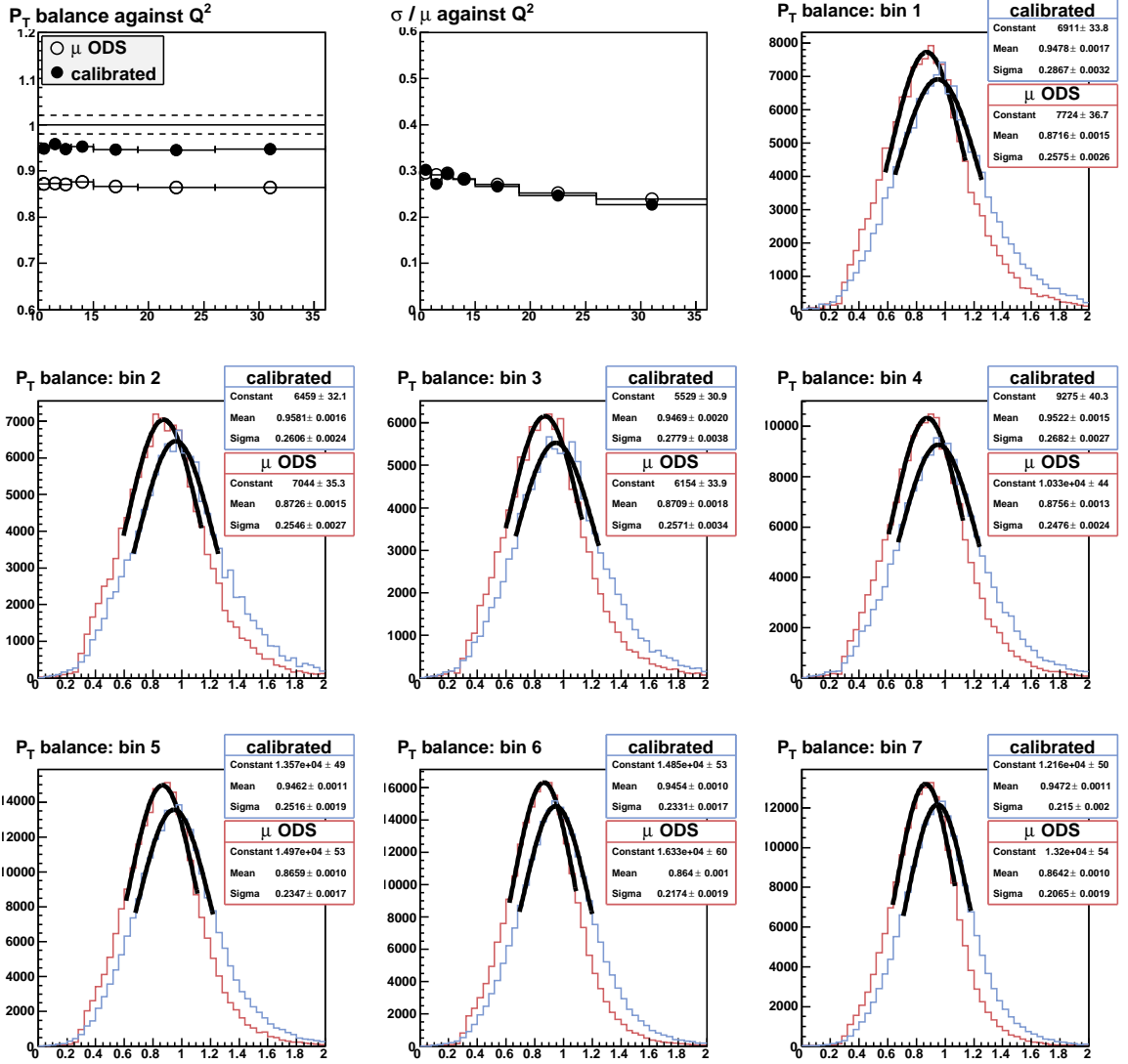


Figure A.4: Comparison of calibrated and uncalibrated  $p_T$  balance distributions in different ranges of  $Q_e^2$ . These distributions are fitted with Gaussians. Parameters of the fits  $\mu$  and  $\sigma/\mu$  are compared in the first two plots. The  $\vec{P}_T$ -projection weighting scheme with  $p_T^{ref} = p_T^e$  and 99/00 fully inclusive data sample are used.

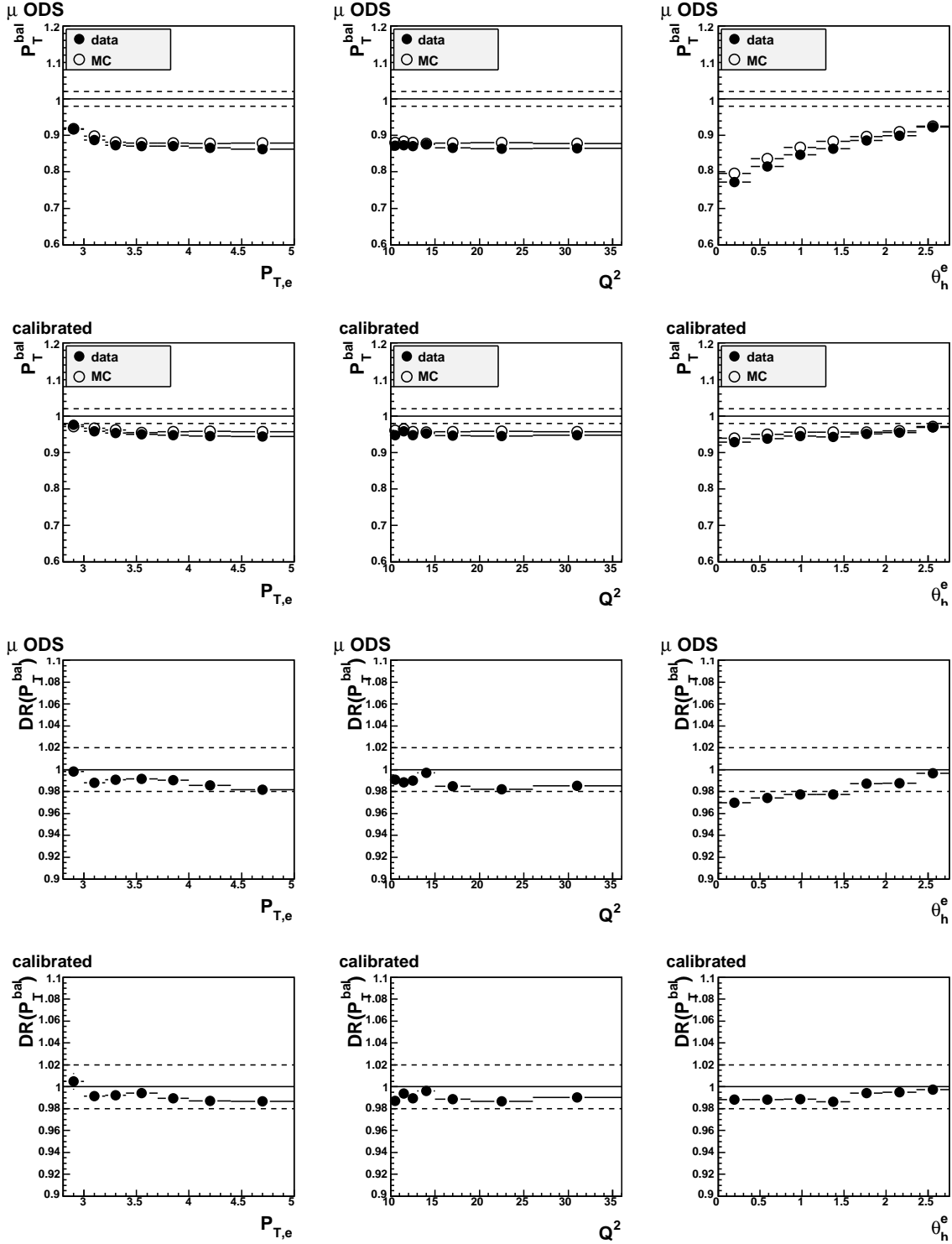


Figure A.5: Comparison of calibrated and uncalibrated  $P_T$  balance and double-ratio distributions in 99/00 data and DJANGO(CDM) model. Both are plotted as functions of  $P_{T,e}$ ,  $Q_e^2$  and  $\theta_h^e$ . The constants have been extracted using the  $\vec{P}_T$ -projection weighting scheme with  $P_T^{ref} = P_{T,e}$  on the fully inclusive sample.

$\langle P_T^{bal} \rangle \sim 0.9$  to  $\langle P_T^{bal} \rangle \sim 0.96$ , similarly as seen in HERA-I. The third (forth) row of plots show the double-ratio agreement before the calibration. These plots reveal that the hadronic energy scale uncertainty is not better than  $\sim 4\%$ . After the Iterative calibration (last row of the plots), the 2% agreement in the energy scale is reached.

### A.5.3 Model Dependence

For all data taking periods, three different models have been used to extract the Monte Carlo calibration constants: DJANGO(CDM), DJANGO(Lepto) and RAPGAP(dir). Results of the Iterative Calibration method for 06/07 period for all three models are shown in Figures A.6, A.7 and A.8. In all three cases the Iterative Calibration constants lead to significant improvement in the double-ratio plots. The 2% level agreement is reached.

The constants from each model have been applied to all three models in order to see whether the constants are model dependent or not. Although all the resulting double-ratio plots strike the 2% level agreement, there are clear differences between the three sets of constants.

- DJANGO(CDM) constants give reasonable results with DJANGO(Lepto) (see Figure A.9. When applied on RAPGAP, the  $P_T$  balance in data is approximately 1% higher than in the model (see Figure A.10).
- For the DJANGO(Lepto) constants applied on DJANGO(CDM) model, the  $P_T$  balance in data is generally 1% higher than in the model. RAPGAP(dir) constants applied on DJANGO(CDM) model give the  $P_T$  balance in data roughly 2% lower than in the model.
- RAPGAP(dir) constants applied on DJANGO(Lepto) model also give the  $P_T$  balance in data roughly 2% lower than in the model.
- Average of DJANGO(CDM) and RAPGAP(dir) constants, and average of DJANGO(CDM) and DJANGO(Lepto) constants have been studied also.

None of the constants extracted from one of the models or the average of constants from different models provide a perfect calibration when applied to another model. The constants obtained from DJANGO(CDM), however, work the best, and have been chosen as a default set. The constants from the other models are available also.

Calibration constants obtained for the data or particular model are similar among all HERA-II data taking periods. Such result is a good check of consistency of the Iterative Calibration method. Constants for data and DJANGO(CDM) model can be compared in Figure A.12.

The Iterative Calibration method is successful in calibrating the hadronic final system so that the systematic uncertainty of the absolute energy scale is 2%. There is also an apparent model dependence of the calibration constants in Monte Carlo.

## A.6 Summary

The way how the Iterative Calibration method retrieves the calibration constants for the hadronic final state clusters was described in the previous sections. The constants

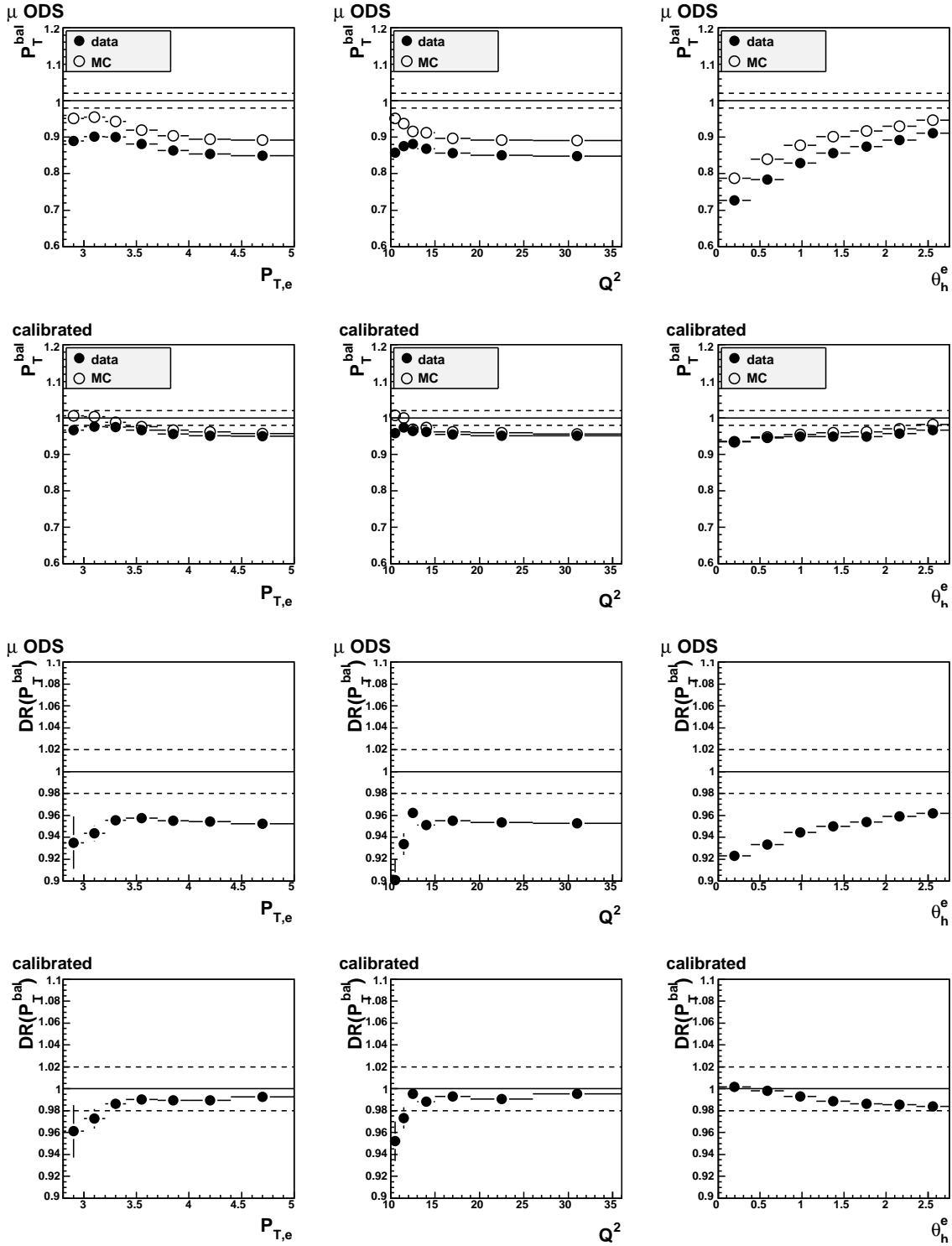


Figure A.6: Comparison of calibrated and uncalibrated  $P_T$  balance and double-ratio distributions in 06/07 period. Data and DJANGO(CDM) are compared using their own calibration constants. Both are plotted as functions of  $P_{T,e}$ ,  $Q_e^2$  and  $\theta_h^e$ .

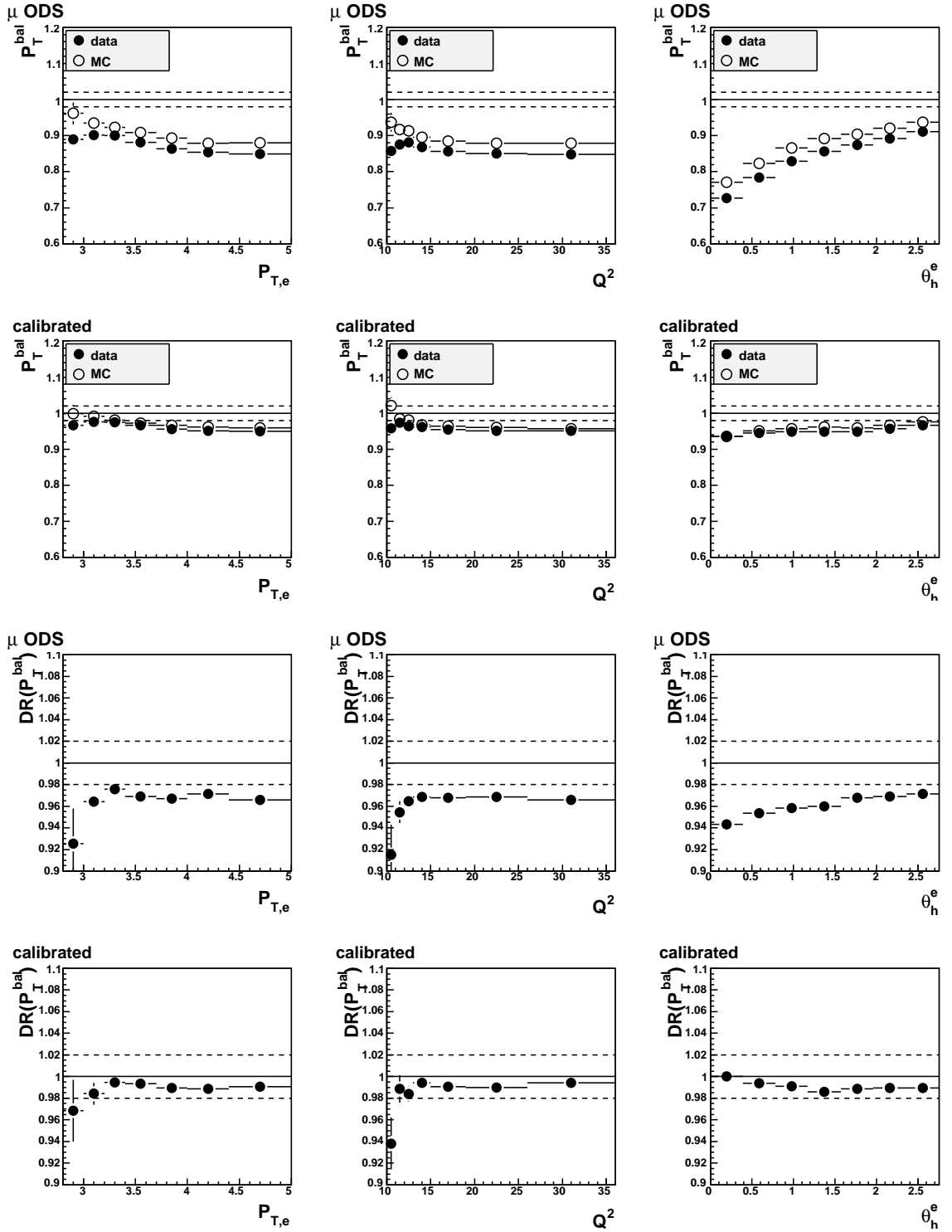


Figure A.7: Comparison of calibrated and uncalibrated  $P_T$  balance and double-ratio distributions in 06/07 period. Data and DJANGO(Lepto) are compared using their own calibration constants. Both are plotted as functions of  $P_{T,e}$ ,  $Q_e^2$  and  $\theta_h^e$ .

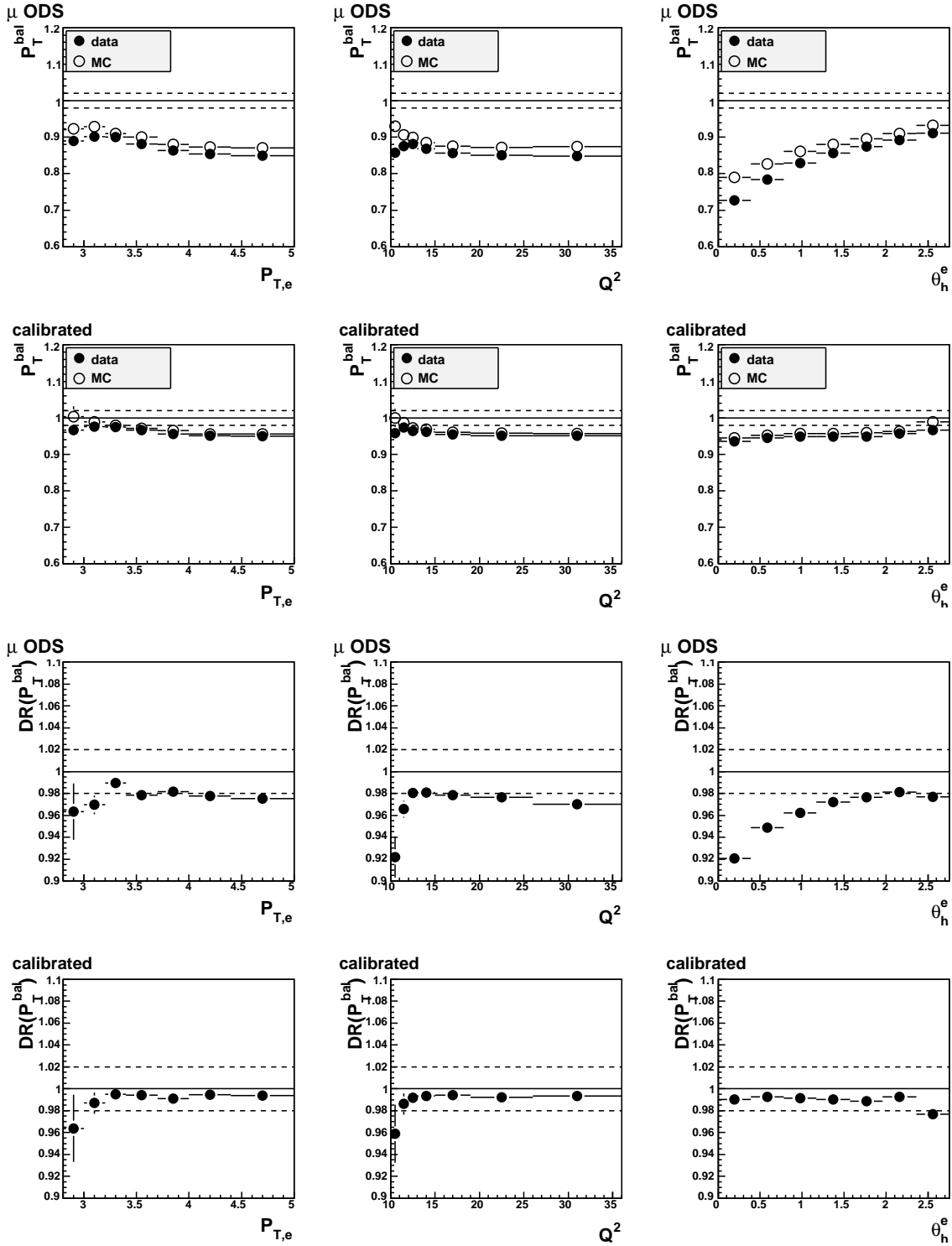


Figure A.8: Comparison of calibrated and uncalibrated  $P_T$  balance and double-ratio distributions in 06/07 period. Data and RAGAP(dir) are compared using their own calibration constants. Both are plotted as functions of  $P_{T,e}$ ,  $Q_e^2$  and  $\theta_h^e$ .

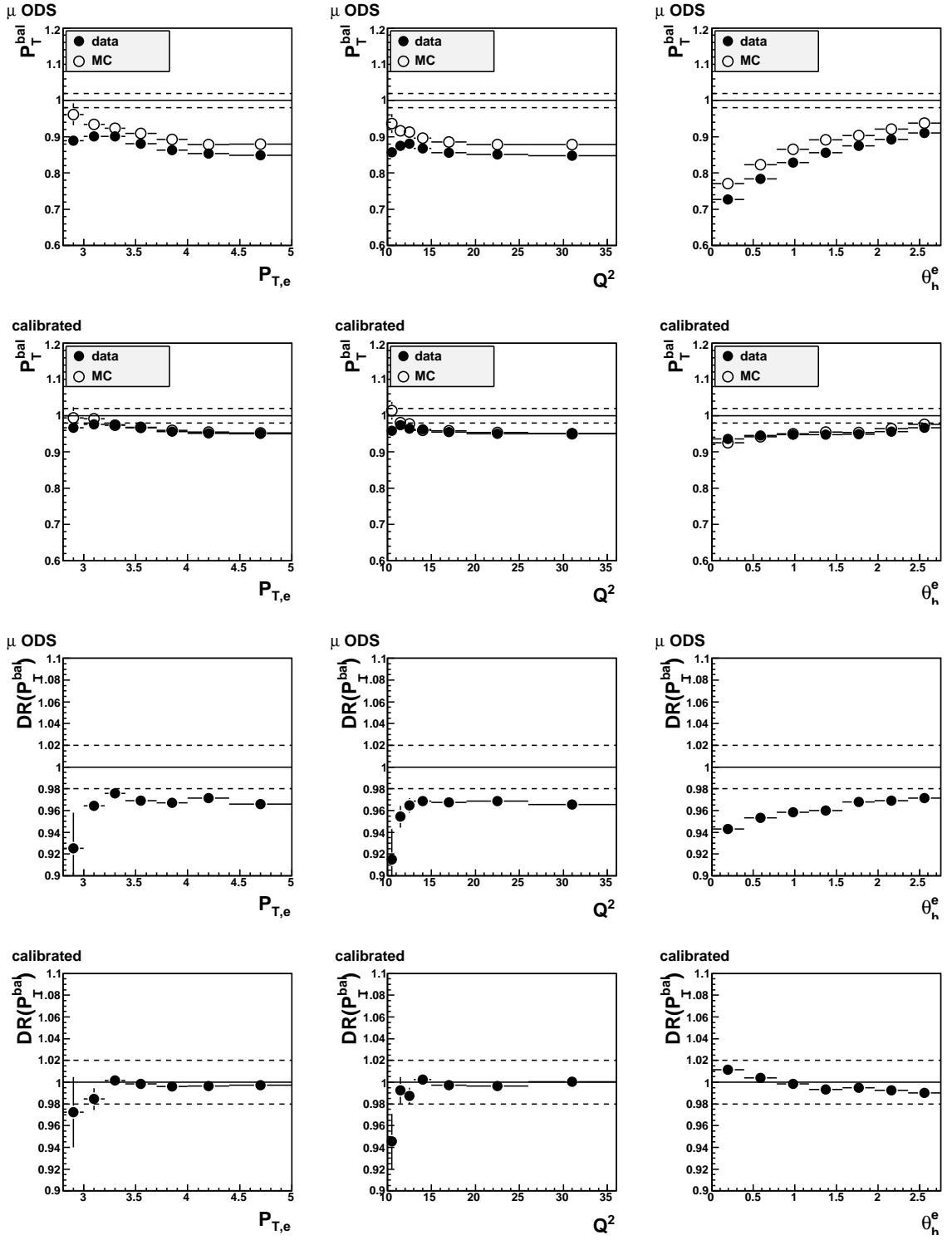


Figure A.9: Comparison of calibrated and uncalibrated  $P_T$  balance and double-ratio distributions in 06/07 period. Data and DJANGO(Lepto) are compared. DJANGO(Lepto) is calibrated with the default set of calibration constants derived from DJANGO(CDM). Both are plotted as functions of  $P_{T,e}$ ,  $Q_e^2$  and  $\theta_h^e$ .

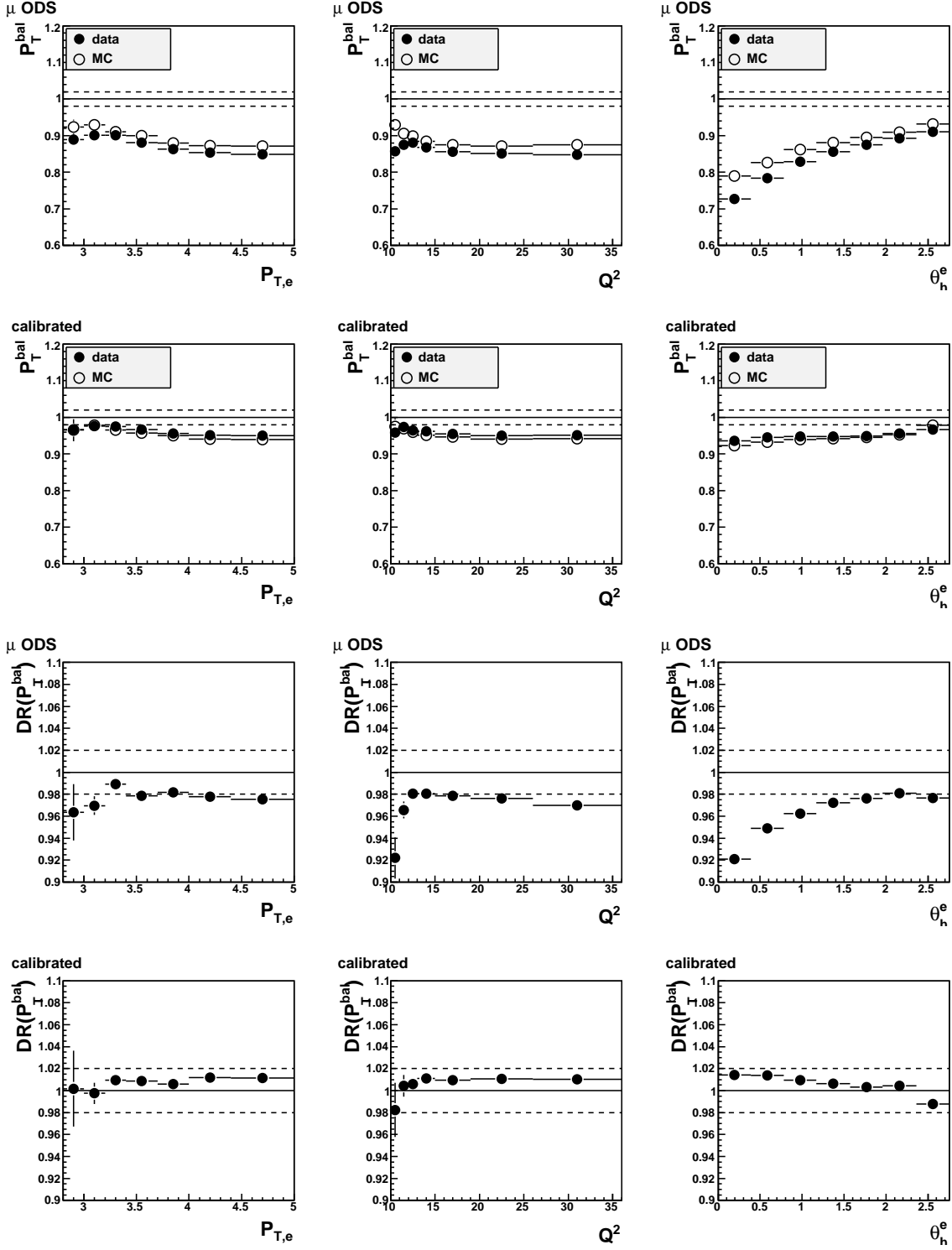


Figure A.10: Comparison of calibrated and uncalibrated  $P_T$  balance and double-ratio distributions in 06/07 period. Data and RAPGAP are compared. RAPGAP is calibrated with the default set of calibration constants derived from DJANGO(CDM). Both are plotted as functions of  $P_{T,e}$ ,  $Q_e^2$  and  $\theta_h^e$ .

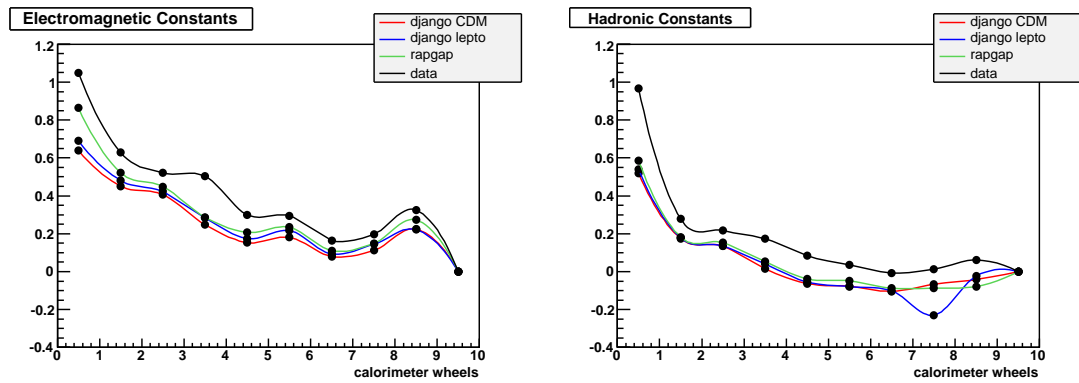


Figure A.11: Comparison of the calibration constants for 06/07 period. The histogram bins correspond to the calorimeter wheels (0 = forward wheel, 9 = SPACAL).

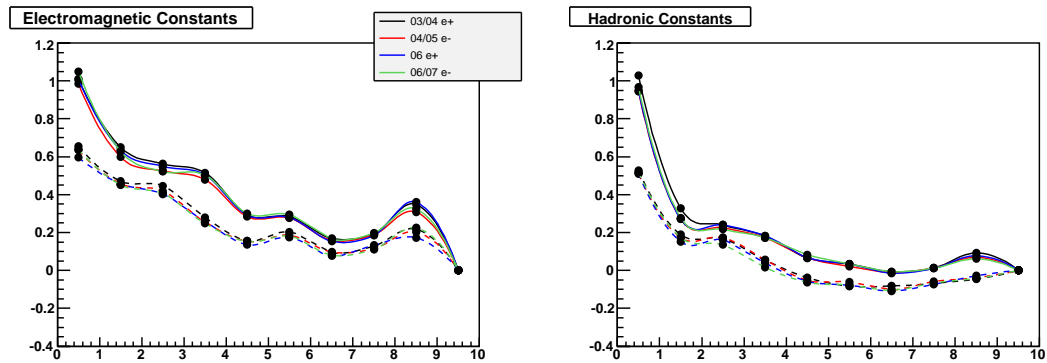


Figure A.12: Comparison of the calibration constants for all HERA-II run periods. Solid lines are the data, dashed lines are the DJANGO(CDM). The histogram bins correspond to the calorimeter wheels (0 = forward wheel, 9 = SPACAL).

can then be easily applied in physics analyses in order to improve the hadronic energy scale uncertainty. The Iterative Calibration claims to reduce this uncertainty down to 2%.

The Iterative Calibration is one of the official calibration methods used by the H1 Collaboration (together with the High Pt Jet Calibration and the Low Pt Jet Calibration). All three methods are implemented in the official object oriented software, where a special class, `H1HadronicCalibration`, was designed to incorporate all three methods in a similar code structure.

The Iterative Calibration is successfully used in the  $F_L^D$  analysis. It was also applied in the most recent measurement of  $\alpha_s$  [86], and the analysis of diffractive jets in DIS with a leading proton.

# Appendix B

## Simulation of Fast Timing Electronics

The following pages contain a copy of the published paper on “**New Developments in Fast-Sampling Readout of Micro-Channel Plate Based Large Area Pico-second Time-of-Flight Detectors**” [7].



# Appendix C

## Geometric Scaling

The following pages contain a copy of the published paper on “**Systematic Analysis of Scaling Properties in Deep Inelastic Scattering**” [1].



# Appendix D

## Cross Section Tables

$x_{\mathcal{P}}$	$Q^2$	$\beta$	$x_{\mathcal{P}}\sigma_r^D$	$\delta_{stat}$	$\delta_{uncor}$	$\delta_{cor}$	$\delta_{tot}$	$\delta_{ele}$	$\delta_{\theta}$	$\delta_{noise}$	$\delta_{spa}$	$\delta_{\beta}$	$\delta_{x_{\mathcal{P}}}$	$\delta_{rlog}$	$\delta_{model}$	$\delta_{asym}$	$\delta_{VM}$	$\delta_{QEDC}$	$\delta_{BCC}$
0.0005	4.0	0.227	0.0175	14.2	17.4	15.4	20.5	2.6	0.7	6.3	0.3	2.5	3.9	0.9	6.2	0.8	8.2	0.4	7.1
0.0005	4.0	0.323	0.0301	10.4	11.6	9.6	18.3	2.5	1.4	6.6	0.7	0.9	3.1	0.0	0.1	0.0	4.7	0.0	2.0
$x_{\mathcal{P}}$	$Q^2$	$\beta$	$x_{\mathcal{P}}\sigma_r^D$	$\delta_{stat}$	$\delta_{uncor}$	$\delta_{cor}$	$\delta_{tot}$	$\delta_{ele}$	$\delta_{\theta}$	$\delta_{noise}$	$\delta_{spa}$	$\delta_{\beta}$	$\delta_{x_{\mathcal{P}}}$	$\delta_{rlog}$	$\delta_{model}$	$\delta_{asym}$	$\delta_{VM}$	$\delta_{QEDC}$	$\delta_{BCC}$
0.0005	11.5	0.570	0.0446	13.2	11.1	8.7	18.3	1.9	0.2	7.0	2.6	0.4	1.3	2.4	0.4	1.3	0.8	8.1	1.0
0.0005	11.5	0.699	0.0640	14.0	12.1	14.9	23.7	1.7	1.3	12.5	0.9	1.0	1.6	0.5	1.2	0.0	6.7	0.5	3.8
0.0005	11.5	0.755 < $\beta$ < 1.0	0.0185	8.8	10.7	15.0	20.4	2.4	0.6	12.6	1.8	0.7	1.2	0.0	0.4	0.0	4.5	0.0	0.0
$x_{\mathcal{P}}$	$Q^2$	$\beta$	$x_{\mathcal{P}}\sigma_r^D$	$\delta_{stat}$	$\delta_{uncor}$	$\delta_{cor}$	$\delta_{tot}$	$\delta_{ele}$	$\delta_{\theta}$	$\delta_{noise}$	$\delta_{spa}$	$\delta_{\beta}$	$\delta_{x_{\mathcal{P}}}$	$\delta_{rlog}$	$\delta_{model}$	$\delta_{asym}$	$\delta_{VM}$	$\delta_{QEDC}$	$\delta_{BCC}$
0.003	4.0	0.033	0.0119	9.5	5.2	11.0	22.7	1.8	0.6	0.0	2.8	0.2	0.1	2.4	15.6	3.0	0.6	0.1	0.8
0.003	4.0	0.041	0.0132	8.0	4.9	7.8	12.2	1.0	1.0	0.6	1.4	1.2	0.0	0.5	6.6	0.4	0.3	0.0	0.6
0.003	4.0	0.054	0.0135	5.6	3.7	4.5	8.0	2.2	0.7	0.6	0.2	1.8	0.3	0.0	2.2	0.0	0.4	0.1	0.6
0.003	4.0	0.085	0.0188	8.3	4.9	5.5	11.1	1.4	1.8	1.9	0.1	2.0	0.0	0.0	0.9	0.0	0.7	0.0	3.0
0.003	4.0	0.125	0.0261	15.0	8.8	9.0	19.7	4.4	3.5	1.4	0.0	0.9	1.5	0.0	0.3	0.0	1.1	0.0	6.3
$x_{\mathcal{P}}$	$Q^2$	$\beta$	$x_{\mathcal{P}}\sigma_r^D$	$\delta_{stat}$	$\delta_{uncor}$	$\delta_{cor}$	$\delta_{tot}$	$\delta_{ele}$	$\delta_{\theta}$	$\delta_{noise}$	$\delta_{spa}$	$\delta_{\beta}$	$\delta_{x_{\mathcal{P}}}$	$\delta_{rlog}$	$\delta_{model}$	$\delta_{asym}$	$\delta_{VM}$	$\delta_{QEDC}$	$\delta_{BCC}$
0.003	11.5	0.089	0.0216	11.9	4.2	6.9	14.4	2.1	0.8	1.7	3.0	0.8	0.5	3.2	3.2	2.9	0.8	0.5	1.2
0.003	11.5	0.101	0.0190	8.3	3.5	4.1	9.9	1.1	0.6	0.5	1.3	0.6	0.1	1.6	1.7	1.1	0.9	0.0	0.9
0.003	11.5	0.117	0.0230	6.3	3.3	3.2	7.8	1.0	1.2	0.3	0.7	0.2	0.2	0.5	0.4	0.3	0.6	0.0	0.8
0.003	11.5	0.155	0.0251	3.2	2.5	2.8	4.9	1.5	0.9	0.2	0.3	0.0	0.2	0.0	0.0	0.0	0.1	0.0	0.7
0.003	11.5	0.244	0.0262	3.0	2.4	3.0	4.9	1.3	0.9	0.5	0.1	0.3	0.4	0.0	0.1	0.0	0.8	0.2	0.5
0.003	11.5	0.361	0.0317	3.1	2.5	2.7	4.8	0.8	1.1	1.0	0.0	0.1	0.7	0.0	0.1	0.0	0.2	0.1	0.0
0.003	11.5	0.631	0.0410	4.7	3.0	5.9	8.1	5.0	1.7	0.4	0.1	0.2	0.5	0.0	0.0	0.0	0.0	0.1	1.1
$x_{\mathcal{P}}$	$Q^2$	$\beta$	$x_{\mathcal{P}}\sigma_r^D$	$\delta_{stat}$	$\delta_{uncor}$	$\delta_{cor}$	$\delta_{tot}$	$\delta_{ele}$	$\delta_{\theta}$	$\delta_{noise}$	$\delta_{spa}$	$\delta_{\beta}$	$\delta_{x_{\mathcal{P}}}$	$\delta_{rlog}$	$\delta_{model}$	$\delta_{asym}$	$\delta_{VM}$	$\delta_{QEDC}$	$\delta_{BCC}$
0.003	44.0	0.341	0.0200	29.8	8.0	7.5	31.8	3.3	1.7	1.7	2.1	1.3	0.6	3.2	2.2	1.8	2.9	0.0	0.7
0.003	44.0	0.386	0.0355	8.6	4.2	3.2	10.1	0.6	0.5	0.3	0.8	0.5	0.5	1.6	0.4	0.3	0.1	0.4	0.7
0.003	44.0	0.446	0.0327	7.0	3.5	3.6	8.6	1.3	0.6	0.4	0.3	0.3	0.1	0.5	0.2	0.2	0.3	0.1	2.3
0.003	44.0	0.592	0.0387	3.8	2.6	5.5	7.2	0.6	1.2	1.4	0.0	0.2	0.3	0.0	0.0	0.0	0.7	1.0	4.8
0.003	44.0	0.76 < $\beta$ < 1.0	0.0157	4.1	2.7	9.9	11.0	0.3	1.6	2.1	0.0	0.1	0.4	0.0	0.0	0.0	0.7	1.7	0.0

Table D.1: The reduced diffractive cross section  $x_{\mathcal{P}}\sigma_r^D$  at 460 GeV. The normalisation uncertainty of 7.4% is not included.

$x_{\mathcal{P}}$	$Q^2$	$\beta$	$x_{\mathcal{P}}\sigma_r^D$	$\delta_{stat}$	$\delta_{uncor}$	$\delta_{cor}$	$\delta_{tot}$	$\delta_{ele}$	$\delta_{\theta}$	$\delta_{noise}$	$\delta_{spa}$	$\delta_{\beta}$	$\delta_{x_{\mathcal{P}}}$	$\delta_{rlog}$	$\delta_{model}$	$\delta_{asym}$	$\delta_{VM}$	$\delta_{QEDC}$	$\delta_{BCC}$
0.0005	4.0	0.186	0.0192	20.2	17.1	16.5	29.7	1.9	0.5	6.7	1.2	2.9	4.5	0.7	5.1	0.6	6.1	0.0	14.0
0.0005	4.0	0.227	0.0269	11.6	13.3	11.7	16.8	2.8	1.0	5.0	0.2	1.7	3.8	0.1	0.8	0.1	5.8	0.0	6.8
$x_{\mathcal{P}}$	$Q^2$	$\beta$	$x_{\mathcal{P}}\sigma_r^D$	$\delta_{stat}$	$\delta_{uncor}$	$\delta_{cor}$	$\delta_{tot}$	$\delta_{ele}$	$\delta_{\theta}$	$\delta_{noise}$	$\delta_{spa}$	$\delta_{\beta}$	$\delta_{x_{\mathcal{P}}}$	$\delta_{rlog}$	$\delta_{model}$	$\delta_{asym}$	$\delta_{VM}$	$\delta_{QEDC}$	$\delta_{BCC}$
0.0005	11.5	0.570	0.0456	11.6	12.4	13.8	16.3	1.5	1.8	8.3	0.2	1.0	1.8	0.5	1.0	0.2	6.8	0.2	1.1
0.0005	11.5	0.699	0.0498	14.5	11.1	10.2	20.9	1.0	1.8	7.7	0.9	1.0	1.3	0.0	0.6	0.0	4.9	0.0	3.5
0.0005	11.5	0.755 < $\beta$ < 1.0	0.0189	8.0	10.4	10.9	17.0	2.0	1.2	8.8	0.7	0.4	0.1	0.0	0.1	0.0	1.2	0.0	0.0
$x_{\mathcal{P}}$	$Q^2$	$\beta$	$x_{\mathcal{P}}\sigma_r^D$	$\delta_{stat}$	$\delta_{uncor}$	$\delta_{cor}$	$\delta_{tot}$	$\delta_{ele}$	$\delta_{\theta}$	$\delta_{noise}$	$\delta_{spa}$	$\delta_{\beta}$	$\delta_{x_{\mathcal{P}}}$	$\delta_{rlog}$	$\delta_{model}$	$\delta_{asym}$	$\delta_{VM}$	$\delta_{QEDC}$	$\delta_{BCC}$
0.003	4.0	0.033	0.0159	6.6	4.4	5.7	9.1	2.1	0.9	0.5	0.9	1.1	0.0	0.5	5.9	0.3	0.3	0.0	1.3
0.003	4.0	0.041	0.0164	9.5	4.8	5.4	11.9	0.9	0.6	0.5	0.3	1.9	0.1	0.0	3.7	0.0	0.2	0.0	0.7
0.003	4.0	0.054	0.0160	7.4	3.7	5.0	9.7	1.5	1.7	0.6	0.2	2.5	0.8	0.0	1.5	0.0	0.3	0.1	0.4
0.003	4.0	0.085	0.0171	13.9	5.8	5.9	16.2	2.2	2.3	0.5	0.2	2.6	0.2	0.0	0.7	0.0	0.3	0.0	2.9
0.003	4.0	0.125	0.0115	36.3	11.2	9.1	39.1	2.6	5.3	2.0	0.0	1.4	1.1	0.0	0.2	0.0	1.4	0.0	6.2
$x_{\mathcal{P}}$	$Q^2$	$\beta$	$x_{\mathcal{P}}\sigma_r^D$	$\delta_{stat}$	$\delta_{uncor}$	$\delta_{cor}$	$\delta_{tot}$	$\delta_{ele}$	$\delta_{\theta}$	$\delta_{noise}$	$\delta_{spa}$	$\delta_{\beta}$	$\delta_{x_{\mathcal{P}}}$	$\delta_{rlog}$	$\delta_{model}$	$\delta_{asym}$	$\delta_{VM}$	$\delta_{QEDC}$	$\delta_{BCC}$
0.003	11.5	0.089	0.0222	9.2	3.4	3.3	10.3	0.9	0.8	0.4	0.9	0.4	0.1	0.8	1.1	0.5	0.5	0.3	0.7
0.003	11.5	0.101	0.0227	7.5	3.2	3.0	8.7	1.0	1.4	0.1	0.6	0.1	0.2	0.2	0.5	0.1	0.5	0.1	0.7
0.003	11.5	0.117	0.0256	6.5	3.0	2.7	7.7	0.9	1.4	0.3	0.2	0.0	0.4	0.0	0.3	0.0	0.4	0.1	0.7
0.003	11.5	0.155	0.0288	3.4	2.4	3.0	5.1	1.6	1.1	0.1	0.1	0.4	0.4	0.0	0.2	0.0	0.1	0.1	0.7
0.003	11.5	0.244	0.0282	3.5	2.4	2.7	5.0	1.1	1.1	0.1	0.1	0.4	0.1	0.0	0.1	0.0	0.6	0.1	0.5
0.003	11.5	0.361	0.0284	4.1	2.5	2.9	5.6	0.8	1.3	0.5	0.0	0.1	0.7	0.0	0.0	0.0	0.1	0.1	0.0
$x_{\mathcal{P}}$	$Q^2$	$\beta$	$x_{\mathcal{P}}\sigma_r^D$	$\delta_{stat}$	$\delta_{uncor}$	$\delta_{cor}$	$\delta_{tot}$	$\delta_{ele}$	$\delta_{\theta}$	$\delta_{noise}$	$\delta_{spa}$	$\delta_{\beta}$	$\delta_{x_{\mathcal{P}}}$	$\delta_{rlog}$	$\delta_{model}$	$\delta_{asym}$	$\delta_{VM}$	$\delta_{QEDC}$	$\delta_{BCC}$
0.003	44.0	0.341	0.0379	8.6	3.6	2.6	9.7	1.0	0.9	0.2	0.6	0.5	0.2	0.7	0.4	0.1	0.0	0.1	0.1
0.003	44.0	0.386	0.0350	8.0	3.4	3.1	9.2	1.0	0.8	0.5	0.1	0.2	0.0	0.2	0.1	0.0	0.2	0.2	1.2
0.003	44.0	0.446	0.0316	7.7	3.2	4.0	9.2	0.9	1.4	0.8	0.1	0.2	0.3	0.0	0.0	0.0	0.1	0.5	2.6
0.003	44.0	0.592	0.0412	4.1	2.5	5.7	7.4	0.7	1.4	1.5	0.0	0.1	0.2	0.0	0.0	0.0	0.0	1.2	4.8
0.003	44.0	0.76 < $\beta$ < 1.0	0.0148	4.8	2.6	9.8	11.2	0.1	1.7	2.1	0.0	0.1	0.0	0.0	0.0	0.0	0.3	1.1	0.0

Table D.2: The reduced diffractive cross section  $x_{\mathcal{P}}\sigma_r^D$  at 575 GeV. The normalisation uncertainty of 7.4% is not included.

$x_{\mathbb{P}}$	$Q^2$	$\beta$	$x_{\mathbb{P}}\sigma_r^D$	$\delta_{stat}$	$\delta_{uncor}$	$\delta_{cor}$	$\delta_{tot}$	$\delta_{ele}$	$\delta_{\theta}$	$\delta_{noise}$	$\delta_{spa}$	$\delta_{\beta}$	$\delta_{x_{\mathbb{P}}}$	$\delta_{rlog}$	$\delta_{model}$	$\delta_{asym}$	$\delta_{VM}$	$\delta_{QEDC}$	$\delta_{BCC}$
0.0005	11.5	0.570	0.0556	1.3	10.6	7.1	8.8	0.9	2.8	4.0	0.2	0.8	1.0	0.2	0.3	0.0	3.6	0.1	1.1
0.0005	11.5	0.699	0.0581	1.6	10.2	6.7	12.3	0.9	3.2	3.8	0.2	0.5	0.7	0.1	0.1	0.0	2.2	0.1	3.2
0.0005	11.5	0.755 < $\beta$ < 1.0	0.0200	1.2	10.1	8.5	13.2	0.4	3.3	4.3	0.3	0.2	0.4	0.0	0.0	0.0	1.3	2.4	0.0
$x_{\mathbb{P}}$	$Q^2$	$\beta$	$x_{\mathbb{P}}\sigma_r^D$	$\delta_{stat}$	$\delta_{uncor}$	$\delta_{cor}$	$\delta_{tot}$	$\delta_{ele}$	$\delta_{\theta}$	$\delta_{noise}$	$\delta_{spa}$	$\delta_{\beta}$	$\delta_{x_{\mathbb{P}}}$	$\delta_{rlog}$	$\delta_{model}$	$\delta_{asym}$	$\delta_{VM}$	$\delta_{QEDC}$	$\delta_{BCC}$
0.003	11.5	0.089	0.0273	1.4	2.6	3.2	4.3	0.3	2.3	0.3	0.2	0.1	0.2	0.1	0.1	0.0	0.2	0.3	0.5
0.003	11.5	0.101	0.0276	1.3	2.5	3.3	4.4	0.1	2.2	0.2	0.5	0.2	0.1	0.1	0.1	0.0	0.2	0.2	0.6
0.003	11.5	0.117	0.0269	1.2	2.4	3.3	4.2	0.4	2.3	0.2	0.4	0.2	0.1	0.0	0.0	0.0	0.0	0.1	0.6
0.003	11.5	0.155	0.0268	0.7	2.1	3.4	4.1	0.2	2.4	0.7	0.2	0.2	0.1	0.1	0.1	0.0	0.3	0.2	0.7
0.003	11.5	0.244	0.0271	0.7	2.1	3.6	4.2	0.3	2.6	0.7	0.3	0.2	0.3	0.3	0.3	0.0	0.5	0.3	0.6
0.003	11.5	0.361	0.0296	1.3	2.4	5.3	6.0	4.3	2.3	0.3	0.3	0.3	0.4	0.3	0.3	0.0	0.7	0.1	0.5
$x_{\mathbb{P}}$	$Q^2$	$\beta$	$x_{\mathbb{P}}\sigma_r^D$	$\delta_{stat}$	$\delta_{uncor}$	$\delta_{cor}$	$\delta_{tot}$	$\delta_{ele}$	$\delta_{\theta}$	$\delta_{noise}$	$\delta_{spa}$	$\delta_{\beta}$	$\delta_{x_{\mathbb{P}}}$	$\delta_{rlog}$	$\delta_{model}$	$\delta_{asym}$	$\delta_{VM}$	$\delta_{QEDC}$	$\delta_{BCC}$
0.003	44.0	0.341	0.0379	1.8	2.8	3.1	4.5	0.5	1.2	0.5	0.2	0.2	0.2	0.2	0.2	0.0	0.1	1.6	0.8
0.003	44.0	0.386	0.0391	1.7	2.7	3.6	4.8	0.5	1.4	0.4	0.1	0.1	0.1	0.1	0.1	0.0	0.3	1.6	1.6
0.003	44.0	0.446	0.0413	1.4	2.6	4.0	5.0	0.2	1.3	1.0	0.1	0.1	0.1	0.1	0.1	0.0	0.1	1.4	2.8
0.003	44.0	0.592	0.0407	0.9	2.2	5.5	6.0	0.5	1.6	0.8	0.1	0.1	0.1	0.1	0.1	0.0	0.1	1.2	4.8
0.003	44.0	0.76 < $\beta$ < 1.0	0.0162	1.0	2.3	9.8	10.1	0.2	1.6	1.6	0.1	0.1	0.5	0.1	0.1	0.0	0.0	0.7	0.0

Table D.3: The reduced diffractive cross section  $x_{\mathbb{P}}\sigma_r^D$  at 920 GeV. The normalisation uncertainty of 7.4% is not included.

$x_{\mathcal{P}}$	$Q^2$	$\beta$	$x_{\mathcal{P}}F_L^D$	$\delta_{stat}$	$\delta_{stat+uncor}$	$\delta_{cor}$	$\delta_{tot}$	$\delta_{ele}$	$\delta_{\theta}$	$\delta_{noise}$	$\delta_{spa}$	$\delta_{\beta}$	$\delta_{x_{\mathcal{P}}}$	$\delta_{rlog}$	$\delta_{model}$	$\delta_{asym}$	$\delta_{VM}$	$\delta_{QEDC}$	$\delta_{BCC}$
0.0005	4.0	0.227	0.0317	27.0	36.1	5.1	36.4	3.9	1.0	9.4	0.4	3.7	5.8	1.3	9.2	1.2	12.1	0.5	10.6
$x_{\mathcal{P}}$	$Q^2$	$\beta$	$x_{\mathcal{P}}F_L^D$	$\delta_{stat}$	$\delta_{stat+uncor}$	$\delta_{cor}$	$\delta_{tot}$	$\delta_{ele}$	$\delta_{\theta}$	$\delta_{noise}$	$\delta_{spa}$	$\delta_{\beta}$	$\delta_{x_{\mathcal{P}}}$	$\delta_{rlog}$	$\delta_{model}$	$\delta_{asym}$	$\delta_{VM}$	$\delta_{QEDC}$	$\delta_{BCC}$
0.0005	11.5	0.570	0.0220	44.6	69.2	14.0	70.6	3.1	12.9	10.7	10.3	1.9	0.9	8.8	0.6	4.9	10.1	28.0	1.5
0.0005	11.5	0.699	-0.0087	551.8	461.4	556.1	722.6	16.0	42.9	197.9	19.3	14.5	22.1	9.7	24.5	0.0	109.0	7.1	15.9
$x_{\mathcal{P}}$	$Q^2$	$\beta$	$x_{\mathcal{P}}F_L^D$	$\delta_{stat}$	$\delta_{stat+uncor}$	$\delta_{cor}$	$\delta_{tot}$	$\delta_{ele}$	$\delta_{\theta}$	$\delta_{noise}$	$\delta_{spa}$	$\delta_{\beta}$	$\delta_{x_{\mathcal{P}}}$	$\delta_{rlog}$	$\delta_{model}$	$\delta_{asym}$	$\delta_{VM}$	$\delta_{QEDC}$	$\delta_{BCC}$
0.003	4.0	0.033	0.0147	24.2	28.3	6.7	29.1	1.8	0.6	0.4	4.6	0.3	0.3	4.0	24.4	5.4	0.8	0.1	0.5
0.003	4.0	0.041	0.0187	27.5	32.6	2.5	32.7	2.1	2.2	1.4	3.2	2.3	0.1	1.2	14.6	1.1	0.7	0.0	1.3
0.003	4.0	0.054	0.0287	28.1	33.5	1.2	33.5	6.3	1.3	1.8	0.7	4.5	0.5	0.0	6.2	0.0	1.4	0.2	1.7
$x_{\mathcal{P}}$	$Q^2$	$\beta$	$x_{\mathcal{P}}F_L^D$	$\delta_{stat}$	$\delta_{stat+uncor}$	$\delta_{cor}$	$\delta_{tot}$	$\delta_{ele}$	$\delta_{\theta}$	$\delta_{noise}$	$\delta_{spa}$	$\delta_{\beta}$	$\delta_{x_{\mathcal{P}}}$	$\delta_{rlog}$	$\delta_{model}$	$\delta_{asym}$	$\delta_{VM}$	$\delta_{QEDC}$	$\delta_{BCC}$
0.003	11.5	0.089	0.0106	35.7	41.4	5.4	41.7	6.5	8.5	6.5	8.4	2.6	2.5	9.9	10.6	8.8	1.6	0.2	1.8
0.003	11.5	0.101	0.0189	18.0	22.0	0.9	22.0	2.3	6.1	1.2	1.2	0.7	0.6	3.3	3.7	2.3	1.3	0.6	0.2
0.003	11.5	0.117	0.0106	43.1	53.6	3.2	53.7	11.2	10.5	0.5	1.4	0.7	0.5	3.1	3.2	2.0	4.3	0.7	0.7
0.003	11.5	0.155	0.0055	142.5	142.8	62.1	155.7	52.0	47.0	25.2	3.1	5.0	2.3	2.9	3.6	0.0	4.4	3.7	0.8
$x_{\mathcal{P}}$	$Q^2$	$\beta$	$x_{\mathcal{P}}F_L^D$	$\delta_{stat}$	$\delta_{stat+uncor}$	$\delta_{cor}$	$\delta_{tot}$	$\delta_{ele}$	$\delta_{\theta}$	$\delta_{noise}$	$\delta_{spa}$	$\delta_{\beta}$	$\delta_{x_{\mathcal{P}}}$	$\delta_{rlog}$	$\delta_{model}$	$\delta_{asym}$	$\delta_{VM}$	$\delta_{QEDC}$	$\delta_{BCC}$
0.003	44.0	0.341	0.0167	51.9	51.8	2.8	51.8	3.0	4.7	4.7	4.0	2.9	2.1	6.1	3.8	2.7	4.3	7.9	4.6
0.003	44.0	0.386	0.0086	73.6	89.8	9.0	90.2	4.3	10.3	5.3	5.0	5.0	5.2	12.8	3.2	2.3	4.2	15.7	10.5
0.003	44.0	0.446	0.0300	22.9	29.6	1.3	29.6	5.7	3.4	3.0	0.7	1.4	0.7	1.5	0.8	0.5	0.4	6.1	4.7
0.003	44.0	0.592	0.0071	155.9	187.5	37.9	191.3	43.2	17.5	21.0	6.3	3.7	7.1	3.1	2.4	0.0	24.1	8.9	5.2

Table D.4: The diffractive longitudinal structure function  $x_{\mathcal{P}}F_L^D$ . The normalisation uncertainty of 7.4% is not included.



# Appendix E

## H1 Preliminary $F_L^D$ Results

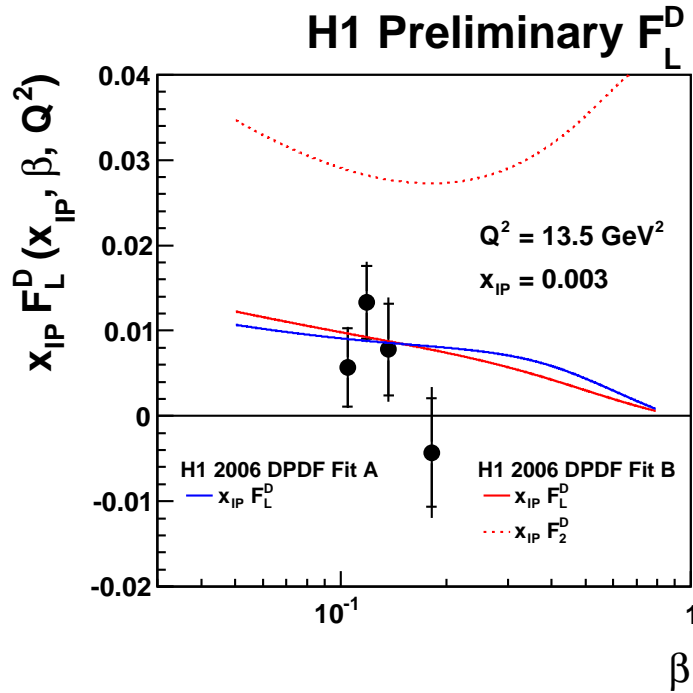


Figure E.1: The H1 Preliminary  $F_L^D$  measurement shown for the first time at the DIS 2009 conference.

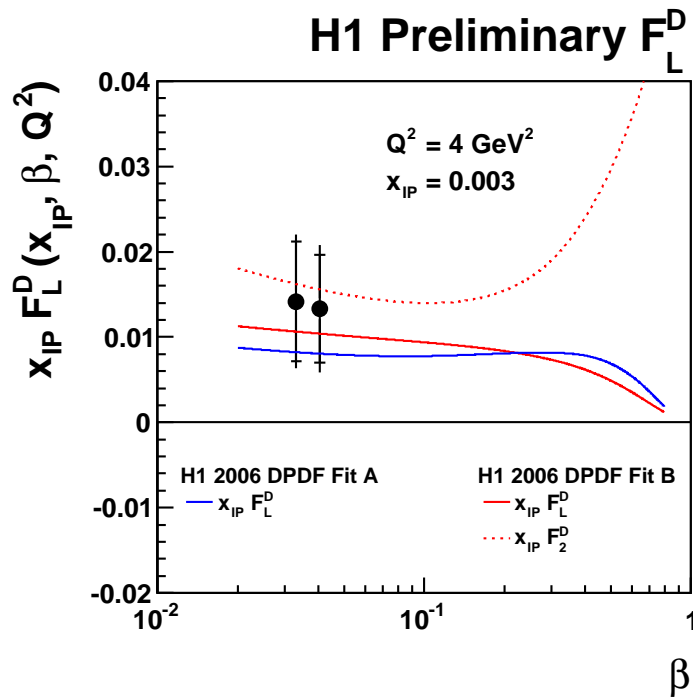


Figure E.2: The H1 Preliminary  $F_L^D$  measurement at low  $Q^2$  shown for the first time at the DIS 2010 conference.